Advanced FEA Evaluation of Growth of Postulated Circumferential PWSCC Flaws in Pressurizer Nozzle Dissimilar Metal Welds (MRP-216)

Evaluations Specific to Nine Subject Plants

1015383

Final Report DRAFT B, July 24, 2007

EPRI Project Managers
C. Harrington
C. King

EPRI • 3412 Hillview Avenue, Palo Alto, California 94304 • PO Box 10412, Palo Alto, California 94303 • USA
800.313.3774 • 650.855.2121 • askepri@epri.com • www.epri.com

DISCLAIMER OF WARRANTIES AND LIMITATION OF LIABILITIES

ORGANIZATION(S) THAT PREPARED THIS DOCUMENT

Dominion Engineering, Inc. (Except Appendix A)

Structural Integrity Associates, Inc. (Appendix A)

ORDERING INFORMATION

Requests for copies of this report should be directed to EPRI Orders and Conferences, 1355 Willow Way, Suite 278, Concord, CA 94520. Toll-free number: 800.313.3774, press 2, or internally x5379; voice: 925.609.9169; fax: 925.609.1310.

CITATIONS

This report except Appendix A was prepared by

Dominion Engineering, Inc.
11730 Plaza America Drive
Suite 310
Reston, VA 20190

Principal Investigators
G. A. White
J. E. Broussard

Contributors
J. E. Collin
M. T. Klug
D. J. Gross
V. D. Moroney

Appendix A of this report, "Supporting Probabilistic Evaluation," was prepared by

Structural Integrity Associates, Inc.
6855 South Havana Street
Suite 350
Centennial, CO 80112

Principal Investigator
P. C. Riccardella

This report describes research sponsored by EPRI.

The report is a corporate document that should be cited in the literature in the following manner:

Advanced FEA Evaluation of Growth of Postulated Circumferential PWSCC Flaws in Pressurizer Nozzle Dissimilar Metal Welds (MRP-216): Evaluations Specific to Nine Subject Plants, EPRI, Palo Alto, CA: 2007. 1015383.

REPORT SUMMARY

Background
[to be completed]

Objectives
[to be completed]

Approach
[to be completed]

Results
[to be completed]

EPRI Perspective
[to be completed]

Keywords
Alloy 600
Alloy 82/182
Crack growth modeling
Dissimilar metal piping butt welds
Dissimilar metal piping girth welds
Leak before break (LBB)
Pressurizer nozzles
Primary water stress corrosion cracking (PWSCC)

ABSTRACT

[Abstract to be completed]

ACKNOWLEDGMENTS

This study was completed with the detailed support and input of the expert review panel assembled by EPRI and of utility reviewers:

EPRI Project Management and Support

C. Harrington (EPRI), C. King (EPRI), and T. Gilman (Structural Integrity Associates)

EPRI Expert Review Panel

T. Anderson (Quest Reliability, LLC), W. Bamford (Westinghouse), D. Harris (Structural Integrity Associates), D. Killian (AREVA), P. Riccardella (Structural Integrity Associates), and K. Yoon (AREVA)

Utility Reviewers

G. Deboo (Exelon), M. Dove (Southern Co.), L. Goyette (PG&E), T. McAlister (SCANA), M. Melton (NEI), W. Sims (Entergy), D. Sutton (Southern Co.), and C. Tran (TXU Energy)

In direct support of this study, Quest Reliability, LLC extended its FEACrack software to model the growth of circumferential flaws having a custom profile. G. Thorwald and D. Revelle led the software development effort at Quest Reliability, LLC.

ACRONYMS

The following acronyms are used in this report:

ANSC	Arbitrary Net Section Collapse software
CE	Combustion Engineering
CGR	crack growth rate
COA	crack opening area
COD	crack opening displacement
DPZP	dimensionless plastic zone parameter
EPFM	elastic-plastic fracture mechanics
FEA	finite-element analysis
LBB	leak before break
MRP	Materials Reliability Program
NDE	non-destructive examination
NSC	net section collapse
NSSS	nuclear steam supply system
PWR	pressurized water reactor
PWSCC	primary water stress corrosion cracking
RCS	reactor coolant system
SCC	stress corrosion cracking
UT	ultrasonic testing

[other acronyms used in report to be added]

CONTENTS

LIST OF TABLES

LIST OF FIGURES

1 INTRODUCTION

This introductory section provides a brief background discussion, defines the purpose and scope of this study, and outlines the approach used. This section also outlines how this report is organized.

1.1 Background

1.1.1 Fall 2006 Wolf Creek Inspection Results and MRP White Paper

In October 2006, several indications of circumferential flaws were reported in the Wolf Creek pressurizer nozzles. The indications were reported to be located in the nickel-based Alloy 82/182 dissimilar metal weld material, which is known to be susceptible to primary water stress corrosion cracking (PWSCC). During its fall 2006 outage, Wolf Creek addressed the concern for growth of these circumferential indications through the previously scheduled weld overlay applications. Because of the concern that circumferential flaws could grow via the PWSCC mechanism to critical size, the Materials Reliability Program (MRP) performed a series of short-term evaluations of the implications of the Wolf Creek indications for other PWR plants. The results of those short-term evaluations were released in January 2007 in the form of an MRP "white paper"[1-1].

1.1.2 December 2006 Crack Growth Evaluations

On November 30, 2006, the NRC staff presented the results of crack growth calculations investigating past and hypothetical future growth of the circumferential indications that were reported in three of the Wolf Creek pressurizer nozzle-to-safe-end dissimilar metal welds, assuming mitigation was not applied [1-2, 1-3]. In December 2006 under sponsorship of the MRP, Dominion Engineering, Inc. (DEI) performed crack growth calculations [Section 5 of 1-1] using a finite-element analysis (FEA) approach to calculate stress intensity factors (SIFs, also denoted as K) and crack growth for comparison with the crack growth time results presented by the NRC. The circumferential indication reported for the Wolf Creek relief nozzle was the largest indication reported relative to the weld cross sectional area. Therefore, the relief nozzle was selected as the geometry to investigate for this previous calculation. Basic weld geometry and piping load inputs were maintained identical in the NRC and previous MRP calculations. Key findings of the previous MRP calculation were as follows:

- The MRP results showed significantly longer time to through-wall penetration (4.4 years for the MRP calculation) than did the NRC calculation. The main source for this difference was identified as being due to the use of conservative extrapolations of published SIF

solutions in the NRC calculation versus use of FEA calculations specific to the geometry of interest in the MRP calculation. Using the FEA approach to calculate crack tip SIFs allowed evaluation of the actual low radius-to-thickness ratio (Ri/t = 2.00) for the Wolf Creek relief nozzle dissimilar metal weld instead of extrapolating from available stress intensity factor correlations for higher Ri/t ratios.

- Although the MRP calculation showed longer time to leakage, both calculations showed no time between through-wall penetration and rupture for the case of axisymmetric welding residual stress investigated in the MRP calculation.

- The FEA approach was also used to consider the potential effect of redistribution and relaxation of welding residual stress with crack growth, which is not possible through use of standard stress intensity factor correlations based on the superposition principle. This effect did not appear to be a significant factor for the flaws considered and assumptions made in simulating welding residual stress.

- The FEA analysis results were used to calculate crack tip SIFs along the entire crack front for all flaw cases considered. These results showed that many of the larger flaw geometries had considerably lower crack tip SIFs at locations between flaw surface and the flaw center, including in many cases a region of partial crack tip closure. Therefore, assuming that the flaw maintains a semi-elliptical shape may not accurately reflect the actual crack growth under the assumed loading conditions.

In the current study presented in this report, an extensive matrix of crack growth cases was evaluated using newly developed software that models the growth of arbitrary shape flaws based on the SIF at each point along the crack front, reflecting the change in crack shape due to the influence of the complex crack loading.

1.2 Objective

The objective of this study is to evaluate the viability of on-line detection of through-wall leakage to preclude the potential for rupture for the pressurizer nozzle dissimilar metal (DM) welds in the group of nine PWRs scheduled to performed PDI inspection or mitigation during the spring 2008 outage season, given the potential concern for growing circumferential stress corrosion cracks.

1.3 Scope

The scope of this study is limited to the pressurizer nozzle DM welds in the group of nine PWRs scheduled to performed PDI inspection or mitigation during the spring 2008 outage season. All other U.S. PWR plants either do not have any Alloy 82/182 pressurizer nozzle DM welds or are scheduled to have completed PDI inspection or mitigation before December 31, 2007, the original implementation date recommended by the MRP for the pressurizer DM weld locations.

The nine subject PWR plants are Braidwood 2, Comanche Peak 2, Diablo Canyon 2, Palo Verde 2, Seabrook, South Texas Project 1, V.C. Summer, Vogtle 1, and Waterford 3. Fifty-one of the total number of 53 pressurizer nozzles in these plants are within the scope of this study. One of the spray nozzles in one plant was PDI inspected in 2005, and as such is not included in

the scope. In addition, one of the surge nozzles in one plant has already had weld overlay application, and as such is not included in the scope. Figures 1-1 through 1-3 illustrate the nozzle locations and example configurations for pressurizer nozzles in Westinghouse and CE design plants. Seven of the nine subject plants are Westinghouse design plants, and the other two are CE design plants. As discussed in Section 2, detailed weld-specific geometry, load, and fabrication parameters were collected for all 51 subject welds.

1.4 Approach

In order to facilitate modeling of the crack shape development and in direct support of this study, Quest Reliability, LLC extended its FEACrack software to model the growth of circumferential flaws having a custom profile. In Phase I of this study, the new software tools were applied to the same basic weld geometry, piping load inputs, and welding residual stress distribution assumed in the previous MRP calculation [Section 5 of 1-1]. In Phase II, an extensive crack growth sensitivity matrix was investigated to cover the geometry, load, and fabrication factors for each of the 51 subject welds, as well as the uncertainty in key modeling parameters such as those associated with welding residual stress, initial crack shape and depth, the K-dependence of the crack growth rate equation, and the effect of multiple flaws. Key Phase II activities also included detailed welding residual stress simulations covering the subject welds, development of a conservative crack stability calculation methodology, development of a leak rate calculation procedure using existing software tools (EPRI PICEP and NRC SQUIRT), and verification and validation studies.

1.5 Expert Panel

In support of this study, EPRI assembled a panel of experts experienced in the application of fracture mechanics tools to the evaluation of stress corrosion cracking. The panel included representation of individuals not recently involved in the evaluation of PWSCC in PWR components. The panel provided detail input into all phases of the project as the work was completed.

1.6 Report Structure

The organization of this report is described below.

1. PLANT INPUTS (SECTION 2)

   Section 2 summarizes the extensive weld-specific dimensional, piping load, fabrication, and weld repair history inputs that were collected for the group of 51 subject pressurizer nozzles. Detailed geometry and piping load inputs were collected for each subject weld to ensure that all welds are appropriately addressed by the crack growth sensitivity matrix (Section 7) developed as part of this study. Weld-specific fabrication and weld repair data were also collected as a key input to the welding residual stress simulations addressing the subject population (Section 3).

2. WELDING RESIDUAL STRESS (SECTION 3)

Section 3 discusses the matrix of welding residual stress (WRS) simulations were performed on the basis of the detailed design, fabrication, and weld repair information collected. Axisymmetric and non-axisymmetric weld repair WRS profiles were developed for input to the crack growth simulations under various assumptions in recognition of the uncertainty in calculation of WRS values. Validation work is still being completed comparing WRS simulation results to mockup stress measurements.

3. CRACK GROWTH MODELING (SECTION 4)

Section 4 describes the new crack growth simulation methodology, including development of the new extensions to the FEACrack software and application of the new software in the Phase I calculations based on the same Wolf Creek relief nozzle inputs previously evaluated on the basis of an assumed semi-elliptical crack shape. Section 4 also includes the results of verification and validation work, including calculation convergence checks.

4. CRITICAL CRACK SIZE CALCULATIONS (SECTION 5)

Section 5 describes the development of a conservative critical crack size methodology specific to the subject nozzle-to-safe-end geometry and materials. This methodology is based on the net section collapse (NSC) equations for an arbitrary circumferential crack profile in a thin-walled pipe. As discussed in Section 5 and for the purposes of this project, normal thermal piping loads were included in the crack stability calculations, and a Z-factor approach reducing the NSC failure load was implemented in consideration of the possibility of an EPFM failure mechanism. Finally, in support of the methodology, available experimental failure data for complex cracks in materials similar to Alloy 82/182 were evaluated.

5. LEAK RATE MODELING (SECTION 6)

Section 6 describes the leak rate calculation procedure applied to the through-wall portion of the crack growth simulations using EPRI's PICEP software. The crack opening area at the weld OD calculated in the crack growth finite-element simulations was applied directly in the PICEP leak rate calculations. NRC's SQUIRT software was also applied in a scoping study for the purpose of comparison.

6. SENSITIVITY CASE MATRIX (SECTION 7)

Section 7 discusses the development and application of an extensive crack growth sensitivity matrix covering the geometry, load, and fabrication factors for each of the 51 subject welds, as well as the uncertainty in key modeling parameters such as those associated with welding residual stress, initial crack shape and depth, the K-dependence of the crack growth rate equation, and the effect of multiple flaws. Section 7 also presents a set of evaluation criteria that was developed to guide interpretation of the matrix results. The evaluation criteria are based on explicit consideration of leak rate detection sensitivity, plant response time, and uncertainty in the crack stability calculations.

7. SUMMARY AND CONCLUSIONS (SECTION 8)

Section 8 summarizes this study, including the main conclusions. It is concluded that all 51 subject welds are adequately covered by crack growth sensitivity cases that satisfy the evaluation criteria presented in Section 7.2.

8. REFERENCES (SECTION 9)

   Section 9 lists the references cited in the main body of this report.

9. APPENDIX A: SUPPORTING PROBABILISTIC EVALUATION

   It is planned that a report on the complementary probabilistic modeling work completed by Structural Integrity Associates will be included as Appendix A in a subsequent draft of this report.

1.7 References

1-1. "Implications of Wolf Creek Pressurizer Butt Weld Indications Relative to Safety Assessment and Inspection Requirements," MRP 2007-003 Attachment 1, January 2007.

1-2. US NRC, "NRC Wolf Creek Flaw Evaluation," presented at November 30, 2006, public meeting between US NRC and MRP, North Bethesda, Maryland.

1-3. US NRC, "Safety Concerns Regarding Potential Pressurizer Weld Cracking," presented at December 20, 2006, public meeting between US NRC and MRP, Rockville, Maryland.

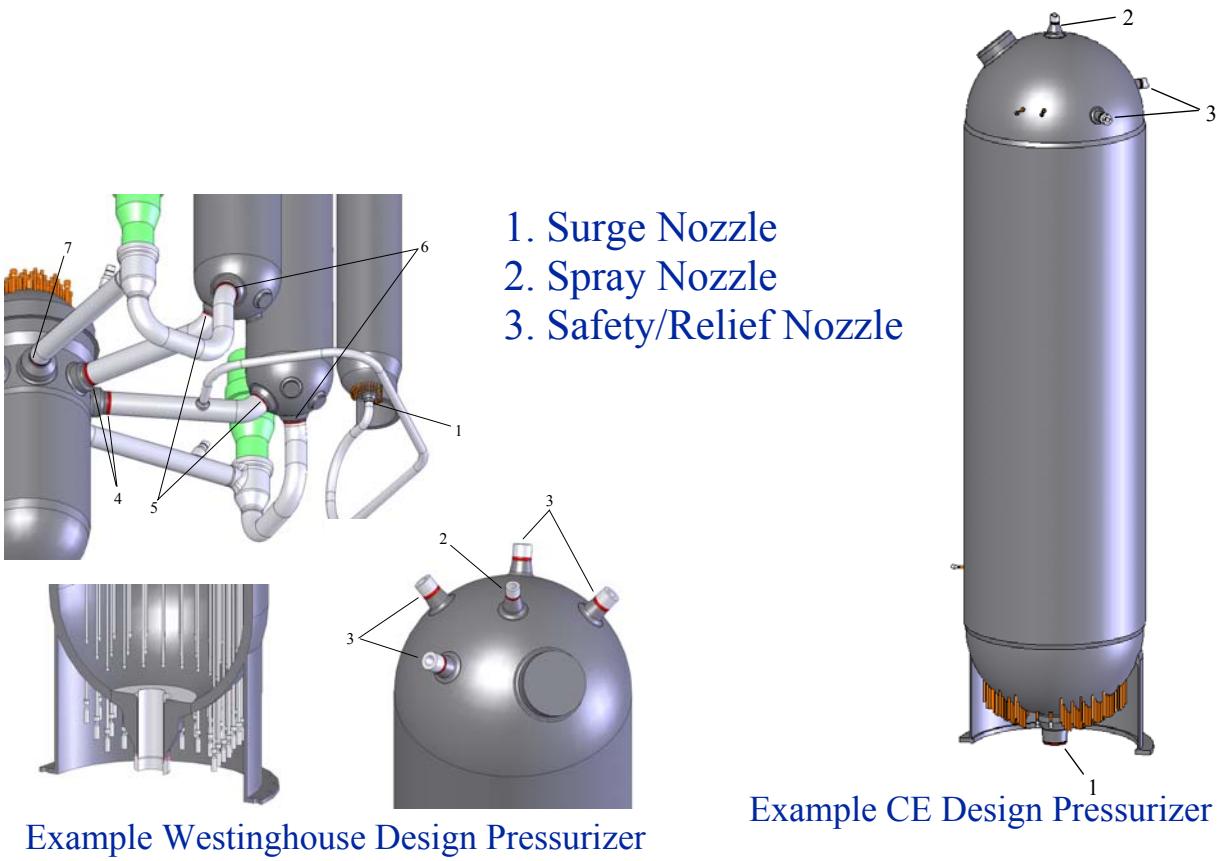

Figure 1-1
Pressurizer Nozzle Locations for Westinghouse and CE Design Plants

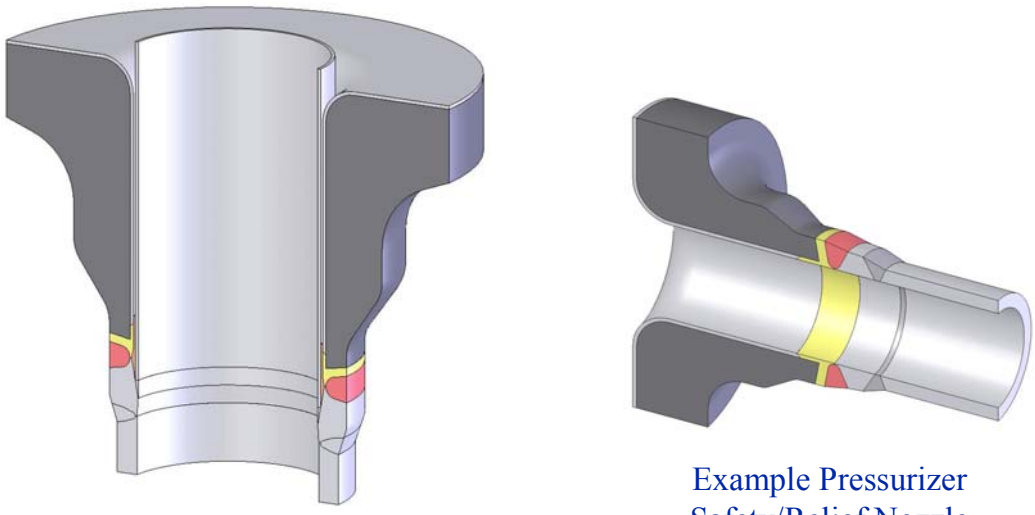

Figure 1-2
Example Westinghouse Design Pressurizer Nozzles

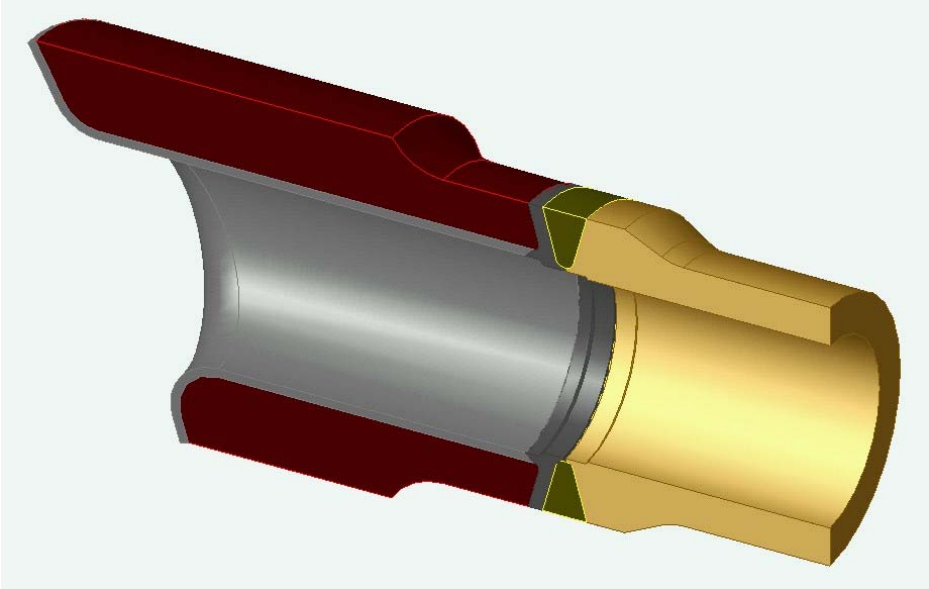

Figure 1-3
Example CE Design Pressurizer Safety/Relief Nozzle

2
PLANT INPUTS

This section summarizes the extensive weld-specific dimensional, piping load, fabrication, and weld repair history inputs that were collected for the group of 51 subject pressurizer nozzles. Detailed geometry and piping load inputs were collected for each subject weld to ensure that all welds are appropriately addressed by the crack growth sensitivity matrix (Section 7) developed as part of this study. Weld-specific fabrication and weld repair data were also collected as a key input to the welding residual stress simulations addressing the subject population (Section 3).

2.1 Geometry Cases

Among the nine plants covered by this scope of work, there are a total of 51 pressurizer dissimilar metal welds of concern comprising: a) 35 safety and relief (S&R) nozzles, b) 8 surge nozzles, and c) 8 spray nozzles. Design details for each of the nozzles at each of the plants are summarized in Table 2-1 and Figure 2-1. The 51 nozzles may be further categorized into the following nozzle geometry cases:

S&R nozzles

- Types 1a and 1b: Westinghouse design without liner, connected to 6" pipe, used at plants A, E, and H (Type 1a) and plant F (Type 1b).
- Types 2a and 2b: Westinghouse design with liner directly covering DM weld, connected to 6" pipe, used at plants B, C, and G.
- Type 3: CE design (no liner), connected to 6" pipe, used at plants D and I.

Spray nozzles

- Type 4: Westinghouse design with liner (does not extend to most of DM weld), connected to 4" pipe, used at plants A and E.
- Type 5: Westinghouse design with liner directly covering DM weld, connected to 4" pipe, used at plants B, C, and G.
- Type 6: Westinghouse design without liner, connected to 6" pipe, used at plant F.
- Type 7: CE design (no liner, sleeve not extending to DM weld), connected to 4" pipe, used at plants D and I.

Surge nozzles

- Type 8: Westinghouse design (sleeve directly covers fill-in weld under nozzle-to-safe-end weld), connected to 14" pipe, used at plants A, B, C, E, G, and H.
- Type 9: CE design (sleeve not extending to DM weld), connected to 12" pipe, used at plants D and I.

2.2 Piping Load Inputs

The piping loads for the 51 subject nozzle welds at the nine plants were also provided in Reference [2-1]. The loads are summarized in Figure 2-2 through Figure 2-6. In these figures, each point along the x-axis of the plots represents an individual nozzle weld. From left to right, the safety/relief nozzles at all plants are grouped together, followed by the spray nozzles, with the surge nozzles at the far right. The axial loads are displayed in Figure 2-2 and the bending moment loads are displayed in Figure 2-3 and Figure 2-4. Pressure and deadweight stresses (i.e., primary stresses) are displayed in Figure 2-5, and primary plus normal thermal stresses are displayed in Figure 2-6.

2.3 Weld Fabrication

The fabrication information for the 51 subject nozzle welds is summarized in Table 2-1. Based on the design drawings for the nozzles and discussions with Westinghouse, the following information was identified regarding the fabrication process for the pressurizer dissimilar metal welds.

Safety/Relief Nozzles

The safety/relief nozzle weld preparation design for all plants except D, H, and I is a U-groove type design with a specified backweld. In this design, the two sides of the weld meet at an initial land that is 0.060 inches thick. Initial passes are applied to melt through the land and join the two sections. The weld is performed from ID to OD from the outside of the weld preparation. Once the initial weld is complete, the inside surface at the land joint is dye penetrant inspected, and the ID is ground until no separation is observed between the two sides of the land. While the design of the initial passes was intended to melt through and join the land, it is possible that the land region was ground in a fully circumferential manner to the approximate thickness of the land. Any material removed by grinding was filled in with a backweld. The complete weld was then radiographed, and repairs were made as necessary.

The safety/relief nozzle weld preparation design for the plants D, H, I differs in that the ID of the weld prep was smaller than the desired finished ID. The weld is completed from ID to OD. After the weld is complete, the inside surface material is machined away to the desired finished dimension. Typically, in this type of joint, the initial root passes are machined away as part of the final machining to the finished ID.

Spray Nozzles

Design drawings for the spray nozzles indicate that these nozzles tended to be fabricated similarly to the safety/relief nozzles. Generally, these welds are considered represented by the safety/relief nozzle fabrication process.

Surge Nozzles

The surge nozzle weld preparation design for plants A, B, C, and G is a U-groove type design, conceptually (but not geometrically) similar to the safety/relief nozzles. The initial land thickness and weld process are the same: the weld proceeds from ID to OD, followed by a backweld at the land as necessary to create a solid weld joint. The complete weld was radiographed, and repairs were made as necessary. Following this step, a weld cladding layer (referred to as a fill-in weld) was deposited over the ID of the weld region to create a flat mating surface for the thermal sleeve. At its thickest point, the fill-in weld is about 0.3 inches thick. The fill-in weld layer was not radiographed.

The surge nozzle weld preparation for plants D, E, H, and I differs in that the ID of the weld prep was smaller than the desired finished ID. After the weld is complete, the inside surface material is machined away to the desired finished dimension. There are no fill-in welds for the surge nozzles at these plants.

2.4 Weld Repair History

The weld repair history for the 51 subject nozzle welds is noted in Table 2-1, and is described in greater detail in Table 2-2. Table 2-2 shows, when available, the number, depth, and length of the repairs for each weld.

2.5 References

2-1. Westinghouse Transmittal Package.

Table 2-1
Nozzle Geometry and Repair History Summary Table

Plant Code	Relief											Safety A									
	Design #	Piping NPS	Liner?	Land Thick (in.)	Fill-In Weld Thick. (in.)	DM Weld t (in.)	DM Weld R_i/t	Weld Sep. (in.)	Butter Weld Repairs	ID Weld Repairs	OD Weld Repairs	Design #	Piping NPS	Liner?	Land Thick (in.)	Fill-In Weld Thick. (in.)	DM Weld t (in.)	DM Weld R_i/t	Weld Sep. (in.)	Butter Weld Repairs	ID Weld Repairs	OD Weld Repairs
Plant A	1a	6"	N	0.06	None	1.29	2.0	2.2	NR	NR	NR	1a	6"	N	0.06	None	1.29	2.0	2.2	NR	NR	R4
Plant E	1a	6"	N	0.06	None	1.29	2.0	2.2	NR	NR	R	1a	6"	N	0.06	None	1.29	2.0	2.2	NR	NR	NR
Plant H	1a	6"	N	Mach	None	1.29	2.0	2.2	NR	NR	NR	1a	6"	N	Mach	None	1.29	2.0	2.2	NR	R	R
Plant B	2a	6"	Y	0.06	None	1.07	2.6	2.6	NR	NR	R1	2a	6"	Y	0.06	None	1.07	2.6	2.6	NR	NR	NR
Plant G	2a	6"	Y	0.06	None	1.07	2.6	2.6	NR	NR	NR	2a	6"	Y	0.06	None	1.07	2.6	2.6	NR	NR	NR
Plant C	2b	6"	Y	0.06	None	1.07	2.6	2.3	NR	NR	NR	2b	6"	Y	0.06	None	1.07	2.6	2.3	NR	NR	NR
Plant F	1b	6"	N	N/A	None	1.41	1.8	3.3	NR	NR	NR	1b	6"	N	N/A	None	1.41	1.8	3.3	NR	NR	NR
Plant D	3	6"	N	Mach	None	1.41	1.8	6.8	NR	NR	NR	3	6"	N	Mach	None	1.41	1.8	6.8	R	NR	NR
Plant I	3	6"	N	Mach	None	1.41	1.8	6.8	NR	Rx2		3	6"	N	Mach	None	1.41	1.8	6.8	NR	NR	NR
Plant J	1a	6"	N	0.06	None	1.29	2.0	2.2	Rx5	R1	R1	1a	6"	N	0.06	None	1.29	2.0	2.2	R	R2	NR

Notes:
1. For Designs #2a, #2b, and #5, liner directly covers DM weld.
2. For Design #4, liner does not extend to most of DM weld.
3. For Designs #4, #5, and #6, sleeve covers but does not contact DM weld.
4. For Design #8, sleeve directly covers DM weld.
5. For Designs #7 and #9, sleeve does not extend to DM weld.
6. NR = No weld repairs reported
7. Rn = Repairs reported (n indicates number of defect or repaired areas if reported; "x" indicates repeat weld repair operations)
8. N/A = Results for fabrication records review not available
9. All pressurizer nozzle DM welds in Plant H are reported to be Alloy 82, not Alloy 82/182.
10. Mach = Initial land thickness of 0.1" machined away as part of weld prep design.
11. Plant I capped relief nozzle listed under "Relief" heading.

Table 2-1 (cont'd)
Nozzle Geometry and Repair History Summary Table

Plant Code	Safety B										Safety C									
	Design #	Piping NPS	Liner?	Land Thick (in.)	Fill-In Weld Thick. (in.)	DM Weld t (in.)	DM Weld R_i/t	Weld Sep. (in.)	Butter Weld Repairs	ID Weld Repairs	OD Weld Repairs	Design #	Piping NPS	Liner?	Land Thick (in.)	Fill-In Weld Thick. (in.)	DM Weld t (in.)	DM Weld R_i/t	Weld Sep. (in.)	Butter Weld Repairs	ID Weld Repairs	OD Weld Repairs
Plant A	1a	6"	N	0.06	None	1.29	2.0	2.2	NR	R1	NR	1a	6"	N	0.06	None	1.29	2.0	2.2	NR	NR	NR
Plant E	1a	6"	N	0.06	None	1.29	2.0	2.2	NR	NR	NR	1a	6"	N	0.06	None	1.29	2.0	2.2	NR	R	NR
Plant H	1a	6"	N	Mach	None	1.29	2.0	2.2	NR	NR	NR	1a	6"	N	Mach	None	1.29	2.0	2.2	NR	NR	NR
Plant B	2a	6"	Y	0.06	None	1.07	2.6	2.6	NR	NR	NR	2a	6"	Y	0.06	None	1.07	2.6	2.6	NR	NR	NR
Plant G	2a	6"	Y	0.06	None	1.07	2.6	2.6	NR	NR	NR	2a	6"	Y	0.06	None	1.07	2.6	2.6	NR	NR	NR
Plant C	2b	6"	Y	0.06	None	1.07	2.6	2.3	NR	NR	NR	2b	6"	Y	0.06	None	1.07	2.6	2.3	NR	NR	NR
Plant F	1b	6"	N	N/A	None	1.41	1.8	3.3	NR	NR	NR	1b	6"	N	N/A	None	1.41	1.8	3.3	NR	NR	NR
Plant D	3	6"	N	Mach	None	1.41	1.8	6.8	NR	NR	NR	3	6"	N	Mach	None	1.41	1.8	6.8	NR	NR	NR
Plant I	3	6"	N	Mach	None	1.41	1.8	6.8	NR	NR	NR	No Safety C										
Plant J	1a	6"	N	0.06	None	1.29	2.0	2.2	NR	R6x2	NR	1a	6"	N	0.06	None	1.29	2.0	2.2	NR	NR	NR

Notes:
1. For Designs #2a, #2b, and #5, liner directly covers DM weld.
2. For Design #4, liner does not extend to most of DM weld.
3. For Designs #4, #5, and #6, sleeve covers but does not contact DM weld.
4. For Design #8, sleeve directly covers DM weld.
5. For Designs #7 and #9, sleeve does not extend to DM weld.
6. NR = No weld repairs reported
7. Rn = Repairs reported (n indicates number of defect or repaired areas if reported; "x" indicates repeat weld repair operations)
8. N/A = Results for fabrication records review not available
9. All pressurizer nozzle DM welds in Plant H are reported to be Alloy 82, not Alloy 82/182.
10. Mach = Initial land thickness of 0.1" machined away as part of weld prep design.
11. Plant I capped relief nozzle listed under "Relief" heading.

Table 2-1 (cont'd)
Nozzle Geometry and Repair History Summary Table

Plant Code	Spray (all have thermal sleeve)										Surge (all have thermal sleeve)									
	Design #	Piping NPS	Liner?	Land Thick (in.)	Fill-In Weld Thick. (in.)	DM Weld t (in.)	DM Weld R_i/t	Weld Sep. (in.)	Butter Weld Repairs	ID Weld Repairs	OD Weld Repairs	Design #	Piping NPS	Liner?	Land Thick (in.)	Fill-In Weld Thick. (in.)	DM Weld t (in.)	DM Weld R_i/t	Weld Sep. (in.)	Butter Weld Repairs	ID Weld Repairs	OD Weld Repairs
Plant A	4	4"	Y	0.06	None	0.90	2.2	~2.3	NR	NR	NR	8	14"	N	0.06	0.30	1.58	3.8	3.4	NR	R5	R3
Plant E	4	4"	Y	0.06	None	0.90	2.2	~2.3	R	NR	R	8	14"	N	Mach	None	1.58	3.8	3.4	NR	R3	NR
Plant H	Already PDI examined											8	14"	N	Mach	None	1.58	3.8	3.4	NR	NR	NR
Plant B	5	4"	Y	0.06	None	0.78	2.7	2.2	NR	NR	NR	8	14"	N	0.06	0.30	1.58	3.8	3.4	R1	R1x2	R2
Plant G	5	4"	Y	0.06	None	0.78	2.7	2.2	NR	NR	NR	8	14"	N	0.06	0.30	1.58	3.8	3.4	NR	NR	NR
Plant C	5	4"	Y	0.06	None	0.78	2.7	~2.2	NR	NR	NR	8	14"	N	0.06	0.29	1.56	3.8	3.5	NR	NR	NR
Plant F	6	6"	N	N/A	None	1.15	2.5	3.6	R	NR	NR	Already structural overlayed										
Plant D	7	4"	N	Mach	None	1.06	1.4	3.3	NR	NR	NR	9	12"	N	Mach	None	1.47	3.4	3.0	NR	NR	NR
Plant I	7	4"	N	Mach	None	1.06	1.4	3.3	NR	NR	NR	9	12"	N	Mach	None	1.47	3.4	3.0	NR	Rx2	
Plant J	4	4"	Y	0.06	None	0.90	2.2	~2.3	R	NR	NR	8	14"	N	0.06	0.30	1.58	3.8	3.4	R2	R1	NR

Notes:

1. For Designs #2a, #2b, and #5, liner directly covers DM weld.
2. For Design #4, liner does not extend to most of DM weld.
3. For Designs #4, #5, and #6, sleeve covers but does not contact DM weld.
4. For Design #8, sleeve directly covers DM weld.
5. For Designs #7 and #9, sleeve does not extend to DM weld.
6. NR = No weld repairs reported
7. Rn = Repairs reported (n indicates number of defect or repaired areas if reported; "x" indicates repeat weld repair operations)
8. N/A = Results for fabrication records review not available
9. All pressurizer nozzle DM welds in Plant H are reported to be Alloy 82, not Alloy 82/182.
10. Mach = Initial land thickness of 0.1" machined away as part of weld prep design.
11. Plant I capped relief nozzle listed under "Relief" heading.

Table 2-2
Weld Repair Summary Table

Table Line	Plant Code	Nozzle Type	Nozzle Count	Design #	Buttering or Weld	ID/OD (% circ.)	Alloy 82 or 182	PWHT after Repair?	# Defect or Repair Areas	Defect/Repair Area #1		Defect/Repair Area #2		Defect/Repair Area #3		Defect/Repair Area #4		Defect/Repair Area #5		Defect/Repair Area #6	
										Length (in.)	Depth (in.)	Length (in.)	Depth (in.)	Length (in.)	Depth (in.)	Length (in.)	Depth (in.)	Length (in.)	Depth (in.)	Length (in.)	Depth (in.)
1	A	Safety A	1	1a	weld	OD	N/A	N/A	4	N/A	~1/2	N/A	~1/2	N/A	~1/2	N/A	~1/2				
2	A	Safety B	2	1a	weld	ID	N/A	N/A	1	1/2	5/8										
3	E	Relief	3	1a	weld	OD	N/A	N	N/A	N/A	N/A										
4	E	Safety C	4	1a	weld	ID<22%	N/A	N	N/A	N/A	N/A										
5	H	Safety A	5	1a	weld	ID	82	Y	N/A	N/A	N/A										
6						OD	82	Y	N/A	N/A	N/A										
7	B	Relief	6	2a	weld	OD	182	N/A	1	0.5	0.375										
8	D	Safety A	7	3	butter	N/A	N/A	Y	N/A	N/A	N/A										
9	I	Relief	8	3	weld	N/A	N/A	N	8	N/A	N/A										
10	E	Spray	9	4	butter	ID	82	Y	N/A	N/A	~0.3										
11					weld	OD	N/A	N	N/A	N/A	N/A										
12	F	Spray	10	6	butter	N/A	82	Y	N/A	N/A	N/A										
13	A	Surge	11	8	weld	ID	N/A	N/A	5	1.5	5/16	3.75	0.5	2	3/16	2.5	5/16	2	5/16		
14						OD	N/A	N/A	3	2.5	0.5	2	0.5	1	3/16						
15	E	Surge	12	8	weld	ID<10%	82	N	3	N/A	N/A	N/A	N/A	N/A	N/A						
16	B	Surge	13	8	butter	N/A	82	Y	1	N/A	N/A										
17					weld	OD	182	N/A	2	1.75	0.875	1.5	1								
18						ID	182	N/A	1	1.0	0.625										
19						ID	182	N/A	1	4	0.75										
20	I	Surge	14	9	weld	N/A	N/A	N	4	N/A	N/A										
WC1	J	Relief	WC1	1a	butter	N/A	82/182	Y	N/A	N/A	N/A										
WC2						ID+OD	82	Y	2	1/2	7/16ID	1	7/16OD								
WC3						OD	182	Y	1	1	3/4										
WC4						ID	82	Y	3	3/4	3/4	2-1/4	3/4	1/2	3/4						
WC5						OD	182	Y	3	1	3/4	2-1/4	3/4	1/2	3/4						
WC6					weld	OD	82	N/A	1	1-1/4	1/2										
WC7						ID	82	N/A	1	1/2	1/2										
WC8	J	Safety A	WC2	1a	butter	N/A	182	Y	N/A	N/A	1/8										
WC9					weld	ID	82	N/A	2	1-1/4	11/32	7/8	11/32								
WC10	J	Safety B	WC3	1a	weld	ID	82	N/A	6	2-1/2	3/4	1	1/2	1-1/2	1/2	1	1/2	2-1/2	3/4	2-1/2	3/4
WC11							82	N/A	6	1-1/2	1/2	1-1/4	1	3/4	7/8	1-1/2	3/8	1	1-1/16	1/2	1/2
WC12	J	Spray	WC4	4	butter	lip/bondline	82	Y	N/A	N/A	N/A										
WC13	J	Surge	WC5	8	butter	OD	182	Y	2	7/8	9/16	1-1/8	1								
WC14					weld	ID	82	Y	1	1	7/16										

Notes:

1. For Designs #2a, #2b, and #5, liner directly covers DM weld.
2. For Design #4, liner does not extend to most of DM weld.
3. For Designs #4, #5, and #6, sleeve covers but does not contact DM weld.
4. For Design #8, sleeve directly covers DM weld.
5. NR = Information not yet reported (or may not be available)
6. N/A = Information not available

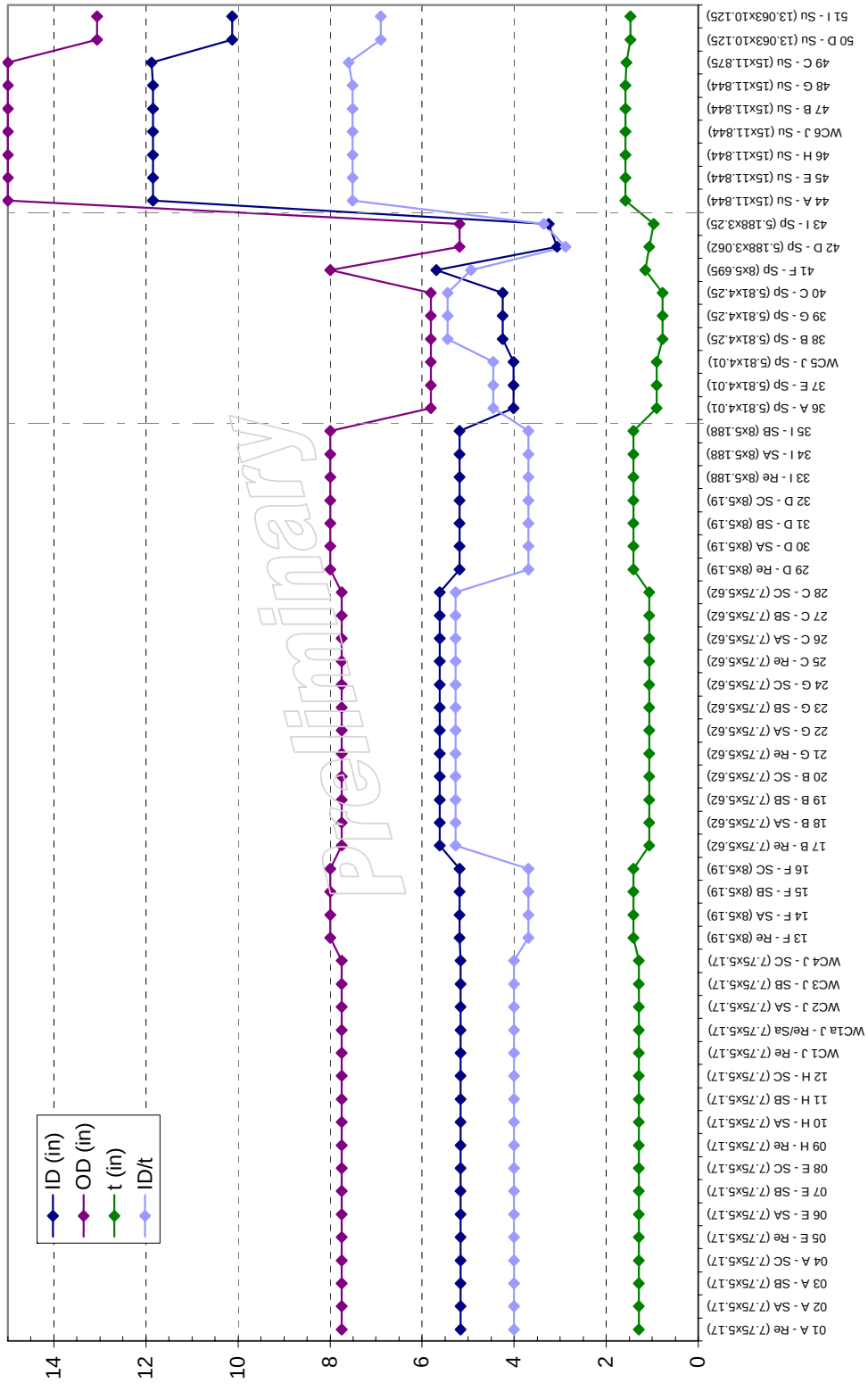

Figure 2-1
Nominal Basic Design Dimensions for Each Subject Weld

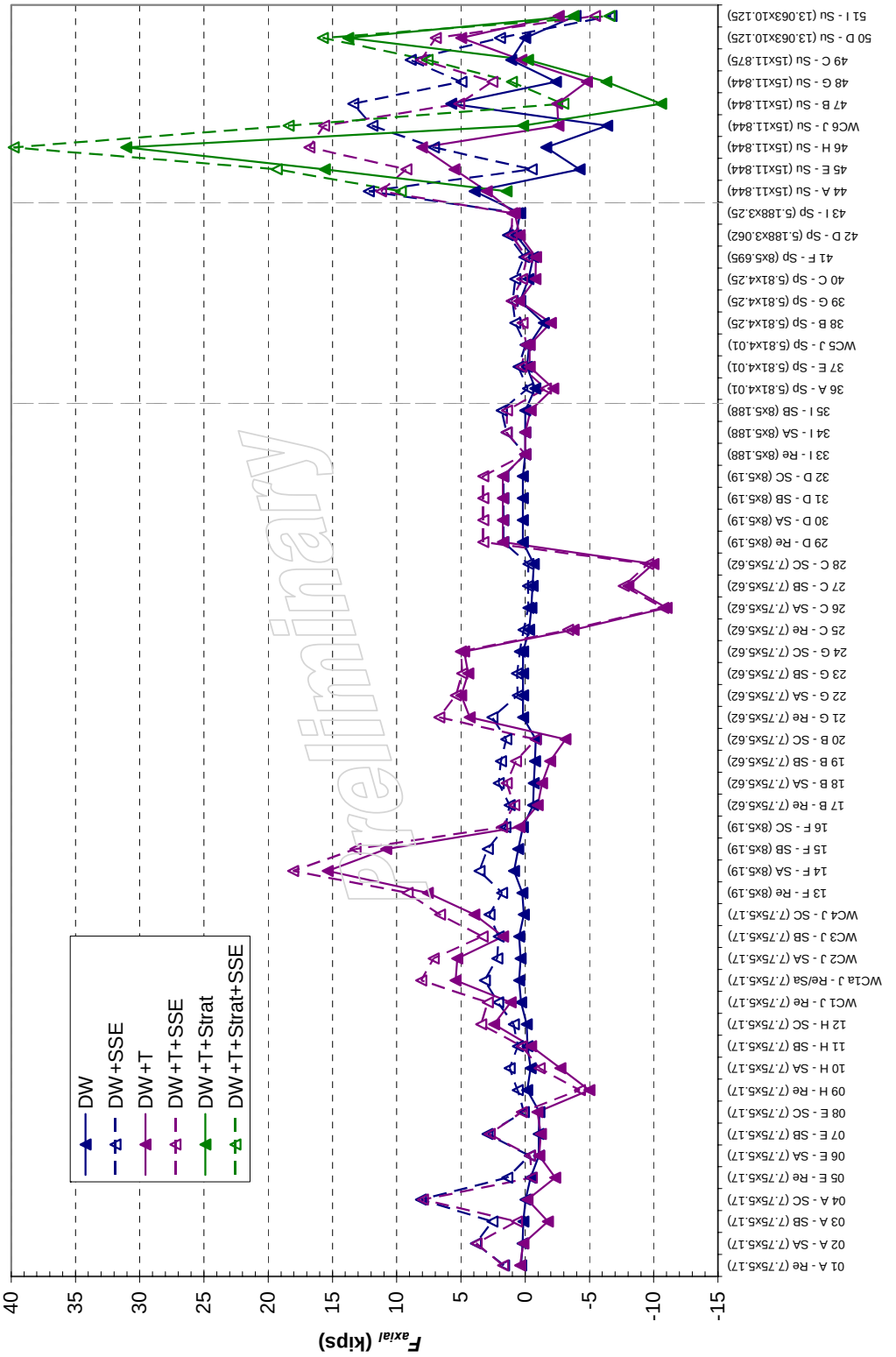

Figure 2-2
Nominal Axial Piping Loads (Not Including Endcap Pressure Load)

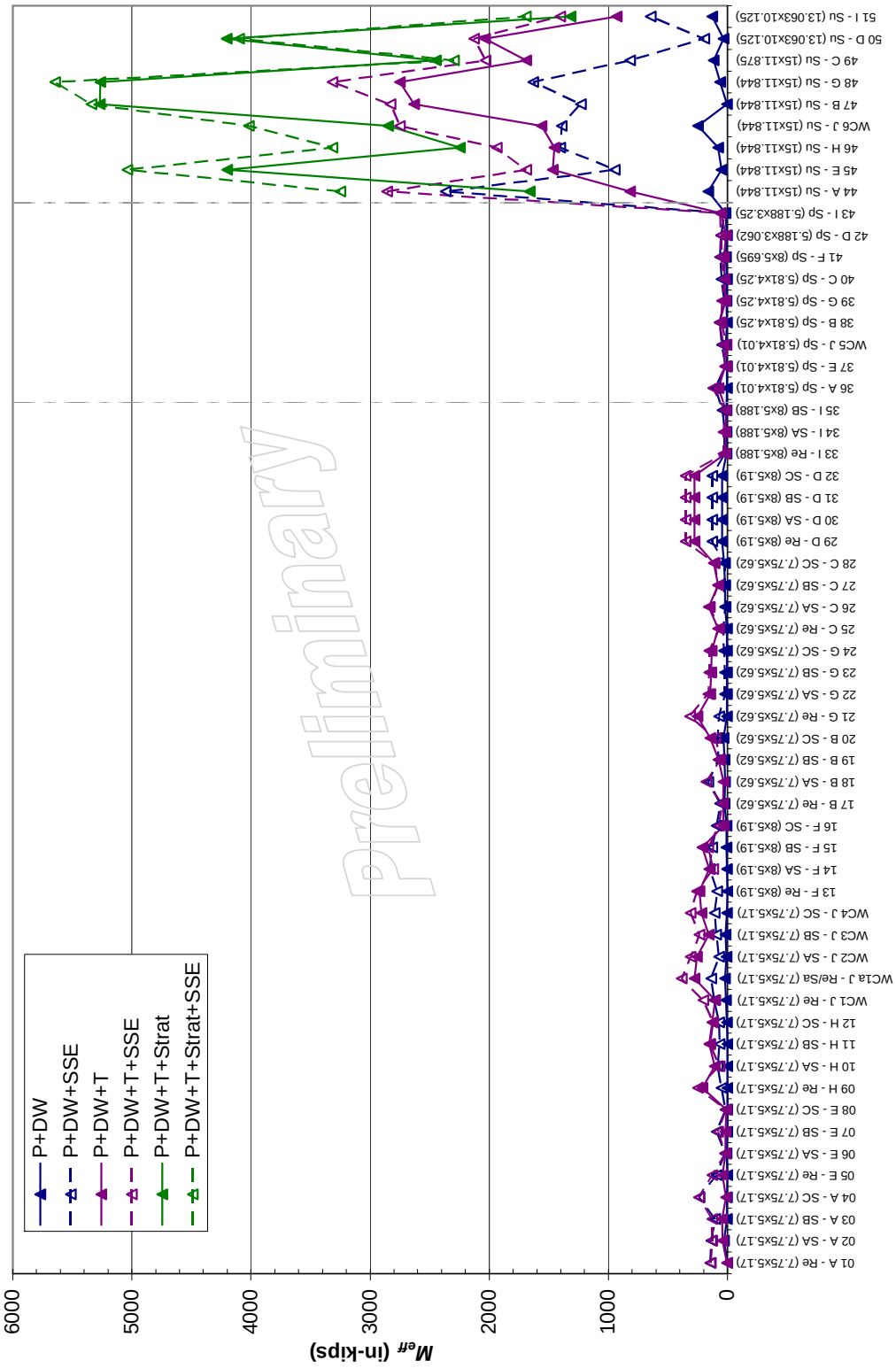

Figure 2-3
Nominal Effective Bending Moment Loads (Full Scale)

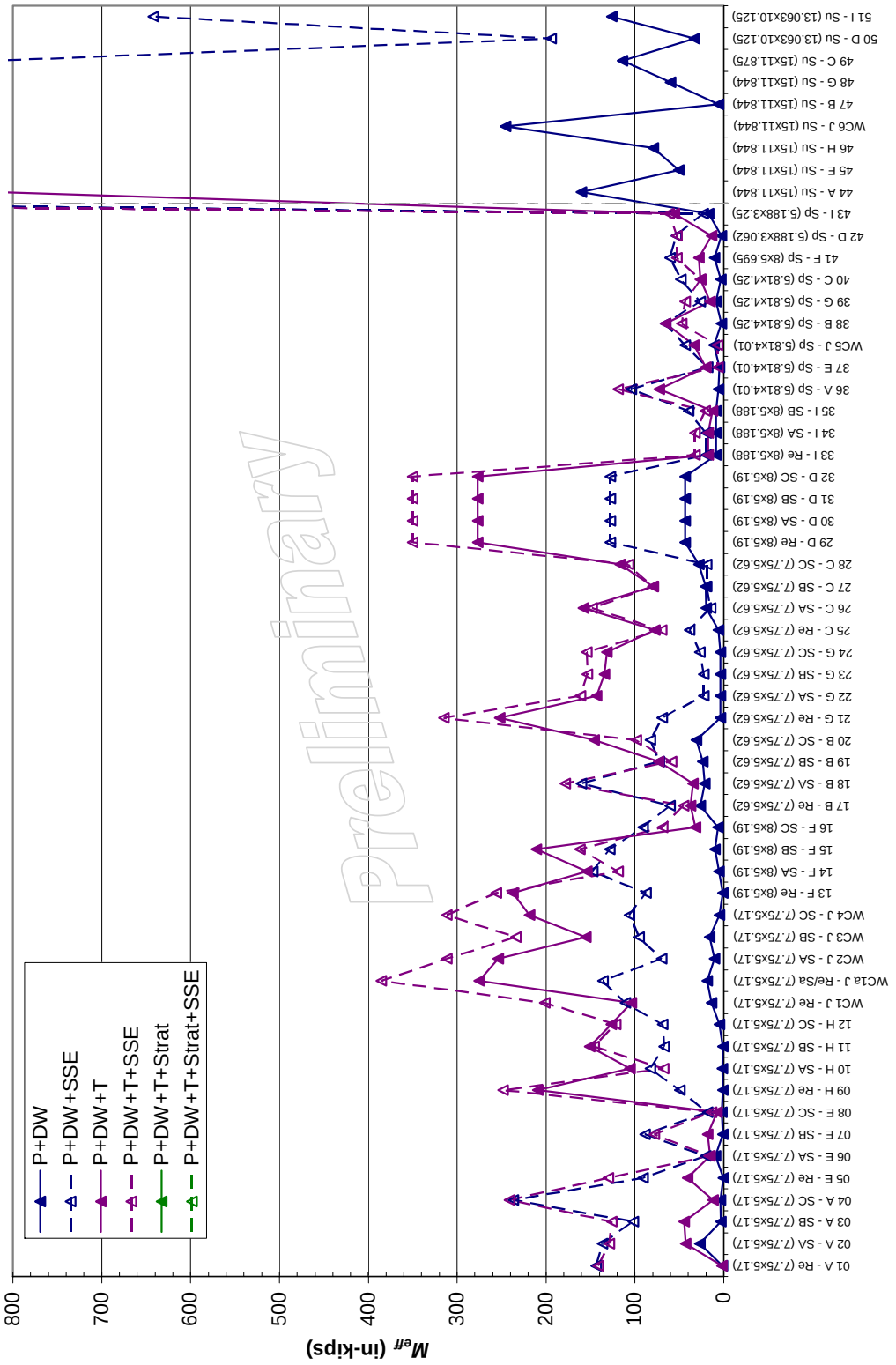

Figure 2-4
Nominal Effective Bending Moment Loads (Partial Scale)

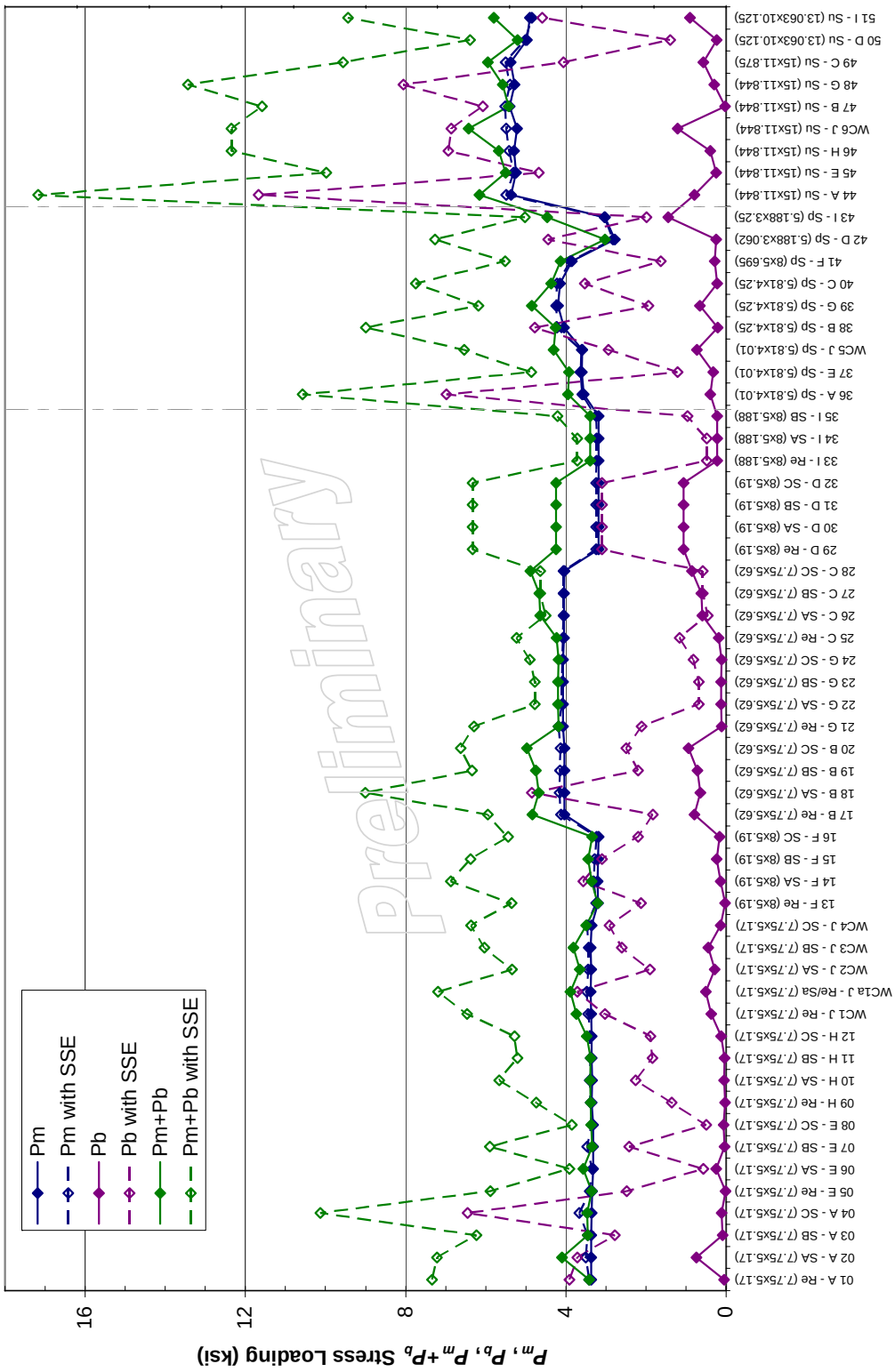

Figure 2-5
ASME Code Nominal Stress Loading for Pressure and Dead Weight Loading

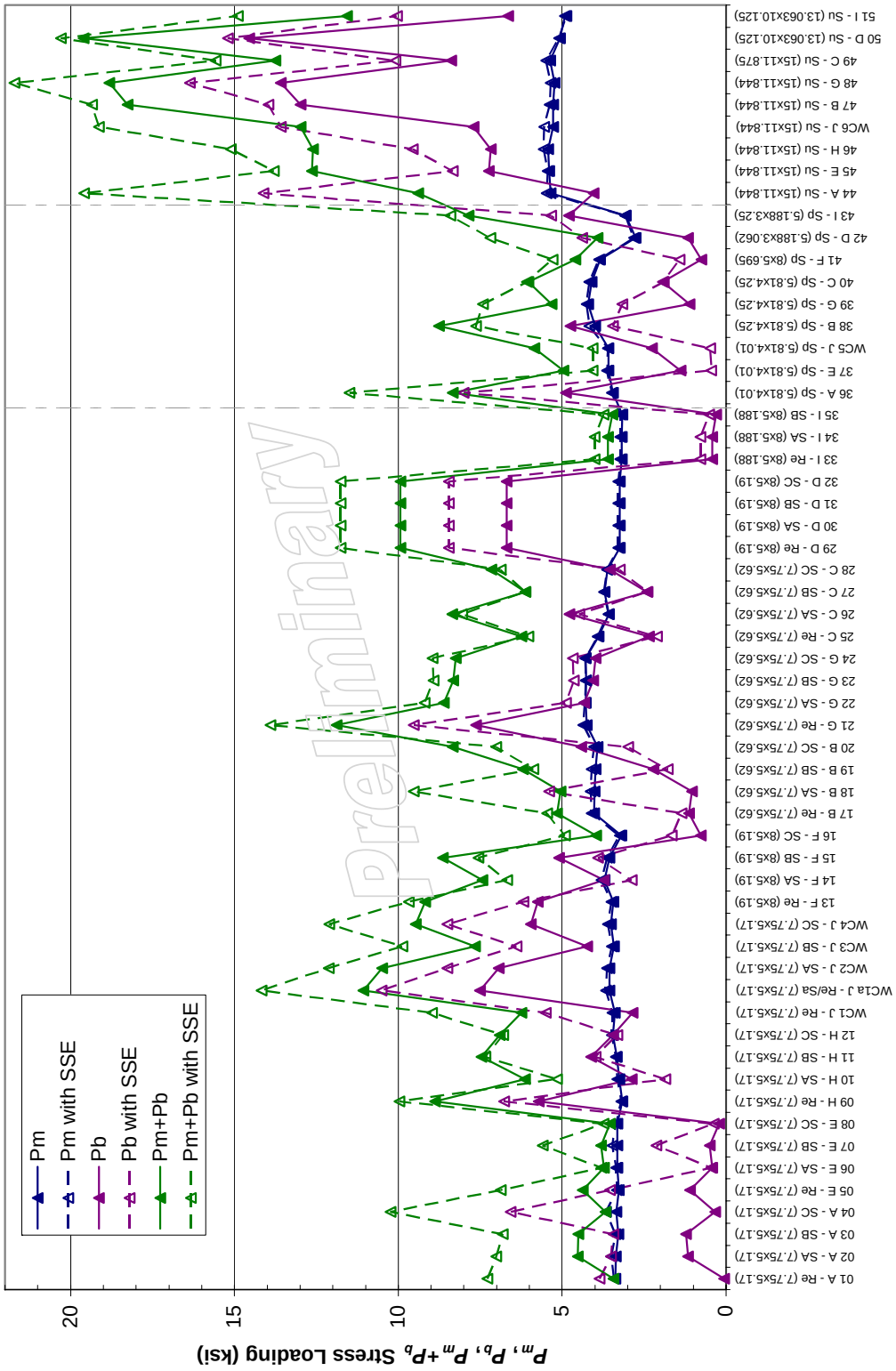

Figure 2-6
ASME Code Nominal Stress Loading for Pressure, Dead Weight, and Normal Thermal Loading

3
WELDING RESIDUAL STRESS

The purpose of this section is to describe analyses which investigate the residual stress distributions in a range of nozzle to safe end dissimilar metal welds in the as welded condition and in the presence of weld repairs. The axial stress distributions calculated from these analyses are used as inputs to the matrix of fracture mechanics calculations, described in Section 7 of this report. Finite element analysis is used to simulate the thermal and mechanical effects of the welds and any repairs of the weld region. Select details regarding the model and relevant stress results are provided in the remainder of this section. Additionally, the analysis results are discussed in the context of additional work on welding residual stresses identified in existing literature. Finally, validation work on the welding residual stress methods used is discussed in this section.

3.1 Finite Element Analysis of Welding Residual Stress

3.1.1 Cases Considered

Safety/Relief Nozzle Cases

The safety and relief nozzles generally have the same geometry and configuration within the plants considered. Two similar configurations were considered for welding residual stress analysis: the Type 1a and Type 2b safety/relief nozzles described in Section 2. The difference between the two is that Type 1a safety/relief nozzles have no liner, and Type 2b nozzles have an ID liner. Figure 3-1 and Figure 3-2 show the geometry of the two safety/relief nozzle models considered. The following cases were analyzed:

- Nozzle butt weld alone with and without safe end to pipe weld
- Nozzle butt weld with weld buildup at safe end ID (with safe end weld)
- Nozzle butt weld with liner fillet weld (with safe end weld)
- Nozzle butt weld with 0.75-inch deep x 360° ID weld repair (no safe end weld)
- Nozzle butt weld with 0.75-inch deep x 20° ID weld repair (no safe end weld)

Additionally, the safety/relief nozzle cases were considered to be representative of the smaller, but similarly configured, spray nozzle dissimilar metal welds. No spray nozzle analysis cases were performed.

Surge Nozzle Cases

Two different surge nozzle models were considered: one for the Type 8 nozzles and one for the Type 9 nozzles. Figure 3-3 and Figure 3-4 show the geometry of the Type 8 and Type 9 nozzles, respectively. The following surge nozzle cases were considered:

- Type 8 nozzle butt weld alone with and without safe end to pipe weld
- Type 8 nozzle butt weld with 5/16-inch deep x 360° ID weld repair (with safe end weld)
- Type 9 nozzle butt weld alone

3.1.2 FEA Modeling and Methodology

Model Geometry and Boundary Conditions

Figure 3-3 shows the overall model geometry for the Type 8 surge nozzle butt weld analysis cases. As shown in the figure, the model includes the low alloy steel nozzle, the nozzle buttering, the stainless steel safe end, a section of stainless steel piping, and the welds attaching a) the nozzle to the safe end, and b) the safe end to the piping. Similar model geometry plots for the safety/relief nozzle cases and the Type 9 surge nozzle are included in Figure 3-1, Figure 3-2, and Figure 3-4. All but one of the analysis cases are performed using two-dimensional axisymmetric models. These models simulate a welding process that is simultaneous around the entire circumference of the model. This is appropriate given that the standard fabrication steps described in Section 2 are fully circumferential in nature. Repairs, however, are typically not fully circumferential. In order to consider the circumferential effects of a limited repair zone, one analysis case performs a 180° symmetric three-dimensional analysis of a weld followed by a repair. Figure 3-5 shows the three dimensional model used to simulate the safety/relief nozzle repair case.

The model geometry is developed from the nozzle, weld, and piping dimensions described in Section 2. Where appropriate, minor simplifications are made to the overall geometry in developing the model geometry. A view of the finite element mesh for the Type 8 surge nozzle, which also shows the layers used to simulate the weld process, is shown in Figure 3-6.

The welding residual stress model performs a thermal and structural analysis of the nozzle region. During the thermal analysis, convection cooling from the nozzle, safe end and piping to air at an ambient temperature of 70°F was modeled using a heat transfer coefficient of 5 BTU/hr-ft^2-°F, consistent with natural convection cooling in still air. Convection cooling of the weld elements was not included in the model, i.e., only the dominant effects of conduction cooling of the weld metal to the base metal sections was simulated. During the structural analysis, the nozzle end of the model was fixed in the axial direction. In addition, the entire plane of nodes at the opposite end of the pipe was coupled in the axial direction (constrained to have the same axial displacement) to simulate continuation of the pipe beyond the model boundary. When the model is pressurized, internal pressure is applied to the wetted surface, and an endcap axial load was applied at the coupled side of the model.

The welding residual stress analysis was performed using ANSYS finite element analysis software. When two-dimensional axisymmetric analyses were performed, four-node planar thermal and structural elements were used to develop the FEA mesh; eight-node structural solid elements were used for the three dimensional analysis. Higher order elements were not used since they provide no greater accuracy for elastic-plastic analyses than the four-node planes and eight-node solids [3-1].

Material Properties

Four materials were used in the modeling of the nozzle butt welds: the nozzle is low alloy steel, the nozzle buttering and weld metal is Inconel Alloy 82/182, the safe end and attached piping are stainless steel, and the safe end to piping attachment is a stainless steel weld. Temperature dependent thermal and mechanical properties were input for each of these materials. All materials were assumed to strain-harden isotropically using the von Mises yield criterion with a bilinear input curve and a tangent modulus of zero (elastic-perfectly plastic). When using ANSYS, this assumption gives more realistic stresses where a high degree of plastic strain occurs at elevated temperatures, such as within the welds and the base material HAZ.

Specific information regarding the properties for the materials is as follows:

Alloy 82/182 Weld and Buttering

The bilinear elastic limit for these materials is based on an average of the yield and tensile strengths reported in Reference [3-2]. An elastic limit of 75.0 ksi was used at 70°F, and an elastic limit of 60.0 ksi was used at 600°F. A Poisson's ratio of 0.29 was used; this value was assumed to be invariant with temperature. Additional material property data were taken from a number of sources, including the 1992 ASME Boiler and Pressure Vessel Code [3-3], data provided by EdF for EPRI analyses [3-4], and Inconel product literature [3-2].

Low Alloy Steel Nozzle

The elastic limit values for the low alloy steel are based on typical values for the 0.2% offset yield strength of this material. An elastic limit of 50.0 ksi was used at 70°F, and an elastic limit of 41.7 ksi was used at 600°F. A Poisson's ratio of 0.29 was used; this value was assumed to be invariant with temperature. Additional material property data were taken from a number of sources, including the 1992 ASME Boiler and Pressure Vessel Code [3-3], low alloy steel data provided by EdF for EPRI analyses [3-4], and research by Karlsson [3-5].

Stainless Steel Base Metal

The stainless steel base metal (safe end and piping) uses elastic limit values that are based on the 0.2% offset yield strength for the material. An elastic limit of 40.0 ksi was used at 70°F, and an elastic limit of 28.9 ksi was used at 600°F. A Poisson's ratio of 0.29 was used; this value was assumed to be invariant with temperature. Additional material property data were taken from a number of sources, including the 1992 ASME Boiler and Pressure Vessel Code [3-3], data

provided by EdF for EPRI analyses [3-4], and research by Rybicki [3-6]. The values used in this analysis are identical to those used for BWR stainless steel shroud welds in [3-7].

Stainless Steel Weld Metal

The stainless steel material used to join the safe end to the piping uses different material strength properties during the structural analysis. An elastic limit of 67.0 ksi was used at 70°F, and an elastic limit of 50.7 ksi was used at 600°F. The values for the elastic limit were taken from previous analytical work performed for BWR stainless steel shroud welds [3-7]. All other material property data for the weld material is the same as the base metal.

Analysis Load Steps

The welding residual stress analysis involves four general loading steps: (a) welding, (b) weld repair (if applicable), (c) hydrostatic testing, and (d) operating conditions. These processes are simulated as follows:

Welding Simulation

The welding process was simulated by combined thermal and structural analyses. A transient thermal analysis was used to generate nodal temperature distributions throughout the welding process. These nodal temperatures were then used as inputs to the structural analysis which calculates resultant thermally-induced stresses. The sequence of thermal analyses followed by structural analyses was duplicated for each simulated weld pass. When the model is three-dimensional, the base welding simulation was performed in an axisymmetric fashion, with welding passes simulated as rings of weld metal. In all cases, the weld passes were simulated using layers of material, with layers approximately 0.1 inches thick. The details of the procedure used for each analysis case are detailed in Section 3.2.4 below..

Heat is rapidly input to the weld pass material, using internal volumetric heat generation, at a rate which raises the peak weld metal temperature to 3,000–3,500 °F and the base metal adjacent to the weld to about 2,000 °F. These are approximately the temperatures that the weld metal and surrounding base materials reach during welding [3-8]. Additionally, the penetration of temperatures above 1,000°F is limited by adjusting the heat input rate and time. Rapid heating of the weld material is necessary in order to reach the desired peak weld puddle temperatures without overheating the surrounding base metal. Conversely, if the heat is applied too rapidly, the surrounding base metal materials do not reach a high enough temperature for good fusion. As noted above, thermal properties for the materials are specified in the model for temperatures up to 3,500 °F; properties at elevated temperatures are estimated or extrapolated from those at lower temperatures.

Weld Repairs

Weld repairs were simulated by deactivating elements associated with previously welded material and reapplying new weld metal in its place. Deactivation of elements essentially results in elimination of the conductive capacity and stiffness of the deactivated element in heat transfer

and structural analyses, respectively. Repair welds are also done in layers approximately 0.1 inches thick.

Hydrostatic Testing

Components were hydrostatically tested to approximately 3,110 psig after installation. This step was included in the analysis since applied hydrostatic pressure further yields any material stressed to near yield by welding and, therefore, results in a reduction of the peak residual tensile stresses after the hydrostatic test pressure is released. In this manner, the hydrostatic testing represents a form of "mechanical stress improvement" in areas of high stress. In addition to applying pressure to all wetted inside surfaces, an axial tensile stress is applied to the end of the pipe equal to the longitudinal pressure stress in the pipe wall.

Operating Conditions

Operating conditions are simulated by pressurizing the inside of the model to 2,235 psig and heating all of the material uniformly to the 653°F operating temperature. The pressure and thermal conditions are added to the model which has already been subjected to welding (and weld repairs) and hydrostatic testing. Operating loads due to piping forces and moments are not considered in this analysis. The operating temperature is applied first as a separate load case, since this analysis result is the one that will be used to load the fracture mechanics models.

Case Specific Analysis Steps

Because of the different geometries and conditions being considered, each of the analysis models have case-specific analysis steps. While each were done using the general procedures outlined in Section 3.2.3 above, case-specific methods were used as follows.

Type 8 Surge Nozzle

The fabrication records for the Type 8 surge nozzle show that the dissimilar metal weld has the following aspects as part of its fabrication: 1) the initial weld is built radially outwards starting from the ID, 2) the initial weld land (approximately 0.075 to 0.10 inches thick) is ground until sound weld metal is reached, 3) the ground region is rewelded to the original inner diameter, 4) the weld is inspected and any repairs are made, and 5) a fill-in weld cladding layer is deposited to seat the thermal liner. Following these weld steps, the pressurizer is delivered and the stainless steel weld is made connecting the safe end to the plant piping. This sequence is depicted in Figure 3-7, which shows the model geometry at various points during this process. This figure also shows the repaired model condition prior to starting the repair.

Type 9 Surge Nozzle

The fabrication records for this surge nozzle type indicate that it was fabricated with a smaller than nominal inner diameter, which was then ground out to the finished ID. Therefore, no inside surface finishing pass was considered for this analysis case. For this analysis case, a butt weld similar to the Type 8 weld is performed, but the inside surface is 0.25 inches smaller than the

finished radius. After completion of the weld, the inner region is removed back to the finished inside radius.

Type 1a/2b Safety/Relief Nozzle

Similar to the Type 8 surge nozzle, the weld cases for this nozzle geometry were completed with an initial v-weld, followed by an ID grindout and backweld, both with and without the stainless steel safe end to pipe weld. A 0.75-inch deep repair case was also considered; this case. The Type 2b nozzle liner fillet weld was performed in two layers following the ID grindout and backweld. Additionally, a case was considered where a single weld layer, 0.1 inches thick, was deposited at the ID of the safe end.

3.1.3 Analysis Results

In examining the results of the welding residual stress models, stresses in the axial direction are of particular interest since they are the driving force behind circumferential cracking. Therefore, in this section, axial stress contour plots and graphs comparing axial stress data are presented. The operating temperature welding residual stress condition is primarily used for reporting results. The through-wall stresses at this condition are most appropriate for application to the fracture mechanics model, since pressure and other external force loads are applied separately to the fracture mechanics model.

Stress Contour Plots

Figure 3-8 through Figure 3-13 present the axial stresses at operating temperature conditions for the various safety/relief nozzle geometry cases described in Section 3.1.1. Figure 3-8 and Figure 3-9 show results for the "standard" weld case (including backweld), with and without the presence of the stainless steel safe end to pipe weld. Figure 3-10 shows the results from the safe end ID weld buildup case, and the liner fillet weld case is included in Figure 3-11. Finally, Figure 3-12 and Figure 3-13 show the stress results for the 0.75-inch deep ID repair; Figure 3-12 is for an axisymmetric (360°) version of the repair and Figure 3-13 shows the results for the 20° (total) extent repair three-dimensional model.

Figure 3-14 through Figure 3-17 present the axial stress results for the surge nozzle cases described in Section 3.1.2. Figure 3-14 and Figure 3-15 show results for the standard weld case (including backweld and fill-in weld), with and without the presence of the safe end to pipe weld. Figure 3-16 shows the results for the 5/16-inch ID repair case. Figure 3-17 presents the results for the Type 9 surge nozzle, after the inner region has been machined away.

Through-Wall Stress Distributions

In addition to the stress contour plots, through-wall stress distributions were taken for the various analysis cases considered. Stress paths were taken that considered the regions of elevated stress at the ID surface of the model, and that remained mostly perpendicular to the axial direction were used. The purpose of these distributions was to determine the through-wall stress profiles that would be applied to the fracture mechanics analysis models, described in Section 4. The

paths used for the stress distributions are shown on the stress contour plots described above. Unless otherwise noted, all stresses are axial stresses at operating temperature conditions.

Figure 3-18 is a plot comparing the various safety/relief nozzle analysis cases. This figure demonstrates that the safe end ID weld buildup and the liner fillet weld stress distributions are similar to the base analysis model (that includes the stainless steel weld). Therefore, it can be concluded that the impact of these conditions is negligible for the purposes of the overall analysis work. Figure 3-18 also demonstrates the impact of the stainless steel weld on the through-wall stress distribution location selected. The stainless steel weld imparts a through-wall bending moment to the model, one that reduces the ID stress by about 10 to 15 ksi. Additionally, Figure 3-18 demonstrates that the 360° ID repair case with a deep repair imparts tensile stresses at the ID surface that are balanced by compressive stresses towards the OD; further analysis of this repair is included in Figure 3-19, discussed below. Finally, the stress results may also be compared to the through-wall stress distribution selected for previous analysis work considering through-wall circumferential crack growth, labeled "ASME Modified". This stress distribution is less compressive than the ones predicted by the welding residual stress analysis model.

Figure 3-19 is a plot that focuses on the 0.75-inch deep ID repair case considered for the safety/relief nozzle geometry. The repair geometry was considered both as a 360° repair and as a limited extent (and more realistic) 20° ID arc length repair. The stress distributions shown in Figure 3-19 are at a series of circumferential positions around the nozzle. Because the model is a 180° symmetric model, the center of the repair zone is at 0°, and the edge of the repair zone is at 10°. Also shown in this figure are the results for the axisymmetric unrepaired case and the axisymmetric 0.75-inch ID repair case. This figure shows that, for a limited circumferential extent repair, the center of the repair is differs substantially from the 360° version of the same repair geometry. The figure also shows that the effect of the repair on through-wall axial stresses extends for approximately 20° beyond the edge of the repair, after which the through-wall stress distributions become: 1) similar to one another and 2) similar to the unrepaired axisymmetric model results.

Figure 3-20 presents the results from the surge nozzle analysis cases. This figure demonstrates that the safe end to pipe weld has a similar through-wall bending effect as seen in the safety/relief analysis cases. The analysis results may also be compared to the results used in previous analyses for the surge nozzle case; it is noted that these results are for a different type of geometry that does not have a fill-in weld. The axisymmetric repair analysis results show a more tensile ID region balanced by a more compressive OD section; limited extent repairs were not analyzed for the surge nozzle geometry. Figure 3-20 also demonstrates that the Type 9 surge nozzle geometry, as analyzed, has compressive stresses on the ID surface.

3.2 WRS Literature Data

In addition to the new work on welding residual stress simulation performed in support of this project, a review of existing literature on welding residual stress was conducted. A number of papers were identified that described analysis results and residual stress measurements for axial

stresses in piping butt welds, particularly in the presence of partial arc extent repairs. The papers identified the following characteristics of butt weld axial stresses:

- Repair regions tend to cause more compressive axial stresses in the approximately 20° of material beyond the edge of the repair zone [3-9]
- Repair regions may have significantly higher axial through-wall stresses since the repair through-wall section is balanced by the remainder of the pipe cross section [3-10]

As demonstrated by the results in Figure 3-13 and Figure 3-19, the welding residual stress results for the safety/relief nozzle with a partial arc repair region are in agreement with these characteristics.

3.3 Welding Residual Stress Validation

The finite element analysis methodologies described in this section were also used to simulate the fabrication of a mockup where residual stresses were measured and compared to analyzed residual stresses. Comparisons were performed using geometry and results from a research project completed by the European Commission Joint Research Centre's (JRC) Institute for Energy [3-11]. The project investigated a wide range of issues related to the structural integrity assessment of a stainless steel weld joining stainless steel and low alloy steel components.

One of the task groups implemented by the JRC research project focused on the reliability of finite element analyses to predict residual stress in the welded joint. This task group organized a series of round-robin exercises that compared predicted welding residual stress distributions to those measured for a welded joint mockup. Complete details of the mockup geometry and welding process were made available to all participants in the round-robin, and their welding residual stress analysis results were compared to each other and to through-wall stresses measured by neutron diffraction (ND).

A drawing of the welded joint mockup as described in the round robin task group problem definition [3-12] is shown in Figure 3-21. This figure depicts the finished weld preparation geometry, following deposition and machining of the stainless steel butter layer on the A508 spool piece. As shown in Figure 3-21, the mockup comprised two piping spool pieces, each approximately 500 mm (20 inches) long, one made of 316L stainless steel and one from A508 low alloy steel. The weld preparation for the mockup was a V-bevel type, with the 316L piping spool forming a backing strip for the initial weld layers. The initial A508 spool piece was 64 mm (2.5 inches) thick, and the initial 316L spool piece was 73 mm (2.9 inches) thick. According to Figure 5 of [3-12], the dissimilar metal weld was performed in 96 total passes, comprising roughly 18 layers. Following completion of the weld, the assembly was heat treated at about 600°C (1,100°F); then the assembly was machined to the final dimensions depicted in Figure 3-21.

As noted above, the finite element analysis methodologies described in Section 3.1 were used to analyze the mockup geometry prepared for the JRC report. While the round robin problem definition provided extensive material property characterization data for the base and weld materials used for the mockup, the materials as defined in Section 3.1 were used for the

comparison analysis. Additionally, since the models described in Section 3.1 did not simulate the butter weld deposition, the mockup simulation model likewise did not simulate the butter welding and machining process. Rather, the model started in a stress free condition from the machined weld preparation state depicted in Figure 3-21. While the specific bead sequence and weld process was provided for the round robin participants, the analysis model used 18 layers spanning the width of the weld groove. The geometry and the boundary conditions of the analysis model were specified to match the mockup conditions. In particular, the mockup was welded on rollers with no axial constraint; this boundary condition was preserved in the analysis model. The post weld heat treatment process was simulated using a uniform application of the 1,100°F temperature in a single structural load step, then removing the temperature in a single structural load step. Simulation of the ramp heating and cooling process was not performed, and creep relaxation properties for the materials were not included.

The final machining welding residual stresses for the analysis mockup are presented as contour plots in Figure 3-22 and Figure 3-23 for the axial and hoop directions, respectively. In addition to these contour plots, section lines were taken as appropriate to compare with data presented in the JRC report [3-11]. Figure 3-24 through Figure 3-27 are reproductions of Figure 6.10 through 6.13 in the JRC report, with data from the DEI analysis model also included. Figure 3-24 and Figure 3-25 examine the hoop and axial stresses along an axial cut line starting in the 316L material, running through the weld and butter, and into the A508 material, all located at 4.25 mm below the OD surface. The DEI model is seen to compare very well for hoop stresses, and somewhat high for axial stresses along this cut line. The JRC report notes when describing these figures that the measured hoop stresses using ND are considered more reliable and complete than the axial or radial results, and that the equivalent of Figure 3-24 is particularly important for verifying the finite element analysis results. Figure 3-26 and Figure 3-27 examine hoop and axial stresses along a through-wall cut line at the center of the butter. Despite not simulating the butter weld deposition process, the DEI model axial stress results compare well with the other finite element models from the JRC round robin, all of which did simulate the butter weld process. The hoop stress results compare less favorably. The JRC report places particular emphasis, for model validation purposes, on the transition from tension to compression in the hoop direction from the weld to the A508 material in Figure 3-24; it is noted that the DEI model also captures this trend.

3.4 References

3-1. *Modeling and Meshing Guide*, ANSYS 10.0 Documentation, ANSYS, Inc

3-2. *Inconel Alloy 600*, Special Metals Corporation Publication No. SMC 027, September 2002.

3-3. ASME Boiler and Pressure Vessel Code, Section II, Part D, Properties, 1992 Edition.

3-4. M. H. Duc. "Specification de Calcul de Maquettes d'adaptateurs." EdF Specification MS-92-090-A-GPE: A667M.

3-5. L. Karlsson, M. Jonsson, L-E. Lindgren, M. Näsström, and L. Troive, "Residual Stresses and Deformations in a Welded Thin-Walled Pipe.", *ASME Pressure Vessels & Piping Conference*, Honolulu, Hawaii, USA, July 1989.

3-6. E. F. Rybicki and R. B. Stonesifer, "Computation of Residual Stresses due to Multipass Welds in Piping Systems," Journal of Pressure Vessel Technology, Volume 101, May 1979, pp. 149-154.

3-7. *BWR Vessel and Internals Project: Evaluation of Crack Growth in BWR Stainless Steel RPV Internals (BWRVIP-14)*, EPRI No. TR-105873, Appendix H. Palo Alto, CA: Electric Power Research Institute, March 1996.

3-8. "Welding Handbook." Volume One, Seventh Edition, p. 94, American Welding Society, 1981.

3-9. P. Dong, J. Zhang, and P.J. Bouchard, "Effects of Repair Weld Length on Residual Stress Distribution," *Journal of Pressure Vessel Technology,* vol. 124, February 2002.

3-10. T. McGaughy and L. Boyles, "Significance of Changes in Residual Stresses and Fracture Toughness due to SMAW Repair of Girth Welds in Line Pipe," *Pipeline Technology Conference,* Oostende, Belgium, vol. 2., pp. 16.29-16.36, 1990.

3-11. *Assessment of Dissimilar Metal Weld Integrity: Final Report of the NESC-III Project*, EUR 22510 EN, European Commission Joint Research Centre, 2006.

3-12. *NESC-III Project, TG6 2nd (Detailed) Computational Round Robin,* NESCDOC TG6 (04) 01, Rev. 2, February 26, 2004.

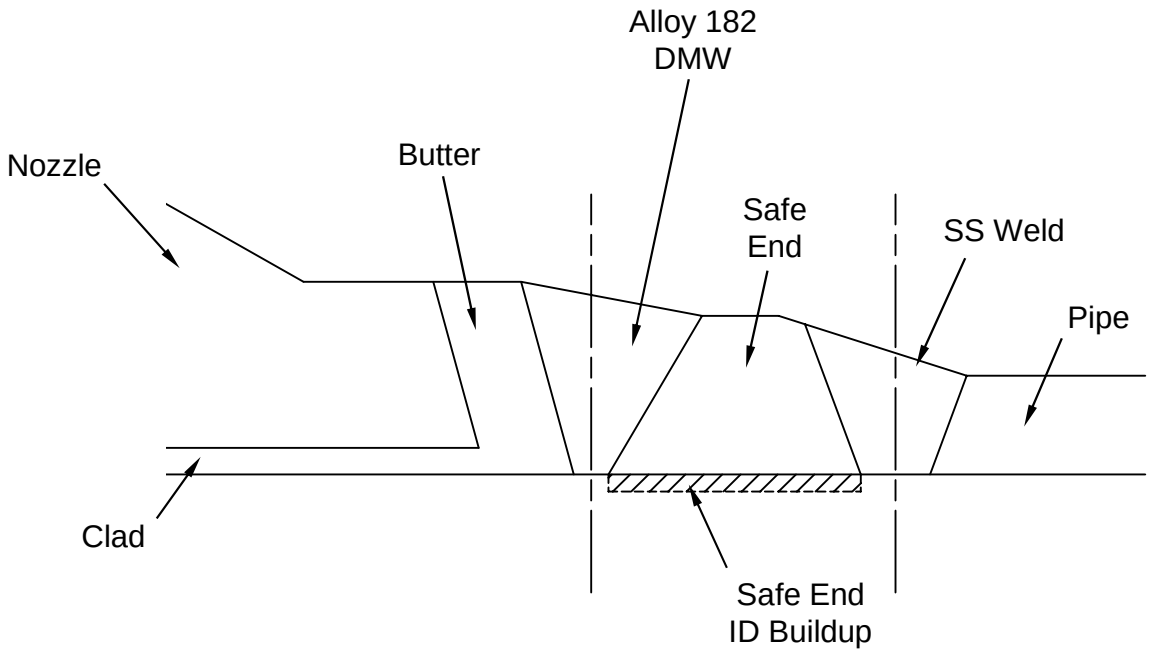

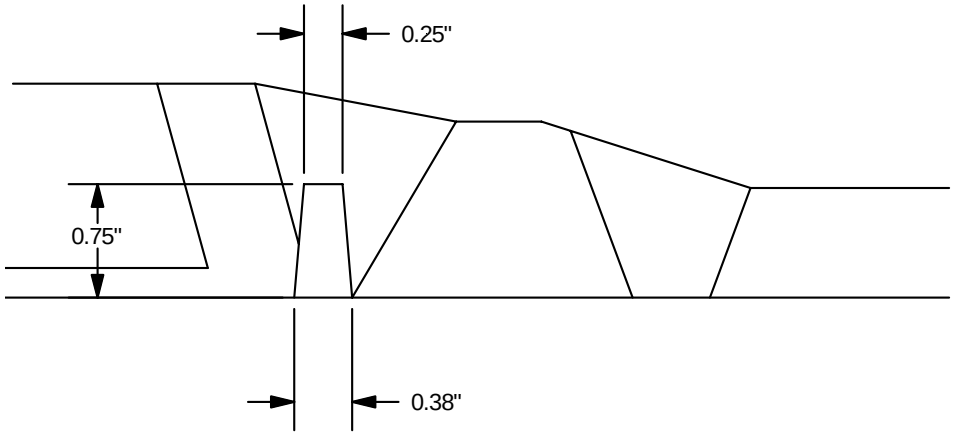

Figure 3-1
Type 1a Safety/Relief Nozzle Model Geometry

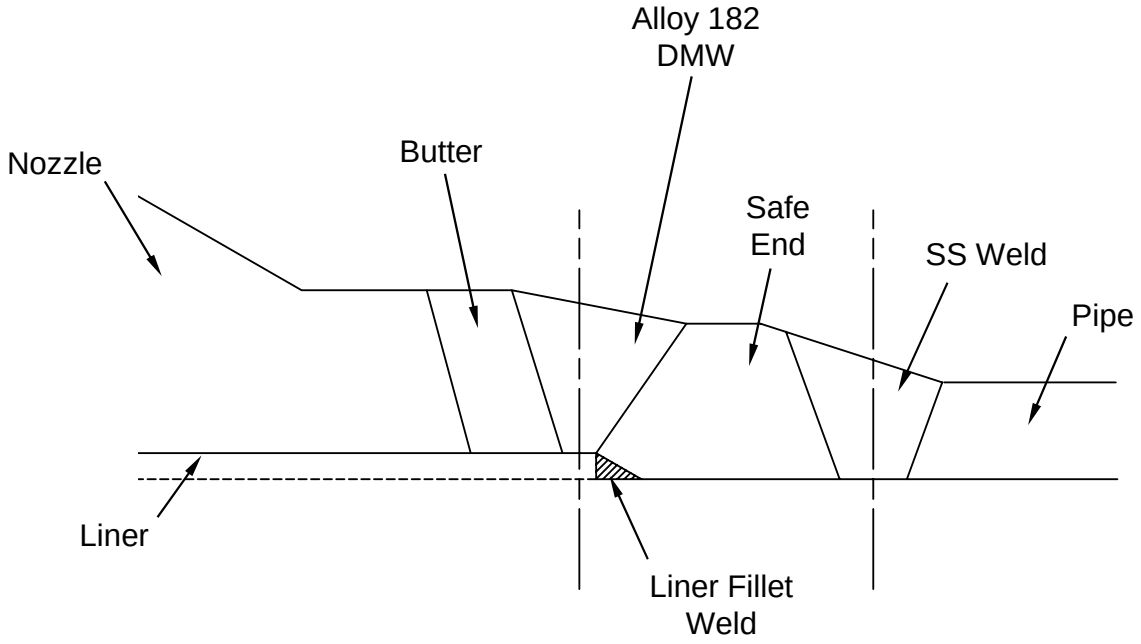

Figure 3-2
Type 2b Safety/Relief Nozzle Model Geometry

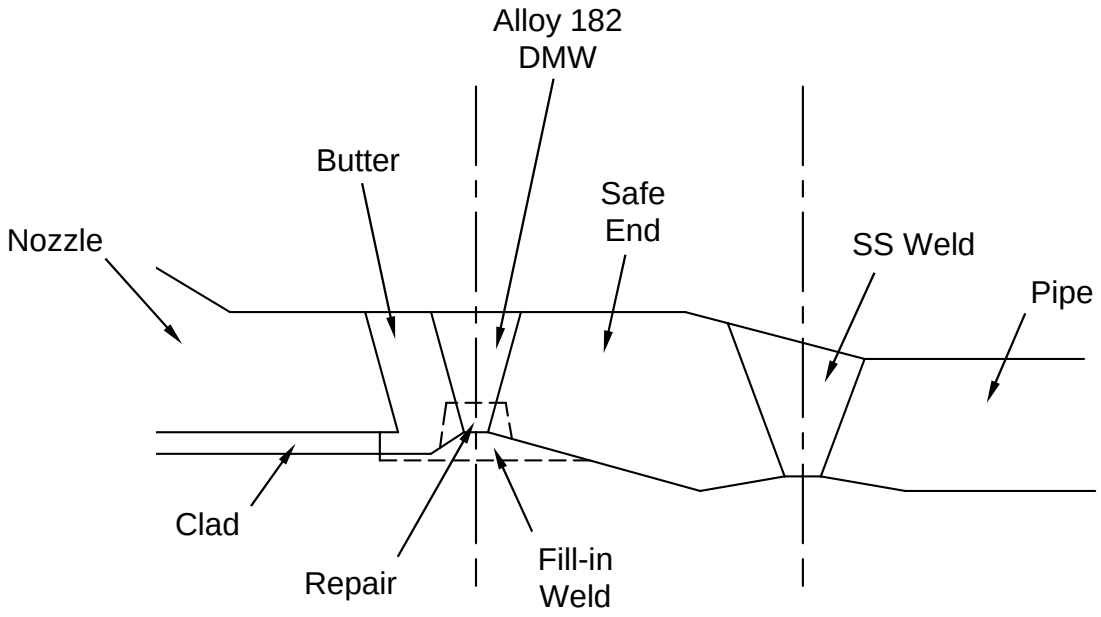

Figure 3-3
Type 8 Surge Nozzle Model Geometry

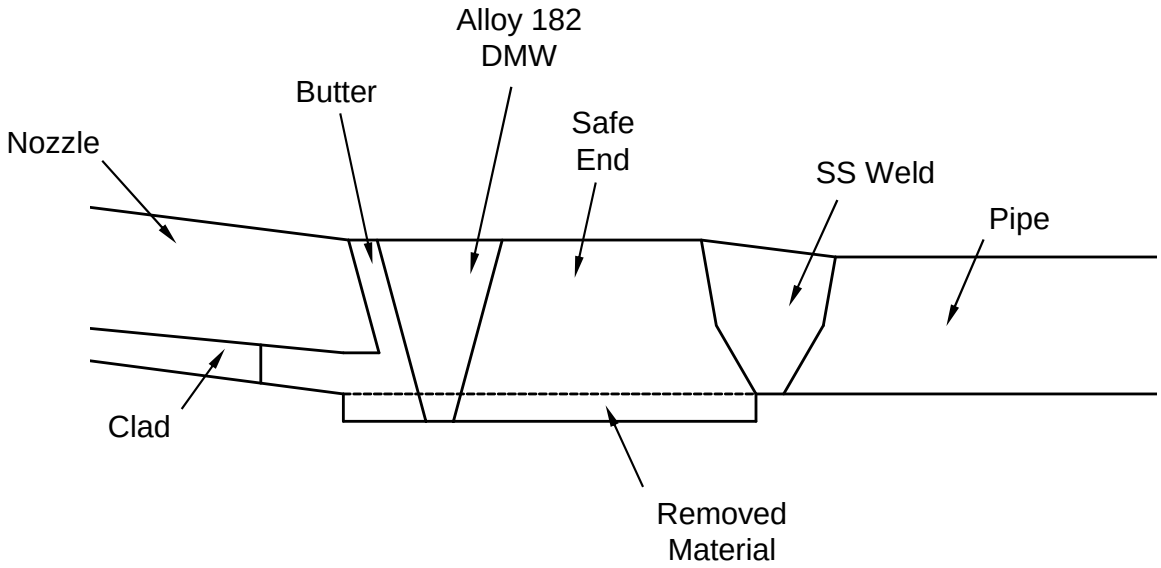

Figure 3-4
Type 9 Surge Nozzle Model Geometry

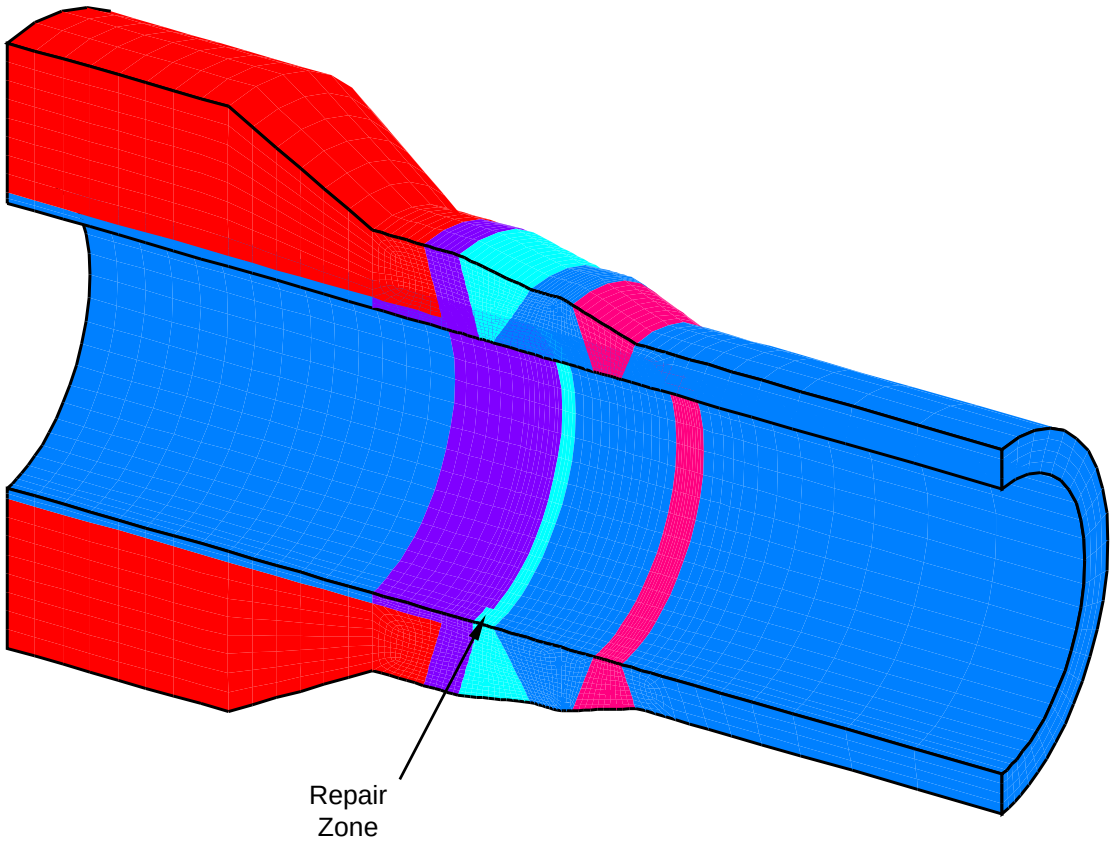

Figure 3-5
Safety/Relief Nozzle Repair Model Geometry

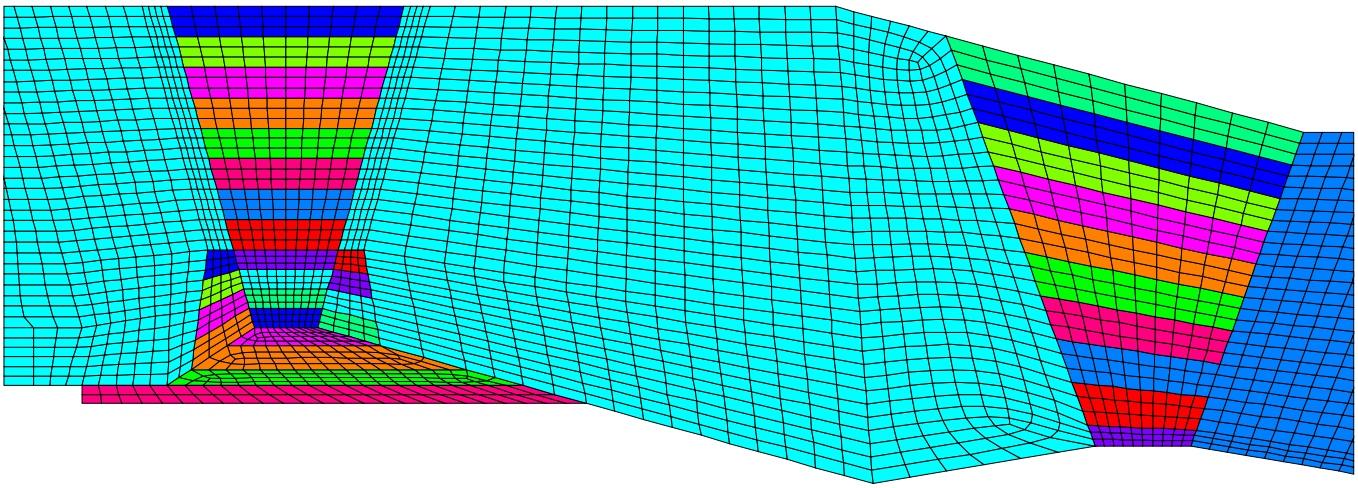

Figure 3-6
Type 8 Surge Nozzle Model – Element Mesh and Weld Layers

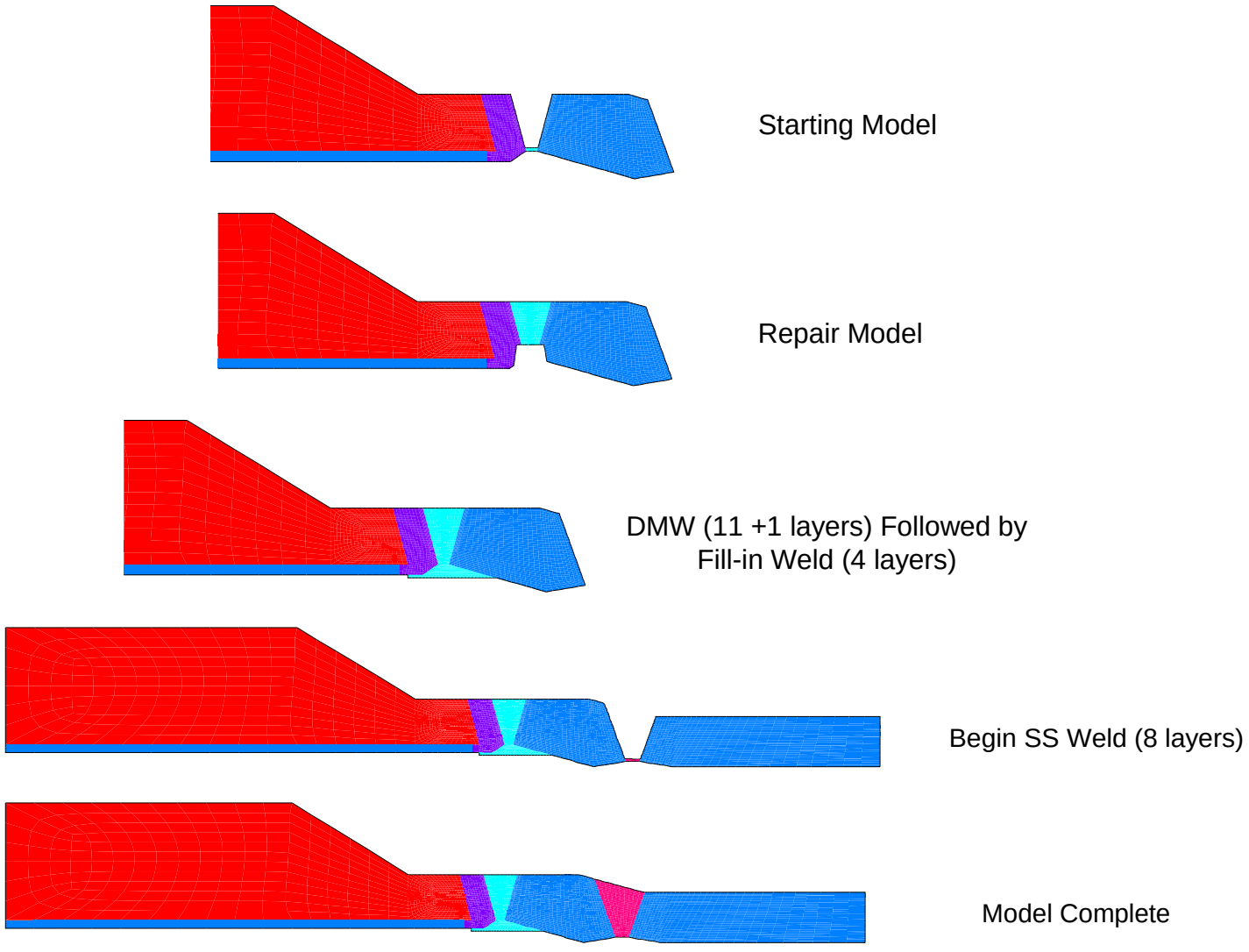

Figure 3-7
Type 8 Surge Nozzle Analysis Progression

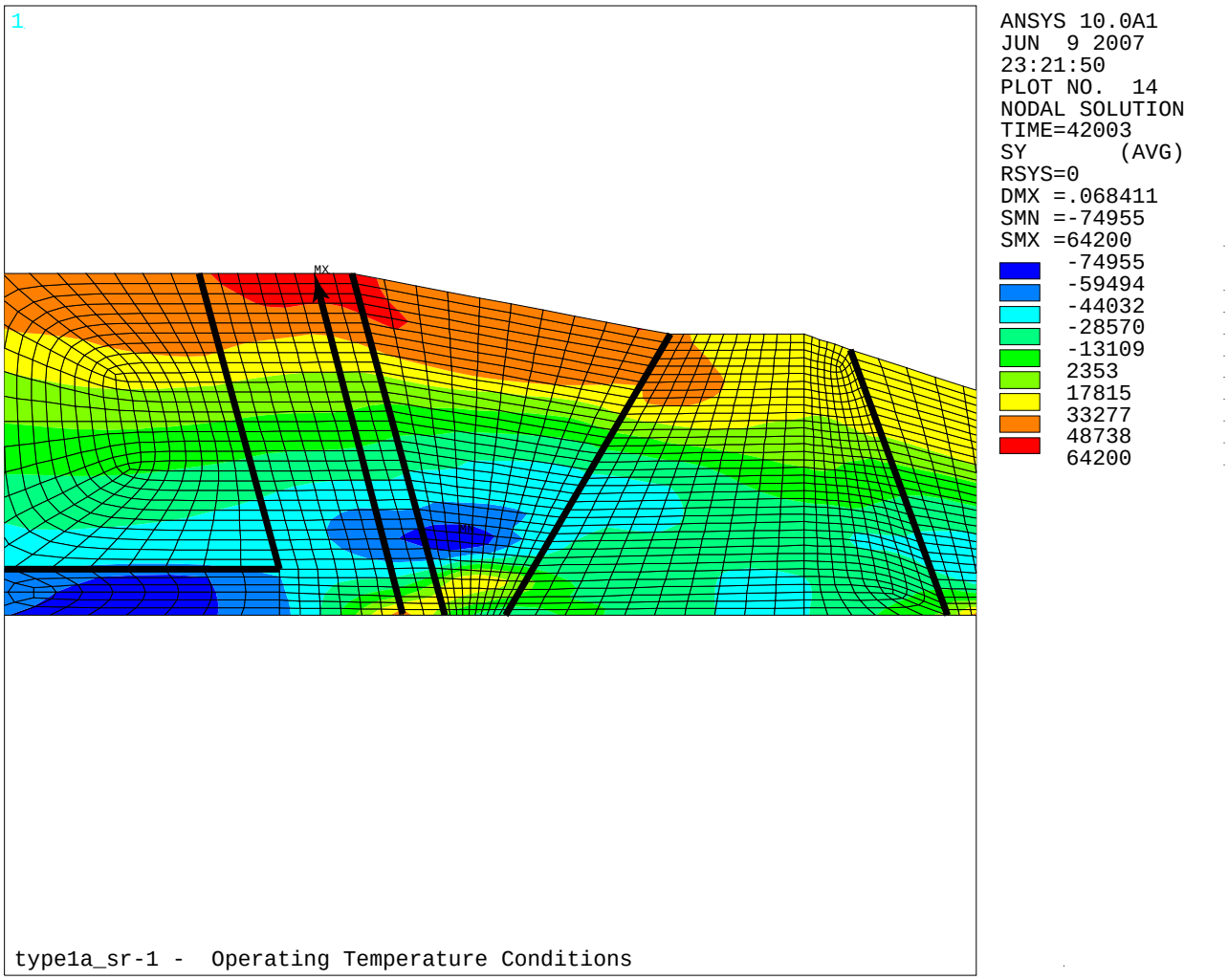

Figure 3-8
Safety/Relief (DMW + backweld + SS weld)

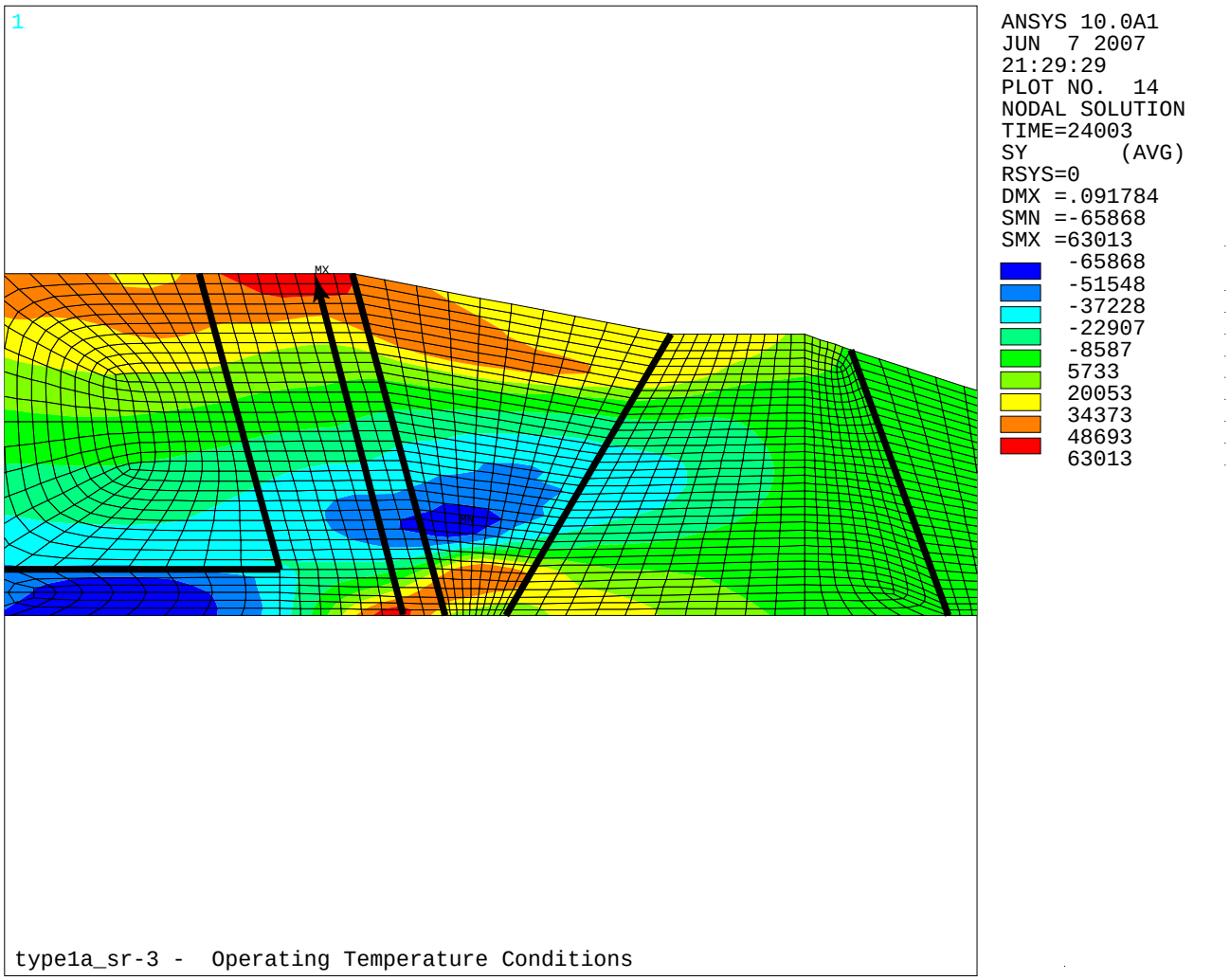

Figure 3-9
Safety/Relief (DMW + backweld, no SS weld)

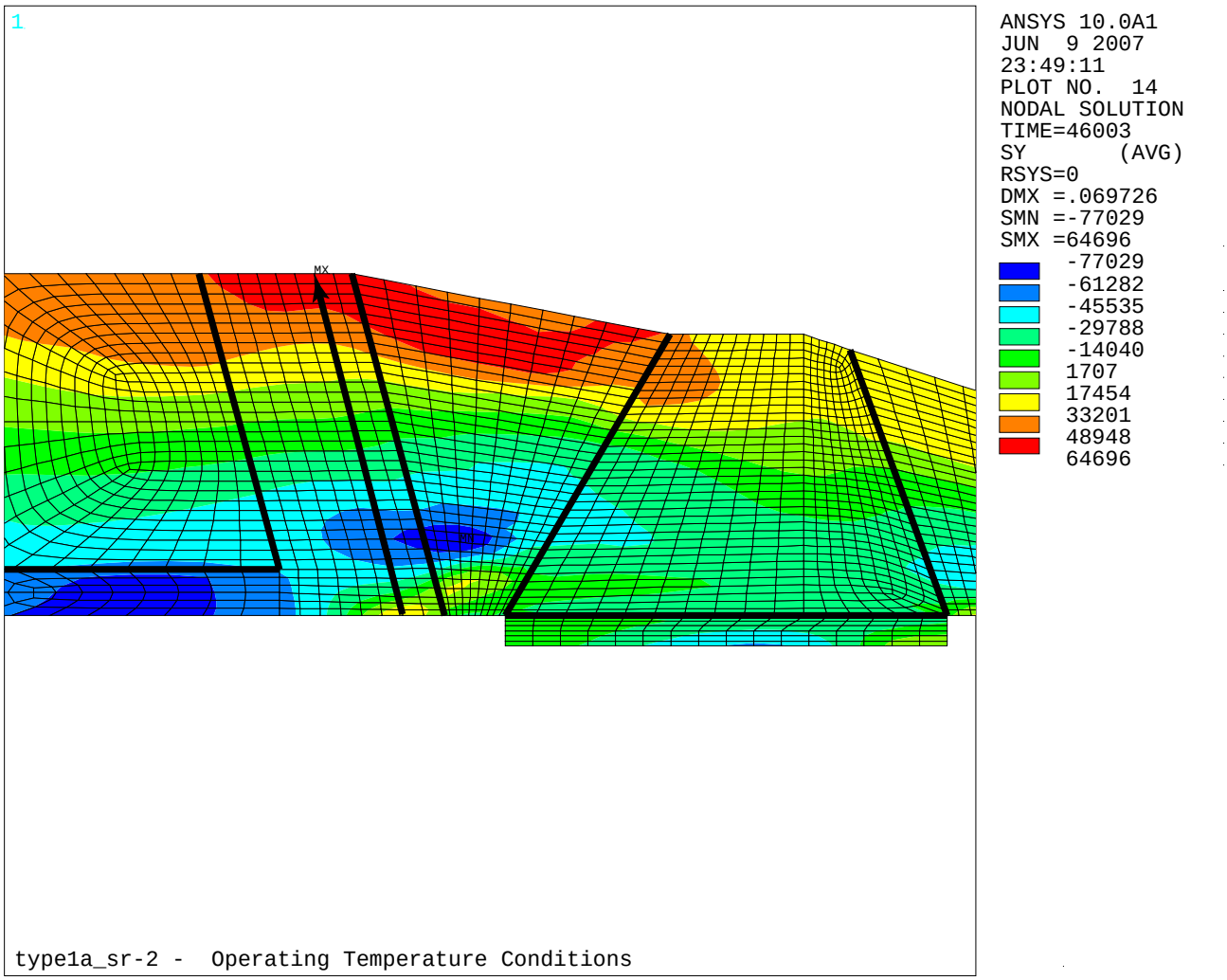

Figure 3-10
Safety/Relief (DMW + backweld + safe end ID weld + SS weld)

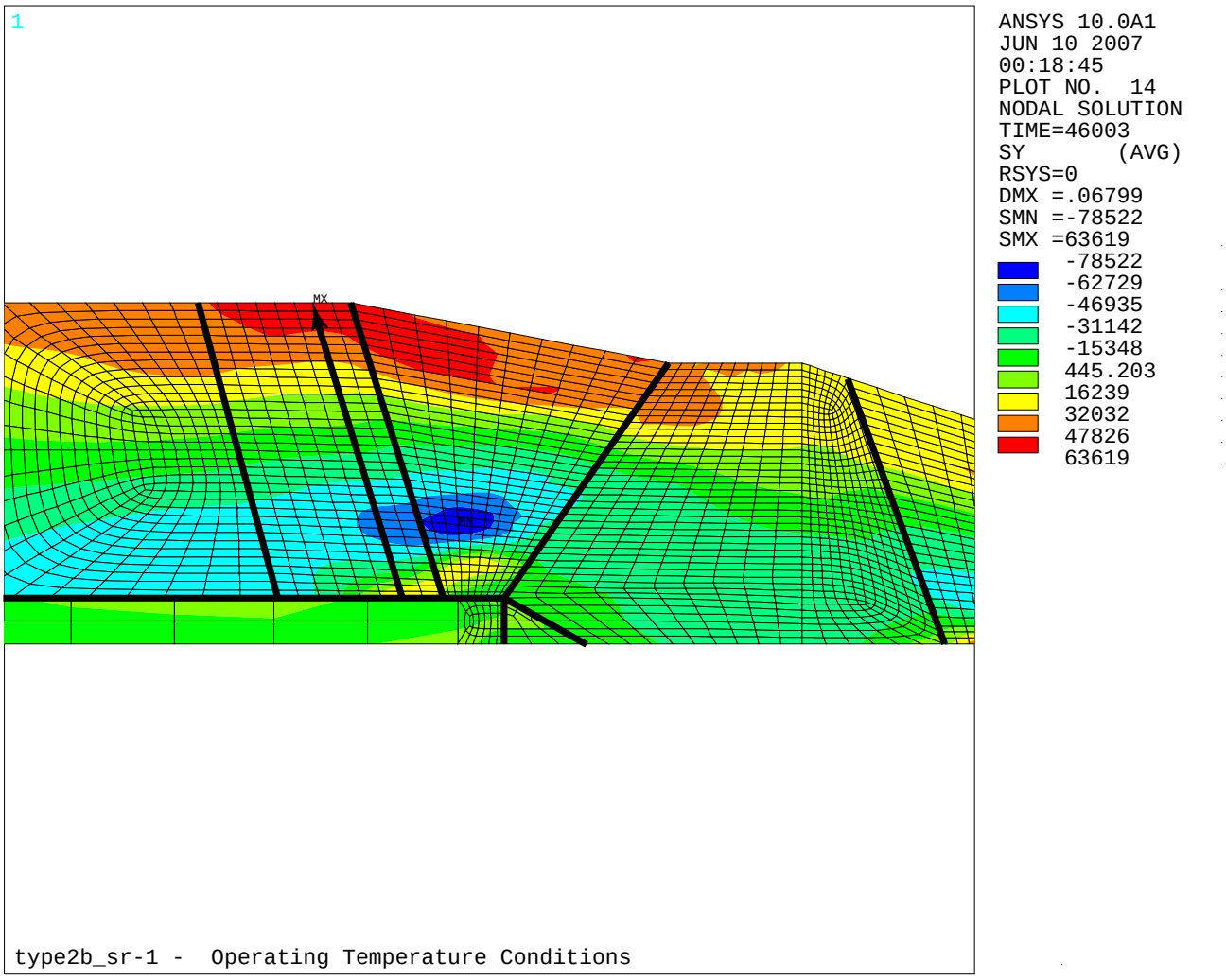

Figure 3-11
Safety/Relief (DMW + backweld + liner fillet weld + SS weld)

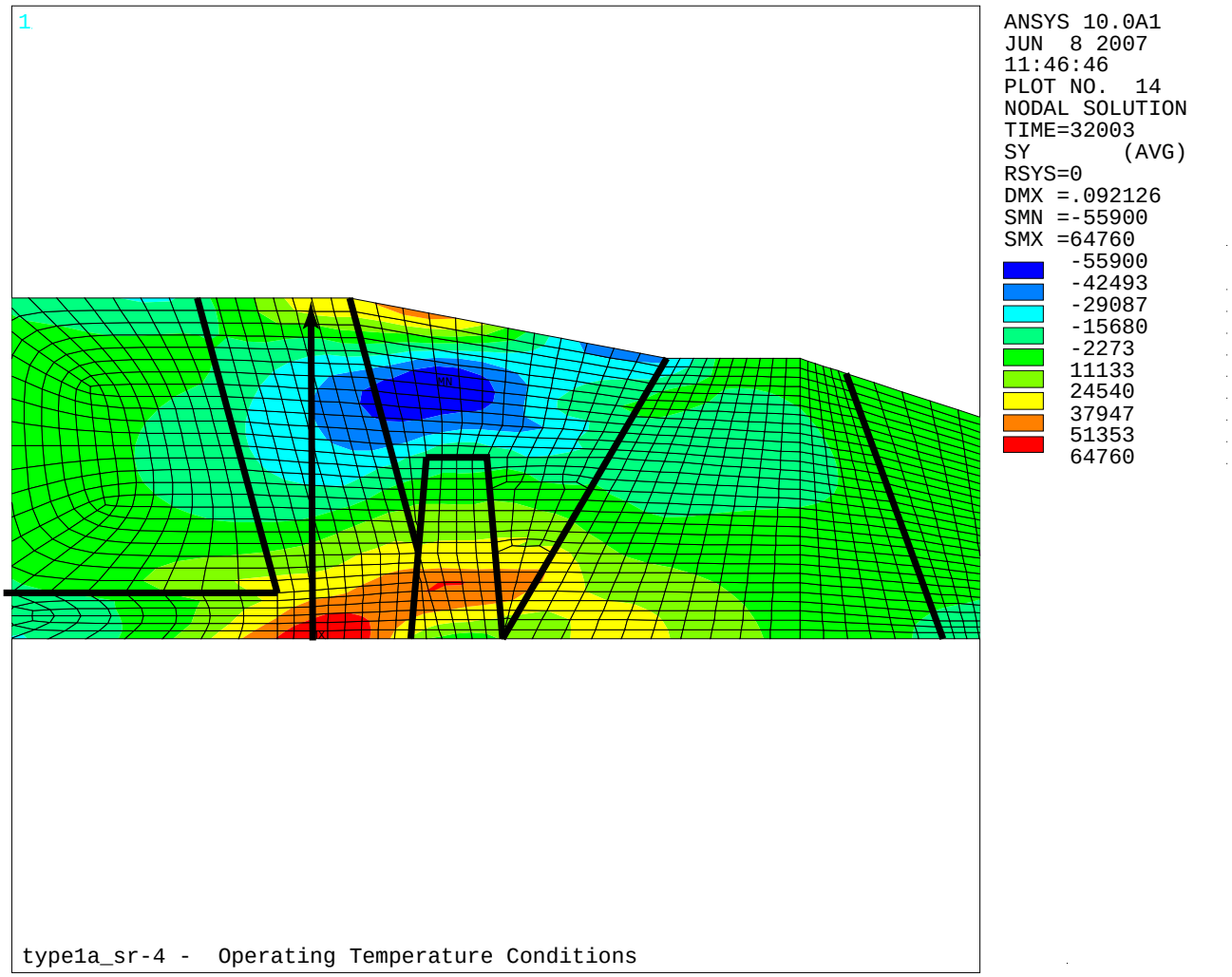

Figure 3-12
Safety/Relief (DMW + backweld + 360° ID repair, no SS weld)

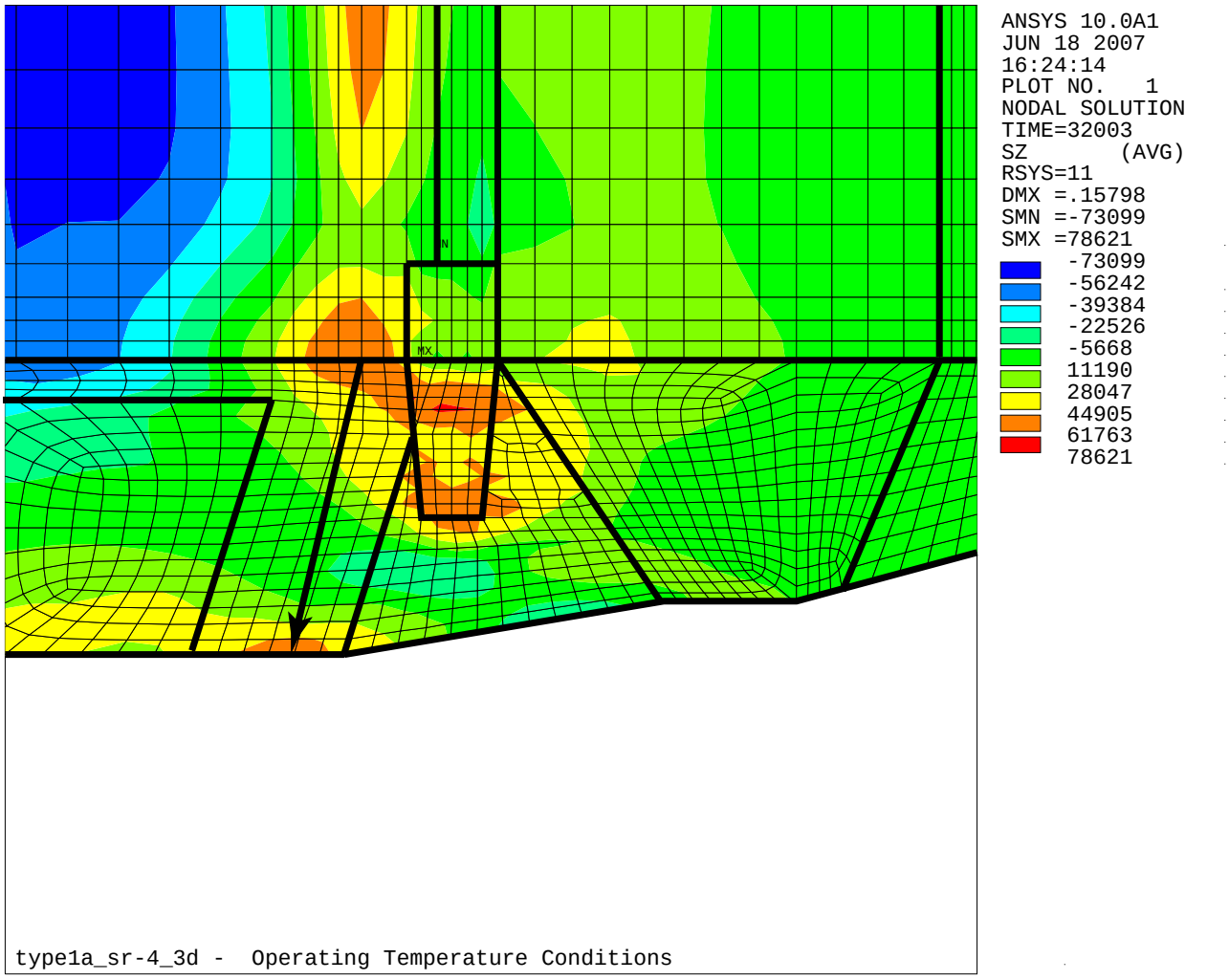

Figure 3-13
Safety/Relief (DMW + backweld + 20° ID repair, no SS weld)

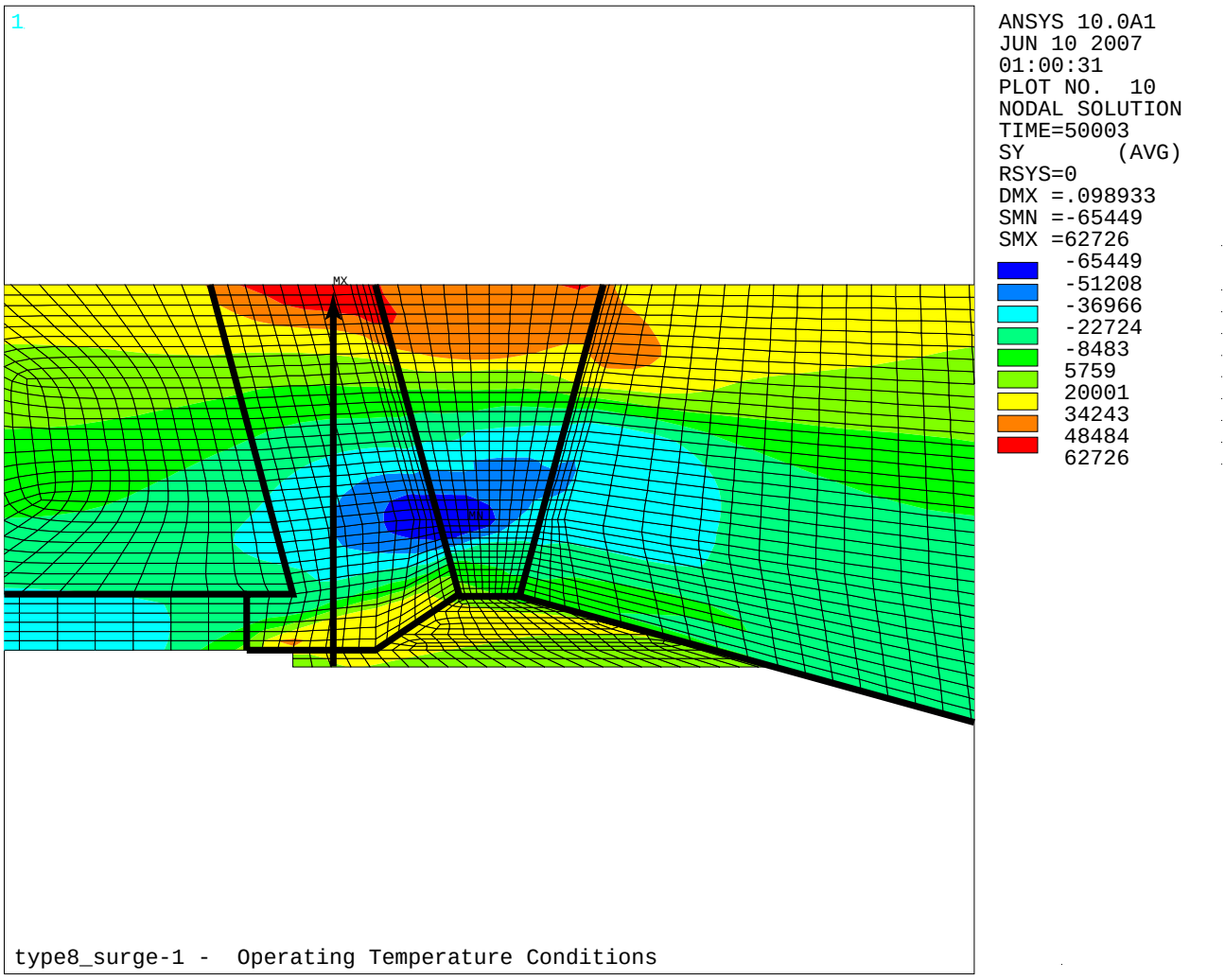

Figure 3-14
Type 8 Surge (DMW + backweld + fill-in weld + SS weld)

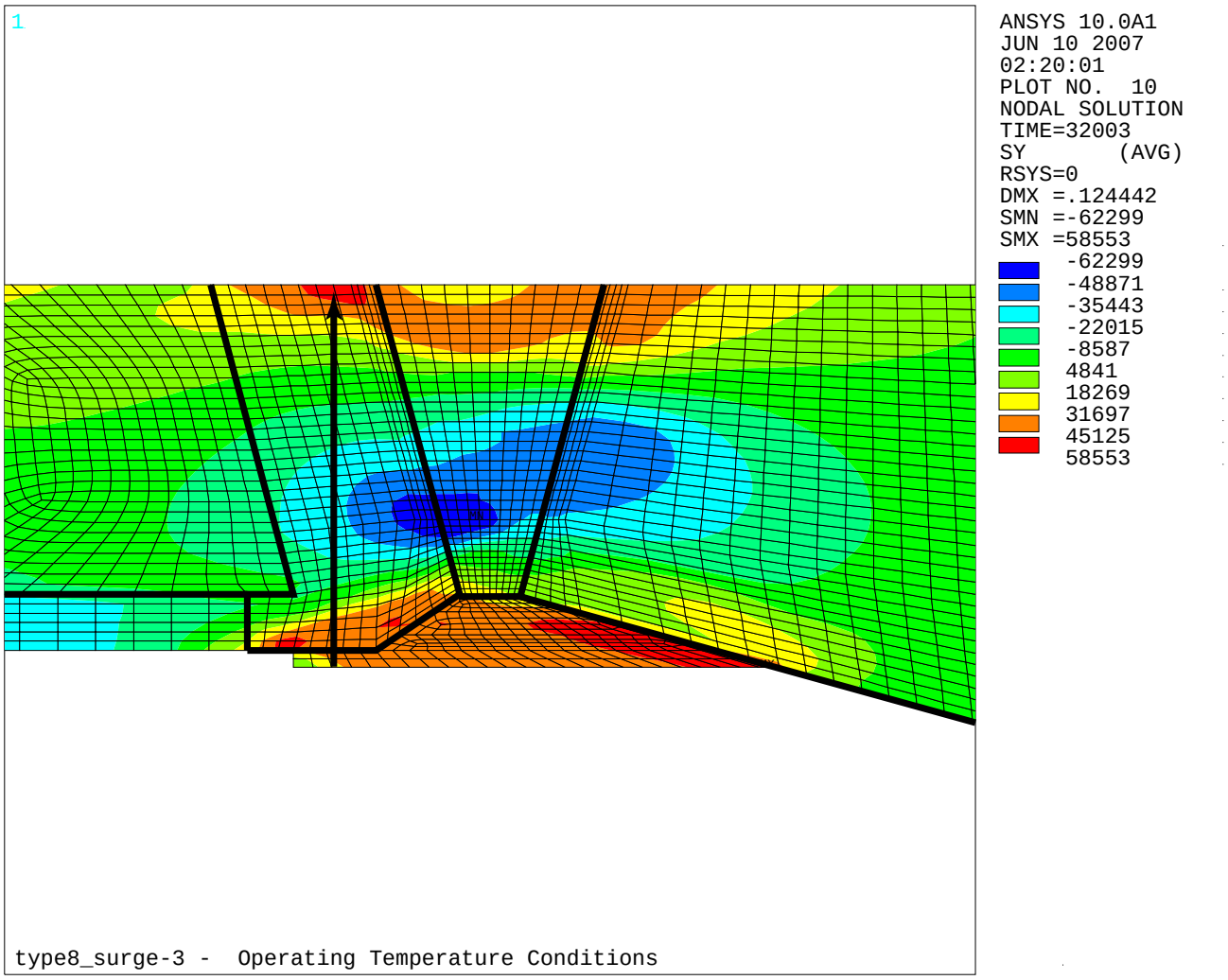

Figure 3-15
Type 8 Surge (DMW + backweld + fill-in weld, no SS weld)

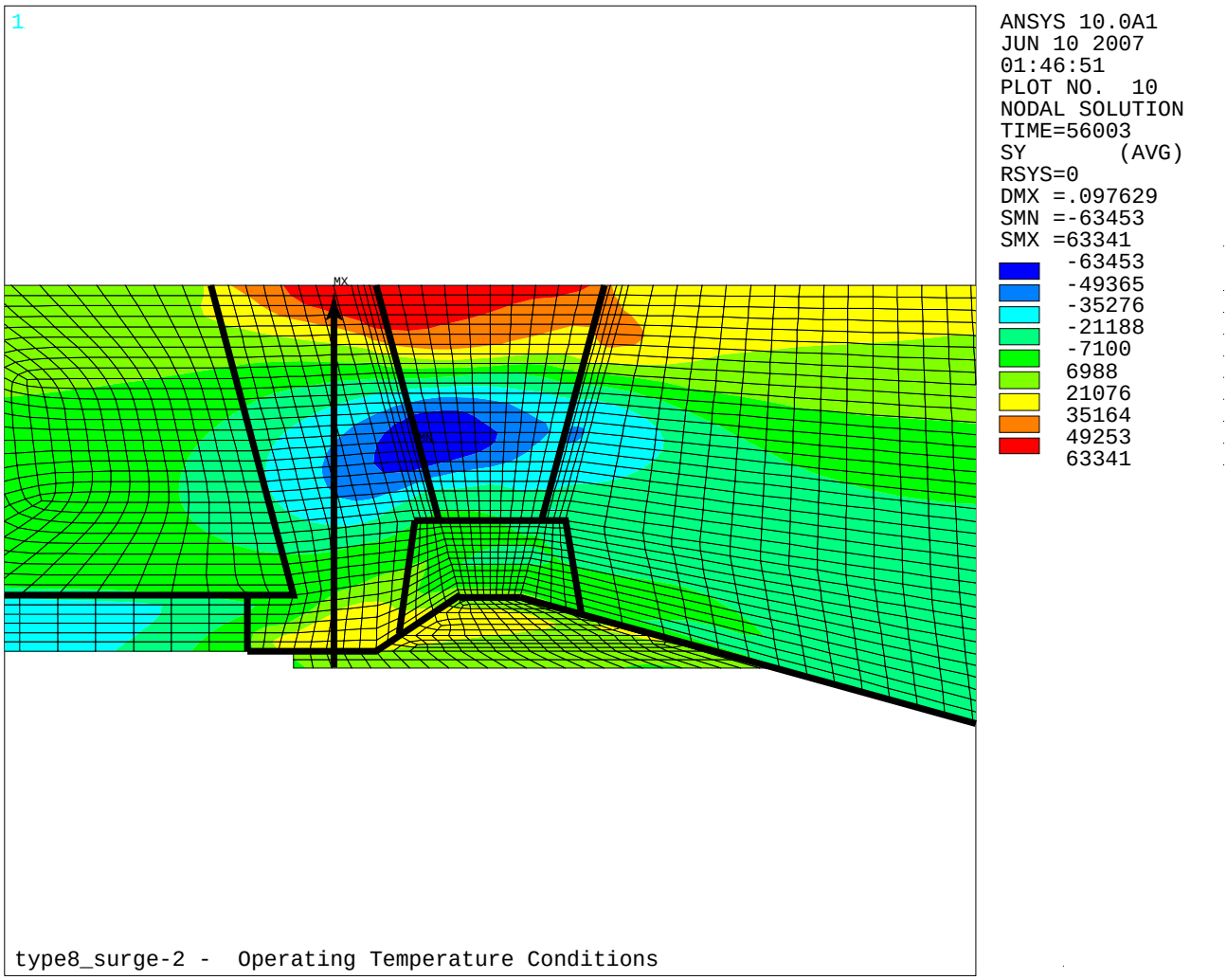

Figure 3-16
Type 8 Surge (DMW + ID repair + fill-in weld + SS weld)

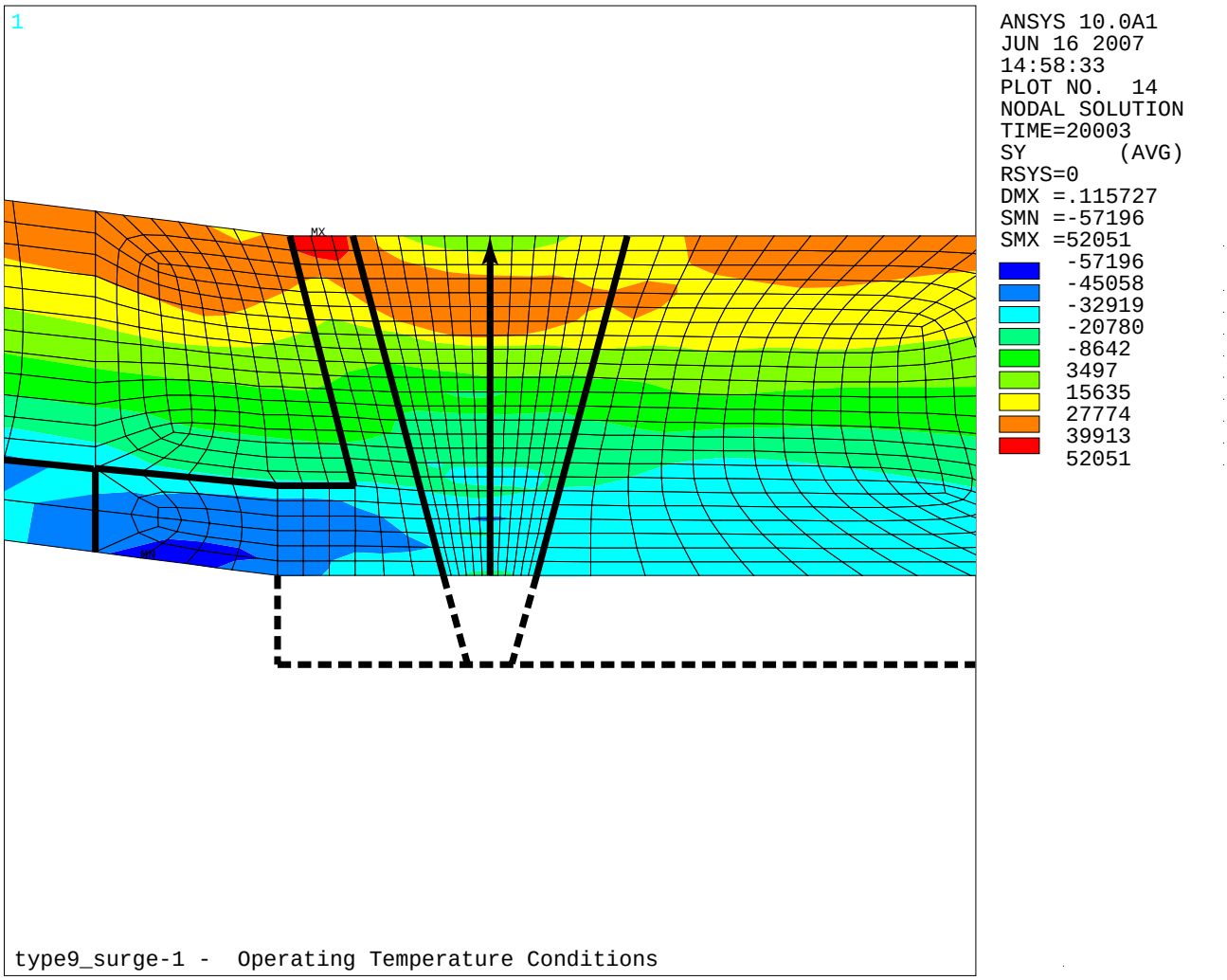

Figure 3-17
Type 9 Surge (DMW + final machining, no SS weld)

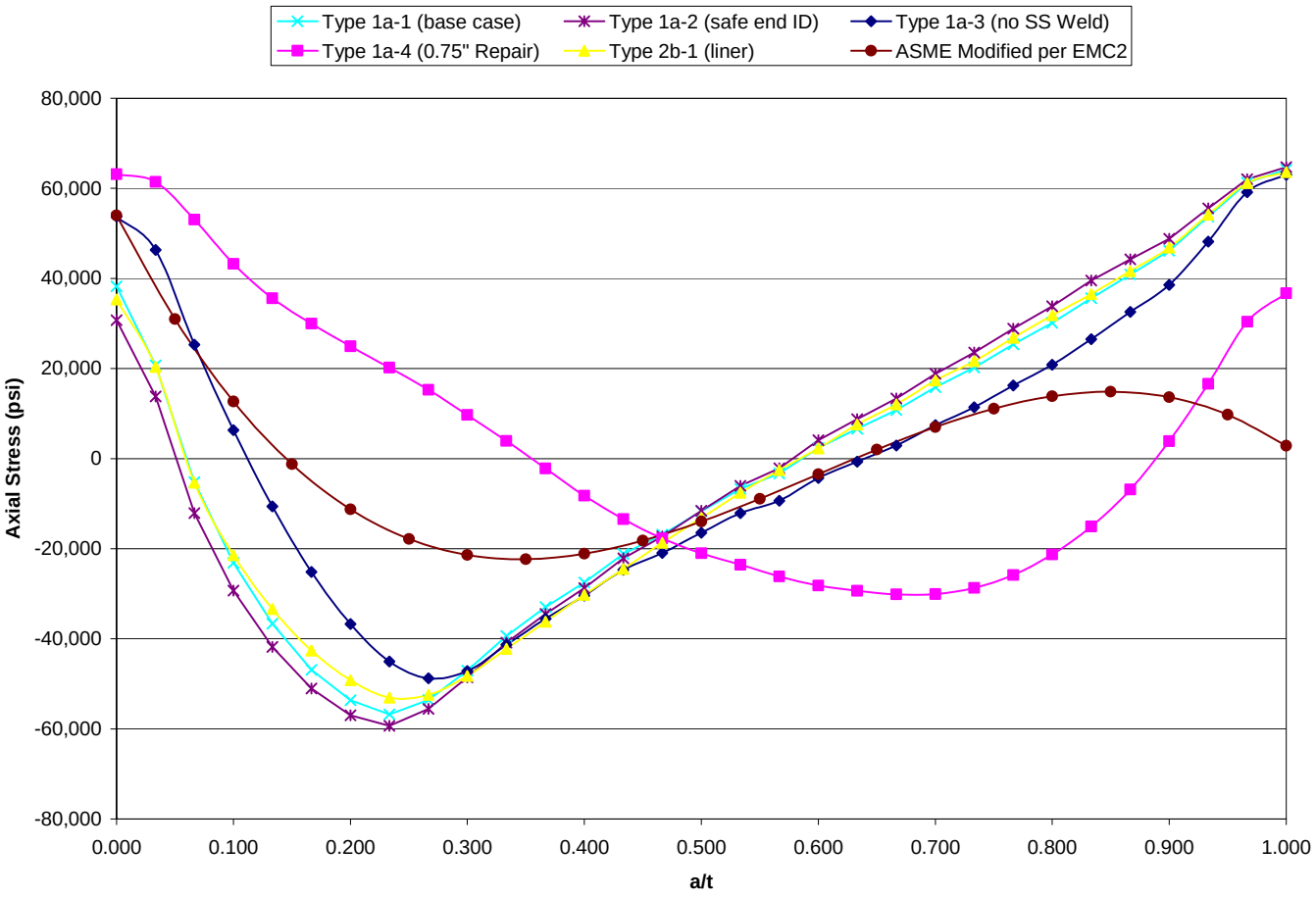

Figure 3-18
Axial Stress Comparison – Safety/Relief Nozzle Analysis Cases

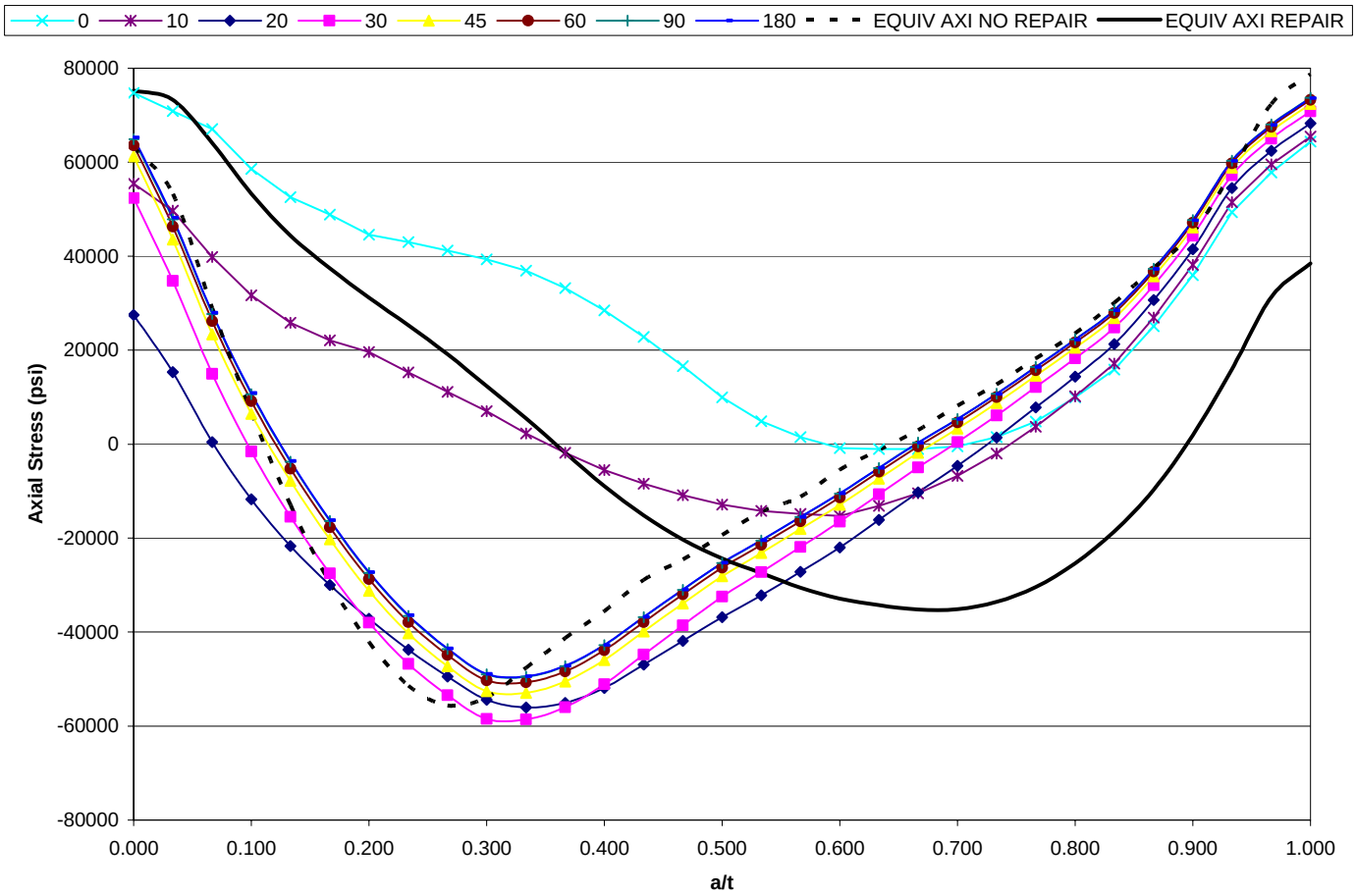

Figure 3-19
Axial Stress Comparison – Safety/Relief Partial Arc ID Repair Case

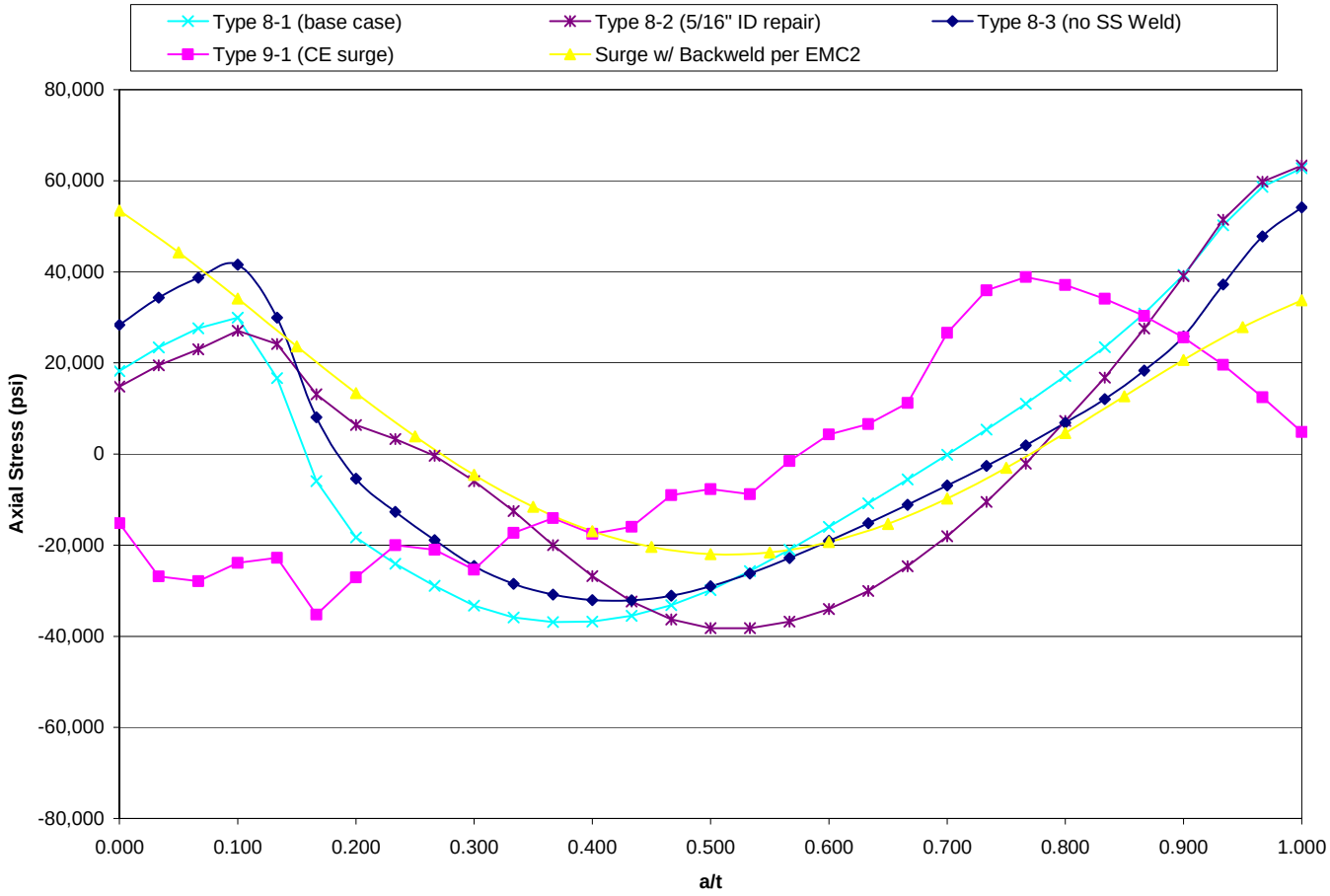

Figure 3-20
Axial Stress Comparison – Surge Nozzle Analysis Cases

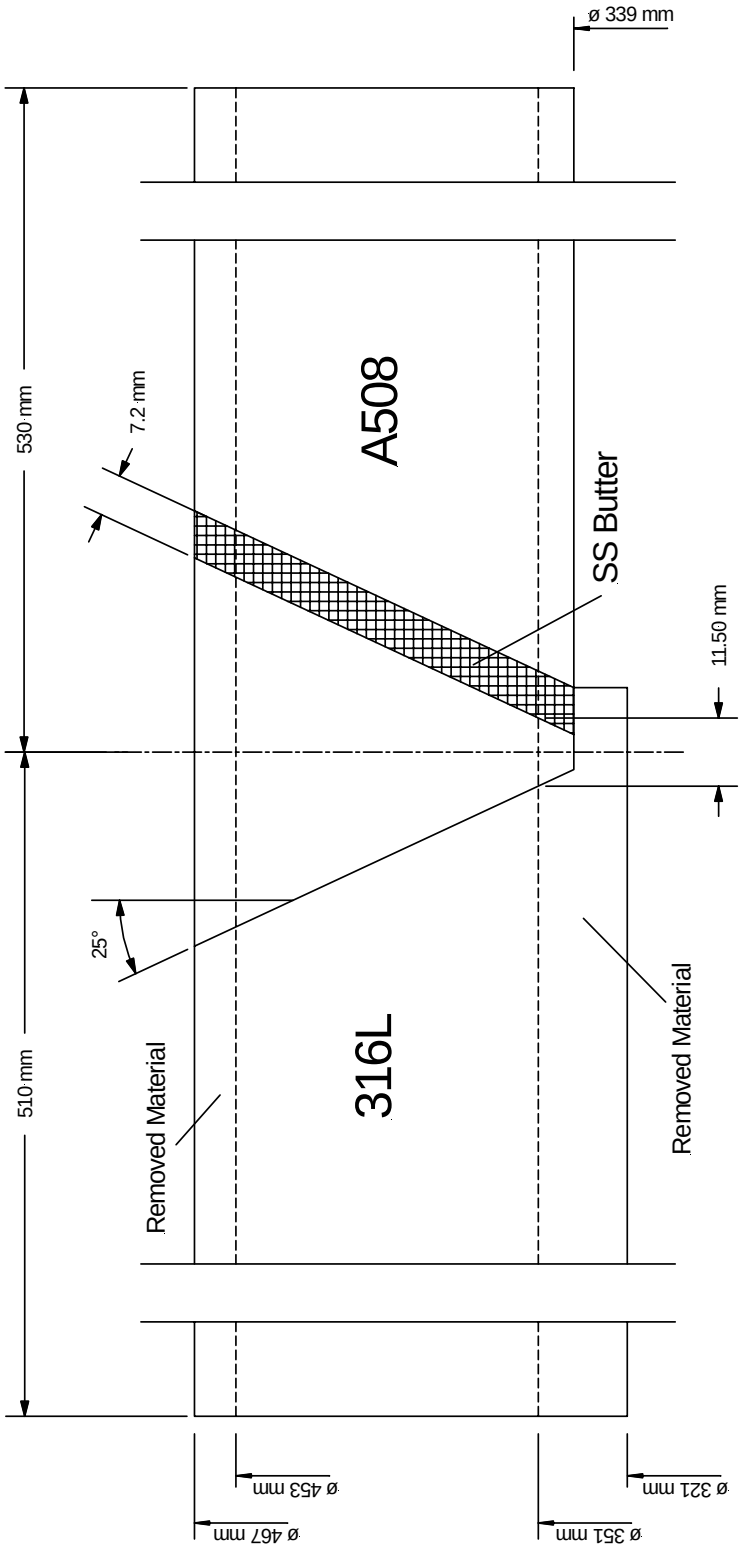

Figure 3-21
Welding Residual Stress Validation Mockup Drawing

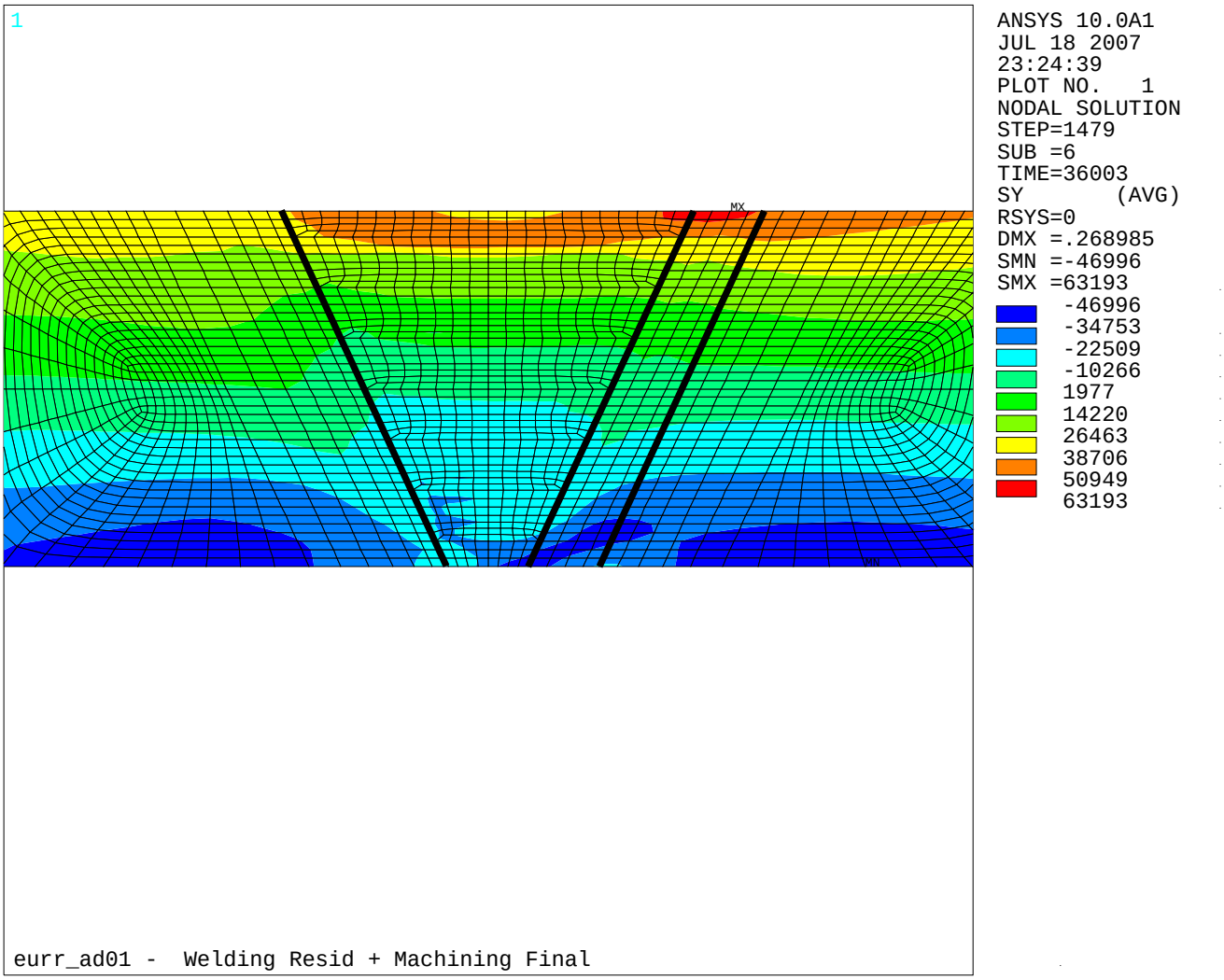

Figure 3-22
Validation Model Axial Stress Results – Final Machining

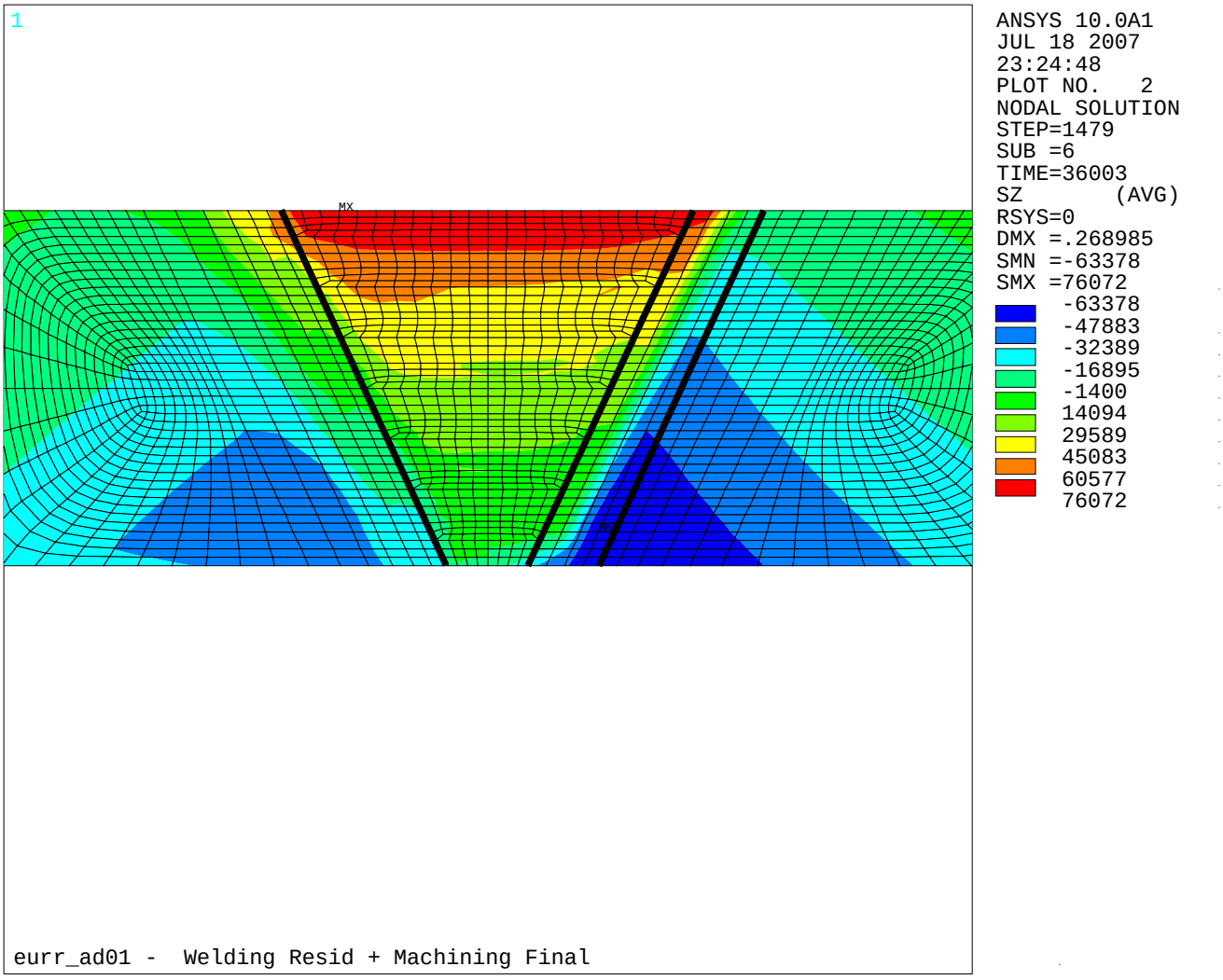

Figure 3-23
Validation Model Hoop Stress Results – Final Machining

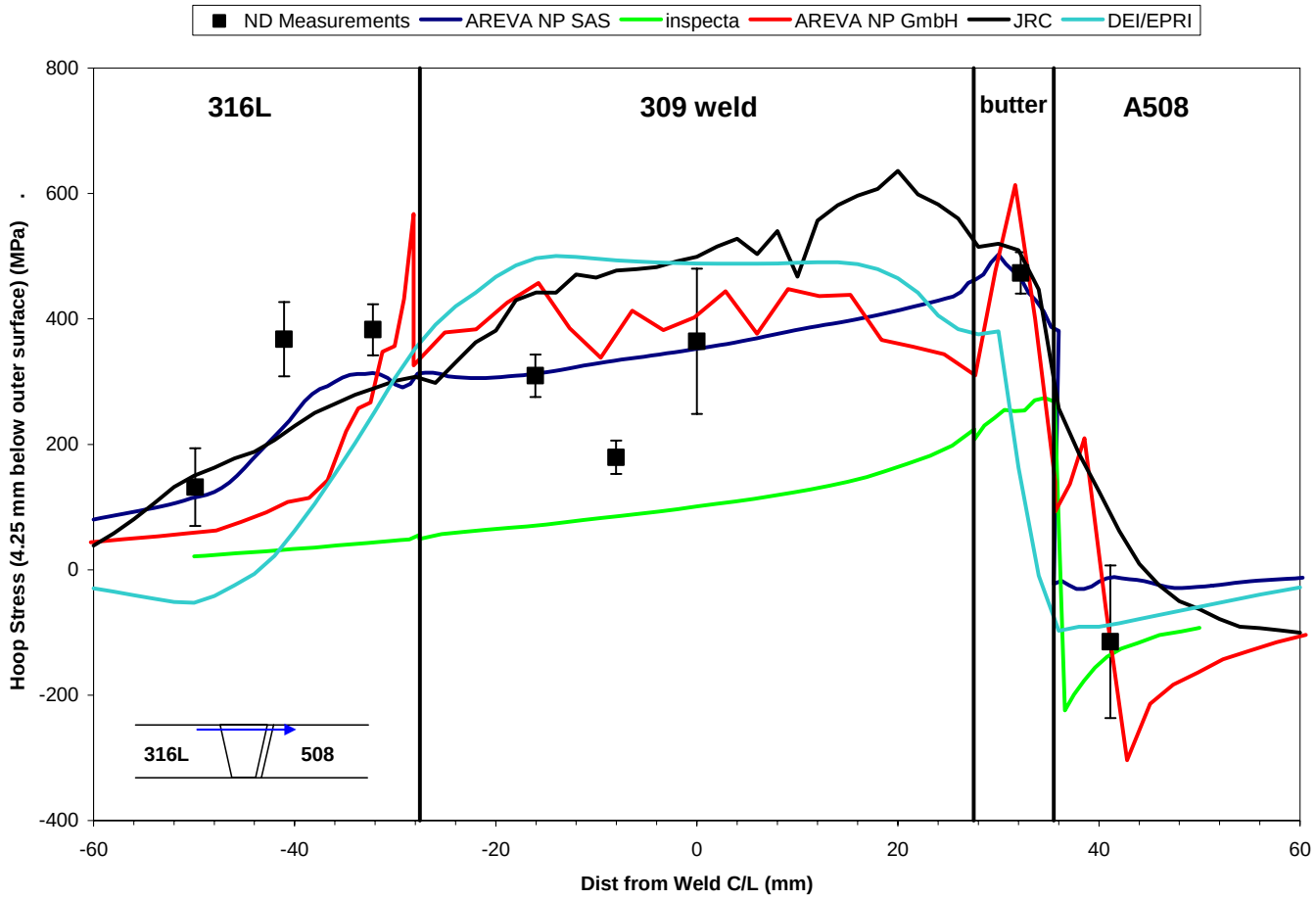

Figure 3-24
Validation Model Predicted vs. Measured Results, Hoop Direction, 4.25 mm Below the Outer Surface

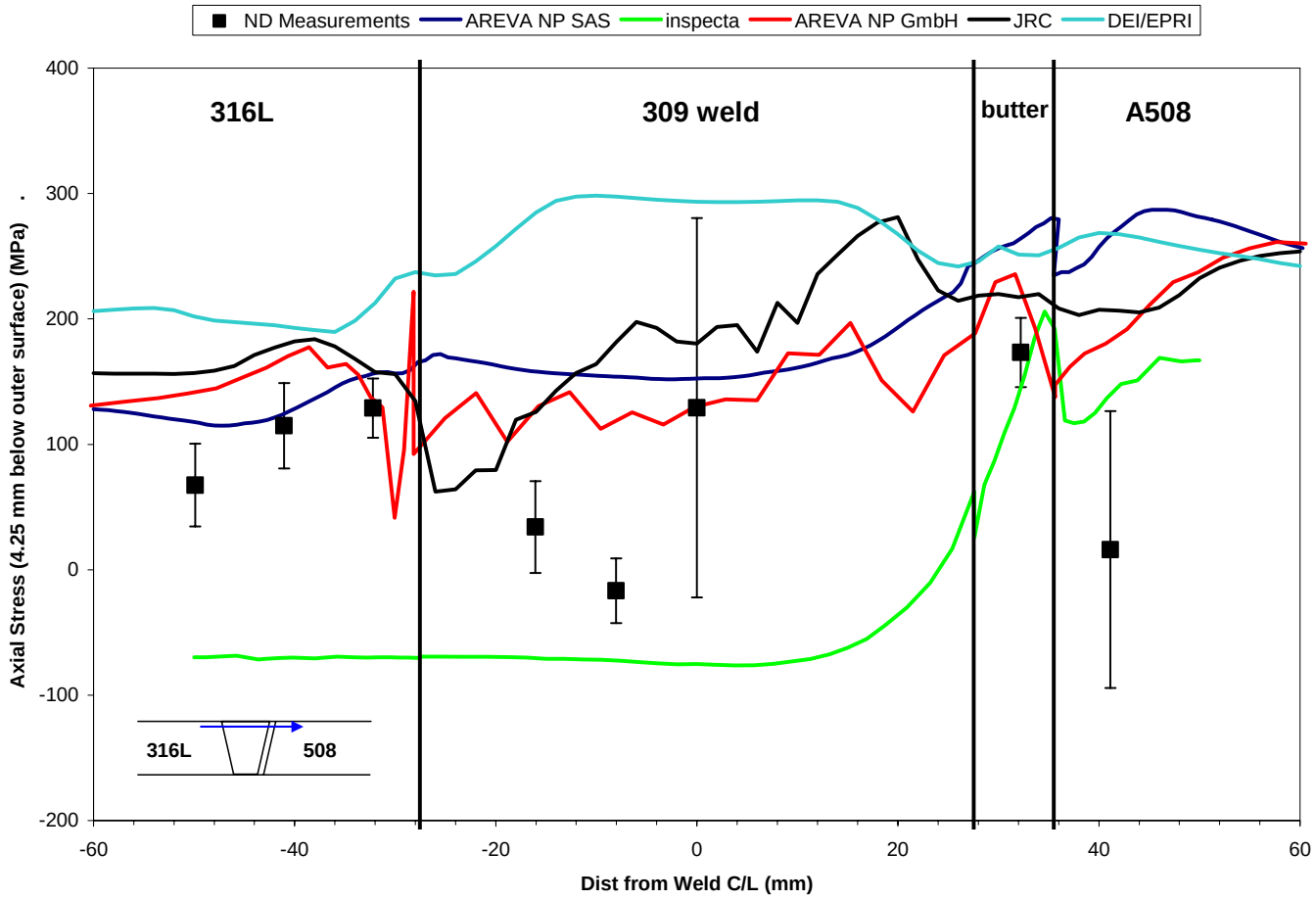

Figure 3-25
Validation Model Predicted vs. Measured Results, Axial Direction, 4.25 mm Below the Outer Surface

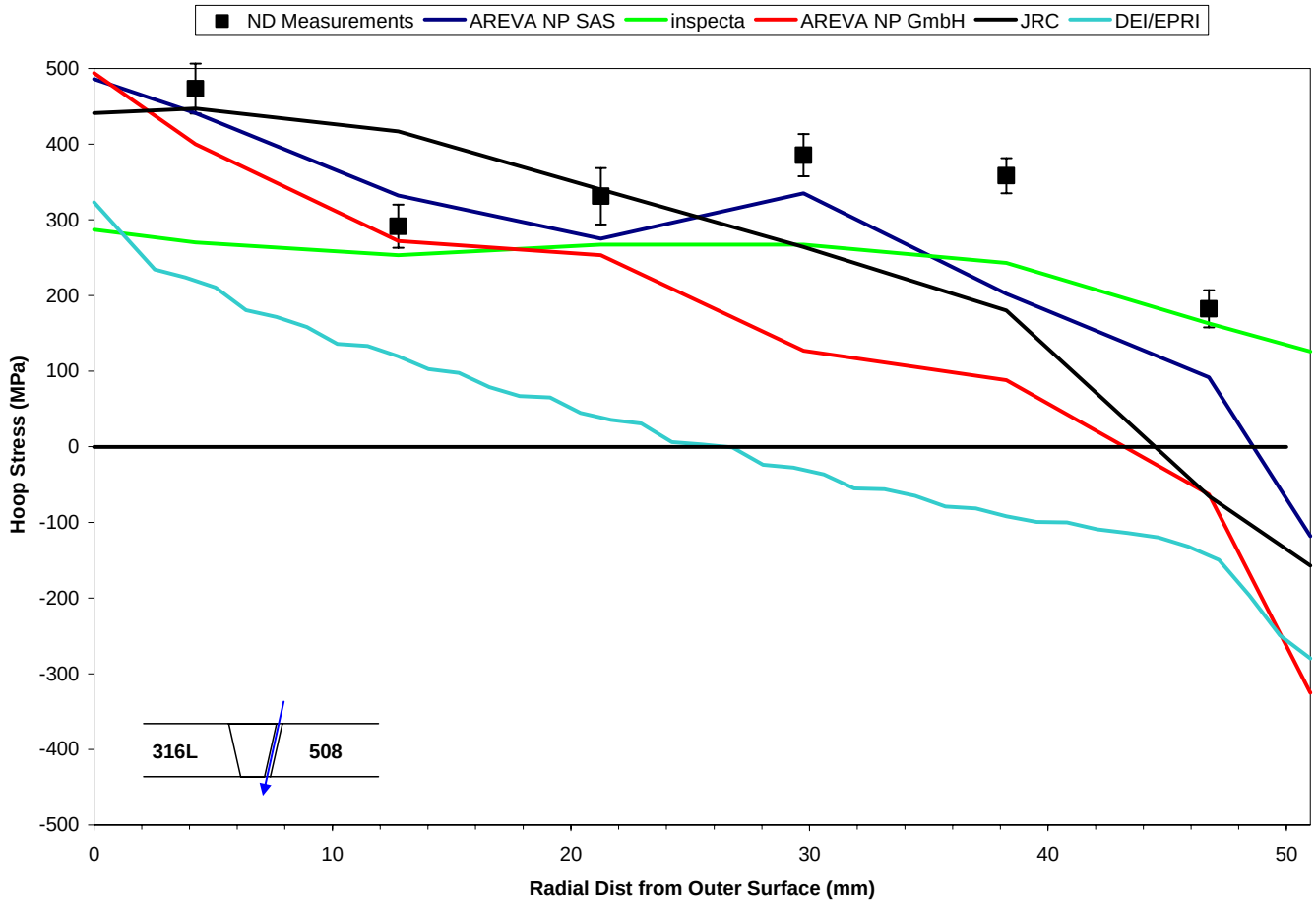

Figure 3-26
Validation Model Predicted vs. Measured Results, Hoop Direction, Through-Wall Section at Butter Layer Center

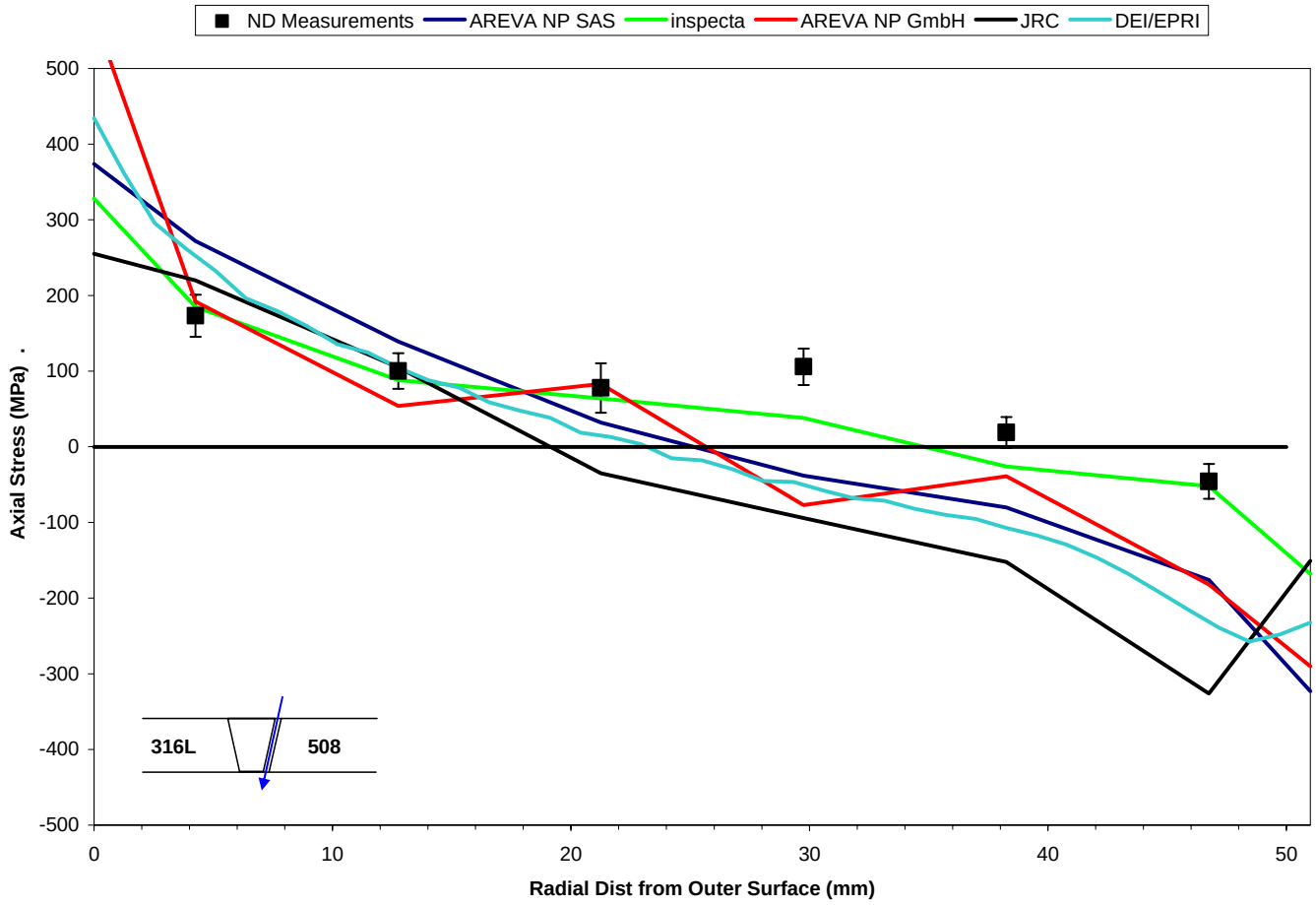

Figure 3-27
Validation Model Predicted vs. Measured Results, Axial Direction, Through-Wall Section at Butter Layer Center

4
CRACK GROWTH MODELING

The purpose of this section is to describe the fracture mechanics and crack growth calculations that were used to take into account the change in flaw shape that will occur with varying crack tip stress intensity factors (SIFs, also denoted as K) along the crack front. These calculations were performed using software developed specifically to consider crack growth with an arbitrary profile geometry. This section describes the overall approach used for the calculations. Additional results from a sensitivity matrix of loading cases are provided in Section 7. This section also includes, as an example, the detailed results from the Phase I portion of the overall work scope, where the loads and initial flaw geometry used in previous flaw growth analyses were used to perform the arbitrary profile crack growth calculations.

4.1 Modeling Approach

4.1.1 FEA Model

Finite element analysis was used to calculate the crack tip stress intensity factor (SIF) for all flaws considered in this calculation. Figure 4-1 shows the FEA model geometry for a typical starting surface flaw case. As shown in Figure 4-1, the analysis model is three-dimensional and is symmetric about both the plane of the flaw and about the deepest point of the flaw (quarter symmetric). The geometries of the nozzle welds are simplified to be represented by a basic cylindrical geometry with a strip of material representing the weld. As shown in Section 2 and Section 3 of this report, the actual geometry of the dissimilar metal welds is a single U-groove attachment to a safe end, which then transitions both in thickness and in diameter over a short length to the attached relief piping. The simplified geometry assumption permits more analysis cases to be performed since the models are smaller and solve more quickly. Additionally, the simplified cylindrical geometry more readily permits application of arbitrary through-wall stress distributions. The effect of the actual nozzle geometry is also considered as part of the sensitivity case matrix in Section 7.

The meshes generated for this calculation make use of 8-node brick elements, with collapsed-front crack-tip nodes. The crack front region of the fracture mechanics model's mesh is detailed in Figure 4-1. This figure shows the arrangement of the nodes near the crack front region, demonstrating the concentric rings of nodes that radiate outwards from the crack front location. The rings are used to perform J-integral calculations as part of the analysis model post-processing.

External forces and moments are applied as pressures at the edge of the model, with moments applied as a pressure gradient. The desired through-wall stress distribution is applied to the

model using differential thermal expansion loading in the strip of weld material. Because the simulated residual stress distribution is generated through displacement, any effect of stress redistribution caused by elastic unloading in the model is captured in the analysis. A sensitivity case that considers the axial thickness of the strip of weld material is included in Section 7. Stress distributions are typically applied to the three-dimensional model in an axisymmetric fashion, varying through the wall the same at all circumferential positions. However, in some cases, they are applied as varying in the circumferential direction as well as through the wall to simulate the effect of local repairs. Figure 4-2 is an example axial stress plot showing an applied axisymmetric through-wall stress distribution in the fracture mechanics model. Figure 4-3 is an example axial stress plot for a local repair stress field distribution. In order to generate these stress plots, a zero axial displacement boundary condition is applied to the crack face.

4.1.2 Calculation of Crack Tip Stress Intensity Factor

Because the model is linear elastic, the J-integral calculations are not of the total strain energy (since there is no plastic strain), but of the elastic strain energy, frequently referred to as G. For convenience and for consistency with the software outputs, the strain energy values calculated from the ANSYS results files are hereafter referred to as J values. Using the relationship between J and K for the special case of linear elastic materials and using plane strain conditions, the crack tip stress intensity is calculated from the J-integral values with the following equation:

$$K = \sqrt{J \times E'}$$

where,

K = crack tip stress intensity factor (psi√in)
J = calculated J-integral value (psi•in)
$E' = E / (1-\nu^2)$
E = Young's modulus
ν = Poisson's ratio = 0.30

It is noted that the J-integral value calculated by the software results from Mode I loading due to the symmetry boundary conditions of the model.

4.1.3 Crack Growth for an Arbitrary Flaw Shape

Once the crack tip SIF along the entire front has been calculated, the results are used to determine the shape of a flaw after a small time increment has passed. The crack growth increment at each point (i.e., node) on the crack front is based on the SIF calculated at that point, with growth occurring in the direction normal to the crack front. The crack growth rate is calculated using the SIF in combination with the MRP-115 [4-1] crack growth rate equation for Alloy 182 weld metal, which recommends a SIF exponent of 1.6 and the use of a zero SIF threshold. Sensitivity cases for the crack growth rate are also performed as part of the case matrix described in Section 7.

The crack growth rate values were input directly to the FEACrack software. The change in crack profile for each growth step and the time required for each growth step are calculated in a fully explicit manner from the previous step, based on an input step size for growth at the point of maximum SIF.

4.1.4 Flaw Shape Transition

For every fracture mechanics analysis case considered in the sensitivity case matrix described in Section 7, the initial flaw is either a partially circumferential or fully circumferential (depending on the case) ID surface flaw. The flaw is allowed to grow at an appropriately refined growth step until the deepest part reaches about 93% of the wall thickness. At this point, the flaw size is projected to where the deepest part reaches 100% wall thickness, and a new, through-wall (either true through-wall or complex crack) mesh is generated. In some cases, a partially circumferential ID surface flaw reaches around to become a fully circumferential ID surface flaw before it reaches through-wall; an intermediate variable depth circumferential surface flaw profile is generated in these cases. When the new through-wall mesh geometry is generated, the projected crack front from the surface flaw case is used as the through-wall flaw profile, and any regions where the remaining ligament is less than 10% of the wall thickness are converted to an open crack face (forming the through wall or complex crack). In this way, thin ligaments of material are assumed to break through immediately, without taking credit for additional time to grow through the region. An example of this mesh transition is included in Figure 4-4, which shows the final step of the surface crack growth and the first step of the complex crack growth.

4.2 Fracture Mechanics Calculation Software Background

The fracture mechanics model geometry is generated by FEACrack, a specialized fracture mechanics pre- and post-processing software code. The base model geometry, the model external loads, and the initial flaw geometry were all defined with the FEACrack software. Using this information, the software generates a finite element mesh that may be solved to calculate the stress state of the model. FEACrack is not a finite element analysis code; however, it is capable of automating the process used to generate a mesh and analyze that mesh on a variety of commercial analysis software codes. The analyses of the fracture mechanics models were performed using ANSYS Version 10.0, installed on the same computer as FEACrack.

Once the model is analyzed, the post-processing portion of FEACrack reads the ANSYS results and performs J-integral calculations at a number of points along the crack front. J-integral calculations are performed at each of five concentric rings set around the collapsed crack front nodes to determine an average J-integral value. The variation of the average from each of the individual J-integral values determines the “contour dependence” of the average J-integral value, and is performed as an internal check on the numerical accuracy and mesh refinement of the FEA model. The J-integral contour dependencies are generally verified to be lower than 5% per the recommendation of the fracture mechanics software. The exception is at the one or two points near the surface of the flaw. The developers of FEACrack have noted that the J-integral value at the surface point of the flaw is frequently difficult to calculate with path independence.

When this occurs, FEACrack will linearly extrapolate the J-integral value for the points where the path dependence is high, basing the extrapolation on previous values along the crack front.

FEACrack also has the capability of interleaving the fracture mechanics model pre and post processing with model analysis solution to perform crack growth analysis calculations. An initial mesh is generated, the FEA model is solved, the results are read in by FEACrack, and a new mesh is generated by FEACrack to be solved. The new mesh is generated based on the SIF results from the previous mesh and the desired crack growth step.

4.3 Extensions to Fracture Mechanics Software

A key task in performing the analyses described in this report was to extend the capabilities of FEACrack to consider flaws of arbitrary dimensions. For example, instead of specifying a surface crack with depth and length values, then fitting a semi-ellipse (or other flaw shape) through those end points, the analysis model needed to be able to define a flaw shape based on user inputs for coordinates of the entire crack front in the crack depth and crack length directions. Additionally, once the user-defined mesh geometry was input, growth of the flaw was to be calculated at all points along the crack front, rather than only at the depth and surface positions. Similar modifications were required for through-wall flaws. Based on the results for surface crack growth calculations, a new flaw shape was also developed to perform the through wall portion of the crack growth calculations. This flaw shape is 360° on the ID surface and partially circumferential on the OD surface, commonly referred to as a complex crack shape.

The following extensions were incorporated into FEACrack directly as a part of this project:

- Custom surface crack geometry mesh, part circumference, see example in Figure 4-5
- Custom surface crack geometry mesh, full circumference, see example in Figure 4-6
- Custom complex crack geometry mesh (360° on ID and part circumference on OD), see example in Figure 4-7
- Custom through-wall crack geometry mesh (part circumference ID and OD), see example in Figure 4-8
- Automated crack growth of all custom crack geometries, including crack growth at all points along the crack front
- Redistribution of crack front node spacing for automated crack growth to prevent mesh errors during crack growth, see Figure 4-9.

In addition to these meshing extensions, FEACrack was updated to include an optional contact surface plane that enforces crack face symmetry boundary conditions. Generally, the crack front will not grow into a compressive region where the crack face would be pushed through the symmetry boundary condition. As the local stress field grows more compressive, the local crack front K drops, and the crack stops growing. However, in cases where there is a low driving K along the entire crack front, the crack front may step into a region where the crack face is pushed through the symmetry plane of the model. This inward displacement, however, generates strain energy, leading to a positive crack tip SIF and crack growth. In these cases, the contact surface

plane is necessary to prevent the crack face from pushing through the symmetry plane; the calculated strain energy then goes to zero and crack growth does not continue.

4.4 Phase I Crack Growth Results

In order to evaluate the impact of the extensions to FEACrack described above on the predicted crack shape, an initial (Phase I) analysis was performed using the geometry and load inputs from previous Wolf Creek safety/relief nozzle flaw assessments [4-2]. This analysis case was performed for growth from a partially circumferential surface flaw to the final step where the deepest point of the flaw reaches through-wall. The Phase I analysis was intended as a test of the methodologies to see if it produced a different flaw shape at through-wall versus earlier assumptions for semi-elliptical crack growth. The Phase I analysis case was performed a total of three times over the initial weeks of the project, with results of each analysis reported in intermediate meetings. Each time the analysis was performed, the results were used to refine the understanding of the behavior of the model and to improve the methods used to perform the analysis.

The initial Phase I analysis revealed that the through-wall stress distribution, featuring a high ID surface stress, resulted in a part circumference surface crack growing rapidly to a full circumference surface crack before any significant advance through the wall at the deepest point. Addressing this result required the addition of the custom full circumference surface crack mesh extension to FEACrack. The initial analysis was also performed without nodal redistribution along the crack front, a feature that was added as a result of this initial trial. While performing the analysis, it was necessary to manually readjust the crack front nodes at every growth step in order to maintain an appropriate mesh. The limitations on automation restricted the crack growth refinement that could reasonably be used, including using only five steps growing through-wall once the flaw reached full circumference. Despite these limitations, the initial Phase I analysis results demonstrated that the resulting flaw shape was significantly different from one that was assumed to maintain a semi-elliptical shape, and that the remaining uncracked cross section was significantly greater than previously calculated. An illustration of the flaw growth for this analysis is shown in Figure 4-10. The time to reach through wall in the first analysis was calculated to be 5.1 years.

The Phase I analysis was performed a second time using the improvements to FEACrack to address the limitations from the previous iteration, including automatic node redistribution and the use of a full circumference ID surface flaw when appropriate. In addition, a number of other refinements were made to the calculation methodology. The analysis mesh was adjusted to have more crack front nodes at the surface point of the mesh, instead of evenly distributed. Much greater growth step refinement was also used to maintain flaw shape stability during the automatic growth of the crack. Additionally, analyses were performed to determine a “natural” flaw shape for the applied through-wall stress distribution, rather than starting from a semi-elliptical flaw shape. It was found that a semi-ellipse starting flaw tended to become rapidly deeper towards the surface side of the flaw; the natural flaw shape would tend to remain self-similar during growth. The natural flaw shape was estimated by starting from a semi-elliptical flaw slightly smaller than the desired depth and length, then allowing the flaw to grow until the desired depth and length were reached. Finally, minor adjustments were made to the through-

wall temperature distribution to improve the resulting stress distribution. An illustration of the flaw growth for this analysis is shown in Figure 4-11. The time to reach through wall in the second analysis was calculated to be 7.5 years.

At the completion of the second Phase I analysis, it was assumed that the increase in time was the result of the refined time step and other improvements to the meshing routines. However, in order to examine the impact of the through-wall stress distribution alone on the crack growth time, a final Phase I model analysis was performed with all other refinements and improvements included, but the applied temperature was identical to the first Phase I analysis. An illustration of the flaw growth for this analysis is shown in Figure 4-12. The time to reach through wall in the third analysis was calculated to be 5.36 years.

The results of the iterations on the Phase I analysis methodologies demonstrated that the overall time to reach through-wall could be affected by the through-wall distribution. However, despite the time differences, the shape of the final through-wall flaw remained similar among all three analysis iterations, as demonstrated by Figure 4-13.

4.5 Stress Intensity Factor Verification

The methodologies used in this report to generate, solve, and post-process a finite element analysis mesh for an arbitrary surface crack front profile were compared to an independent calculation performed by EMC^2, a contractor to the NRC, as a means of benchmarking the calculations. A set of four proposed crack front profiles were generated from specified combinations of mathematical functions; by doing so, the crack front generation process remained completely independent of the number of specified geometry points. The four profiles selected are shown in Figure 4-14**,** both in planar coordinates and in the cylindrical coordinates used to generate the actual mesh. A common set of external loads (membrane plus bending stress) were applied to the crack models.

The calculation was performed using FEACrack to generate the mesh, ANSYS to solve the FEA mesh, and FEACrack to post-process the analysis results and calculate the crack tip SIF along the crack front. The independent calculation performed by EMC^2 used their own software to generate the mesh, and ABAQUS to solve the model and calculate the crack tip SIF along the crack front. The comparison for K solutions for all four crack fronts is shown in Figure 4-15**.** This figure demonstrates excellent agreement between the two independent analyses.

4.6 Crack Growth Convergence Checks

4.6.1 Temporal Convergence Check

As noted above, the amount of growth between successive crack growth steps is a specified parameter in the crack growth analysis, and the cumulative amount of time required to grow the specified distance is an output from the analysis. If the specified growth step is too large to capture the variations in loading through the wall of the model, an inaccurate final crack size will result. In order to check that sufficient growth refinement was being used, comparisons were

performed for surface crack and complex crack growth progressions with about twice the normal growth step refinement. Case 1c defined in Section 7, which corresponds to an initial 10% through-wall 360° surface flaw, was used as the base case for this study. The normal surface crack growth procedure was applied in each case, meaning that the final growth step was made from a depth of 93% through-wall to 100% through-wall because of the difficulty in meshing very deep flaws. For the complex crack portion of the convergence check, the cracks were grown from the same initial complex crack profile, with both the original and refined growth step size until a desired number of steps were achieved. For the refined growth step size case, the step size was half and the number of growth steps doubled, resulting in the same final crack length on the weld OD. This convergence check is referred to as the temporal convergence check since a reduced growth step size also corresponds to refinement in the time step size.

The comparison results for the temporal convergence check are shown in Table 4-1 and Figure 4-16, which demonstrate an acceptably small level of temporal numerical convergence error. The final surface crack and complex crack profiles are nearly identical for the case of varying growth step size. Based on these results, it is concluded that a sufficient level of growth step refinement is assumed in the sensitivity matrix of crack growth calculations of Section 7.

4.6.2 Spatial Convergence Check

In addition to the preceding temporal convergence check, a spatial grid refinement convergence study was also performed using the same initial surface crack and complex crack cases. For the refined grid case, the number of elements in the radial and axial directions was increased by about 50%. The number of elements in the circumferential direction was maintained at the same normal level because of a software limitation.

The comparison results for the spatial convergence check are shown in Table 4-1 and Figure 4-17, which also demonstrate an acceptably small level of spatial numerical convergence error. The final surface crack and complex crack profiles are nearly identical for the case of varying grid refinement. Based on these results and the relatively large number of nodes assumed in the circumferential direction (typically 100 over 180°), it is concluded that a sufficient level of grid refinement is assumed in the sensitivity matrix of crack growth calculations of Section 7.

4.7 Validation Cases

As a consistency check of the ability of the crack growth methodology described above to predict actual plant experience, the large circumferential crack detected at the BWR Duane Arnold plant was applied as a validation case. A cross section through the 360° part-depth crack at Duane Arnold is shown in Figure 4-18 [4-3]. Crack initiation and growth were attributed to the presence of a fully circumferential crevice that led to development of an acidic environment because of the oxygen in the normal BWR water chemistry, combined with high residual and applied stresses as a result of the geometry and nearby welds, including the unusual repair weld made on the outside of the Alloy 600 safe end to correct a safe end fabrication error. The water

chemistry conditions that contributed to cracking at Duane Arnold do not exist for the case of Alloy 82/182 piping butt welds in PWR plants.

In order to apply the Duane Arnold experience to the crack growth methodology described above, a welding residual stress analysis of the Duane Arnold configuration, including the weld repair, was performed [4-4]. The calculated through-wall variation in welding residual stress (including application of normal operating temperature but not pressure) at the general crack location is shown in Figure 4-19. The polynomial fit shown in this figure was assumed in the validation case, as were reported operating pressure and design piping loads [4-4].

The crack profile calculated in the validation check is shown in Figure 4-20 versus the actual Duane Arnold crack profile. This profile is based on the assumption of an initial 30% through-wall uniform depth 360° surface flaw, in combination with the MRP-115 [4-1] crack growth rate dependence on stress intensity factor. (The assumption of an initial 360° surface flaw is reasonable given that the crevice between the thermal sleeve and safe end is expected to have acted as a crack starter.) The agreement shown in the predicted and actual crack profiles in Figure 4-20 is reasonable. However, because the simulated crack profile attained is sensitive to the particular assumed initial crack profile and no information is available on the actual crack profile at earlier times, this validation case must be interpreted as a consistency check of the crack growth methodology versus the Duane Arnold experience. In addition, it is recognized that the effective turn in flaw direction from the axial direction of the crevice to the general radial direction of the crack is a complication that cannot be directly addressed by the crack growth methodology.

4.8 References

4-1. *Materials Reliability Program (MRP) Crack Growth Rates for Evaluating Primary Water Stress Corrosion Cracking (PWSCC) of Alloy 82, 182, and 132 Welds (MRP-115)*, EPRI, Palo Alto, CA: 2004. 1006696.

4-2. "Implications of Wolf Creek Pressurizer Butt Weld Indications Relative to Safety Assessment and Inspection Requirements," MRP 2007-003 Attachment 1, Section 5, January 2007.

4-3. *Materials Handbook for Nuclear Plant Pressure Boundary Applications*, EPRI, Palo Alto, CA: 2002. 1002792.

4-4. P. Riccardella, Private Communication to G. White, May 25, 2007.

Table 4-1
Results of Temporal and Spatial Convergence Study for Case 1 360° Surface and Complex Crack Growth Progressions

	Case	Sensitivity Description	Time (years) (Note 1)	% Difference in Time	Maximum Absolute Difference in Depth (in)	Maximum Abs. Difference in ID Circumferential Position (in)
360° Surface Crack	30 Steps - Original Mesh	Base Case	17.42			
	70 Steps - Original Mesh	Temporal	17.18	-1.40%	0.0158	0.0102
	30 Steps - Refined Mesh	Spatial	17.21	-1.24%	0.0021	0.0005
Complex Crack	65 Steps - Original Mesh	Base Case	0.725			
	130 Steps - Original Mesh	Temporal	0.701	-3.27%	0.0127	0.0371
	65 Steps - Refined Mesh	Spatial	0.721	-0.52%	0.0013	0.0021

Note 1: Time for the 360° surface crack case is time to through-wall and for the complex crack case is time until desired number of steps has been executed.

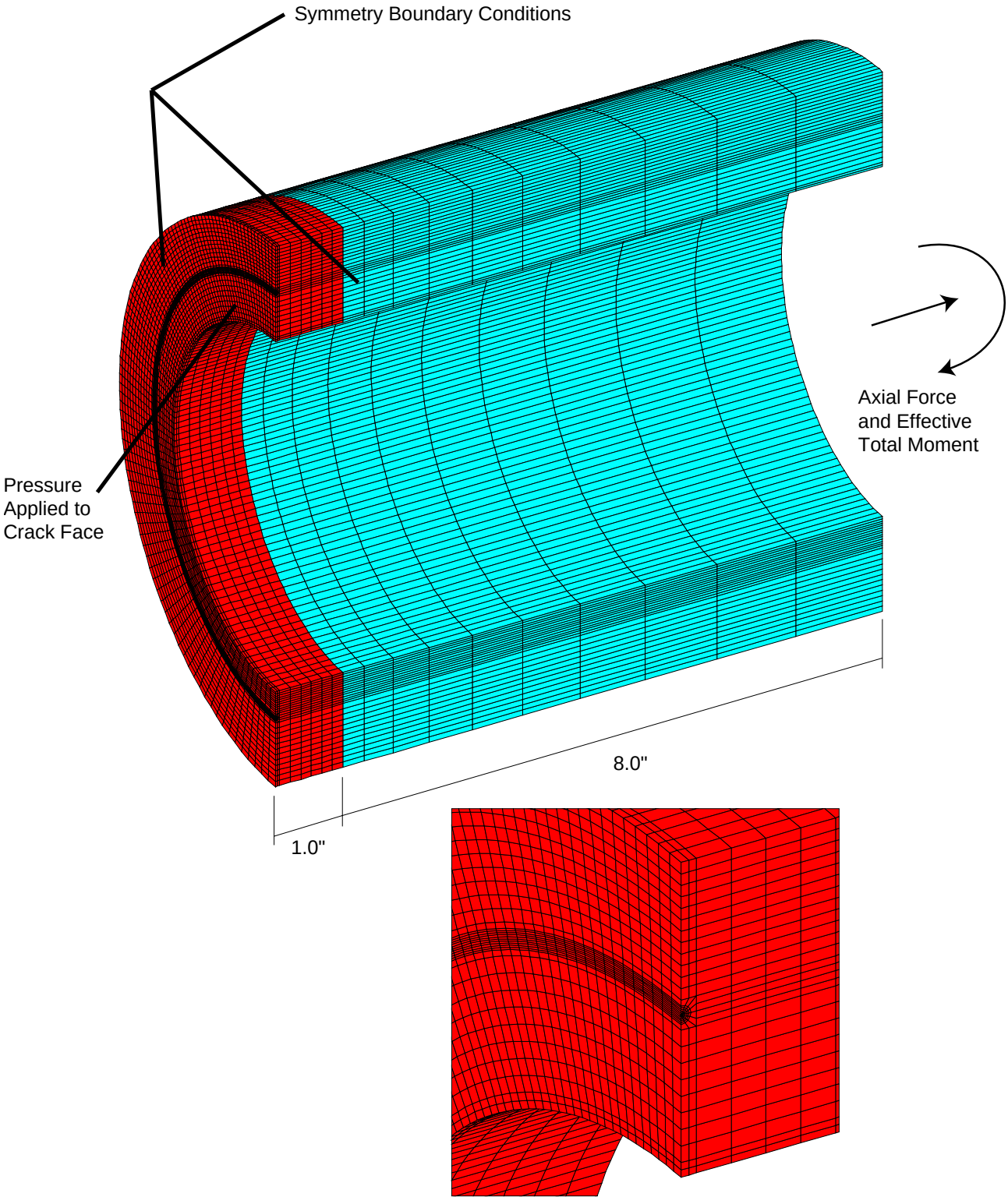

Figure 4-1
Fracture Mechanics Finite Element Analysis Model

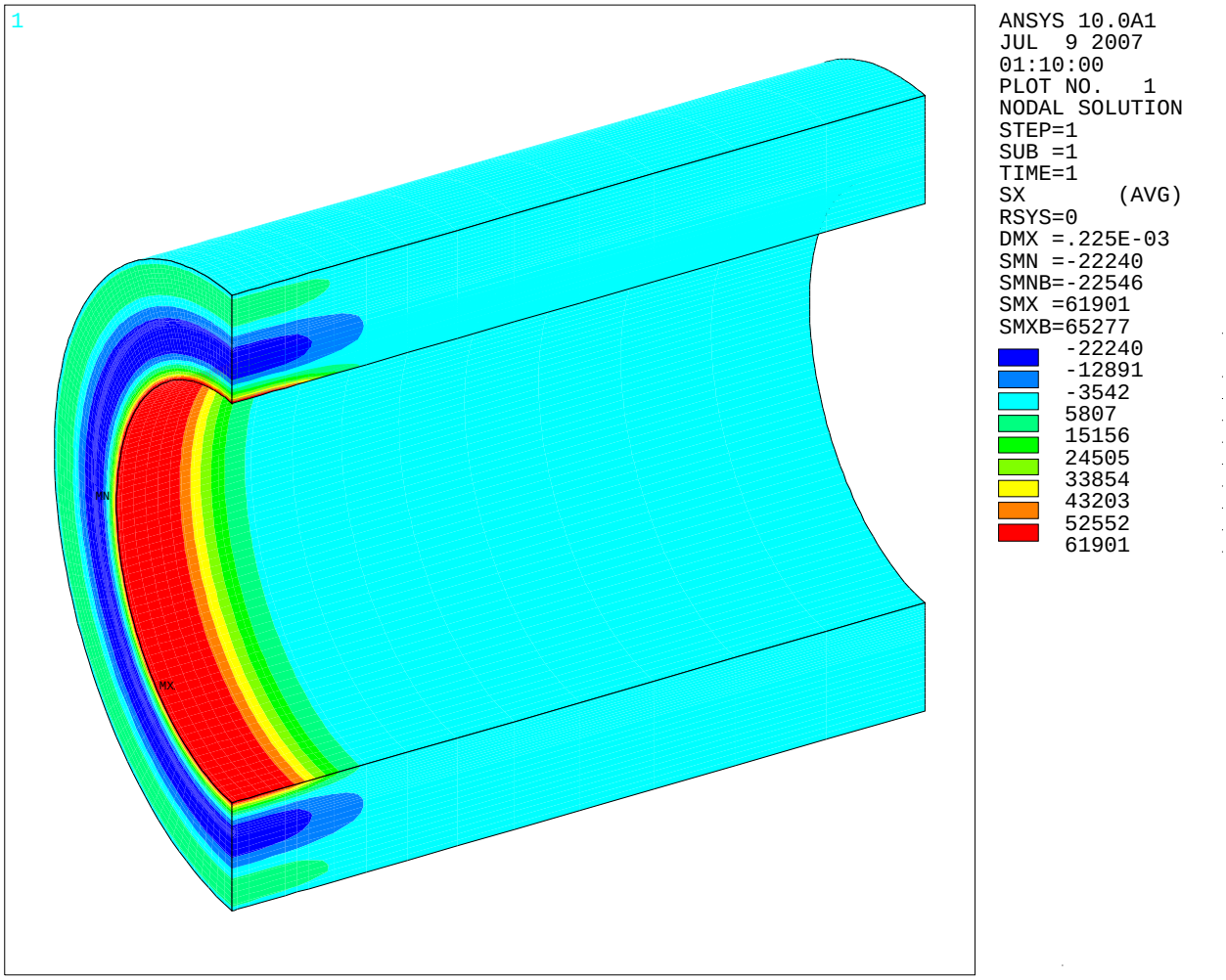

Figure 4-2
Axisymmetric Through Wall Stress Distribution Example

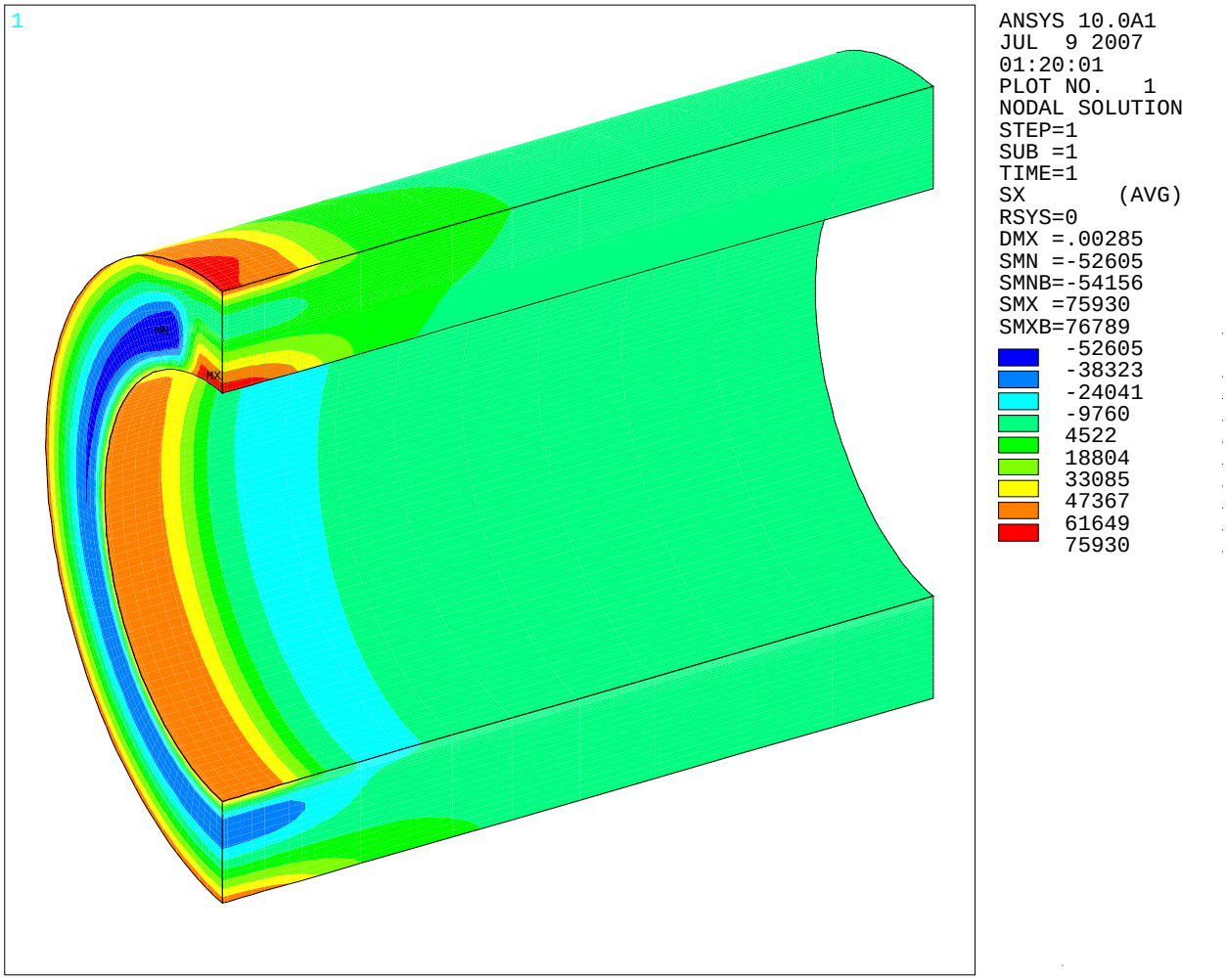

Figure 4-3
Circumferentially Varying Through Wall Stress Distribution Example

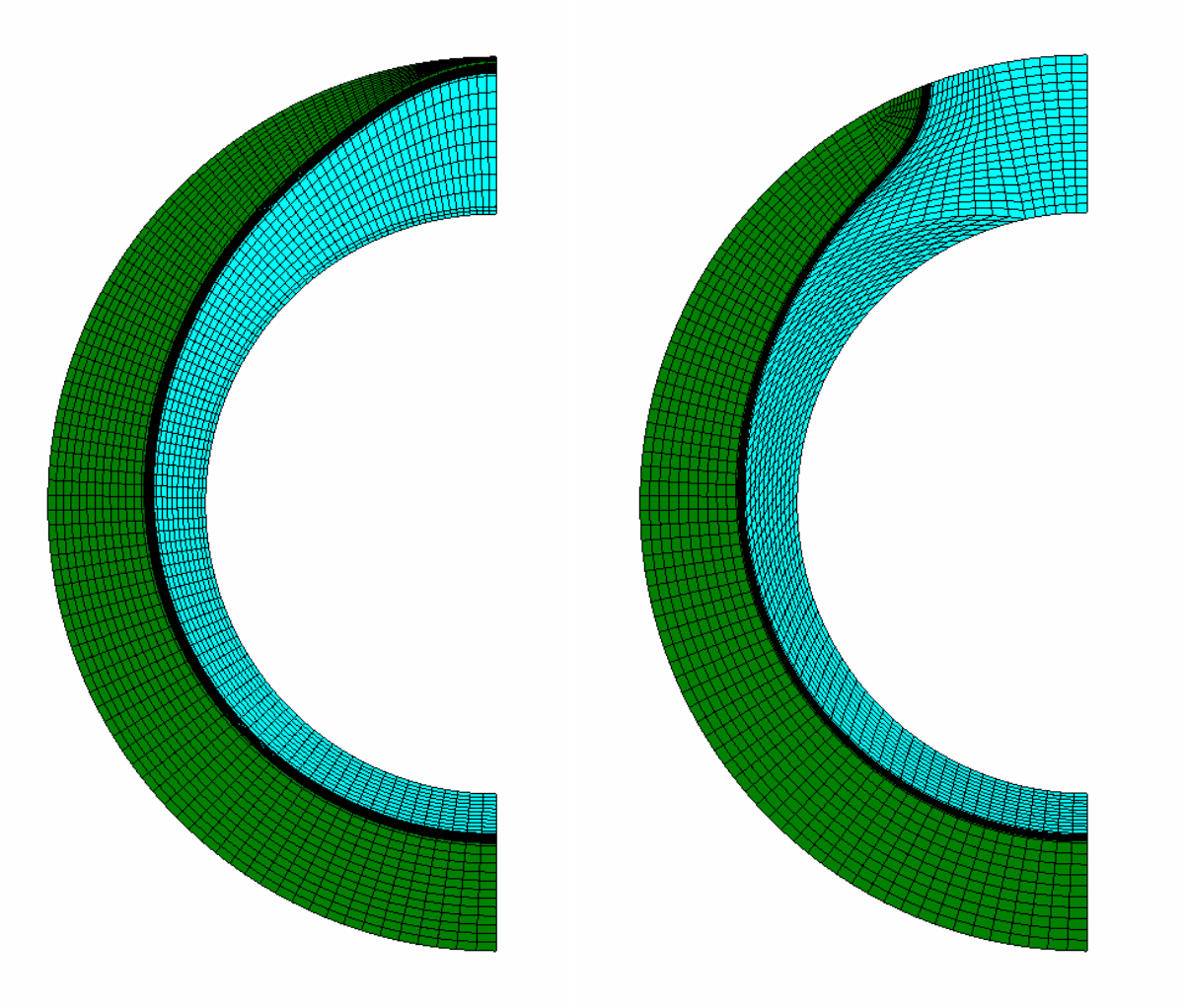

Figure 4-4
Example Mesh Transition from Surface Flaw to Complex Flaw

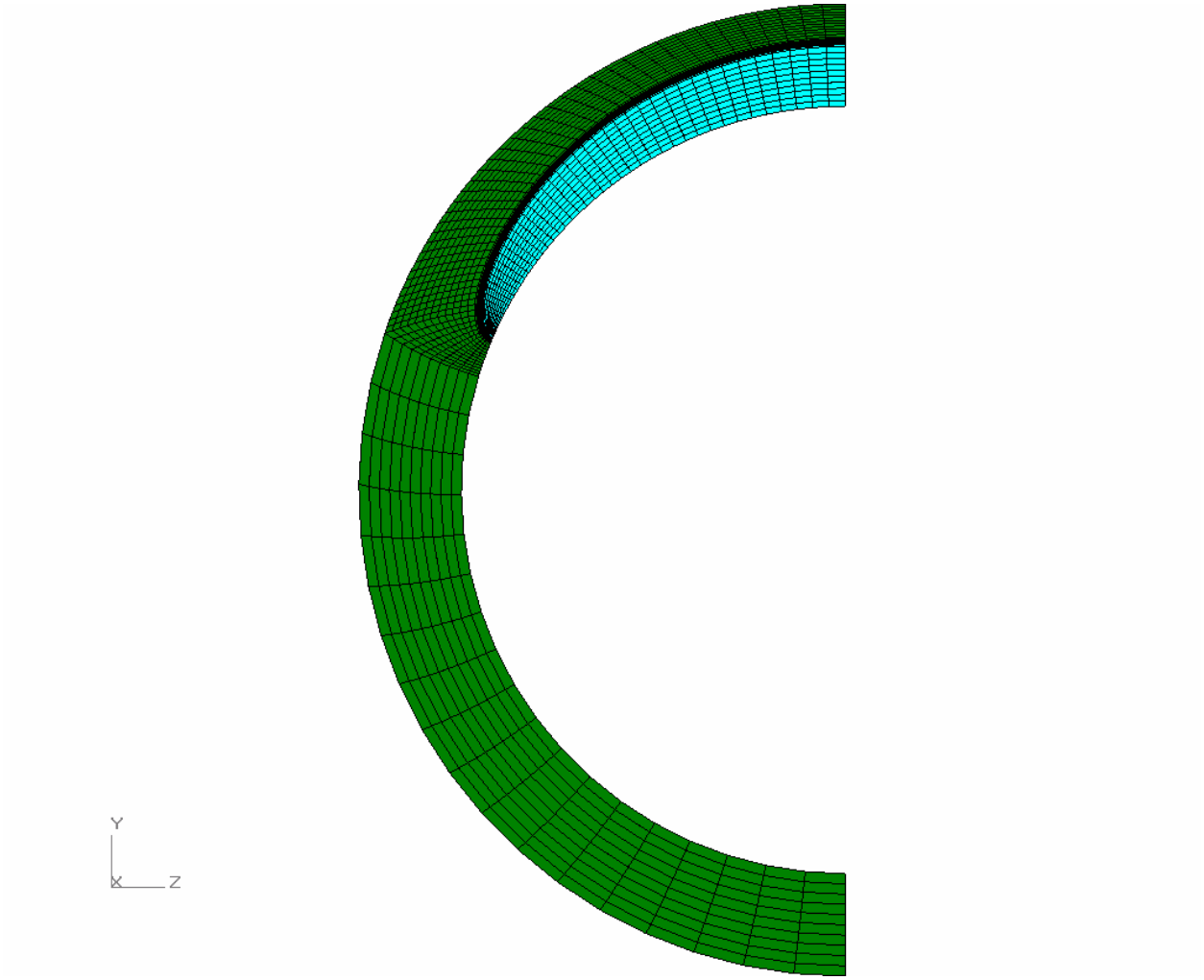

Figure 4-5
Part Circumference Custom Surface Crack Geometry Example

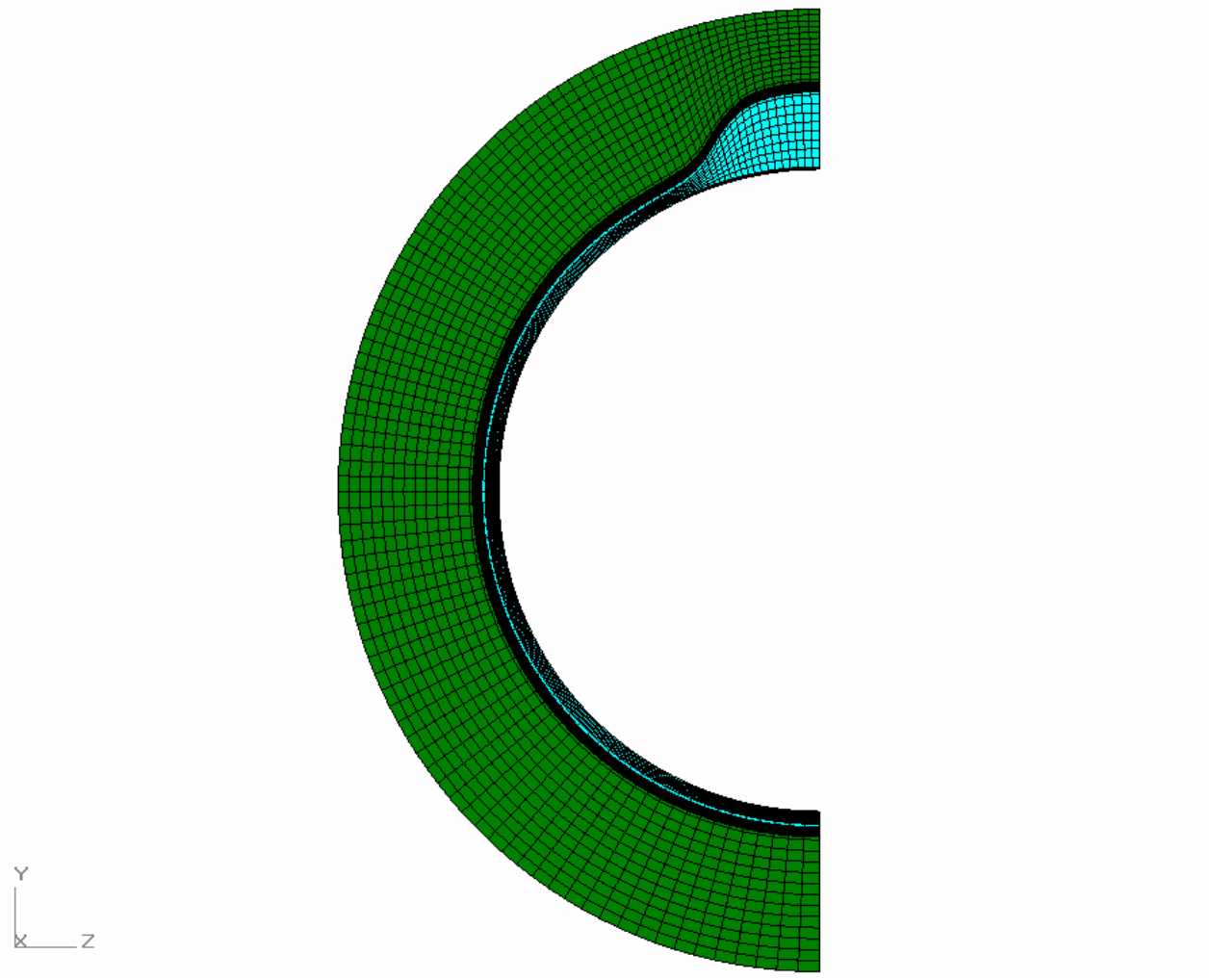

Figure 4-6
Full Circumference Custom Surface Crack Geometry Example

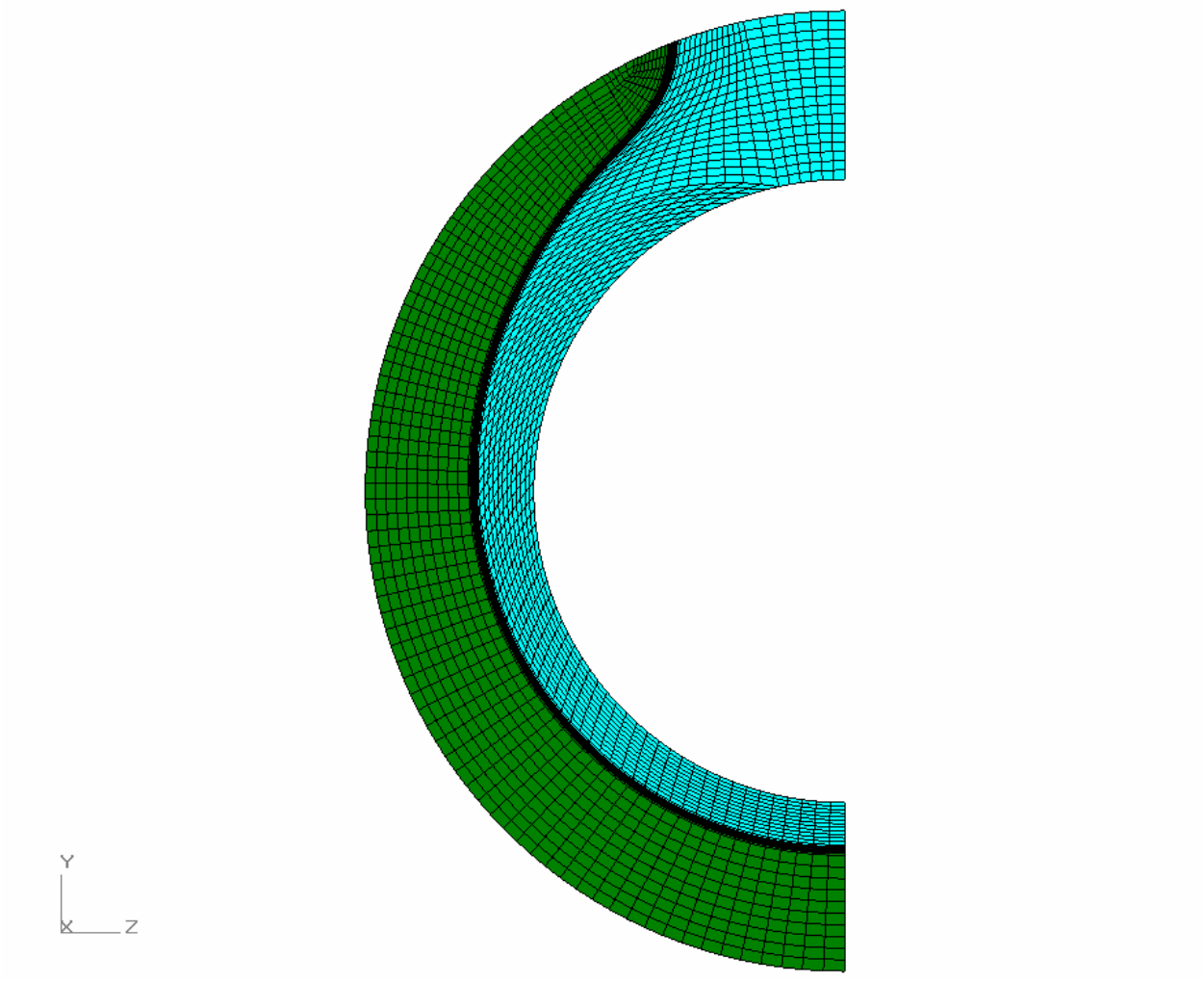

Figure 4-7
Complex Crack Geometry Example

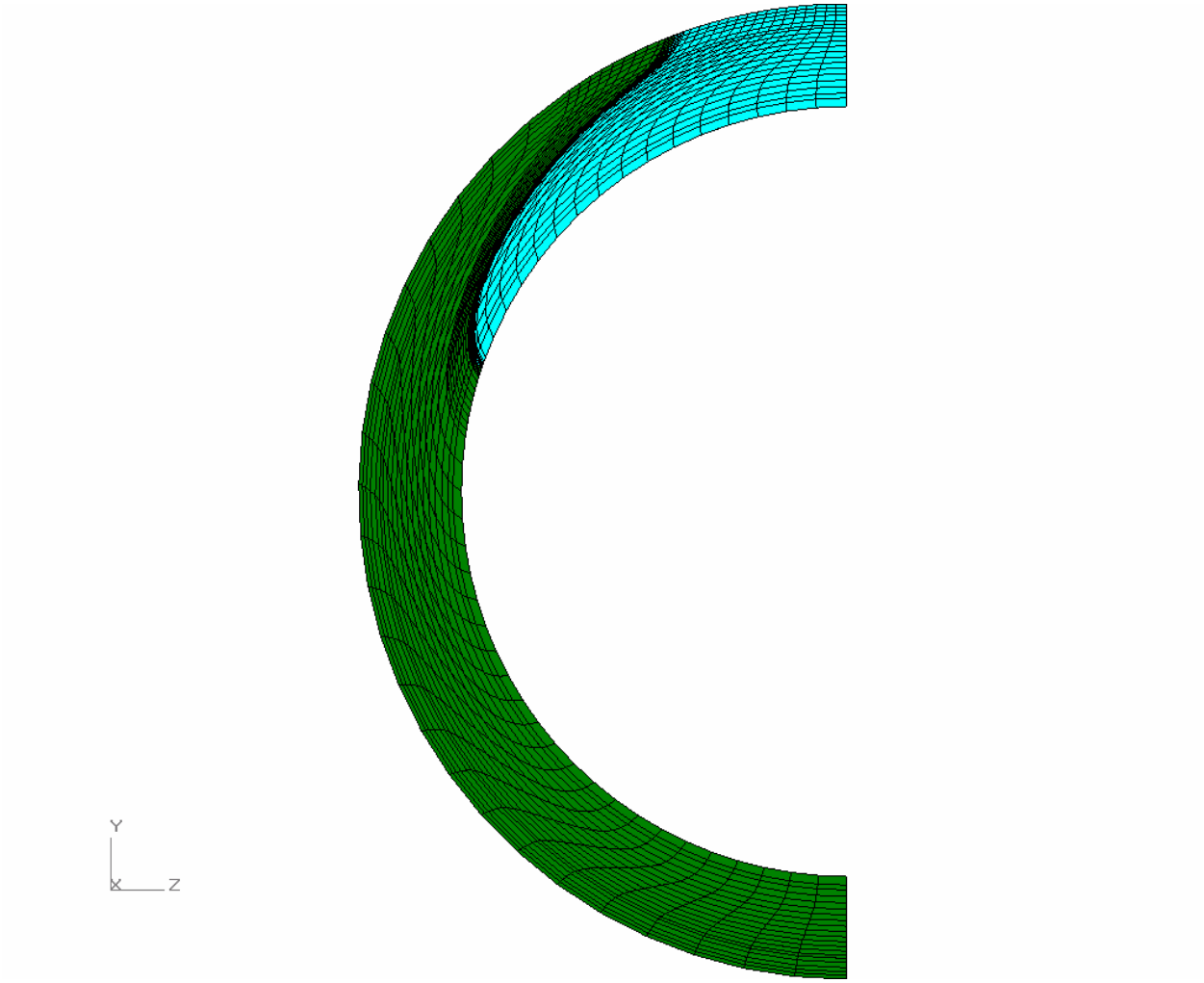

Figure 4-8
Custom Through-Wall Crack Geometry Example

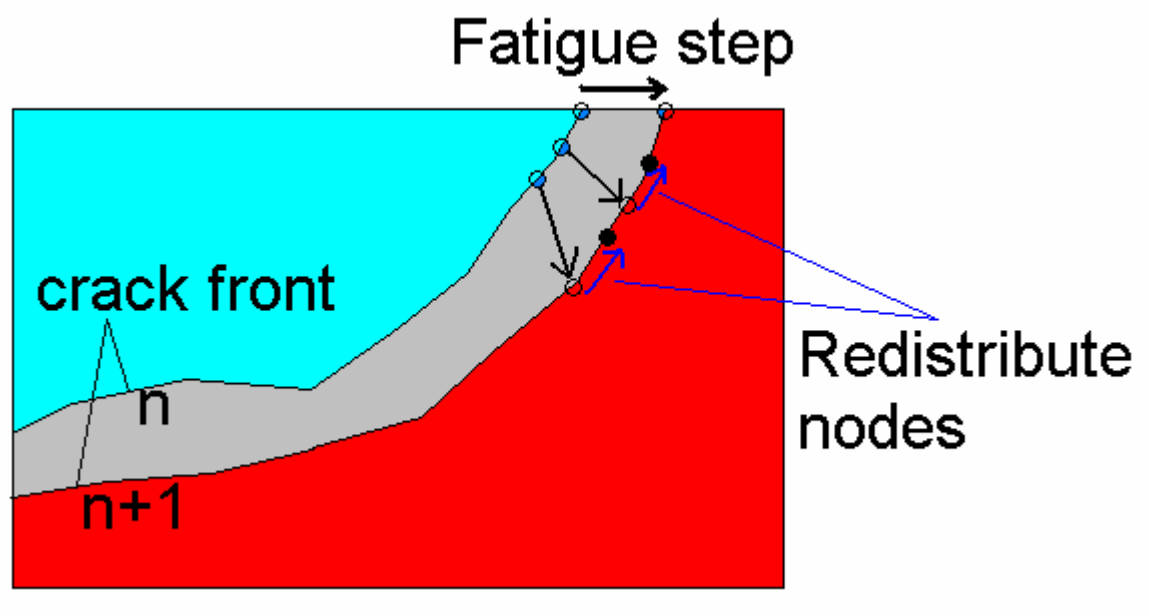

Figure 4-9
Illustration of Crack Front Redistribution During Crack Growth Calculations

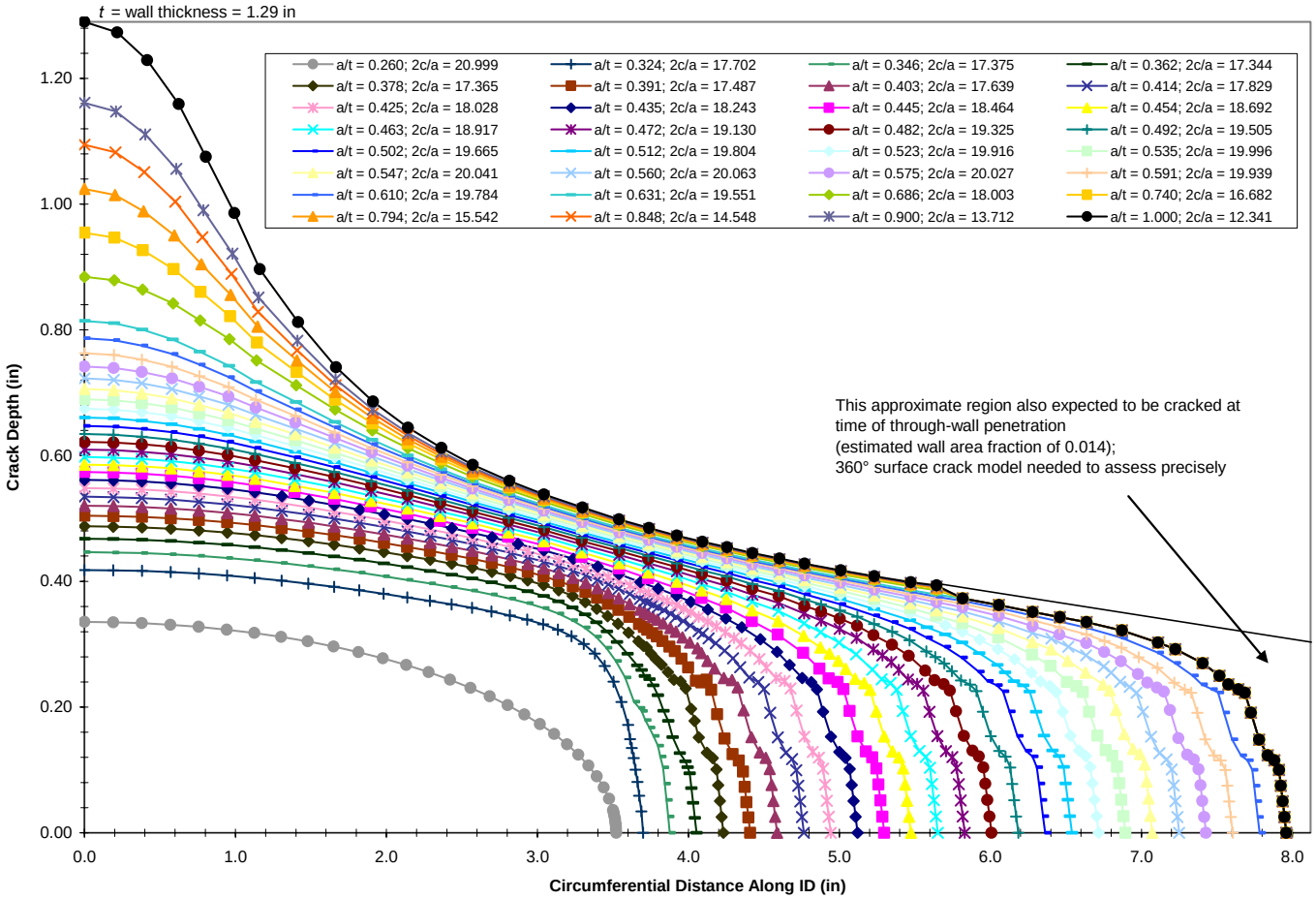

Figure 4-10
Phase I Initial Calculation Flaw Profile Growth

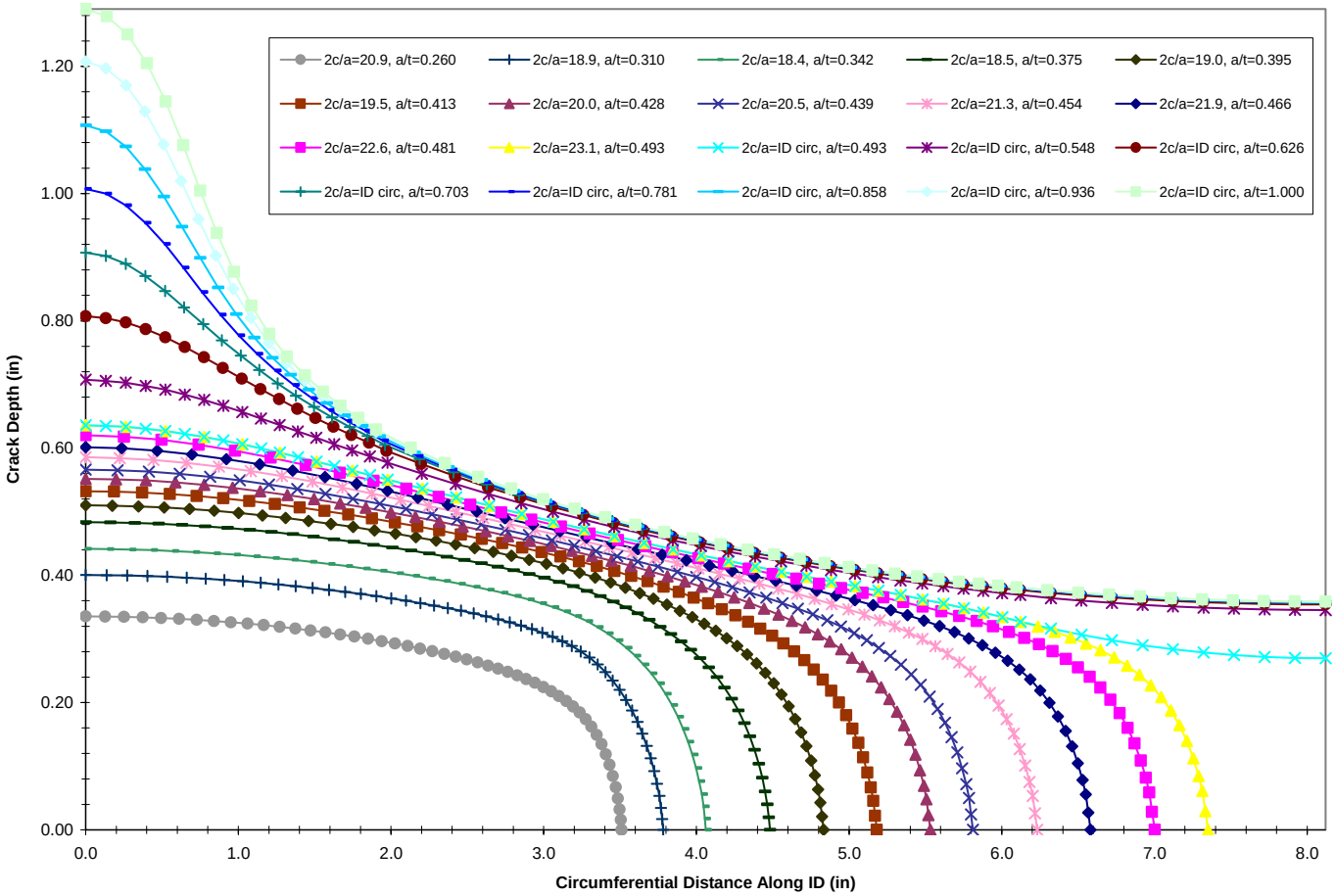

Figure 4-11
Phase I Second Calculation Flaw Profile Growth

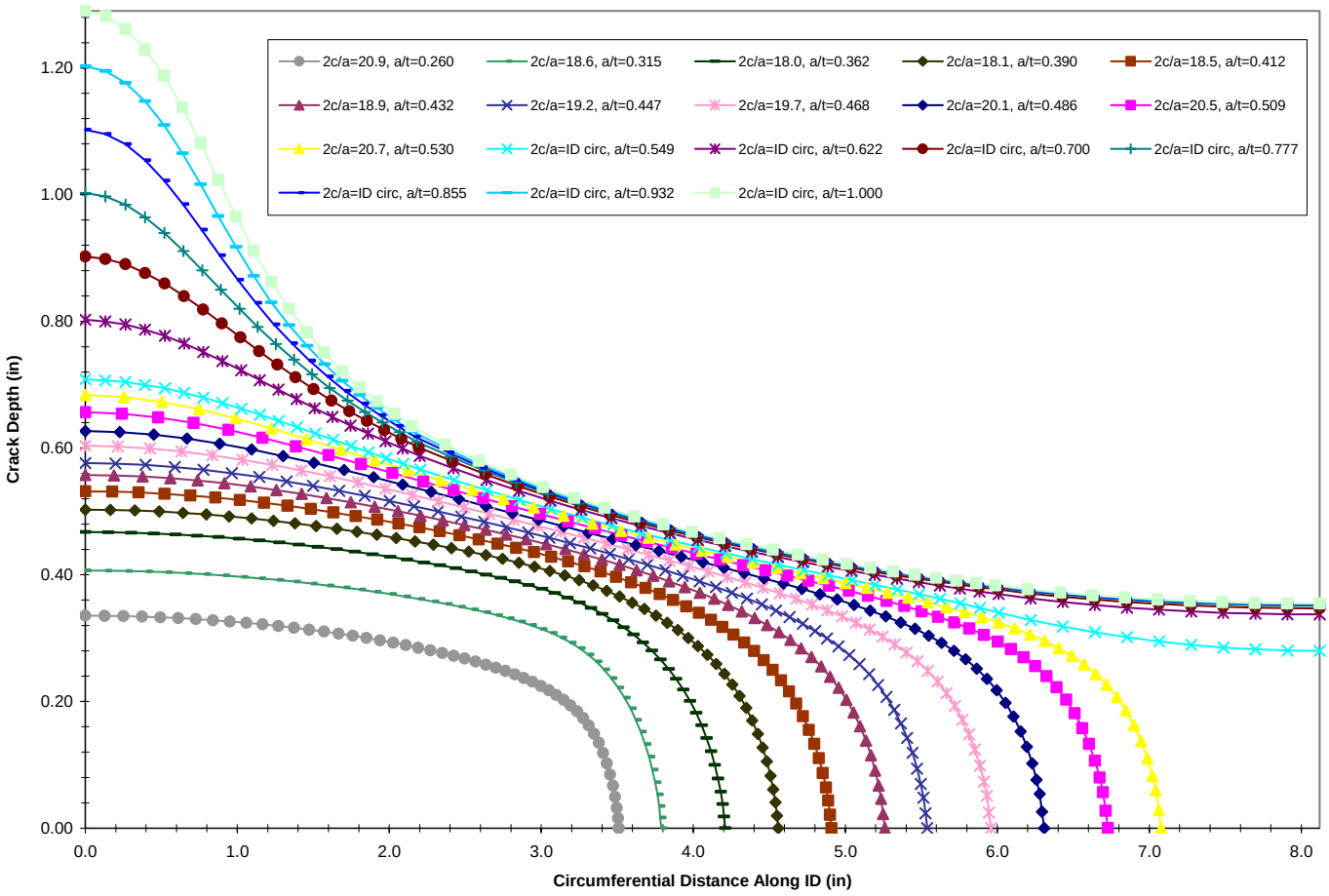

Figure 4-12
Phase I Third Calculation Flaw Profile Growth

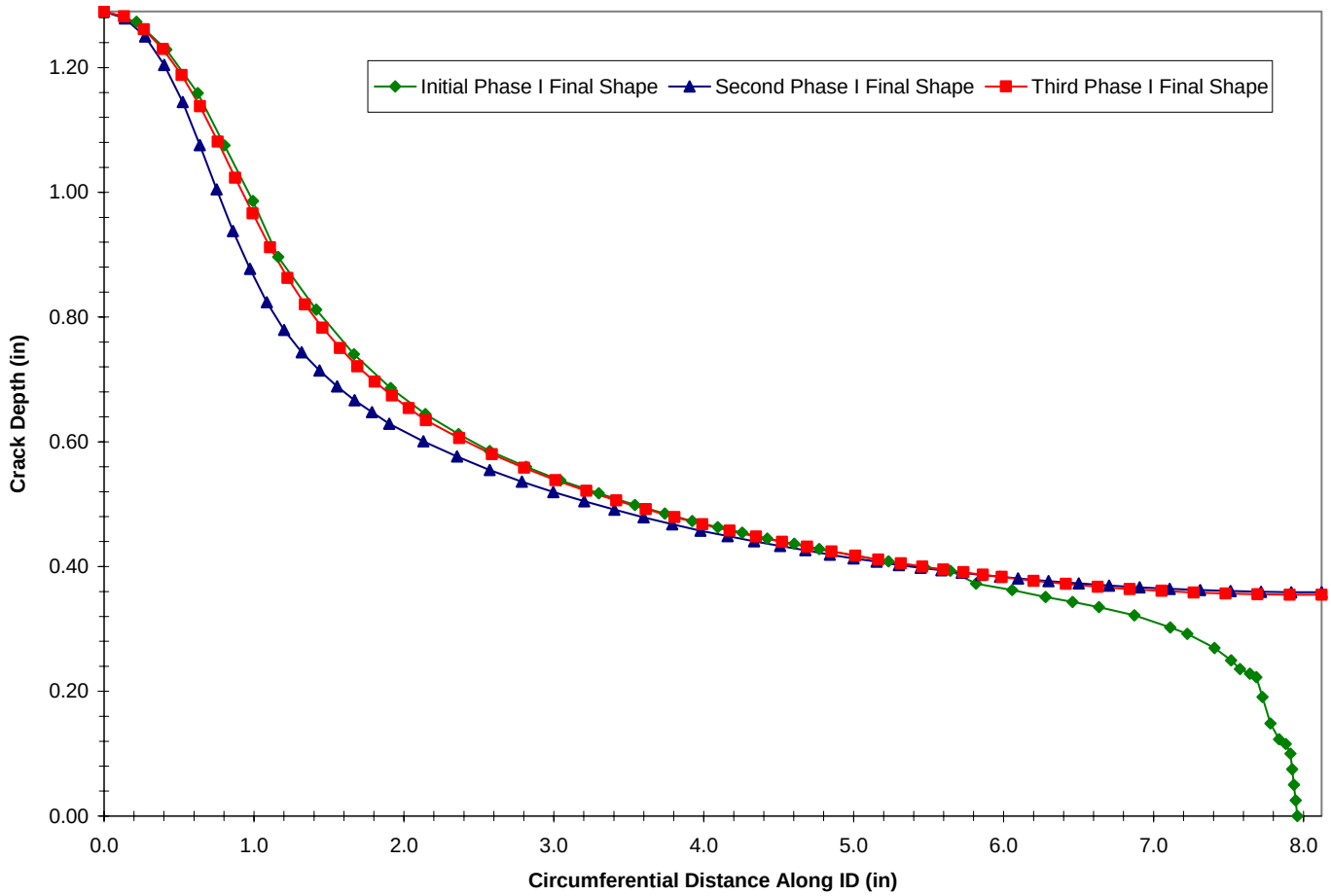

Figure 4-13
Comparison of Through-Wall Flaw Profiles for Phase I Calculation Analyses

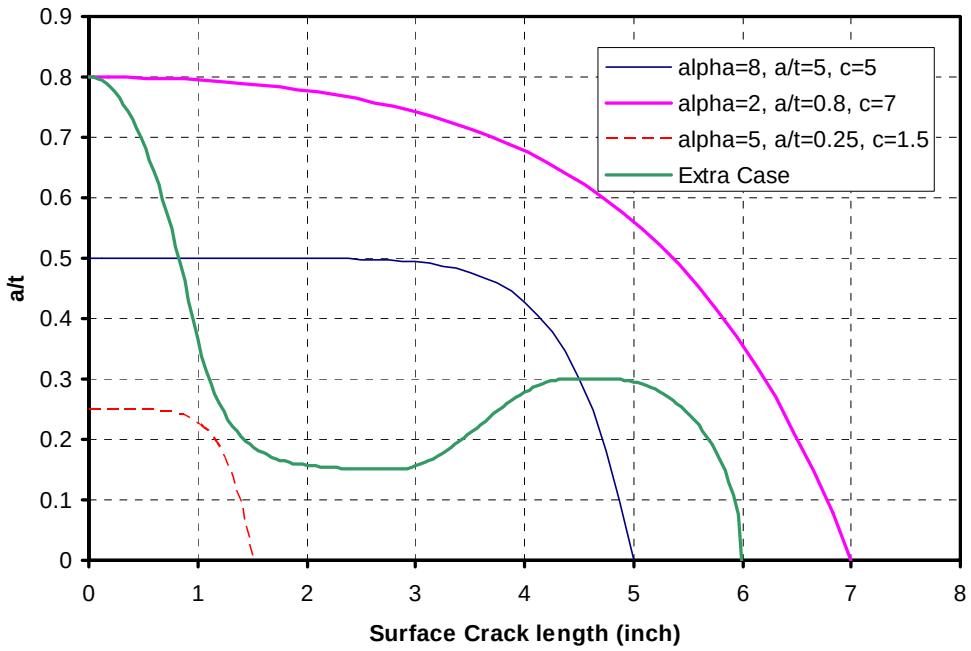

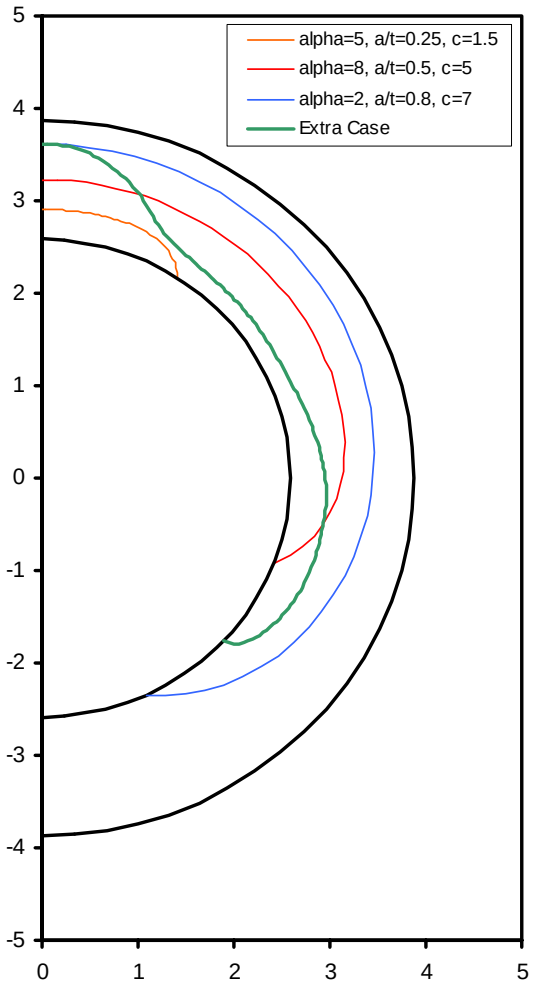

Figure 4-14
Flaw Profiles Used for Crack Tip SIF Calculation Verification

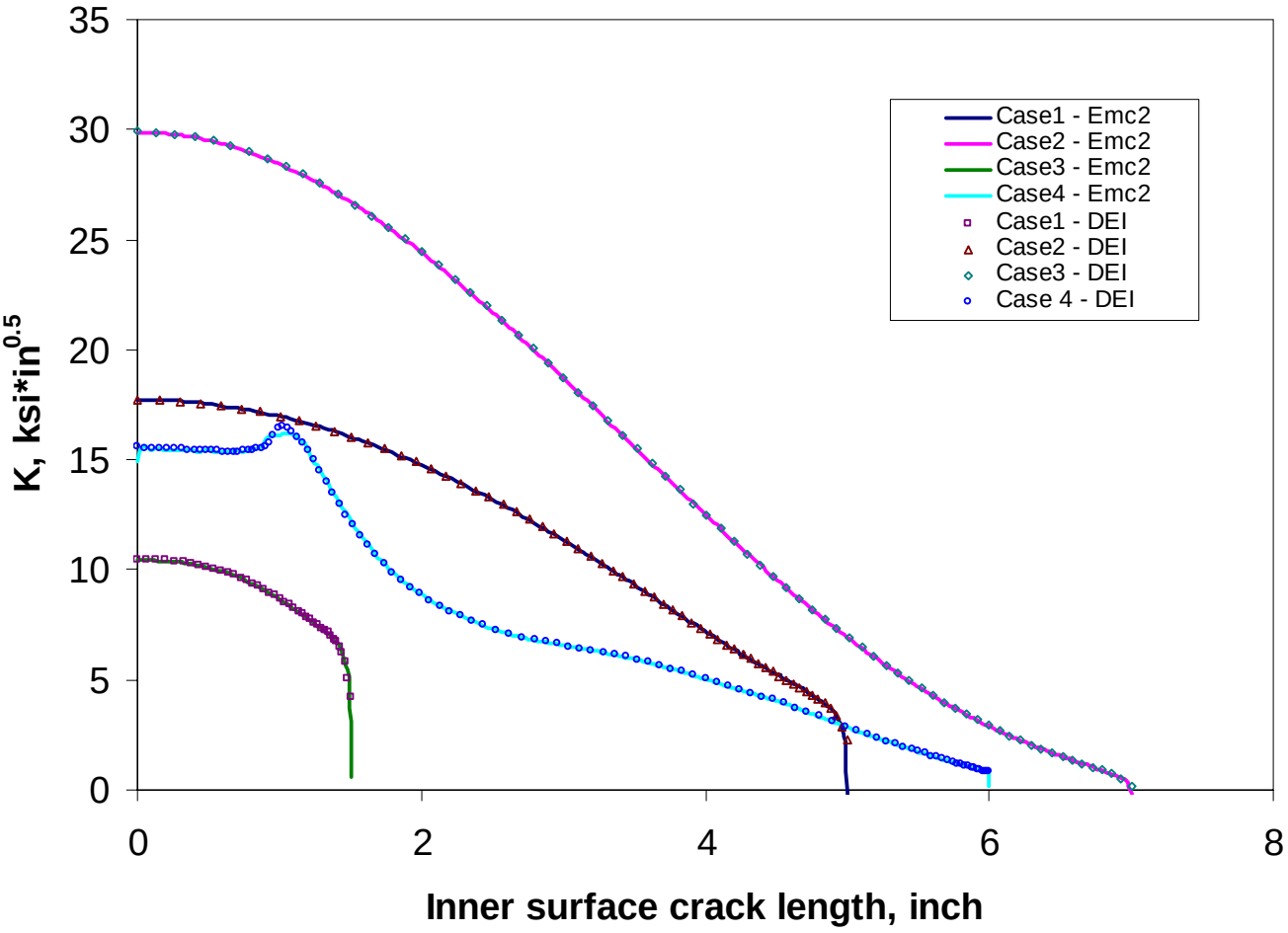

Figure 4-15
Crack Tip SIF Verification Results

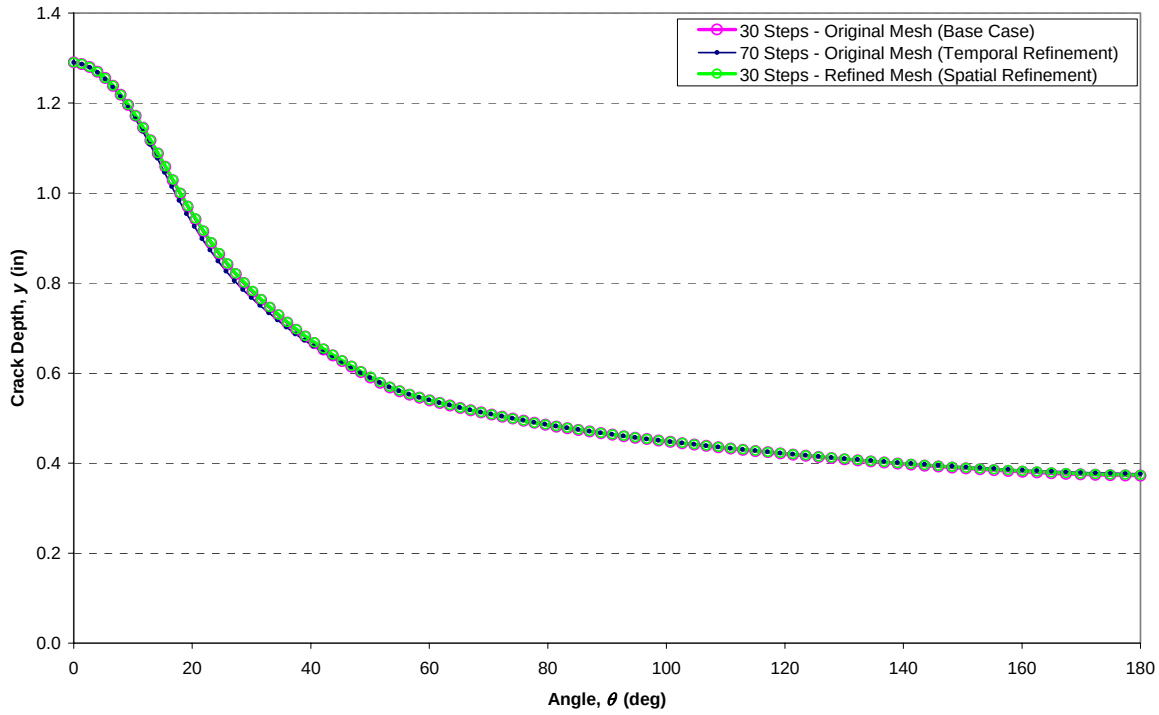

Figure 4-16
Temporal and Spatial Convergence Results for Case 1 360° Surface Crack Growth Progression

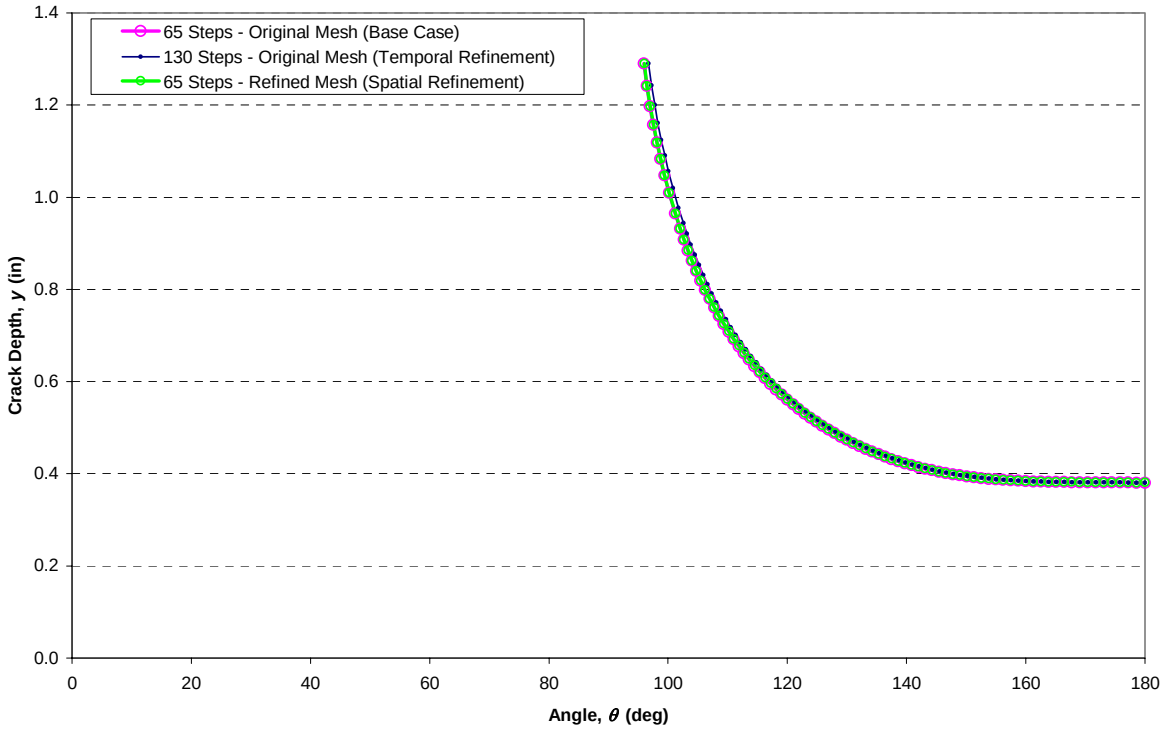

Figure 4-17
Temporal and Spatial Convergence Results for Case 1 Complex Crack Growth Progression

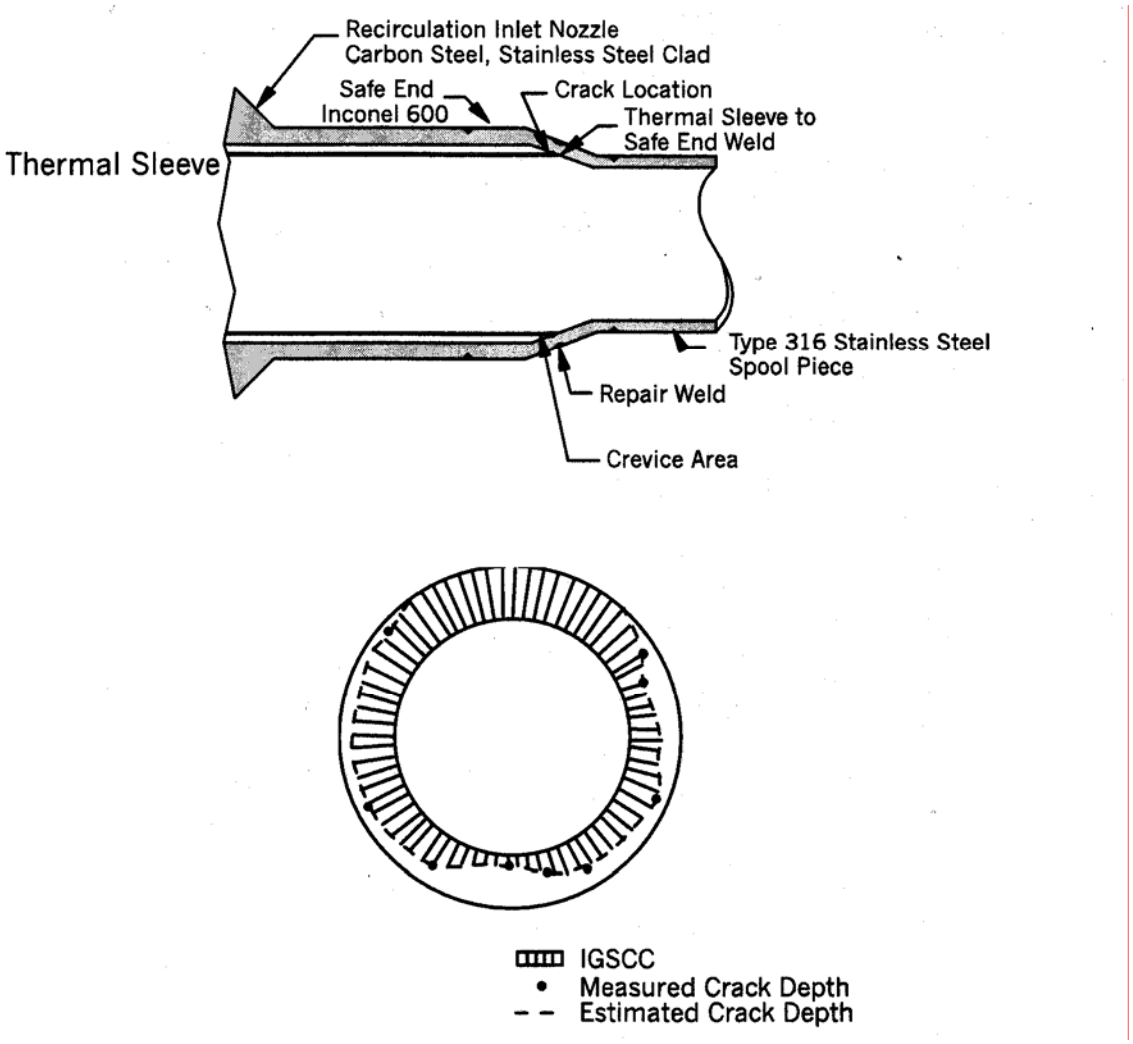

Figure 4-18
Cross Section Through 360° Part Depth Crack at Duane Arnold [4-3]

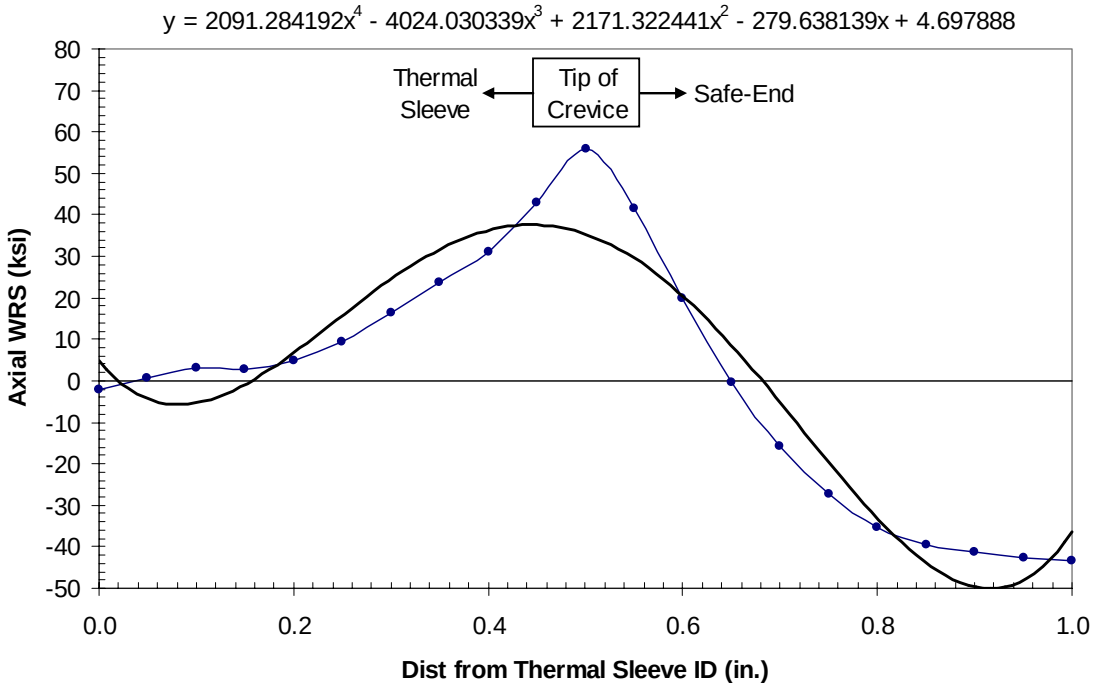

Figure 4-19
Polynomial Fit to Duane Arnold WRS Finite-Element Analysis Results

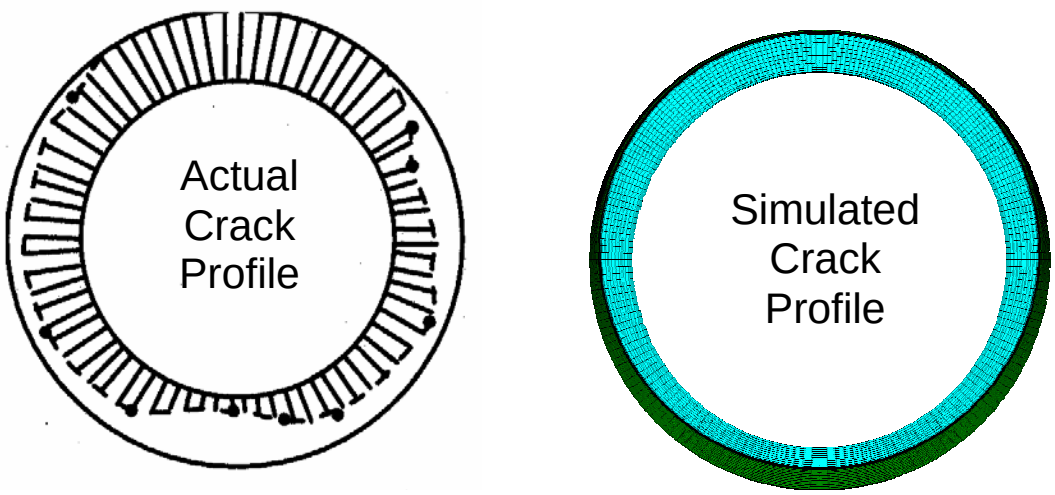

Figure 4-20
Comparison of Actual Duane Arnold Crack Profile with Simulated Crack Profile Assuming Initial 30% through-wall 360° Surface Flaw

5
CRITICAL CRACK SIZE CALCULATIONS

This section describes the development of a conservative critical crack size methodology specific to the subject nozzle-to-safe-end geometry and materials. This methodology is based on the net section collapse (NSC) equations for an arbitrary circumferential crack profile in a thin-walled pipe. For the purposes of this project, normal thermal piping loads were included in the crack stability calculations, and a Z-factor approach reducing the NSC failure load was implemented in consideration of the possibility of an EPFM failure mechanism. Finally, in support of the methodology, available experimental failure data for complex cracks in materials similar to Alloy 82/182 were evaluated.

5.1 Methodology

Critical crack sizes were computed using a spreadsheet implementation of the Net Section Collapse (NSC) solution for an arbitrary circumferential crack profile, assuming thin wall equilibrium [5-1]. Since crack front coordinates were available for each step of the crack growth simulations, stability calculations could be performed at every increment of crack growth with the net section collapse model. Combined with the leak rate simulations discussed in Section 6, which could also be performed at each increment of through-wall crack growth, evolutions of leak rate and stability margin on load versus time were computed and are presented in Section 7. The NSC solution presented in [5-1] allows for the calculation of net section collapse loads under three different scenarios. The first is used when the crack is entirely in tension. The second and third scenarios are used when part of the crack is below the cracked section's neutral axis; the second scenario allows the crack to take compression while the third scenario assumes that the crack cannot take compression. For all calculations in this report, if part of the crack was below the cracked section's neutral axis, it was conservatively assumed not to take compression.

Given that any hypothetical stress corrosion cracking could be located near the safe end, the flow strength used in the critical crack size calculations was based on the safe end material. Based on design drawings and CMTR information for the nine plants considered in this analysis, most of the stainless steel safe ends were constructed from SA182 Grade F316L. The remaining safe ends were constructed from SA182 Grade F316. The room-temperature yield and ultimate tensile strengths obtained from the various CMTRs are plotted in Figure 5-1 along with the flow strength calculated as the average of the yield strength and ultimate tensile strength. These were adjusted to a temperature of 650°F based on the relative dependence of yield strength and ultimate tensile strength on temperature in the ASME Boiler & Pressure Vessel Code per Equation [5-1].

$$S_{650°\mathrm{F}} = CMTR \times \left(\frac{Code_{650°\mathrm{F}}}{Code_{RT}} \right) \quad [5\text{-}1]$$

The resulting at-temperature properties are plotted in Figure 5-2, which supports the use of 45.6 ksi for the flow strength in the limit load calculations. This also corresponds to the flow stress used in previous limit load calculations pertaining to the Wolf Creek relief nozzle safe end.

Dead weight and internal pressure were included in all of the limit load calculations. The treatment of secondary loads is discussed in the next section.

5.2 Treatment of Secondary Loads

Although there is evidence [5-6, 5-7] that secondary loads may be relieved after a crack goes through wall, normal thermal expansion loads were taken into account during both crack growth and the calculation of limit load (unless otherwise noted in the case matrix – see cases 50 and 51). Given this conservative modeling assumption, it was considered overly conservative to add the thermal stratification loads to the normal thermal expansion loads already included in the crack stability analyses.

Through-wall bending stresses caused by radial differential thermal expansion between the stainless steel piping and the carbon steel nozzle were not included as part of the limit load analyses since they only are local secondary stresses.

Seismic loads were also neglected from the critical crack size calculations since it was considered overly conservative to consider such an unlikely event given the time frame under investigation (~6 months). It should be noted that the loads resulting from an SSE event were not significantly higher than those resulting from the combination of pressure, dead weight, and normal operation thermal.

Using load data from all nine plants included in this investigation, effective moments (see Figure 2-3 and Figure 2-4) were calculated for each nozzle based on a Von Mises stress approach using Equation [5-2]

$$M_{eff} = \sqrt{\left(\frac{\sqrt{3}}{2} M_x \right)^2 + M_y^2 + M_z^2} \quad [5\text{-}2]$$

where M_x (torsion, T), M_y, and M_z are taken as the sum of the individual moment components (i.e., dead weight + thermal expansion). Similarly, as shown in Equation [5-3], the total axial force was taken as the scalar sum of the relevant individual axial forces (dead weight + thermal expansion), plus the end cap pressure (p) load calculated based on the pressure times the cross sectional area of the weld inside diameter plus the area of the crack face.

$$F_{tot} = F_{x_{DW}} + F_{x_{NOT}} + p\left(\frac{\pi D_i^2}{4} + f_{cracked}\frac{\pi\left(D_o^2 - D_i^2\right)}{4}\right) \quad [5\text{-}3]$$

5.3 EPFM Considerations

Though the crack growth calculations were performed elastically, the critical crack size calculations included elastic-plastic considerations through the use of a Z factor. The Z factor acts as a correction factor on the limit load solution and is a function of the material toughness and pipe diameter. It is used to reduce the supportable moment when elastic-plastic fracture mechanics conditions control rather than limit load conditions. Per Reference [5-2], for a given material, the Z factor is solely a function of the size of a weld (NPS). For the case of Alloy 82/182, Z factor curves were calculated [5-9, 5-10] using the stainless steel base metal strength and the toughness of the Alloy 182 weld metal. Fits to the calculation results yielded Equation [5-4].

$$Z = \begin{cases} 0.00065NPS^3 - 0.01386NPS^2 + 0.1034NPS + 0.902 & , \quad NPS \le 8" \\ 0.0000022NPS^3 - 0.0002NPS^2 + 0.0064NPS + 1.1355 & , \quad NPS > 8" \end{cases} \quad [5\text{-}4]$$

In this analysis, the Z factor as calculated using Equation [5-4] was used to reduce the supportable moment thereby reducing the margin on stability for a given crack profile. However, experimental evidence suggests that a Z factor needs only be applied when the Dimensionless Plastic Zone Parameter (DPZP), an empirically based parameter providing a measure of the size of the plastic zone at the crack tip relative to the pipe size (see Section 5.5), is less than unity. In the analyses conducted, a Z factor was conservatively applied to all limit load calculations regardless of the DPZP for the case under consideration. It is expected that in most cases investigated, the DPZP factor would be greater than unity.

5.4 Calculations Verification

The Arbitrary Net Section Collapse (ANSC) software [5-8] was used to validate the spreadsheet implementation of the NSC solution to an arbitrary crack profile. Unlike the model developed in [5-1], the ANSC software allows the moment loading to be arbitrarily positioned around the pipe relative to the location of the crack. However, when half symmetry conditions exist in the pipe cross-section and the moment is applied such that its axis is perpendicular to the symmetry plane, as is assumed throughout this report, the ANSC program's solution should default to that of the regular NSC model implemented in spreadsheet form in support of this project. Several crack profiles under various loads were investigated and in all cases, exact agreement (within three significant figures) was obtained between the results of the ANSC program and the spreadsheet implementation of the NSC solution.

5.5 Model Validation Comparison with Experiment

The predictions obtained from the spreadsheet implementation of the net section collapse model were also compared to experimental complex crack data from bending failure tests [5-3, 5-4, 5-5]. Complex crack data were deemed most applicable to this project since the model predictions for the majority of cases investigated resulted in either complex cracks or through-wall cracks with a long ID surface component. The data from the test programs [5-3, 5-4, 5-5] were taken for materials with higher toughness (Alloy 600 and Stainless Steel) than those considered here.

Using the geometric data from each test, the DPZP was calculated as in Reference [5-6] (see Equation [5-5]) and the moment corresponding to net section collapse was computed with DEI's spreadsheet implementation of the net section collapse model. These calculated moments were then compared with the maximum moments obtained from the experimental programs. The results of this comparison are shown in Figure 5-3 and Figure 5-4. As shown, the net section collapse model in which the crack is not allowed to take compression provides a better and more conservative estimate of the experimental maximum moments. Hence, this version of the net section collapse model was used for all the stability calculations in this report. Additionally, the results shown in Figure 5-3 and Figure 5-4 appear to support the need for a correction factor (i.e., Z factor) at DPZP's below unity. Hence, the Z-factor was conservatively applied in all cases considered in this report.

$$DPZP = \begin{cases} \left(\frac{EJ_i}{2\pi\sigma_f^2}\right) \Big/ \left(\frac{\pi-\alpha}{4}\right) D & , \text{ for surface cracks} \\ \left(\frac{EJ_i}{2\pi\sigma_f^2}\right) \Big/ \left[\left(\frac{\pi+\left(d/t\right)\alpha}{\pi}\right)\frac{D\pi}{4}\right] & , \text{ for through-wall cracks} \\ \left(\frac{EJ_i}{2\pi\sigma_f^2}\right) \Big/ \left\{\left[\pi-\left(\alpha+d/t\,(\pi-\alpha)\right)\right]\frac{D}{4}\right\} & , \text{ for complex cracks} \end{cases} \quad [5\text{-}5]$$

5.6 References

5-1. S. Rahman, G. Wilkowski, "Net-Section-Collapse Analysis of Circumferentially Cracked Cylinders—Part I: Arbitrary-Shaped Cracks and Generalized Equations," *Engineering Fracture Mechanics*, Vol. 61, pp. 191-211, 1998.

5-2. G. Wilkowski, H. Xu, D.-J. Shim, D. Rudland, "Determination of the Elastic-Plastic Fracture Mechanics Z-factor for Alloy 82/182 Weld Metal Flaws for Use in the ASME Section XI Appendix C Flaw Evaluation Procedures," (DRAFT), PVP2007-26733, *Proceedings of ASME-PVP 2007: 2007 ASME Pressure Vessels and Piping Division Conference*, San Antonio, TX, 2007.

5-3. *An Assessment of Circumferentially Complex-Cracked Pipe Subjected to Bending*, Battelle, Columbus, OH, 1986. NUREG/CR-4687.

5-4. *Fracture Analysis of Welded Type 304 Stainless Steel Pipe: J-R Curve Characterization and Limit Load Analysis*, David W. Taylor Naval Ship Research and Development Center, Bethesda, MD, 1986. NUREG/CR-4538-V1.

5-5. *Instability Predictions for Circumferentially Cracked Type-304 Stainless Steel Pipes Under Dynamic Loading*, EPRI, Palo Alto, CA: 1982. NP-2347 Volumes 1 and 2.

5-6. P. Riccardella, "Secondary Stress Evaluation: Surge Line Rotation Study," Presentation given at DEI Offices on May 31, 2007.

5-7. T. Anderson, E. Scheibler, G. Thorwald, "Final Report on Secondary Stress Study," June 19, 2007.

5-8. *ANSC for Determining Net Section Collapse of Arbitrarily Thinned Cylinder, Software User Manual*, Structural Integrity Associates, San Jose, CA: 1994.

5-9. G. Wilkowski, H. Xu, P. Krishnaswamy, N. Chokshi, S. Shaukat, A. Hiser, G. Degrassi, J. Johnson, and R. Olson, "Seismic Considerations for the Transition Break Size," PVP2006-ICPVT11-93994, *Proceedings of ASME-PVP 2006 Pressure Vessels and Piping Division Conference*, 2006, Vancouver, BC, Canada.

5-10. D. S. Kupperman, S. H. Sheen, W. J. Shack, D. R. Diercks, P. Krishnaswamy, D. Rudland, and G. M. Wilkowski, "Barrier Integrity Research Program: Final Report," NUREG/CR-6861, December 2004.

5-11. ASME Boiler and Pressure Vessel Code, Section II, Part D, Properties, 1992 Edition.

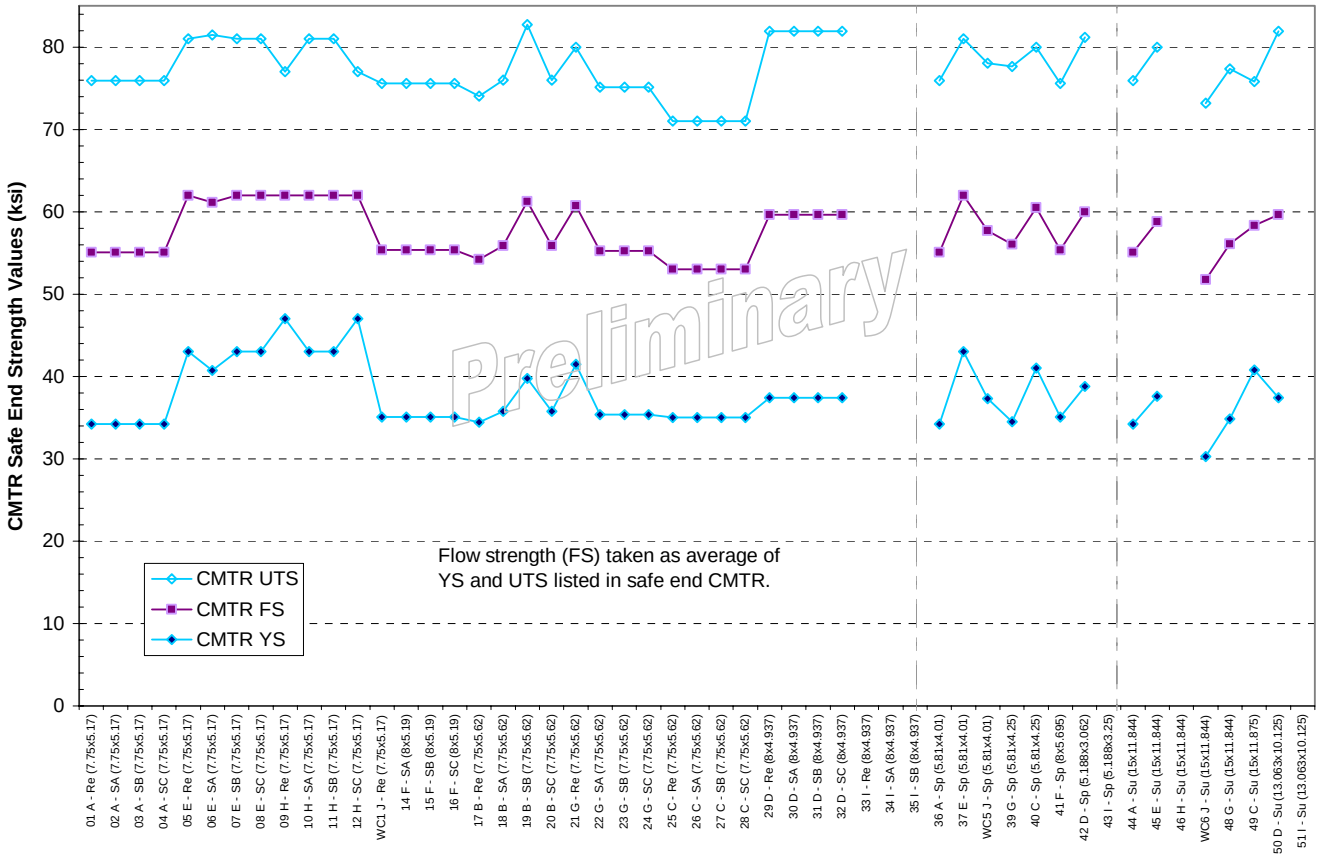

Figure 5-1
Available CMTR Strength Data for Subject Stainless Steel Safe Ends

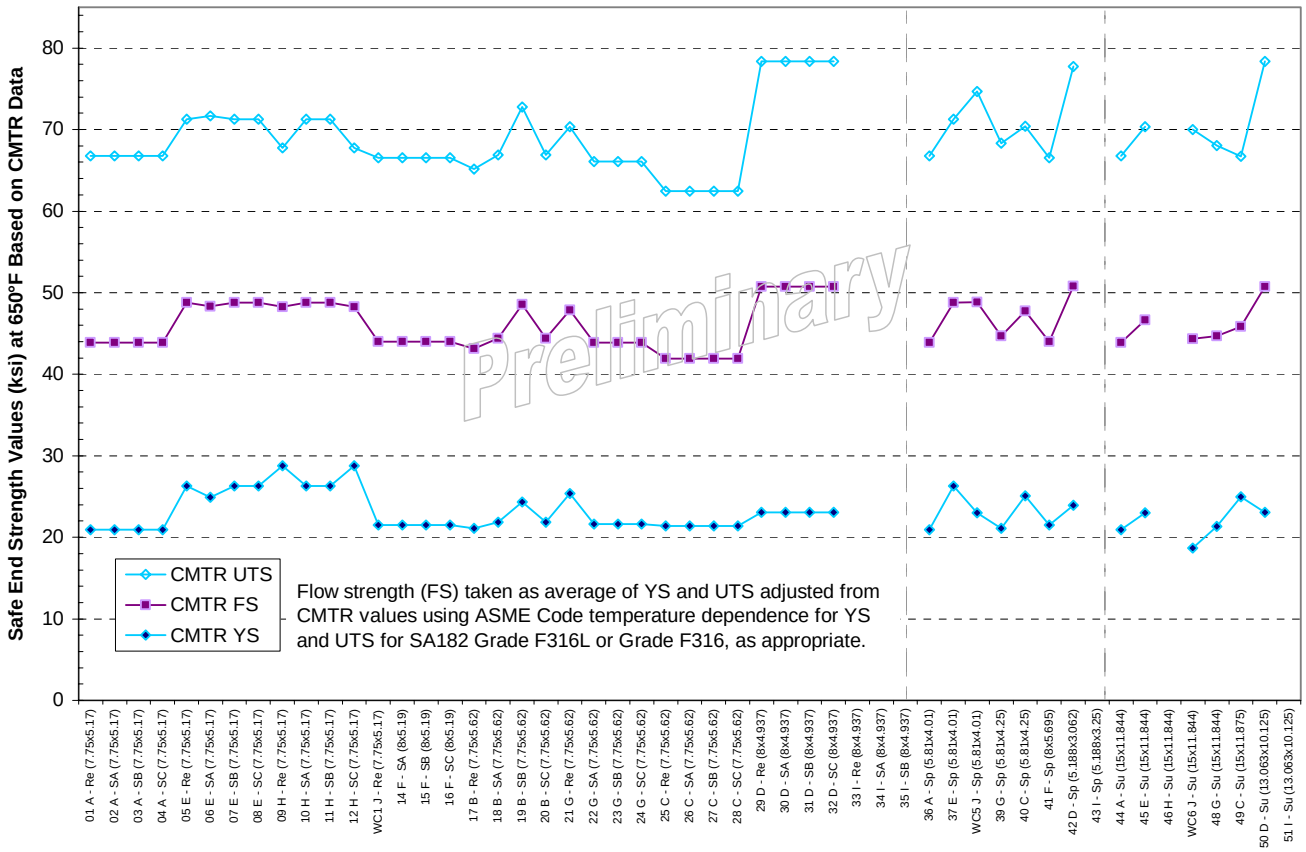

Figure 5-2
Available CMTR Strength Data for Subject Stainless Steel Safe Ends Adjusted to a Temperature of 650°F Based on the Relative Dependence of Yield Strength and Ultimate Tensile Strength on Temperature in the ASME Boiler & Pressure Vessel Code [5-11]

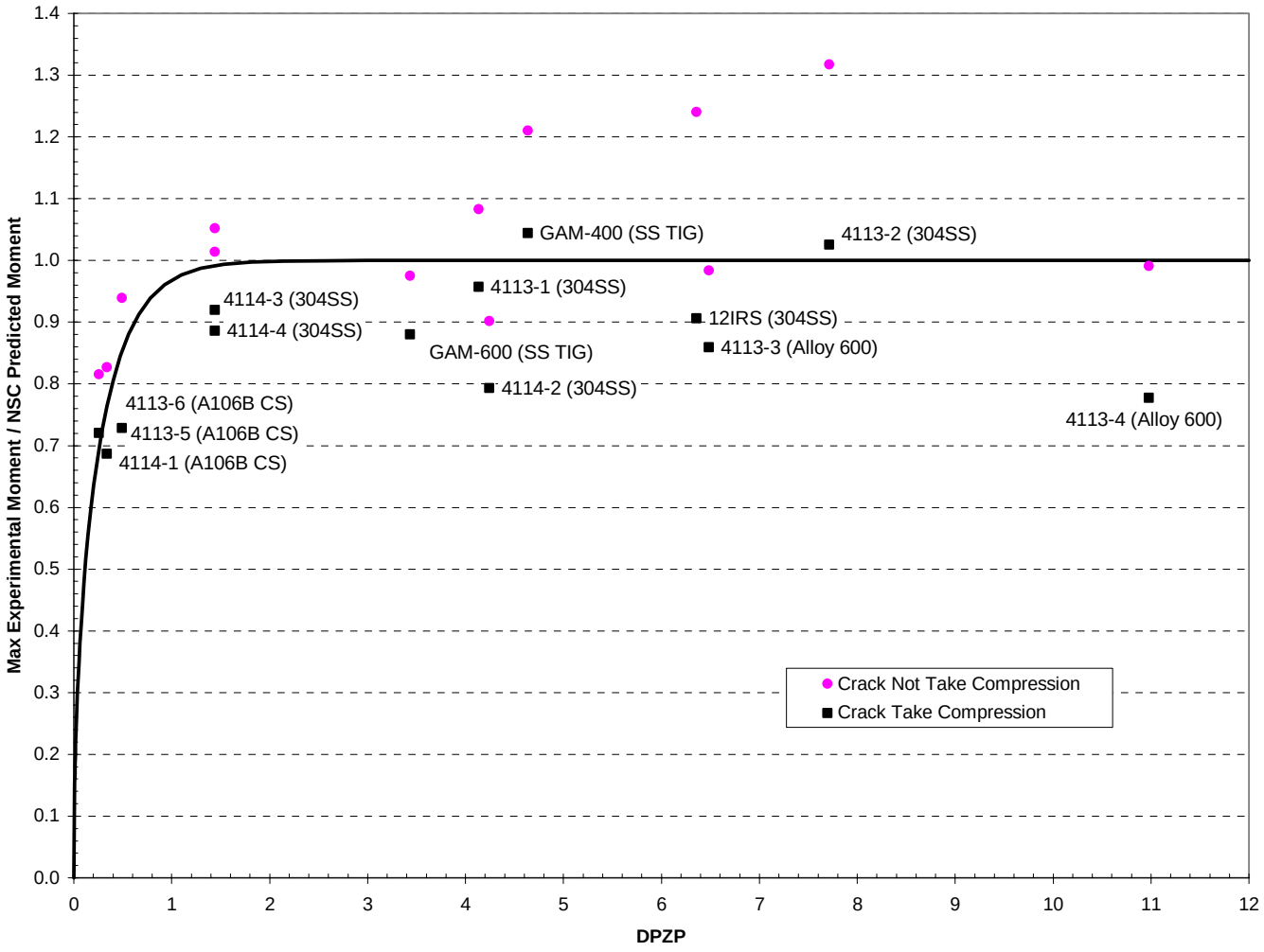

Figure 5-3
Maximum Experimental Moment Divided by NSC Predicted Moment for Available Complex Crack Tests

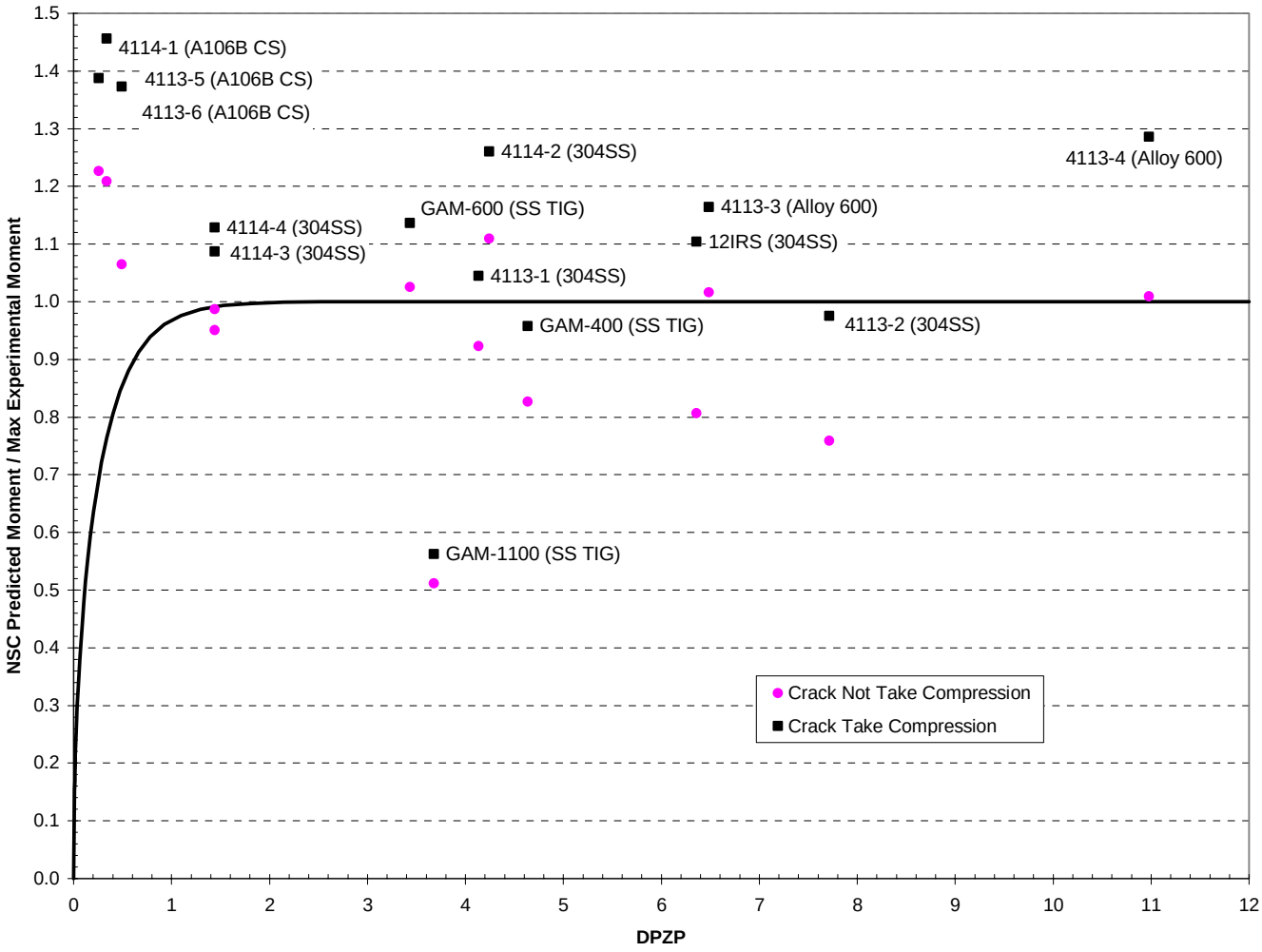

Figure 5-4
NSC Predicted Moment Divided by Maximum Experimental Moment for Available Complex Crack Tests

6
LEAK RATE MODELING

This section describes the leak rate calculation procedure applied to the through-wall portion of the crack growth simulations using EPRI's PICEP software. The crack opening area at the weld OD calculated in the crack growth finite-element simulations was applied directly in the PICEP leak rate calculations. NRC's SQUIRT software was also applied in a scoping study for the purpose of comparison.

6.1 PICEP Modeling

The leak rates discussed in this report were calculated using EPRI's Pipe Crack Evaluation Program (PICEP), a computer program developed for LWR pipe and SG tube leaks [6-1]. Although PICEP can be used to compute crack opening displacements and leak rates (see Section 6.3), in this analysis, it was used solely to model leak rates since the crack opening displacements calculated during the crack growth modeling were used to generate the required COD inputs. Therefore, no material property inputs were required for the leak rate calculations and the effects of pipe loads on leak rates were captured through the crack opening displacements calculated during crack growth.

All leak rate simulations were performed using crack opening displacements at the outside diameter of the fracture mechanics models described in Sections 4 and 7. Specifically, the outer diameter crack opening displacements were used to compute a crack opening area which was then used in conjunction with the length of the crack and an assumed crack shape to calculate the single-value crack opening displacement input for PICEP.

For longer through-wall cracks predicted in this project (which are mostly complex or through wall with a long ID surface component), the crack opening area is generally smallest at the OD. However, as shown in Figure 6-2, under some conditions, displacements near the mid-radius were computed to be less than those at the OD (albeit over a longer length) which, in some cases, was found to result in smaller crack opening areas at the mid-radius than at the OD. In order to quantify the impact of using the OD crack opening displacements rather than those at the mid-radius, crack opening displacements at the mid-radius were extracted from the structural calculations for one case (Case 1) and used to calculate a leak rate taking into account the difference in area between the mid-radius and the OD. Though the crack opening area at the outside diameter was 1.5 times that at the mid-radius, the flow rate calculated assuming the crack to have a constant cross sectional area equal to that at the OD was only 20% greater than that calculated using the crack with variable cross sectional area. Given that this effect is considerably smaller than the expected accuracy of the leak rate simulations, the more readily available outside diameter crack opening displacements were used to compute the leak rates in

Tables 7-3 and 7-4. No comparisons were made using crack opening displacements at the inside diameter since, as stated earlier, most cases exhibited either complex cracks or through-wall cracks with long ID surface components leading to even larger crack opening areas than those at the outside diameter.

The inputs to the leak rate calculations are listed in Table 6-1. The fluid flow parameters were selected to be representative of flow through PWSCC cracks [6-1, 6-3]. The results of the leak rate simulations are included with the stability results in Tables 7-3 and 7-4.

6.2 Scoping Results

As part of the leakage calculations, scoping analyses were performed to confirm the appropriate selection of inputs. Specifically, the effect of assuming the crack shape to be elliptical was investigated. The choice of an elliptical shape was motivated by the actual crack opening displacements computed during the crack growth simulations. A plot showing the shape of the crack opening at the OD for Case 1 when the leak rate was calculated to be 1 gpm is shown in Figure 6-3 along with the elliptical, diamond, and rectangular profiles which correspond to the actual profile's crack opening area and length. As seen in the figure, the actual shape of the crack is very well approximated by an ellipse.

In order to quantify the effect of assumed crack shape, leakage simulations were conducted for one case using rectangular and diamond shaped crack openings rather than the default ellipse. The results showed the ellipse to be conservative (i.e., result in lower flow rate) by 2% relative to the other two crack shapes. Therefore, the elliptical crack shape was used to generate all of the leak rate results shown in Tables 7-3 and 7-4.

6.3 Comparison with SQUIRT Modeling

As part of leakage calculation verification studies, comparisons were made between leak rates predicted using PICEP and those predicted using the NRC's Seepage Quantification of Upsets in Reactor Tubes (SQUIRT) program [6-2]. Since these calculations were performed prior to the crack growth calculations, a slightly different approach than that described in Section 6.1 was used. Specifically, PICEP was used to calculate both crack opening displacement and leakage for a given crack length, loading condition, and assumed crack shape. A summary of the structural inputs used in the crack opening displacement calculations is provided in . The crack opening displacement and assumed crack shape were then used to calculate the leak rate using the SQUIRT code for the same assumed crack shape.

When specifying the crack geometry, PICEP allows the user to vary the crack opening area linearly from the ID to the OD whereas SQUIRT allows the user to linearly vary the crack length and opening independently through the thickness. In order to be compatible with the inputs used in PICEP, the crack length and opening used in SQUIRT were kept constant through the thickness resulting in a constant crack cross-sectional area through the thickness. The assumed crack shape for this study was taken to be rectangular. As shown in Section 6.2, the shape of the crack was concluded to have a minimal effect on the predicted leak rates.

The PICEP modeling used the same fluid friction inputs as those used in the final leakage calculations presented in Tables 7-3 and 7-4. The SQUIRT simulations were conducted using its built-in PWSCC modeling inputs.

The leak rate calculations were done for cracks ranging in length from 1 to 10 inches using the geometry and loading applicable to the Wolf Creek relief nozzle and the results are shown in Figure 6-1. As shown in the figure, the PICEP calculations spanned a range of moments whereas the SQUIRT calculations were performed only for the full moment case. It is clear from the figure that the leak rates obtained using the SQUIRT code, albeit consistently greater than those obtained using PICEP (1% to 30% greater in the figure), are generally in good agreement with those obtained from PICEP. The results in Figure 6-1 also point to the potentially important effect of moment loading, particularly for longer cracks.

6.4 References

6-1. *PICEP: Pipe Crack Evaluation Program (Revision 1),* EPRI, Palo Alto, CA: 1987. NP-3596-SR.

6-2. *SQUIRT Computer Code: Windows Version 1.1 User's Manual*, Battelle, Columbus, OH, 2003. NRC-04-91-063.

6-3. D. Rudland, R. Wolterman, G. Wilkowski, R. Tregoning, "Impact of PWSCC and Current Leak Detection on Leak-Before-Break," *Vessel Head Penetration Inspection, Cracking, and Repairs Conference*, Gaithersburg, MD, 2003.

Table 6-1
Input Parameters to PICEP Leak Rate Calculations Based on PWSCC Flaw Morphology

Quantity	Units	Safety, Relief, and Spray Nozzles	Surge Nozzles
Outside Diameter	in	Case-specific	
Thickness	in	Case-specific	
Crack Orientation	-	Circumferential	
Crack Cross-Sectional Shape	-	Elliptical	
Crack Opening Displacement	in	Case- and Step-specific	
Crack Length	in	Case- and Step-specific	
Fluid Conditions Inside Pipe	in	Wet Steam	Saturated Liquid
Fluid Stagnation Pressure	psia	2250	
Steam Quality	-	100%	-
Stagnation Temperature	°F	-	653
External Pressure	psia	14.7	
Surface Roughness	in	3.94E-04	
Exit to Inlet Crack Area Ratio	-	1	
Number of 90° turns	per inch	24	
Entrance loss coefficient	-	0.61	
Friction Factor	-	0	

Table 6-2
Input Parameters to PICEP Crack Opening Displacement Calculations Used in Leakage Comparison Study with SQUIRT Code

Quantity	Units	Value
Outside Diameter	in	7.75
Thickness	in	1.29
Young's Modulus	ksi	28300
Yield Stress	ksi	34.2
Flow Stress	ksi	45.6
Crack Shape	-	Rectangular
Ramberg-Osgood Exponent (α)	-	3.25
Ramberg-Osgood Parameter (n)	-	3.56
Z factor	-	1
Non-pressure Axial Load	kips	5.41
Effective Bending Moment	in-kips	275.235

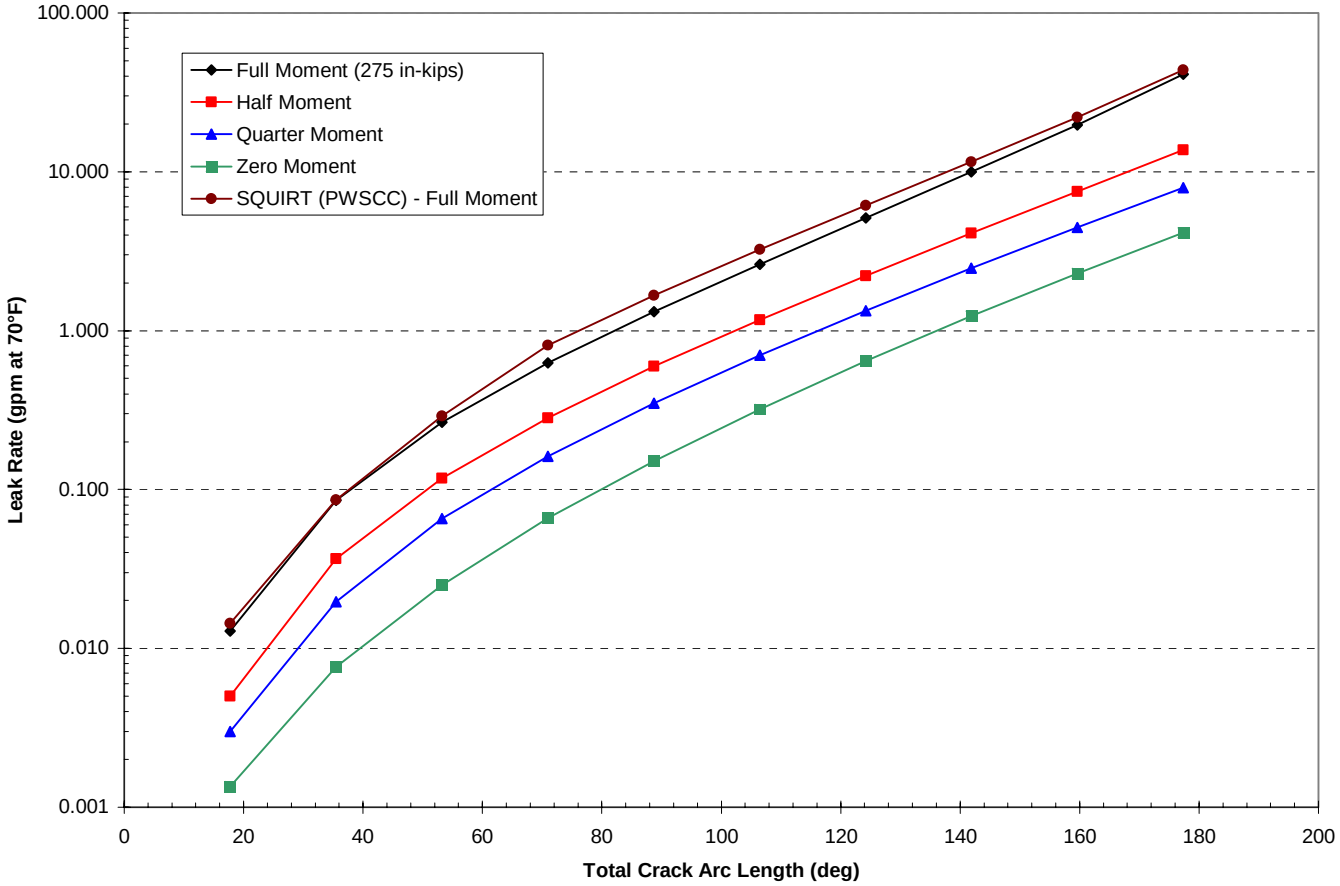

Figure 6-1
Scoping Leak Rate Results Based on Wolf Creek Relief Nozzle Dissimilar Metal Weld Dimensions and Crack Opening Displacement Calculated by PICEP and SQUIRT

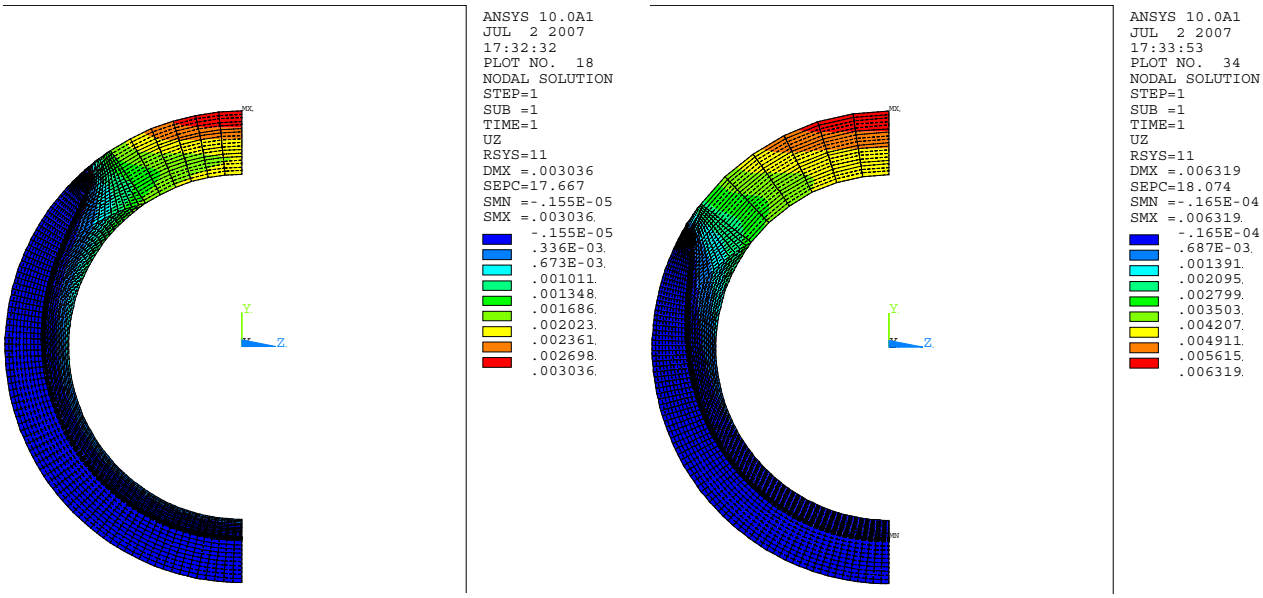

Case 12 – 1 gpm leak rate

Case 12 – Critical for 1.2 Load Margin Factor

Figure 6-2
Crack Opening Displacement Contours for Example Case (Actual COD is Twice Shown Because of Symmetry Condition)

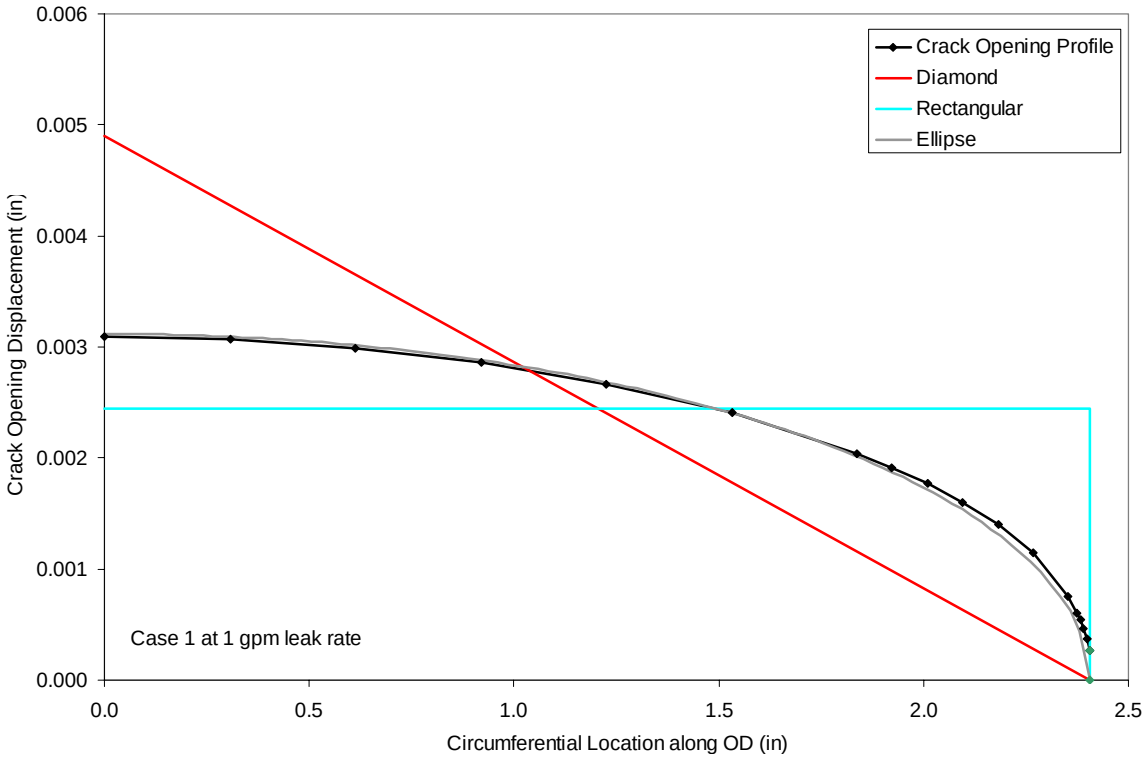

Figure 6-3
Example of Crack Opening Shape on Weld OD

7
SENSITIVITY CASE MATRIX

This section discusses the development and application of an extensive crack growth sensitivity matrix covering the geometry, load, and fabrication factors for each of the 51 subject welds, as well as the uncertainty in key modeling parameters such as those associated with welding residual stress, initial crack shape and depth, the K-dependence of the crack growth rate equation, and the effect of multiple flaws. Section 7 also presents a set of evaluation criteria that was developed to guide interpretation of the matrix results. The evaluation criteria are based on explicit consideration of leak rate detection sensitivity, plant response time, and uncertainty in the crack stability calculations. This section begins with a description of the key modeling outputs that are developed using the crack growth (Section 4), crack stability (Section 5), and leak rate (Section 6) models described in previous sections.

7.1 Modeling Procedure and Outputs

In order to evaluate each crack growth sensitivity case, the following general procedure was applied based on the crack growth, crack stability, and leak rate submodels described in the previous sections:

- *Step 1*. Using FEACrack, the assumed initial crack is grown as a part-depth surface crack until the crack reaches a depth of about 93% of the wall thickness. This is the maximum depth for which the surface crack can be reliably meshed. In the case of partial-arc surface cracks, if the ends of the crack are calculated to join up, then the partial-arc model is transitioned to a 360° surface crack by assuming that the relatively small ligament between the ends of the partial-arc crack is instantaneously eliminated. In some cases, the surface crack may be observed to arrest prior to growing through-wall due to decay in the driving stress intensity factor to zero. In such cases, the analysis case is terminated at this step.

- *Step 2*. The surface crack profile is extended from the 93% depth to 100% depth based on a single step using the stress intensity factors along the crack front at the 93% depth.

- *Step 3*. The final 100% deep surface crack, which intersects the OD surface at a single point, is converted to an initial through-wall or complex crack by eliminating the thin ligament between the final surface crack and the OD surface. It is assumed that any ligaments less than at least about 10% of the wall thickness are instantaneously cracked once the surface crack penetrates to the OD surface. For the case of surge nozzles the initial through-wall total opening angle was typically about 26°, while for the safety/relief and spray nozzles the initial through-wall total opening angle was typically about 42°. However, for the ID repair cases the initial through-wall total opening angle was often about 20° because of the difference in ligament geometry specific to the repair cases.

- *Step 4*. Using FEACrack, the initial through-wall or complex crack profile from Step 3 is grown until the point that subsequent post-processing shows the crack to reach its stability limit. In a few cases in which the initial through-wall crack is much longer on the inside surface than on the outside surface (e.g., 180° compared to 40°), the initial through-wall crack may be converted to a complex crack because of the difficulty in properly meshing the highly slanted through-wall crack geometry. This conversion is a conservative assumption given that the complex crack envelopes the through-wall crack.

- *Step 5*. The crack stability load margin factor and leak rate are determined for various steps in the through-wall or complex crack progression as a post-processing calculation as described in Sections 5 and 6. In the crack stability model, the crack face pressure is applied as an increase in the axial end cap load. The total axial load considers the operating pressure acting on the inside diameter cross section and on the crack face, as well as the dead weight and normal operating piping thermal constraint axial forces. Note that in the crack stability calculation the sum of dead weight and normal thermal axial forces is always taken based on the maximum reported for each geometry configuration, even though the typical (i.e., midrange) axial stress is usually assumed in the crack growth calculations.

Step 5 facilitates calculating the time from detectable leakage to rupture based on different choices for margin factors on the calculated leak rate and on the loads used to calculate crack stability. Closely related to this time interval output are the calculated leak rates at the beginning and end of this interval. In some cases, the initial leak rate upon cracking of the thin surface ligament between the final surface flaw and OD surface may be greater than the detectable leak rate, including consideration of a margin factor applied to the calculated leak rate. Another key output is the load stability margin factor at the time that the leaking flaw produces a detectable level of leakage. A secondary key output parameter is the time from the initial assumed surface flaw until stable through-wall penetration, or alternatively until rupture. This time may be compared to the operating age of the subject weld as a secondary evaluation.

7.2 Evaluation Criteria

7.2.1 Introduction

In order to facilitate interpretation of the main analysis results of this study, a set of evaluation criteria were developed based on the input of the EPRI expert panel. The evaluation criteria were developed in consideration of the many modeling uncertainties addressed in the detailed calculations performed, and they are based on explicit consideration of leak rate detection sensitivity, plant response time, and uncertainty in the crack stability calculations.

It is noted that the determination of the acceptability of the analysis results is not strictly speaking simply a technical question but rather involves licensing and regulatory issues that are not within the scope of this analytically structured study. Hence, the results of this study should be applied by others to make a final determination as to the issue of timing of the initial PDI examination or mitigation for each of the subject welds.

7.2.2 Criteria

Figure 7-1 illustrates the evaluation criteria that were developed from the calculated development of increasing leak rate and decreasing stability margin with time for the through-wall phase of the crack growth progression. The criteria can be stated in either of two equivalent ways:

1. Are there at least 7 days after the calculated leak rate reaches 1.0 gpm prior to the critical crack size being reached based on a margin factor of 1.2 applied to the applicable loads?

or equivalently

2. Is the crack stability margin factor on the applicable loads at least 1.2 seven days after the calculated leak rate reaches 1.0 gpm?

In Figure 7-1, the line marked by squares reflects the calculated leak rate for the predicted through-wall crack as a function of time. The line marked by circles reflects the ratio of the critical supportable load versus the reported operating load (i.e., stability load margin) for the cracked nozzle weld also as a function of time. The plot begins at the time of the initial leaking through-wall crack. Applying a margin factor of four to the 0.25 gpm detection limit applicable to the subject plants accounts for the analytical uncertainties in calculating the leak rate, and results in a value of 1.0 gpm. Where the leak rate curve intersects 1.0 gpm establishes the beginning time when the hypothetical plant could initially recognize the existence of this small leak and initiate its actions in response to a potential unidentified leak source. Within the conservatively long seven-day plant response period, the plant would be in Mode 5. The final criterion evaluates the stability margin on load. This is graphically illustrated by plotting a stability margin value of 1.2 on the seven-day line previously established and determining where the stability curve resides relative to this point.

7.2.3 Basis

The technical basis for the evaluation criteria are as follows:

- Seven days are conservatively required for the plant to shut down in response to a slowly increasing leak rate after it reaches 0.25 gpm more than the baseline leak rate. In early 2007 US PWRs committed to implement enhanced leakage monitoring programs until completion of inspection / mitigation actions on their pressurizer nozzles. These commitments include daily measurement of RCS leakage and specific timetables for plant actions to identify and respond to a change in RCS leakage. Two leakage thresholds were established: a 0.25 gpm leak rate above the plant baseline that is sustained for 72 hours; or a 0.1 gpm leak rate change from one day to the next, which is sustained for 72 hours. If either of these thresholds is exceeded, and it cannot be confirmed that it is from sources other than pressurizer nozzle welds, then the unit will be placed in Mode 3 within 6 hours and Mode 5 within 36 hours. Therefore, the cumulative total elapsed time, assuming that a through-wall leak occurs just after the daily leakage measurement, would be approximately 6 days. However, because key actions in this sequence occur on roughly a daily basis, an additional full day has been

included to conservatively define a minimum plant response period for application within the evaluation criteria.

- A margin factor of 4.0 is applied to a detection leak rate of 0.25 gpm to account for uncertainty in the calculated leak rate. A statistical study comparing the predictions of the SQUIRT leak rate code to leak rate measurements for IGSCC samples [7-1] shows that for measured leak rates greater than about 0.1 gpm, there is a 95% probability that the predicted leak rate is within a factor of 1.5 to 2.0 of the measured value. The EPRI PICEP code, which was used in this study to calculate the leak rate for the matrix of crack growth sensitivity cases, conservatively tends to predict a slightly lower leak rate compared to the SQUIRT code given the modeling inputs appropriate to PWSCC presented in Section 6. The final leak rate margin factor of 4.0 is applied in recognition of other sources of uncertainty in the leak rate calculation not addressed by the statistical evaluation cited above such as the variability in the PWSCC crack morphology parameters (e.g., crack surface roughness and tortuosity) versus the PWSCC type assumptions in Section 6.

- The margin factor of 1.2 on the loads applied in the critical crack size calculation accounts for uncertainty in these loads and in the critical crack size calculation methodology. The factor of 1.2 is appropriate in consideration of the significant conservatisms implemented in the critical crack size calculation methodology of Section 5. First, secondary normal operating piping thermal constraint loads are included in the critical crack size calculation on an equal basis with the primary pressure and dead weight loads, although evaluations tend to demonstrate that such secondary loads are expected to be significantly or completely relaxed prior to failure. Second, the critical supportable load is reduced using a Z-factor approach to account for the possibility of an EPFM failure mechanism, although there is no clear evidence that a purely limit load based approach is insufficient. Third, the safe end strength properties are applied in the critical crack size calculation. This has been shown to be appropriate for cracks located close to the safe end material. However, the WRS simulations tend to show that the highest axial stresses are located toward or within the butter weld material built up on the low alloy steel nozzle material, consistent with the reported location of the Wolf Creek indications. Finally, the statistical crack stability model implemented as part of the complementary statistical evaluations presented in Appendix A supports the conclusion that the load margin factor of 1.2 corresponds to a high confidence prediction of rupture.

- Extensive sensitivity cases are investigated to examine the effect of other modeling uncertainties such as in the basic weld dimensions, welding residual stress, other loads that drive crack growth, and stress intensity factor dependence of the crack growth rate equation.

7.2.4 Application

The general procedure for applying of the evaluation criteria discussed above is as follows:

- Analysis sensitivity cases showing stable crack arrest prior to through-wall penetration are acceptable.

- For each analysis sensitivity case, additional margin beyond the evaluation criteria values may be identified in terms of:

  a. Additional time beyond 7 days after the calculated leak rate reaches 1.0 gpm prior to the critical crack size being reached based on a load factor of 1.2, and

  b. The stability load factor 7 days after a leak rate of 1.0 gpm is reached.

- Additional margin is also indicated by the increased magnitude of the calculated leak rate as the stability margin factor decreases toward 1.2. For some cases, the calculated leak rate may reach several tens of gallons per minute prior to the load margin factor decreasing to 1.2. For such relatively high calculated leak rates, there is increased confidence that prompt plant action would be taken.

- Sensitivity cases not satisfying the above evaluation criteria may be investigated in greater detail through additional cases and/or types of analyses. Such additional analyses may identify unnecessary overconservatisms in the inputs or assumptions of the initial sensitivity case.

- As discussed above, application of the evaluation criteria provides information for guiding a final determination as to the issue of timing of the initial PDI examination or mitigation for each of the subject welds.

7.3 Sensitivity Parameters

A matrix of 118 crack growth sensitivity cases was developed in order to cover the range of design, load, and fabrication conditions, as well as to address key modeling uncertainties. The 118 cases are defined in Table 7-1. Each of the key sets of sensitivity parameters addressed in this table is discussed below (moving from the leftmost columns toward the right). Each case is numbered sequentially from top to bottom (1 through 53), with the supplemental cases S1 through S9 at the bottom of the table. Up to three different welding residual stress (WRS) assumptions are considered for each line in the table, resulting in the total number of 118 analysis cases.

7.3.1 Fracture Mechanics Model Type

For all cases except for 52c and 53b, the simplified cylindrical component geometry is assumed as discussed in Section 4. The effect of this assumption is investigated in Cases 52c and 53b through application of a nozzle-to-safe-end geometry in the fracture mechanics crack growth model.

7.3.2 Geometry Cases

The weld OD and thickness are the main required geometry inputs. In Table 7-1, the relative curvature of the cylindrical geometry is expressed in terms of the inside-radius-to-thickness-ratio

(R_i/t). The R_i/t ratio expresses the relative distance for crack growth to through-wall penetration (leakage) versus the distance for crack growth around the circumference (increased crack size and reduced crack stability). Table 7-1 also lists the EPFM Z-factor calculated on the basis of the equivalent nominal pipe size of the weld as discussed in Section 5.

7.3.3 Piping Load Cases

The next set of inputs relate to the piping loads assumed in each particular case. The nominal axial stress loading (Pm) is based on the nominal operating pressure applied to the weld inside diameter cross sectional area plus the combination of dead weight axial and normal operating piping thermal constraint axial forces, applied over the intact weld cross sectional area. The bending moment listed is based on the effective moment calculated from the two bending moment components and the torsion component as discussed in Section 5. The bending stress (Pb) shown in the table is per the thick-walled section modulus of the weld cross section.

7.3.4 Welding Residual Stress Cases

The WRS assumptions are based on the results of the WRS FEA simulations presented in Section 3 for the fabrication conditions relevant to each nozzle type. The polynomial curve fits shown in Figures 7-2 through 7-9 were applied to develop the temperature inputs to the various FEACrack models to simulate the various WRS profiles. The "a" cases generally reflect nominal WRS modeling assumptions, in which the effect of the stainless steel weld is modeled. The "b" and "c" cases reflect more conservative WRS assumptions. It is noted that because the axisymmetric WRS results for the safety and relief WRS FEA cases were observed to result in crack arrest for all the safety/relief and spray crack growth cases (even without the benefit of the stainless steel weld assumed), the "modified ASME" WRS profile developed by EMC^2 was assumed as the "c" case in many instances. This profile becomes compressive at a greater depth than the profiles calculated in Section 3 for the safety and relief WRS FEA cases.

Figure 7-8 is included for the specific purpose of comparing the WRS profile assumed in Case 17b and its derivative sensitivity cases versus three other key profiles. As discussed below, the surge nozzles covered by Case 17, which have a thermal sleeve fill-in weld and a relatively high normal operating thermal piping bending moment, tend to have the most limiting results in the crack growth sensitivity matrix. In Figure 7-8, the heavy unmarked line is the profile assumed in Case 17b based on the fit from Figure 7-7. The other profiles in Figure 7-8 are the profiles calculated by DEI and the NRC contractor EMC^2 [7-5] for the complete set of nominal fabrication steps for the surge nozzles with fill-in welds (including the beneficial effect of the stainless steel weld), along with the ASME profile as modified by EMC^2 [7-6]. Figure 7-8 shows that the WRS profile applied in Case 17b is conservative with respect to all three of these key profiles. Because the WRS profile applied in Case 17b is shifted significantly in the conservative direction (i.e., tensile for a greater distance radially from the ID) versus each of these three profiles, it appropriately addresses the effect of WRS uncertainty. The size of the shift versus the other profiles is consistent with the level of WRS uncertainty indicated in a comparison study of WRS measurements and multiple predictions for a similar application [7-7].

Furthermore, it is noted that assumption of the EMC^2 WRS FEA results shown in Figure 7-8 leads to stable crack arrest if assumed for the Case 17 set of modeling inputs.

7.3.5 K-Dependence of Crack Growth Rate Equation

The standard power-law form of the MRP-115 deterministic crack growth rate equation is assumed in the crack growth simulations. Table 7-1 shows the assumed exponent applied to the Mode-I stress intensity factor and the power-law constant corresponding to the nominal nozzle operating temperature of 650°F, based on the standard thermal activation energy of 31 kcal/mole from MRP-115. No credit is taken in the crack growth calculations for the possibility of the temperature of the surge nozzle weld being somewhat reduced from the nominal pressurizer temperature, and likewise no credit is taken in the crack growth calculations for the possibility of the temperature of the spray nozzle weld being reduced by the small steady spray flow that is typical of spray line operation.

7.3.6 Initial Flaw Cases

At the rightmost section of Table 7-1, the initial flaw geometry assumptions are listed for each case. For most cases a full arc 360° flaw having a depth of 10% of the wall thickness was assumed as the starting flaw. The Phase I scoping calculations indicated that in many cases a relatively long partial-arc surface flaw tends to grow to the same initial through-wall profile as an initial 360° flaw. Thus, the initial 360° flaw geometry was assumed in most cases to simplify the calculations. The assumption of an initial 360° flaw is also a conservative approach to addressing the concern for multiple flaw initiation and growth.

The flaw shape factor listed in Table 7-1 refers to the area of the initial flaw in comparison to a uniform depth flaw having the same ID length and depth. The "natural" shape refers to the shape that was found to grow in a self-similar manner for the beginning stages of growth under the Phase I set of geometry and load assumptions. This "natural" shape has a somewhat larger shape factor in comparison to the semi-elliptical flaw shape.

7.3.7 Consideration of Multiple Flaws

In the main matrix (Cases 1-53), the effect of multiple initiation is considered either through the assumption of an initially very long partial-arc surface crack (i.e., length-to-depth aspect ratio of 21:1) that can be considered to envelope a series of individual flaws (which typically have an aspect ratio in the range from 2:1 to 6:1 based on plant experience), or through the conservative assumption of an initial 360° full-arc flaw. In the supplemental cases (S1 through S9), alternative approaches are taken specific to the limiting surge nozzle cases in which either a set of two or three assumed flaws are grown in separate models and then combined into one weld cross section for application of the crack stability calculation. This approach is discussed further in Section 7.4.13 below.

7.4 Definition of Case Matrix

This subsection describes each subset of the 118 sensitivity cases, moving from Case 1 at the top of Table 7-1 down to Case S9 at the bottom. Note that the matrix was developed in an adaptive manner in which the initial cases (1-26) were used to determine the most limiting geometry, piping load, and WRS parameters. Then the most limiting conditions were applied to the remainder of the sensitivity matrix to ensure that the overall matrix covers modeling uncertainties in a robust manner.

7.4.1 Geometry and Load Base Cases (1-20)

These cases cover the design dimensions for each of the design configurations per the Westinghouse transmittal package of design sketches (see Section 2). Cases 1-9 cover the safety and relief nozzle configurations, Cases 10-16 cover the variety of spray nozzle configurations, and Cases 17-20 cover the surge nozzle configurations. In the case that the DM weld OD has a designed taper, the average weld thickness was assumed in the setting of the simplified cylindrical geometry. Cases 1-20 also cover the range of bending loads for each geometry configuration. The high load case is for the highest reported effective bending moment for the group of subject welds having the relevant geometry type. The low bending moment case was generally picked to have a value high enough to avoid crack arrest for at least some of the WRS input cases. It is emphasized that the reported moment loads for each subject weld may reflect conservative assumptions taken in piping analyses, and as such should be considered upper bound type values. The variability in axial membrane stress is much lower than the variability in bending stress, so the sensitivity to this other load factor is investigated separately in Section 7.4.5 below. Finally, it is noted that Configurations 2a and 2b are combined in the matrix because they correspond to the same basic weld ID and OD dimensions.

7.4.2 ID Repair Base Cases (21-26)

These cases reflect five different patterns of non-axisymmetric WRS profiles based on the ID repair WRS cases discussed in Section 3.

7.4.3 Further Bending Moment Cases (27-30)

These cases examine in greater detail the effect of a variable bending moment for the case of surge nozzles having a fill-in weld. This type of nozzle is shown in the matrix results to be one of the most limiting cases. These cases ensure that the detailed dependence of the results on bending moment is determined. Although not presented in this report, an additional set of detailed sensitivity cases were also run for the case of the Phase I calculation inputs to investigate the effect of a variable bending moment.

7.4.4 Cases to Investigate Potential Uncertainty in As-Built Dimensions (31-32)

A review of available as-built dimensions for two of the nine subject plants did not reveal any obvious inconsistencies versus the design dimensions. In general, the design dimensions are believed to be the most accurate dimensional data because of the difficulty in accurately determining the locations of the various material interfaces within the joint configuration based on the outside surface appearance of the joint. As a hypothetical exercise, these two cases assume that the weld thickness varies ±10%, while maintaining the same inside diameter and piping loads (axial force and effective moment).

7.4.5 Axial Membrane Load Sensitivity Cases (33-34)

These two cases vary the membrane stress loading based on Case 4. Case 4 covers geometry Configuration 1b, which corresponds to one of the greatest ranges in membrane stress loading as shown in Table 7-2. Configuration 2a/2b corresponds to a larger range of Pm values, but Case 6 explicitly bounds the weld with the highest Pm+Pb stress loading. The other geometry configurations tend to correspond to a relatively tight range on membrane stress loading.

7.4.6 Effect of Length Over Which Thermal Strain Simulating WRS is Applied (35)

This case investigates the effect of the distance over which the temperature load is applied in the cylindrical crack growth model in order to simulate the desired WRS profile. In the sensitivity case, this distance is reduced from 1.0 inch to 0.5 inch in the half-symmetric model (2.0 inch to 1.0 inch for the full geometry). The nominal distance of 2.0 inches is based on the typical axial length of weld metal.

7.4.7 Simulation of Elastic-Plastic Redistribution of Stress at ID (36)

This case is included to investigate the potential effect of elastic-plastic redistribution of stress at locations near the ID surface on the tensile side of the neutral bending axis, where the high assumed tensile WRS combines with tensile bending and axial membrane stresses. A circumferentially varying WRS profile is assumed in this case in order to maintain the maximum total axial stress anywhere on the weld cross section to 54 ksi. It is noted that only a small portion of the cross section, at the immediate ID surface, exceeds the nominal maximum stress of 54 ksi when the axial and bending loads are applied. The desired stress distribution was therefore achieved by adjusting the input thermal distribution at the ID surface such that when the axial and bending loads are applied, the ID surface stress does not exceed the nominal maximum. The compressive side of the bending moment is not adjusted.

7.4.8 Effect of Initial Crack Shape and Depth (37-41)

These cases are included to investigate the sensitivity of the main leakage and stability analysis results to the assumed initial flaw shape and depth given a fixed aspect ratio for the initial flaw.

Case 6 was chosen as the base case conditions for this sensitivity study because it was observed to be the most limiting of the safety/relief and spray nozzle cases.

7.4.9 Effect of Stress Intensity Factor Dependence of Crack Growth Rate Equation (42-47)

These six cases investigate the effect of uncertainty in the K-dependence of the MRP-115 crack growth rate equation. The limiting safety/relief, spray, and surge nozzle configurations are investigated in these cases.

Figures 7-10 through 7-13 illustrate the new Alloy 182 crack growth rate curves developed for the low and high K-exponent cases. Figure 7-10 shows the new crack growth rate curves, and Figures 7-11 through 7-13 show the "weld factor" fits used to develop the deterministic 75^{th} percentile power-law constants corresponding to each new K-exponent. The K-exponent value (n) cannot sensibly be varied independently of the power-law constant C as the units for C depend on the K-exponent n. The procedure to develop the two new curves is identical to that described in detail in MRP-115, except that the K-exponent for the two new cases was forced to be either the 5^{th} (1.0) or 95^{th} (2.2) percentile K-exponent value rather than the best-fit exponent (1.6). The 5^{th} and 95^{th} percentile K-exponent values themselves are based on the standard error for the K-exponent (s.e. = 0.3474) from the original MRP-115 multivariate linearized fit procedure.

7.4.10 Effect of Pressure Drop Along Leaking Crack (48)

This single case investigates the effect of the base assumption made in the matrix that the full operating pressure applies to leaking through-wall cracks as well as to surface cracks. In reality, for a leaking crack there must be a pressure drop along the crack path, resulting in a reduced average crack face pressure. The reduced crack face pressure tends to increase crack stability and reduce the crack growth rate, but it also tends to decrease the leak rate. For this case, PICEP was used to calculate the pressure drop on the crack face, and the average pressure (1330 psig) was applied in the crack growth and critical crack size calculations. The effect on the calculated leak rate was determined through the normal procedure of applying the crack opening area from the crack growth model in PICEP.

7.4.11 Effect of Relaxation of Normal Operating Thermal Load (49-51)

These cases investigated the effect of relaxation of the normal operating thermal loads assumed in the crack growth and crack stability calculations. For these cases, it is assumed that these stresses are 100% relaxed at the point that the crack becomes through wall. Besides decreasing the crack growth rate and increasing crack stability, the effect of removing these stresses is also a decrease in the leak rate through the reduction in the crack opening area. In Section 5, it was conservatively assumed to include the normal operating thermal constraint loads in the calculations although detailed evaluations tend to indicate that such secondary stresses are expected to significantly or completely relax prior to rupture. Cases 49-51 examine the effect of this assumption.

7.4.12 Effect of Nozzle-to-Safe-End Crack Growth Model vs. Standard Cylindrical Crack Growth Model (52-53)

These two cases are included to investigate the effect of the detailed nozzle-to-safe-end geometry versus the simplified cylindrical geometry. [work still in progress]

7.4.13 Supplementary Cases Specific to Effect of Multiple Flaws on Limiting Surge Nozzles (S1-S9)

The supplemental cases S1-S9 were added to further investigate the potential effect of multiple flaws in the subject surge nozzles. Cases S1a, S1b, and S8b examine the effect of assuming a 360° initial flaw on Cases 17a, 17b, and 19b, respectively, rather than a 21:1 initial partial-arc flaw. Case S2b is a further sensitivity study on Case S1b in which the effective moment load (dead weight and normal operating thermal load) is reduced to that corresponding to the surge nozzle for Plant C. The moment load for Cases 17a and 17b bounds the surge nozzles for Plants B and G.

Case S3b was designed to apply the Wolf Creek surge nozzle findings to develop additional multiple flaw assumption cases. Table 7-3 shows detailed summary statistics for the three circumferential indications that were reported in the Wolf Creek surge nozzle. The two largest indications may be enveloped by a flaw having an aspect ratio of 20:1, just less than the standard 21:1 assumption applied in the matrix. The third indication (Indication #1) is located away from the two largest indications, but has an area that is less than 0.2% of the wall cross section. In Case S3b, a flaw having the length and depth reported for this indication is grown with the piping bending moment assumed to line up with the flaw center. After 1.3 years of growth this flaw is predicted to have grown to the profile marked by closed squares shown at the top of Figure 7-14 (with depth of 56% and total length of 67°). The 1.3 years was chosen because it is the elapsed time at which the Case 17b flaw is calculated to reach 7 days of detectable leakage.

Cases S4b through S7b are crack stability cases in which a pair of flaws (one on each half-model) are superimposed on the weld cross section for Case 17b at its growth step corresponding to the point after which 7 days of detectable leakage has occurred. For Cases S4b, S5b, and S6b the pair of flaws that is superimposed is the Case S3b profile after 1.3 years of growth. As shown in Figure 7-14, in Case S4b the pair of additional flaws are inserted on the Case 17b cross section near the bottom of the cross section, with each additional flaw just touching. In Case S6b the pair of additional flaws are assumed to be just in contact with both ends of the Case 17b profile. In Case S5b an intermediate position to these other cases is assumed. In this manner, the sensitivity of the stability results to the assumed location of the pair of additional flaws is checked. This approach to applying the Wolf Creek experience is conservative in that the number of flaws outside the 21:1 envelope is doubled versus the Wolf Creek experience and each of these two flaws is grown based on the moment direction aligning with the flaw center, increasing the size of the grown flaw. Additionally, Case S7b was considered in which a hypothetical pair of flaws, each 95% through-wall and 50° in circumferential extent, was added to the Case 17b cross section.

It is noted that the approach of Cases S4b through S7b of addressing multiple flaws through independent growth of the individual flaws presumes that any crack interaction effects do not have a significant effect on the results. Based on experience, this is in fact a reasonable assumption. Analysis work investigating the flaw interaction effects on the stress intensity factor typically show only mild increases in stress intensity factor versus the single-flaw case. For example, for the simplified case of two identical coplanar through-wall cracks in an infinite plate, the stress intensity factor at the adjoining crack tips is only increased by about 10% when the separation distance is half the total length of each individual crack [7-4].

Finally, Case S9b was designed as another case to further investigate the concern for multiple flaws in the subject surge nozzles. This case is also closely related to Case 17b, but assumes a pair of initial 26% through-wall 21:1 aspect ratio flaws placed at the top and bottom of the weld cross section, rather than a single such flaw placed at the top of the cross section centered at the location of maximum axial bending stress. Because the two flaws when grown in separate crack growth models remain a considerable distance apart for the relevant growth period (see Figures 7-15 and 7-16), it is clear that crack interaction effects are insignificant for this case. Thus, it is appropriate to model growth using separate meshes and then combine the two crack profiles onto a single weld cross section for the purpose of the crack stability calculation. Unlike for Cases S4b through S7b, this process was repeated for multiple times yielding a crack stability curve as a function of time. In addition, because of the lack of crack interaction in this case, the leak rate time dependence of the leaking (i.e., upper) flaw in Case S9b can be taken as identical to that for Case 17b.

7.5 Matrix Results

All 108 cases in the main sensitivity matrix (Cases 1-53) showed either stable crack arrest (59 cases) or crack leakage and crack stability results satisfying the evaluation criteria (47 cases). (Two other of the 108 cases in the main matrix are still being completed.) In most cases, the results showed large evaluation margins in leakage time and in crack stability. In addition, a supplemental set of 10 cases (Cases S1-S9) was investigated to further explore the potential effect of multiple flaws on the limiting surge nozzle cases. Figure 7-17 shows nine example crack meshes covering the variety of crack types.

Tables 7-4, 7-5, and 7-6 present detailed results for the 68 cases that were investigated using the newly developed FEACrack software tools. An additional 50 cases were confirmed to show stable crack arrest using a simplified axisymmetric crack growth model in which the bending moment was conservatively applied as a linear stress profile based on the highest bending stress circumferential position. The axisymmetric model is based on the axisymmetric stress intensity factor solution published by Anderson et al. in WRC Bulletin 471 [7-3]. Table 7-4 shows the key results for the surface crack at the point it becomes through wall. Table 7-5 shows similar key results but also the calculated leak rate for the through-wall growth step that resulted in just above a 1.0 gpm leak (or the initial through-wall leak rate if greater than 1.0 gpm).

For those cases that showed through-wall crack development, Figures 7-18 through 7-21 show in column chart form the main analysis results from Tables 7-4, 7-5, and 7-6. Figures 7-18 and 7-19 cover the first half of the main matrix, while Figures 7-20 and 7-21 cover the second half.

Figures 7-18 and 7-20 shows the key time and leak rate outputs, specifically the time between the leak rate reaching 1.0 gpm and the crack stability margin factor decreasing to 1.2, and the leak rates corresponding to the beginning and end of this interval. (In some cases, the initial through-wall leak rate is greater than 1.0 gpm.) The time intervals shown in these two figures may be directly compared to the 7-day interval of the evaluation criteria. It is observed that all the time intervals in these two plots exceed 7 days. Additional key results are illustrated in Figures 7-19 and 7-21, which show the calculated load margin factor at the time that the leak rate reaches 1.0 gpm (or initial leakage if greater than 1.0 gpm). Lastly, Figures 7-22 through 7-40 show complete leak rate and crack stability margin trends versus time for 19 of the most limiting cases (those cases in which the load margin factor was calculated to be 1.75 or lower when the leak rate was calculated to be 1 gpm). These plots directly illustrate the margin levels that exist versus the evaluation criteria illustrated in Figure 7-1. The results of the individual subsets of cases are discussed below.

7.5.1 Geometry and Load Base Cases (1-20)

All these cases show at least 35 days from the 1.0 gpm leak rate until the load margin factor of 1.2 is reached. The most limiting base cases are 6c (safety/relief), 12c (spray), and 17b (surge). For Case 17b the initial through-wall leak rate is calculated to be 2.6 gpm, with the leak rate increasing to 69 gpm when the stability factor reaches 1.2. These cases also show that the effect of increased piping moment load (Pb) is to decrease somewhat the available margin. This behavior shows that the beneficial actions of an increased moment in pushing the crack through-wall at a more concentrated location on the circumference plus increased leak rate for a given through-wall crack extent are outweighed by the detriment of decreased crack stability.

7.5.2 ID Repair Base Cases (21-26)

These repair cases show relatively high evaluation margins compared to the axisymmetric WRS cases. This behavior is due to the tendency of the high tensile WRS in the repair zone to quickly push the crack through wall at that location. Note that for Cases 21a, 22a, 23a, 24a, and 26a the crack growth progression was terminated with load margin factors much greater than 1.2 because of difficulty in meshing these more extreme crack profiles. However, the existing results clearly illustrate large levels of evaluation margin in these cases.

7.5.3 Further Bending Moment Cases (27-30)

The results of these cases for the limiting surge nozzle configuration confirm that Case 17b reflecting the maximum effective moment value is in fact the limiting surge nozzle case. The competing effects of the moment on crack stability, leak rate, and crack shape development result in the maximum moment case being most limiting.

Note that like Case 17b, Cases 27b and 28b assumes an initial 21:1 aspect ratio flaw. The 21:1 aspect ratio corresponds to the highest aspect ratio reported for any of the Wolf Creek pressurizer nozzle indications (in the relief nozzle) and also bounds the 20:1 aspect ratio enveloping the two largest indications reported in the Wolf Creek surge nozzle (see Table 7-3). The assumption of a

21:1 initial flaw accounts for the possibility of significant growing multiple flaws because the typical aspect ratio for a single flaw is usually in the range of 2:1 to 6:1 based on plant experience. Moreover, these cases tend to show a relatively short time (1.2, 1.3, and 3.4 years, respectively) between the initial flaw depth and through-wall penetration. Within this relatively short time period, it is highly unlikely that a large portion of the 360° length (i.e., 37 inches) of the inside circumference would initiate flaws. Section 7.5.13 below discusses the results of the supplemental cases to further investigate the effect of multiple flaws on the limiting surge nozzle cases.

7.5.4 Cases to Investigate Potential Uncertainty in As-Built Dimensions (31-32)

These cases show that a change of ±10% in the wall thickness (assuming same ID) acts to increase or decrease the time margin by about one third given Case 1 as a baseline. Reducing the wall thickness reduces the time margin. Again the effect on critical crack size of a reduced wall cross section outweighs the benefit of a smaller distance for growth through-wall to leakage. These results show that the analysis results are modestly sensitive to the exact weld diameter and thickness.

7.5.5 Axial Membrane Load Sensitivity Cases (33-34)

Consistent with the previous results, these cases show that an increase in the membrane stress loading results in a slight decrease in the time margin. These cases confirm that the membrane stress variations within each geometry configuration are not significant. Even given this conclusion, it is noted that the most limiting cases in the matrix (Case 6c, 12c, and 17b) do bound the highest Pm+Pb combined stress loads for the subject welds covered in each case.

7.5.6 Effect of Length Over Which Thermal Strain Simulating WRS is Applied (35)

Case 35c shows the time interval result for Case 6c is reduced from 41 to 32 days when the length over which the thermal strain applied to simulate WRS is reduced in half. This behavior is due to a slight increase in the cracked area fraction at the point of through-wall penetration for Case 35c (0.447 vs. 0.435). This case shows that the modeling results are reasonably insensitive to this modeling length assumption. Furthermore, there does not appear to be any evidence of a significant WRS relaxation effect on the crack growth progression. Such effects are apparent in other cases in which there is a clear change in global component stiffness with the presence of a large flaw.

7.5.7 Simulation of Elastic-Plastic Redistribution of Stress at ID (36)

Case 36c shows only small differences in results versus those for its base case (Case 6c). For example, the main time interval result for Case 6c is increased by one day from 41 to 42 days. Very similar behavior in leak rate and stability margin factor development is observed in Figure 7-22 (Case 6c) and Figure 7-31 (Case 36c). These results indicate that the assumption of

elastic combination of the high welding residual stresses assumed at the weld ID with the piping axial membrane and bending stresses does not introduce significant modeling uncertainties.

7.5.8 Effect of Initial Crack Shape and Depth (37-41)

As expected based on Phase I calculation results, these cases confirm that the results in terms of time between detectable leakage and rupture are insensitive to initial partial-arc crack shape factor for a given initial crack length and depth (Cases 37 through 39). Cases 40 and 41 show furthermore that the results are relatively insensitive to the initial crack depth given a fixed initial aspect ratio. Therefore, it was appropriate that these factors (initial shape factor and depth) were investigated in a limited manner in the sensitivity matrix.

7.5.9 Effect of Stress Intensity Factor Dependence of Crack Growth Rate Equation (42-47)

These six cases showed that the limiting base cases are only modestly sensitive to the K-dependence exponent assumed. The limiting surge nozzle case (17b) was shown to be most sensitive of the three limiting cases, with the time interval result reduced from 35 to 22 days when the K-exponent is increased from 1.6 to 2.2 (Case 47b).

7.5.10 Effect of Pressure Drop Along Leaking Crack (48)

This sensitivity case showed a very small benefit of considering the decrease in pressure across the leaking crack face for the limiting surge nozzle case (17b). The time interval result increased from 35 to 39 days. This small difference justifies excluding the modeling complication of reduced crack face pressure for leaking cracks in the base matrix.

7.5.11 Effect of Relaxation of Normal Operating Thermal Load (49-51)

Two of these three sensitivity cases (49c and 50b) show a greatly increased time between a leak rate of 1.0 gpm and the load margin factor of 1.2 being reached, while the third (51b) shows stable crack arrest as does its base case (19b). The time interval result increased from 41 to 145 days for Case 6c, and from 35 to 293 days from Case 17b. These cases clearly show a large benefit if the piping thermal constraint loads are significantly relaxed once the crack grows through-wall. Furthermore, based on the results for low piping moment cases, stable crack arrest could be expected to occur in many cases if the piping thermal constraint loads are significantly relaxed before the crack reaches through-wall penetration.

7.5.12 Effect of Nozzle-to-Safe-End Crack Growth Model vs. Standard Cylindrical Crack Growth Model (52-53)

[calculations still being completed]

7.5.13 Supplementary Cases Specific to Effect of Multiple Flaws on Limiting Surge Nozzles (S1-S9)

The supplemental sensitivity cases assuming an initial 360° flaw do not satisfy the evaluation criteria for the case of surge nozzles having a fill-in weld (used to seat the thermal sleeve) and a relatively high moment load and given the WRS assumption that does not take credit for the benefit of the stainless steel weld (Cases S1b and S2b).* However, these 360° initial flaw cases are not appropriate for making conclusions regarding these surge nozzles, which show relatively fast growth through wall, because of the unlikeliness of initiation over the 37-inch inside circumference during a narrow time band.

As described above in Section 7.4.13, the results of Case S3b were used as an input to stability Cases S4b, S5b, and S6b. In this manner, the three indications found in the Wolf Creek surge nozzle weld were conservatively applied to further investigate the potential effect of multiple flaws for the limiting surge nozzle case. After 7 days of detectable leakage per Case 17b (initial leak rate of 2.6 gpm), Cases S4b, S5b, and S6b show a load margin factor of 1.43, 1.48, and 1.29, respectively. The lowest of the three margin factors (1.29) is for Case S6b, in which the pair of additional flaws is assumed to just touch the leaking crack profile from Case 17b. The highest of the three load margin factors (1.48) is for Case S5b, which is the case in which the additional pair of flaws is closest to the fully plastic NSC neutral axis. Finally, as an additional hypothetical case, Case S7b shows a corresponding load margin factor of 1.44 even given the pair of 95% through-wall additional flaws on the weld cross section of Case 17b after 7 days of detectable leakage.

Also as described above in Section 7.4.13, Case S9b was designed to further investigate the effect of multiple flaws on the subject surge nozzles. Case S9b assumes a pair of initial 26% through-wall 21:1 aspect ratio flaws placed at the top and bottom of the weld cross section, rather than a single such flaw placed at the top of the cross section centered at the location of maximum axial bending stress (Case 17b). As discussed in Section 7.4.13, the leak rate and stability margin trends can be based on separate growth of the two assumed initial flaws, with combination of the flaws in a single weld cross section for the purpose of the crack stability calculation. The resulting crack growth progression for Case S9b is shown in Figure 7-15 in terms of Cartesian coordinates, and in Figure 7-16 in terms of polar coordinates. Because of the lack of crack interaction, the time from the initial flaws to through-wall penetration of the upper flaw is unaffected versus the 1.22 years of Case 17b. Likewise, the leak rate trend with time shown in Figure 7-40 is unaffected versus Case 17b. However, the stability margin factor trend in Figure 7-40 is lowered between 0.10 and 0.12 by the presence of the second flaw. The effect is to reduce the time interval from the initial leak rate of 2.6 gpm until reaching a load margin factor of 1.2 from 35 to 29 days. In summary, Case S9b shows a modest effect on crack stability if two initial flaws covering 46% (167°) of the ID circumference are assumed as opposed to a single initial flaw covering half this circumferential extent and centered at the location of maximum axial bending stress.

* For Case S2b the time interval result is 5 days. Although less than 7 days, the initial leak rate for this case is 4.9 gpm, increasing to 6.0 gpm after 3 days. These relatively high leak rates are expected to be readily detectable even considering a leak rate margin factor of 4 to account for uncertainty in the leak rate calculation. Therefore, despite the time interval result being 5 days in this case, the results may still be acceptable.

On the basis of the supplemental set of cases, it is concluded that the concern for multiple flaws in the limiting surge nozzles is adequately addressed by cases that satisfy the evaluation criteria with additional margin.

7.6 Conclusions

7.6.1 Main Sensitivity Matrix

All 108 cases in the main sensitivity matrix showed either stable crack arrest (59 cases) or crack leakage and crack stability results satisfying the evaluation criteria (47 cases). (Two other of the 108 cases in the main matrix are still being completed.) In most cases, the results showed large evaluation margins in leakage time and in crack stability.

In the base matrix, an initial partial-arc flaw having a length-to-depth aspect ratio of 21:1 was assumed for the surge nozzle cases having a relatively large piping thermal constraint bending moment. The 21:1 aspect ratio corresponds to the highest aspect ratio reported for any of the Wolf Creek pressurizer nozzle indications (in the relief nozzle) and also bounds the 20:1 aspect ratio enveloping the two largest indications reported in the Wolf Creek surge nozzle. The assumption of a 21:1 initial flaw accounts for the possibility of significant growing multiple flaws because the typical aspect ratio for a single flaw is usually in the range of 2:1 to 6:1 based on plant experience. Moreover, the surge nozzle cases that tend to show the least margin between detectable leakage and rupture show a relatively short time (e.g., 1.2 years) between the initial flaw depth and through-wall penetration. Within this relatively short time period, it is highly unlikely that a large portion of the 360° length (i.e., 37 inches) of the inside circumference would initiate flaws.

7.6.2 Supplemental Sensitivity Matrix

However, in order to further investigate the potential effect of multiple flaws in the subject surge nozzles, several supplemental cases were added. The supplemental sensitivity cases assuming an initial 360° flaw do not satisfy the evaluation criteria for the case of surge nozzles having a fill-in weld (used to seat the thermal sleeve) and a relatively high moment load and given the WRS assumption that does not take credit for the benefit of the stainless steel weld. However, these 360° initial flaw cases are not appropriate for making conclusions regarding these surge nozzles, which show relatively fast growth through wall, because of the unlikeliness of initiation over the 37-inch inside circumference during a narrow time band. On the other hand, conservative application of the three indications found in the Wolf Creek surge nozzle weld for surge nozzles with a fill-in weld and relatively high moment load gives results meeting the evaluation criteria. In addition, considering a case with two long initial partial-arc flaws covering 46% of the ID circumference as opposed to a single initial flaw covering half this circumferential extent (and centered at the location of maximum axial bending stress) has only a modest effect on crack stability for these limiting surge nozzles. On this basis, it is concluded that the concern for multiple flaws in the limiting surge nozzles is adequately addressed by cases that satisfy the evaluation criteria with additional margin.

7.6.3 Tendency of Circumferential Surface Cracks to Show Stable Arrest

An additional key finding concerns the significant number of crack growth sensitivity cases that showed stable crack arrest prior to through-wall penetration. This type of behavior is consistent with the relatively narrow band of relative depths reported for the four largest Wolf Creek indications (23%, 25%, 26%, and 31% through-wall). As emphasized in the MRP white paper [7-2], it is statistically unlikely that these four indications would be found in this narrow depth band if they were in fact growing rapidly at the time they were detected. The basic reason that circumferential cracks may tend to arrest prior to through-wall penetration is that to the extent the through-wall welding residual stress profile is axisymmetric, it must be self-balanced at a particular circumferential position, meaning that a significant portion of the wall thickness must have compressive axial welding residual stresses. On the other hand, for axial flaws that are driven largely by tensile hoop welding residual stresses, these hoop welding residual stresses are generally balanced by the compressive residual stresses in the base metal material upstream and downstream from the dissimilar metal weld. Hence, the hoop welding residual stress in the weld material is more likely to remain tensile and drive an axial flaw through-wall than is the case for axial residual stress and circumferential flaws. This expectation is consistent with general PWR plant experience that has shown part-depth and leaking axial PWSCC in Alloy 82/182 piping butt welds, but only indications of circumferential flaws in such weldments.

7.7 References

7-1. D. O. Harris, "A Note on Scatter in Leak Rate Predictions," June 22, 2007 (draft).

7-2. "Implications of Wolf Creek Pressurizer Butt Weld Indications Relative to Safety Assessment and Inspection Requirements," MRP 2007-003 Attachment 1, January 2007.

7-3. T. L. Anderson, et al., "Development of Stress Intensity Factor Solutions for Surface and Embedded Cracks In API 579," Welding Research Council Bulletin 471, May 2002.

7-4. T. L. Anderson, *Fracture Mechanics*, Third Edition, CRC Press, Taylor & Francis Group, New York, 2005, pp. 86-87.

7-5. T. Sullivan and A. Csontos, "NRC Questions and Comments on the Industry Advanced FEA Draft Report," July 12, 2007.

7-6. US NRC, "Safety Concerns Regarding Potential Pressurizer Weld Cracking," presented at December 20, 2006, public meeting between US NRC and MRP, Rockville, Maryland.

7-7. B. Brust and P. Scott, "Battelle Memorial Lab Results: EU Report WRS Round Robin Study Modeling," presented at MRP-NRC meeting of July 12, 2007.

Table 7-1
Sensitivity Matrix Case Definitions

				Geometry Case							Load Case								
Case #	Base Case	Sensitivity Purpose	Model Type	Nozzle Type	Geometry Configuration	Plants	D_o (in)	t (in)	R_i/t	TW Z-factor per PVP paper	Pm Case	p (ksi)	F_{dw+nt} (kips)	F_{axial} (kips)	Pm (ksi)	max F_{dw+nt} (kips)	Pb Case	M (in-kips)	Pb (thick) (ksi)
1	-	geometry/load	cylinder	S&R	Config 1a	AEH	7.750	1.290	2.004	1.170	typical	2.235	-1.28	45.64	1.74	2.42	high	209.28	5.71
2	-	geometry/load	cylinder	S&R	Config 1a	AEH	7.750	1.290	2.004	1.170	typical	2.235	-1.28	45.64	1.74	2.42	intermed	194.09	5.30
3	-	geometry/load	cylinder	S&R	Config 1a	AEH	7.750	1.290	2.004	1.170	typical	2.235	-1.28	45.64	1.74	2.42	low	178.90	4.88
4	-	geometry/load	cylinder	S&R	Config 1b	F	8.000	1.405	1.847	1.171	typical	2.235	7.90	55.19	1.90	15.37	high	237.40	5.74
5	-	geometry/load	cylinder	S&R	Config 1b	F	8.000	1.405	1.847	1.171	typical	2.235	7.90	55.19	1.90	15.37	low	201.91	4.88
6	-	geometry/load	cylinder	S&R	Config 2a/2b	BCG	7.750	1.065	2.638	1.170	typical	2.235	-3.01	52.44	2.34	4.98	high	252.14	7.63
7	-	geometry/load	cylinder	S&R	Config 2a/2b	BCG	7.750	1.065	2.638	1.170	typical	2.235	-3.01	52.44	2.34	4.98	low	158.04	4.78
8	-	geometry/load	cylinder	S&R	Config 3	DI	8.000	1.405	1.847	1.171	typical	2.235	0.66	47.94	1.65	1.74	high	277.18	6.70
9	-	geometry/load	cylinder	S&R	Config 3	DI	8.000	1.405	1.847	1.171	typical	2.235	0.66	47.94	1.65	1.74	low	201.91	4.88
10	-	geometry/load	cylinder	spray	Config 4	AE	5.810	0.900	2.228	1.156	typical	2.235	-1.27	26.96	1.94	-0.35	high	72.78	4.89
11	-	geometry/load	cylinder	spray	Config 4	AE	5.810	0.900	2.228	1.156	typical	2.235	-1.27	26.96	1.94	-0.35	low	66.98	4.50
12	-	geometry/load	cylinder	spray	Config 5	BCG	5.810	0.780	2.724	1.156	typical	2.235	-0.77	30.94	2.51	0.47	high	65.33	4.75
13	-	geometry/load	cylinder	spray	Config 5	BCG	5.810	0.780	2.724	1.156	typical	2.235	-0.77	30.94	2.51	0.47	low	56.76	4.13
14	-	geometry/load	cylinder	spray	Config 6	F	8.000	1.150	2.478	1.171	typical	2.235	-0.84	56.19	2.27	-0.84	high	27.91	0.75
15	-	geometry/load	cylinder	spray	Config 7	DI	5.190	1.045	1.483	1.147	typical	2.235	0.62	17.49	1.29	0.81	high	55.65	4.65
16	-	geometry/load	cylinder	spray	Config 7	DI	5.190	1.045	1.483	1.147	typical	2.235	0.62	17.49	1.29	0.81	low	49.47	4.13
17	-	geometry/load	cylinder	surge	Config 8	AEHBCG	15.000	1.580	3.747	1.194	typical	2.235	1.62	247.70	3.72	8.04	high	2750.77	13.57
18	-	geometry/load	cylinder	surge	Config 8	AEHBCG	15.000	1.580	3.747	1.194	typical	2.235	1.62	247.70	3.72	8.04	low	989.57	4.88
19	-	geometry/load	cylinder	surge	Config 9	DI	13.060	1.470	3.442	1.189	high	2.235	4.97	184.75	3.45	4.97	high	2034.30	14.55
20	-	geometry/load	cylinder	surge	Config 9	DI	13.060	1.470	3.442	1.189	high	2.235	4.97	184.75	3.45	4.97	low	929.97	6.65
21	1	ID repair	cylinder	S&R	Config 1a	AEH	7.750	1.290	2.004	1.170	typical	2.235	-1.28	45.64	1.74	2.42	high	209.28	5.71
22	3	ID repair	cylinder	S&R	Config 1a	AEH	7.750	1.290	2.004	1.170	typical	2.235	-1.28	45.64	1.74	2.42	low	178.90	4.88
23	6	ID repair	cylinder	S&R	Config 2a/2b	BCG	7.750	1.065	2.638	1.170	typical	2.235	-3.01	52.44	2.34	4.98	high	252.14	7.63
24	7	ID repair	cylinder	S&R	Config 2a/2b	BCG	7.750	1.065	2.638	1.170	typical	2.235	-3.01	52.44	2.34	4.98	low	158.04	4.78
25	17	ID repair	cylinder	surge	Config 8	AEHBCG	15.000	1.580	3.747	1.194	typical	2.235	1.62	247.70	3.72	8.04	high	2750.77	13.57
26	18	ID repair	cylinder	surge	Config 8	AEHBCG	15.000	1.580	3.747	1.194	typical	2.235	1.62	247.70	3.72	8.04	low	989.57	4.88
27	17	Pb sensitivity	cylinder	bound	bounding	AEHBCG	15.000	1.580	3.747	1.194	typical	2.235	1.62	247.70	3.72	8.04	sens 1	2635.33	13.00
28	17	Pb sensitivity	cylinder	bound	bounding	AEHBCG	15.000	1.580	3.747	1.194	typical	2.235	1.62	247.70	3.72	8.04	sens 2	2027.18	10.00
29	18	Pb sensitivity	cylinder	bound	bounding	AEHBCG	15.000	1.580	3.747	1.194	typical	2.235	1.62	247.70	3.72	8.04	sens 3	1419.02	7.00
30	18	Pb sensitivity	cylinder	bound	bounding	AEHBCG	15.000	1.580	3.747	1.194	typical	2.235	1.62	247.70	3.72	8.04	sens 4	817.40	4.03
31	1	as-built uncertainty	cylinder	S&R	as-built 1	AEH	8.008	1.419	1.822	1.171	typical	2.235	-1.28	45.64	1.55	2.42	bounding	209.28	5.02
32	1	as-built uncertainty	cylinder	S&R	as-built 2	AEH	7.492	1.161	2.227	1.169	typical	2.235	-1.28	45.64	1.98	2.42	bounding	209.28	6.56
33	4	Pm sensitivity	cylinder	S&R	bounding S&R	F	8.000	1.405	1.847	1.171	low	2.235	0.44	47.73	1.64	15.37	bounding	237.40	5.74
34	4	Pm sensitivity	cylinder	S&R	bounding S&R	F	8.000	1.405	1.847	1.171	high	2.235	15.37	62.65	2.15	15.37	bounding	237.40	5.74
35	6	shortened 0.5″ "weld"	cylinder	S&R	bounding S&R	BCG	7.750	1.065	2.638	1.170	typical	2.235	-3.01	52.44	2.34	4.98	bounding	252.14	7.63
36	6	plastic redistribution	cylinder	S&R	bounding S&R	BCG	7.750	1.065	2.638	1.170	typical	2.235	-3.01	52.44	2.34	4.98	bounding	252.14	7.63
37	6	initial crack shape	cylinder	S&R	bounding S&R	BCG	7.750	1.065	2.638	1.170	typical	2.235	-3.01	52.44	2.34	4.98	bounding	252.14	7.63
38	6	initial crack shape	cylinder	S&R	bounding S&R	BCG	7.750	1.065	2.638	1.170	typical	2.235	-3.01	52.44	2.34	4.98	bounding	252.14	7.63
39	6	initial crack shape	cylinder	S&R	bounding S&R	BCG	7.750	1.065	2.638	1.170	typical	2.235	-3.01	52.44	2.34	4.98	bounding	252.14	7.63
40	6	initial crack depth	cylinder	S&R	bounding S&R	BCG	7.750	1.065	2.638	1.170	typical	2.235	-3.01	52.44	2.34	4.98	bounding	252.14	7.63
41	6	initial crack depth	cylinder	S&R	bounding S&R	BCG	7.750	1.065	2.638	1.170	typical	2.235	-3.01	52.44	2.34	4.98	bounding	252.14	7.63
42	6	CGR K-exponent	cylinder	S&R	bounding S&R	BCG	7.750	1.065	2.638	1.170	typical	2.235	-3.01	52.44	2.34	4.98	bounding	252.14	7.63
43	6	CGR K-exponent	cylinder	S&R	bounding S&R	BCG	7.750	1.065	2.638	1.170	typical	2.235	-3.01	52.44	2.34	4.98	bounding	252.14	7.63
44	12	CGR K-exponent	cylinder	spray	bounding spray	BCG	5.810	0.780	2.724	1.156	typical	2.235	-0.77	30.94	2.51	0.47	bounding	65.33	4.75
45	12	CGR K-exponent	cylinder	spray	bounding spray	BCG	5.810	0.780	2.724	1.156	typical	2.235	-0.77	30.94	2.51	0.47	bounding	65.33	4.75
46	17	CGR K-exponent	cylinder	surge	bounding surge	AEHBCG	15.000	1.580	3.747	1.194	typical	2.235	1.62	247.70	3.72	8.04	bounding	2750.77	13.57
47	17	CGR K-exponent	cylinder	surge	bounding surge	AEHBCG	15.000	1.580	3.747	1.194	typical	2.235	1.62	247.70	3.72	8.04	bounding	2750.77	13.57
48	17	reduced press. on CF	cylinder	bound	bounding	AEHBCG	15.000	1.580	3.747	1.194	typical	2.235	1.62	247.70	3.72	8.04	bounding	2750.77	13.57
49	6	no thermal load for TW	cylinder	bound	bounding	BCG	7.750	1.065	2.638	1.170	typical	2.235	-0.33	55.11	2.46	0.17	bounding	31.10	0.94
50	17	no thermal load for TW	cylinder	bound	bounding	AEHBCG	15.000	1.580	3.747	1.194	typical	2.235	0.76	246.84	3.71	5.76	bounding	160.18	0.79
51	19	no thermal load for TW	cylinder	bound	bounding	DI	13.060	1.470	3.442	1.189	high	2.235	0.00	179.78	3.36	0.00	bounding	126.20	0.90
52	1	detailed geometry	nozzle	S&R	example S&R	AEH	7.750	1.290	2.004	1.170	typical	2.235	-1.28	45.64	1.74	2.42	bounding	209.28	5.71
53	17	detailed geometry	nozzle	surge	example surge	AEHBCG	15.000	1.580	3.747	1.194	typical	2.235	1.62	247.70	3.72	8.04	bounding	2750.77	13.57
S1	17	effect of multiple flaws	cylinder	surge	Config 8	AEHBCG	15.000	1.580	3.747	1.194	typical	2.235	1.62	247.70	3.72	8.04	high	2750.77	13.57
S2	17	effect of multiple flaws	cylinder	surge	Config 8	AEHBCG	15.000	1.580	3.747	1.194	typical	2.235	1.62	247.70	3.72	8.04	high	1702.83	8.40
S3	17	effect of multiple flaws	cylinder	surge	Config 8	AEHBCG	15.000	1.580	3.747	1.194	typical	2.235	1.62	247.70	3.72	8.04	high	2750.77	13.57
S4	17	effect of multiple flaws	cylinder	surge	Config 8	AEHBCG	15.000	1.580	3.747	1.194	typical	2.235	1.62	247.70	3.72	8.04	high	2750.77	13.57
S5	17	effect of multiple flaws	cylinder	surge	Config 8	AEHBCG	15.000	1.580	3.747	1.194	typical	2.235	1.62	247.70	3.72	8.04	high	2750.77	13.57
S6	17	effect of multiple flaws	cylinder	surge	Config 8	AEHBCG	15.000	1.580	3.747	1.194	typical	2.235	1.62	247.70	3.72	8.04	high	2750.77	13.57
S7	17	effect of multiple flaws	cylinder	surge	Config 8	AEHBCG	15.000	1.580	3.747	1.194	typical	2.235	1.62	247.70	3.72	8.04	high	2750.77	13.57
S8	19	effect of multiple flaws	cylinder	surge	Config 9	DI	13.060	1.470	3.442	1.189	high	2.235	4.97	184.75	3.45	4.97	high	2034.30	14.55
S9	17	effect of multiple flaws	cylinder	surge	Config 8	AEHBCG	15.000	1.580	3.747	1.194	typical	2.235	1.62	247.70	3.72	8.04	high	2750.77	13.57

Table 7-1 (continued)
Sensitivity Matrix Case Definitions

Case #	Base Case	WRS Case (see Note 1)				CGR Equation		Initial Flaw		
		Weld Repair Case?	Nominal WRS Case ("a" case)	Conservative WRS Case ("b" case)	More Conservative WRS Case ("c" case)	K-Exp. n	$C_{75th,650°F}$ (in/h; ksi-in$^{0.5}$)	2c/a	Shape Factor	Depth (%tw)
1	-	Axisymm	*1a: Type 1 S&R with SS weld	*1b: Type 1 S&R without SS weld	1c: Mod ASME 3/30 Fit	1.6	8.515E-12	360°	uniform	10%
2	-	Axisymm	*2a: Type 1 S&R with SS weld	*2b: Type 1 S&R without SS weld	2c: Mod ASME 3/30 Fit	1.6	8.515E-12	360°	uniform	10%
3	-	Axisymm	*3a: Type 1 S&R with SS weld	*3b: Type 1 S&R without SS weld	3c: Mod ASME 3/30 Fit	1.6	8.515E-12	360°	uniform	10%
4	-	Axisymm	*4a: Type 1 S&R with SS weld	*4b: Type 1 S&R without SS weld	4c: Mod ASME 3/30 Fit	1.6	8.515E-12	360°	uniform	10%
5	-	Axisymm	*5a: Type 1 S&R with SS weld	*5b: Type 1 S&R without SS weld	5c: Mod ASME 3/30 Fit	1.6	8.515E-12	360°	uniform	10%
6	-	Axisymm	*6a: Type 1 S&R with SS weld	*6b: Type 1 S&R without SS weld	6c: Mod ASME 3/30 Fit	1.6	8.515E-12	360°	uniform	10%
7	-	Axisymm	*7a: Type 1 S&R with SS weld	*7b: Type 1 S&R without SS weld	7c: Mod ASME 3/30 Fit	1.6	8.515E-12	360°	uniform	10%
8	-	Axisymm	*8a: Type 1 S&R with SS weld	*8b: Type 1 S&R without SS weld	8c: Mod ASME 3/30 Fit	1.6	8.515E-12	360°	uniform	10%
9	-	Axisymm	*9a: Type 1 S&R with SS weld	*9b: Type 1 S&R without SS weld	9c: Mod ASME 3/30 Fit	1.6	8.515E-12	360°	uniform	10%
10	-	Axisymm	*10a: Type 1 S&R with SS weld	*10b: Type 1 S&R without SS weld	10c: Mod ASME 3/30 Fit	1.6	8.515E-12	360°	uniform	10%
11	-	Axisymm	*11a: Type 1 S&R with SS weld	*11b: Type 1 S&R without SS weld	11c: Mod ASME 3/30 Fit	1.6	8.515E-12	360°	uniform	10%
12	-	Axisymm	*12a: Type 1 S&R with SS weld	*12b: Type 1 S&R without SS weld	12c: Mod ASME 3/30 Fit	1.6	8.515E-12	360°	uniform	10%
13	-	Axisymm	*13a: Type 1 S&R with SS weld	*13b: Type 1 S&R without SS weld	13c: Mod ASME 3/30 Fit	1.6	8.515E-12	360°	uniform	10%
14	-	Axisymm	*14a: Type 1 S&R with SS weld	*14b: Type 1 S&R without SS weld	14c: Mod ASME 3/30 Fit	1.6	8.515E-12	360°	uniform	10%
15	-	Axisymm	*15a: Type 1 S&R with SS weld	*15b: Type 1 S&R without SS weld	15c: Mod ASME 3/30 Fit	1.6	8.515E-12	360°	uniform	10%
16	-	Axisymm	*16a: Type 1 S&R with SS weld	*16b: Type 1 S&R without SS weld	16c: Mod ASME 3/30 Fit	1.6	8.515E-12	360°	uniform	10%
17	-	Axisymm	17a: Type 8 surge with SS weld	17b: Type 8 surge without SS weld		1.6	8.515E-12	21	natural	26%
18	-	Axisymm	18a: Type 8 surge with SS weld	18b: Type 8 surge without SS weld		1.6	8.515E-12	360°	uniform	10%
19	-	Axisymm	*19a: Type 9 surge	19b: Type 8 surge with SS weld		1.6	8.515E-12	21	natural	26%
20	-	Axisymm	*20a: Type 9 surge	20b: Type 8 surge with SS weld		1.6	8.515E-12	360°	uniform	10%
21	1	ID Repair	21a: S&R 20° ID repair / wo SS weld			1.6	8.515E-12	360°	uniform	10%
22	3	ID Repair	22a: S&R 20° ID repair / wo SS weld			1.6	8.515E-12	360°	uniform	10%
23	6	ID Repair	23a: S&R 20° ID repair / wo SS weld	23b: S&R 20° ID repair / mod ASME	23c: 23a with 3 repairs	1.6	8.515E-12	360°	uniform	10%
24	7	ID Repair	24a: S&R 20° ID repair / wo SS weld			1.6	8.515E-12	360°	uniform	10%
25	17	ID Repair	25a: surge ID repair / with SS weld	25b: surge ID repair / w/o SS weld		1.6	8.515E-12	21	natural	26%
26	18	ID Repair	26a: surge ID repair / with SS weld			1.6	8.515E-12	360°	uniform	10%
27	17	Axisymm		27b: Type 8 surge without SS weld		1.6	8.515E-12	21	natural	26%
28	17	Axisymm		28b: Type 8 surge without SS weld		1.6	8.515E-12	21	natural	26%
29	18	Axisymm		29b: Type 8 surge without SS weld		1.6	8.515E-12	360°	uniform	10%
30	18	Axisymm		30b: Type 8 surge without SS weld		1.6	8.515E-12	360°	uniform	10%
31	1	Axisymm	*31a: Type 1 S&R with SS weld	*31b: Type 1 S&R without SS weld	31c: Mod ASME 3/30 Fit	1.6	8.515E-12	360°	uniform	10%
32	1	Axisymm	*32a: Type 1 S&R with SS weld	*32b: Type 1 S&R without SS weld	32c: Mod ASME 3/30 Fit	1.6	8.515E-12	360°	uniform	10%
33	4	Axisymm	*33a: Type 1 S&R with SS weld	*33b: Type 1 S&R without SS weld	33c: Mod ASME 3/30 Fit	1.6	8.515E-12	360°	uniform	10%
34	4	Axisymm	*34a: Type 1 S&R with SS weld	*34b: Type 1 S&R without SS weld	34c: Mod ASME 3/30 Fit	1.6	8.515E-12	360°	uniform	10%
35	6	Axisymm			35c: Mod ASME 3/30 Fit	1.6	8.515E-12	360°	uniform	10%
36	6	Axisymm			36c: Mod ASME 3/30 Fit	1.6	8.515E-12	360°	uniform	10%
37	6	Axisymm			37c: Mod ASME 3/30 Fit	1.6	8.515E-12	21	natural	26%
38	6	Axisymm			38c: Mod ASME 3/30 Fit	1.6	8.515E-12	21	semi-ellipse	26%
39	6	Axisymm			39c: Mod ASME 3/30 Fit	1.6	8.515E-12	21	constant	26%
40	6	Axisymm			40c: Mod ASME 3/30 Fit	1.6	8.515E-12	21	natural	15%
41	6	Axisymm			41c: Mod ASME 3/30 Fit	1.6	8.515E-12	21	natural	40%
42	6	Axisymm	*42a: Type 1 S&R with SS weld	*42b: Type 1 S&R without SS weld	42c: Mod ASME 3/30 Fit	1.0	4.313E-09	360°	uniform	10%
43	6	Axisymm	*43a: Type 1 S&R with SS weld	*43b: Type 1 S&R without SS weld	43c: Mod ASME 3/30 Fit	2.2	1.530E-14	360°	uniform	10%
44	12	Axisymm	*44a: Type 1 S&R with SS weld	*44b: Type 1 S&R without SS weld	44c: Mod ASME 3/30 Fit	1.0	4.313E-09	360°	uniform	10%
45	12	Axisymm	*45a: Type 1 S&R with SS weld	*45b: Type 1 S&R without SS weld	45c: Mod ASME 3/30 Fit	2.2	1.530E-14	360°	uniform	10%
46	17	Axisymm		46b: Type 8 surge without SS weld		1.0	4.313E-09	21	natural	26%
47	17	Axisymm		47b: Type 8 surge without SS weld		2.2	1.530E-14	21	natural	26%
48	17	Axisymm		48b: Type 8 surge without SS weld		1.6	8.515E-12	21	natural	26%
49	6	Axisymm			49c: Mod ASME 3/30 Fit	1.6	8.515E-12	360°	uniform	10%
50	17	Axisymm		50b: Type 8 surge without SS weld		1.6	8.515E-12	21	natural	26%
51	19	Axisymm		51b: Type 8 surge with SS weld		1.6	8.515E-12	21	natural	26%
52	1	Axisymm			52c: Mod ASME 3/30 Fit	1.6	8.515E-12	360°	uniform	10%
53	17	Axisymm		53b: Type 8 surge without SS weld		1.6	8.515E-12	21	natural	26%
S1	17	Axisymm	S1a: Type 8 surge with SS weld	S1b: Type 8 surge without SS weld		1.6	8.515E-12	360°	uniform	10%
S2	17	Axisymm		S2b: Type 8 surge without SS weld		1.6	8.515E-12	360°	uniform	10%
S3	17	Axisymm		S3b: Type 8 surge without SS weld		1.6	8.515E-12	5.6	natural	10%
S4	17	Axisymm		S4b: Type 8 surge without SS weld		1.6	8.515E-12	Combine 17b + S3b #1		
S5	17	Axisymm		S5b: Type 8 surge without SS weld		1.6	8.515E-12	Combine 17b + S3b #2		
S6	17	Axisymm		S6b: Type 8 surge without SS weld		1.6	8.515E-12	Combine 17b + S3b #3		
S7	17	Axisymm		S7b: Type 8 surge without SS weld		1.6	8.515E-12	Combine 17b + 95%tw		
S8	19	Axisymm		S8b: Type 8 surge with SS weld		1.6	8.515E-12	360°	uniform	10%
S9	17	Axisymm		S9b: Type 8 surge without SS weld		1.6	8.515E-12	2 Case 17b 21:1 flaws		

Notes
(1) Asterisk before case number indicates stable crack arrest verified using axisymmetric crack growth solution for uniform depth 360° crack.

Table 7-2
Geometry and Load Combination for 51 Subject Welds

Type	Design	# of nozzles	Loads					
			P_m		P_b		$P_b/(P_m+P_b)$	
			(ksi)		(ksi)		-	
			Min	Max	Min	Max	Min	Max
Safety and Relief Nozzles	1a	12	3.17	3.45	0.07	5.71	0.02	0.64
	1b	4	3.20	3.71	0.78	5.74	0.20	0.63
	2a	8	3.93	4.29	1.04	7.63	0.21	0.64
	2b	4	3.57	3.90	2.35	4.78	0.38	0.57
	3	7	3.16	3.24	0.00	6.70	0.00	0.67
Spray Nozzles	4	2	3.45	3.58	1.38	4.89	0.28	0.59
	5	3	4.00	4.20	1.12	4.75	0.21	0.54
	6	1	3.84	3.84	0.75	0.75	0.16	0.16
	7	2	2.76	3.05	1.16	4.80	0.30	0.61
Surge Nozzles	8	6	5.24	5.43	4.04	13.58	0.43	0.72
	9	2	4.92	5.06	6.65	14.55	0.57	0.74

Note:
Pm in this table is based on ASME pressure stress $pD_o/4t$, plus dead weight and normal thermal axial loads divided by metal cross sectional area.

Table 7-3
Summary Statistics for Wolf Creek Pressurizer Surge Nozzle DM Weld Indications Reported in October 2006

Assumed Flaw	Max. Depth		Circ. Position		Length		Length-to-Depth Aspect Ratio	Circ. Position		Circ. Extent		Individual Flaw Lengths			Flaw Area (Note 1)		Individual Flaw Areas		
	(%tw)	(in)	Start on OD (in)	Stop on OD (in)	on OD (in)	on ID (in)		Start (%Circ)	Stop (%Circ)	(%Circ)	(deg)	Total ID Lengths (in)	Total % of Envelope Length	Ind#1% of Envelope Length	(in^2)	(%wall)	Total Areas (%wall)	Total % of Envelope Area	Ind#1% of Envelope Area
Indication #1	10%	0.145	43.0	44.0	1.0	0.81	5.6	91.5%	93.6%	2.1%	7.7				0.12	0.19%			
Indication #2	25%	0.363	28.75	31.5	2.75	2.22	6.1	61.2%	67.0%	5.9%	21.1				0.83	1.3%			
Indication #3	31%	0.450	20.5	25.5	5.0	4.03	9.0	43.6%	54.3%	10.6%	38.3				1.88	3.1%			
Envelope 2&3	31%	0.450	20.5	31.5	11.0	8.87	19.7	43.6%	67.0%	23.4%	84.3	6.25	70.5%		4.13	6.7%	4.4%	65.5%	
Envelope 1,2&3	31%	0.450	20.5	44.0	23.5	18.94	42.1	43.6%	93.6%	50.0%	180.0	7.05	37.2%	4.3%	8.83	14.4%	4.6%	32.0%	1.3%

Weld OD Circumference (in)	47.0
OD (in)	14.96
Weld Thickness, t (in)	1.45
ID (in)	12.06
ID/OD	0.806
Cross Sectional Area (in^2)	61.54

Notes:
(1) Constant depth shape assumed for flaw area calculations.

Table 7-4
Sensitivity Matrix Case Surface Crack Results

Case #	WRS Subcase	Geometry Case				Surface Crack Stability Results (Press + DW + NT loads and Z-factor for Critical Size)							
		Nozzle Type	Geometry Configuration	R_i (in)	t (in)	Time to TW (yrs)	Fraction Xsection Cracked	Crack Face F (kips)	Max tot Faxial (kips)	Max Pm Based on CF (ksi)	Stability Margin Factor	Support. Pm (ksi)	Support. Pb (thick) (ksi)
1	c	S&R	Config 1a	2.585	1.290	17.4	0.400	23.40	72.74	2.78	3.10	8.6	17.7
2	c	S&R	Config 1a	2.585	1.290	21.3	0.395	23.12	72.45	2.77	3.33	9.2	17.6
3	c	S&R	Config 1a	2.585	1.290	26.3	0.383	22.43	71.77	2.74	3.67	10.1	17.9
4	c	S&R	Config 1b	2.595	1.405	18.0	0.400	26.04	88.68	3.05	2.95	9.0	16.9
5	c	S&R	Config 1b	2.595	1.405	25.7	0.381	24.79	87.44	3.00	3.51	10.6	17.2
6	c	S&R	Config 2a/2b	2.810	1.065	3.4	0.435	21.74	82.16	3.67	2.04	7.5	15.6
7	c	S&R	Config 2a/2b	2.810	1.065	10.5	0.440	22.01	82.43	3.69	2.63	9.7	12.6
8	c	S&R	Config 3	2.595	1.405	13.4	0.399	25.94	74.96	2.58	2.87	7.4	19.2
9	c	S&R	Config 3	2.595	1.405	32.2	0.364	23.69	72.71	2.50	4.12	10.3	20.1
10	c	spray	Config 4	2.005	0.900	21.2	0.389	12.06	39.94	2.88	3.57	10.3	17.4
11	c	spray	Config 4	2.005	0.900	25.3	0.378	11.71	39.59	2.85	3.95	11.3	17.8
12	c	spray	Config 5	2.125	0.780	10.5	0.436	12.01	44.18	3.58	2.76	9.9	13.1
13	c	spray	Config 5	2.125	0.780	13.6	0.427	11.76	43.94	3.56	3.05	10.9	12.6
14	c	spray	Config 6	2.850	1.150	Arrest							
15	c	spray	Config 7	1.550	1.045	Arrest							
16	c	spray	Config 7	1.550	1.045	Arrest							
17	a	surge	Config 8	5.920	1.580	Arrest							
17	b	surge	Config 8	5.920	1.580	1.2	0.240	35.80	289.91	4.35	1.73	7.5	23.4
18	a	surge	Config 8	5.920	1.580	Arrest							
18	b	surge	Config 8	5.920	1.580	11.5	0.499	74.22	328.34	4.93	2.05	10.1	10.0
19	b	surge	Config 9	5.060	1.470	Arrest							
20	b	surge	Config 9	5.060	1.470	Arrest							
21	a	S&R	Config 1a	2.585	1.290	0.6	0.212	12.41	61.75	2.36	5.08	12.0	29.0
22	a	S&R	Config 1a	2.585	1.290	0.6	0.213	12.44	61.78	2.36	5.58	13.2	27.2
23	a	S&R	Config 2a/2b	2.810	1.065	0.4	0.208	10.40	70.82	3.17	3.79	12.0	28.9
23	b	S&R	Config 2a/2b	2.810	1.065	0.4	0.275	13.74	74.16	3.32	3.37	11.2	25.7
23	c	S&R	Config 2a/2b	2.810	1.065	0.5	0.298	14.91	75.33	3.37	3.55	12.0	27.1
24	a	S&R	Config 2a/2b	2.810	1.065	0.5	0.210	10.49	70.91	3.17	6.09	19.3	29.1
25	a	surge	Config 8	5.920	1.580	0.8	0.173	25.73	279.84	4.20	2.13	9.0	28.9
25	b	surge	Config 8	5.920	1.580	0.5	0.183	27.21	281.33	4.22	2.07	8.7	28.0
26	a	surge	Config 8	5.920	1.580	2.2	0.359	53.51	307.62	4.62	2.88	13.3	14.1
27	b	surge	bounding	5.920	1.580	1.3	0.243	36.20	290.32	4.36	1.76	7.7	22.9
28	b	surge	bounding	5.920	1.580	2.0	0.271	40.31	294.42	4.42	1.92	8.5	19.2
29	b	surge	bounding	5.920	1.580	7.1	0.527	78.39	332.50	4.99	1.47	7.3	10.3
30	b	surge	bounding	5.920	1.580	Arrest							
31	c	S&R	as-built 1	2.585	1.419	35.2	0.369	24.22	73.55	2.50	3.97	10.0	20.0
32	c	S&R	as-built 2	2.585	1.161	7.5	0.417	21.50	70.83	3.07	2.58	7.9	16.9
33	c	S&R	bounding S&R	2.595	1.405	19.8	0.388	25.22	87.87	3.02	3.10	9.4	17.8
34	c	S&R	bounding S&R	2.595	1.405	14.6	0.407	26.50	89.15	3.06	2.86	8.8	16.4
35	c	S&R	bounding S&R	2.810	1.065	2.9	0.447	22.33	82.75	3.70	1.93	7.2	14.8
36	c	S&R	bounding S&R	2.810	1.065	3.6	0.434	21.69	82.11	3.67	2.05	7.5	15.6
37	c	S&R	bounding S&R	2.810	1.065	3.4	0.332	16.59	77.01	3.44	2.32	8.0	17.7
38	c	S&R	bounding S&R	2.810	1.065	3.4	0.331	16.56	76.98	3.44	2.32	8.0	17.7
39	c	S&R	bounding S&R	2.810	1.065	3.4	0.340	16.99	77.41	3.46	2.29	7.9	17.4
40	c	S&R	bounding S&R	2.810	1.065	3.9	0.308	15.38	75.80	3.39	2.44	8.3	18.6
41	c	S&R	bounding S&R	2.810	1.065	2.6	0.357	17.83	78.25	3.50	2.22	7.8	17.0
42	c	S&R	bounding S&R	2.810	1.065	1.8	0.476	23.79	84.21	3.77	1.68	6.3	12.8
43	c	S&R	bounding S&R	2.810	1.065	7.6	0.408	20.41	80.83	3.61	2.27	8.2	17.3
44	c	spray	bounding spray	2.125	0.780	2.9	0.470	12.94	45.11	3.66	2.34	8.6	11.1
45	c	spray	bounding spray	2.125	0.780	48.1	0.417	11.50	43.67	3.54	2.97	10.5	14.1
46	b	surge	bounding surge	5.920	1.580	1.1	0.236	35.14	289.26	4.34	1.74	7.5	23.6
47	b	surge	bounding surge	5.920	1.580	1.5	0.247	36.77	290.88	4.37	1.71	7.5	23.2
48	b	surge	bounding	5.920	1.580	1.2	0.240	35.80	289.91	4.35	1.73	7.5	23.4
49	c	S&R	bounding	2.810	1.065	3.4	0.435	21.74	77.35	3.46	3.96	13.7	3.7
50	b	surge	bounding	5.920	1.580	1.2	0.240	35.80	287.63	4.32	4.37	18.9	3.5
51	b	surge	bounding	5.060	1.470	Arrest							
52	c	S&R	example S&R	2.585	1.290	In Progress							
53	b	surge	example surge	5.920	1.580	In Progress							
S1	a	surge	Config 8	5.920	1.580	Arrest							
S1	b	surge	Config 8	5.920	1.580	1.2	0.489	72.76	326.88	4.91	1.08	5.3	14.6
S2	b	surge	Config 8	5.920	1.580	3.4	0.518	77.12	331.23	4.97	1.37	6.8	11.5
S3	b	surge	Config 8	5.920	1.580	2.2	0.179	26.63	280.74	4.21	2.10	8.8	28.4
S4	b	surge	Config 8	5.920	1.580	N/A							
S5	b	surge	Config 8	5.920	1.580	N/A							
S6	b	surge	Config 8	5.920	1.580	N/A							
S7	b	surge	Config 8	5.920	1.580	N/A							
S8	b	surge	Config 9	5.060	1.470	Arrest							
S9	b	surge	Config 8	5.920	1.580	N/A							

Table 7-5
Sensitivity Matrix Case Through-Wall Crack Results at 1 gpm or Initial Leak Rate if Higher

Case and Step	Fraction Xsection Cracked	Crack Face Force (kips)	Max tot Faxial (kips)	Max Pm Based on CF (ksi)	Support. Pm (ksi)	Support. Pb (thick) (ksi)	Stability Margin Factor	Time since TW (hrs)	Time since TW (days)	Leak Rate (gpm @ 70°F)
01cS13	0.466	27.27	76.61	2.93	6.55	12.78	2.24	2726	114	1.045
02cS14	0.470	27.48	76.82	2.93	6.79	12.25	2.31	3416	142	1.048
03cS15	0.472	27.59	76.93	2.94	7.04	11.70	2.40	4358	182	1.074
04cS12	0.462	30.06	92.71	3.18	6.95	12.52	2.18	2567	107	1.002
05cS14	0.466	30.30	92.95	3.19	7.50	11.47	2.35	4328	180	1.004
06cS13	0.471	23.53	83.96	3.75	6.37	12.95	1.70	752	31	1.043
07cS21	0.491	24.53	84.95	3.80	7.64	9.62	2.01	1682	70	1.016
08cS12	0.459	29.88	78.91	2.71	5.79	14.32	2.14	2268	94	1.090
09cS16	0.470	30.56	79.58	2.73	6.84	12.21	2.50	5489	229	1.076
10cS20	0.497	15.42	43.30	3.12	6.46	10.13	2.07	4690	195	1.007
11cS22	0.506	15.69	43.57	3.14	6.54	9.38	2.08	6251	260	1.044
12cS17	0.507	13.96	46.13	3.74	6.95	8.82	1.86	2639	110	1.034
13cS18	0.512	14.10	46.28	3.75	7.29	8.03	1.94	3120	130	1.026
14cSna	Arrest									
15cSna	Arrest									
16cSna	Arrest									
17aSna	Arrest									
17bS00	0.243	36.18	290.30	4.36	7.44	23.17	1.71	0	0	2.553
18aSna	Arrest									
18bS00	0.523	77.93	332.04	4.98	8.94	8.75	1.79	0	0	2.706
19bSna	Arrest									
20bSna	Arrest									
21aS16	0.255	14.95	64.28	2.46	10.86	25.26	4.42	1762	73	1.018
22aS17	0.260	15.23	64.57	2.47	11.78	23.31	4.78	1894	79	1.059
23aS13	0.248	12.38	72.80	3.26	10.92	25.59	3.36	1194	50	1.012
23bS02	0.311	15.55	75.98	3.40	10.13	22.75	2.98	194	8	1.065
23cS16	0.369	18.44	78.87	3.53	10.53	22.76	2.99	1799	75	1.003
24aS15	0.255	12.75	73.17	3.27	13.86	20.25	4.24	1607	67	1.030
25aS00	0.175	25.99	280.10	4.20	8.92	28.78	2.12	0	0	5.281
25bS00	0.184	27.43	281.54	4.23	8.69	27.90	2.06	0	0	5.725
26aS00	0.364	54.17	308.29	4.63	13.12	13.84	2.83	0	0	1.177
27bS00	0.246	36.58	290.69	4.36	7.61	22.68	1.74	0	0	2.500
28bS00	0.355	52.84	306.96	4.61	7.71	16.74	1.67	0	0	2.426
29bS00	0.537	79.95	334.07	5.02	6.91	9.65	1.38	0	0	4.052
30bSna	Arrest									
31cS16	0.471	30.90	80.23	2.73	6.73	12.37	2.46	5656	236	1.061
32cS11	0.471	24.32	73.66	3.19	6.26	12.86	1.96	1847	77	1.020
33cS13	0.460	29.94	92.59	3.18	6.98	12.60	2.20	3374	141	1.002
34cS12	0.468	30.45	93.09	3.20	6.77	12.16	2.12	2346	98	1.065
35cS06	0.480	23.98	84.40	3.77	6.13	12.38	1.62	617	26	1.096
36cS08	0.471	23.56	83.98	3.75	6.35	12.89	1.69	857	36	1.048
37cS19	0.419	20.96	81.38	3.64	6.67	13.98	1.83	1024	43	1.007
38cS19	0.420	21.02	81.44	3.64	6.67	13.98	1.83	1035	43	1.005
39cS19	0.424	21.22	81.64	3.65	6.62	13.82	1.81	993	41	1.031
40cS22	0.410	20.47	80.89	3.62	6.82	14.39	1.89	1151	48	1.013
41cS18	0.434	21.68	82.10	3.67	6.51	13.53	1.77	957	40	1.030
42cS00	0.487	24.36	84.79	3.79	5.96	12.00	1.57	0	0	1.065
43cS09	0.452	22.58	83.00	3.71	6.82	14.01	1.84	1035	43	1.001
44cS09	0.528	14.55	46.72	3.79	6.41	8.04	1.69	1228	51	1.012
45cS19	0.501	13.81	45.98	3.73	7.14	9.10	1.91	3284	137	1.063
46bS00	0.240	35.69	289.80	4.35	7.45	23.25	1.71	0	0	4.628
47bS00	0.248	36.95	291.07	4.37	7.42	23.03	1.70	0	0	1.378
48bS00	0.243	21.53	275.65	4.14	7.18	23.54	1.73	0	0	2.423
49cS30	0.502	25.10	80.71	3.61	10.30	2.68	2.85	4004	167	1.006
50bS00	0.243	36.19	288.03	4.32	18.70	3.42	4.33	0	0	1.067
51bS00	Arrest									
52cSna	In Progress									
53bSna	In Progress									
S1aSna	Arrest									
S1bS00	0.496	73.89	328.00	4.92	5.08	14.01	1.03	0	0	7.393
S2bS00	0.529	78.83	332.95	5.00	6.38	10.72	1.28	0	0	4.866
S3bS00	0.188	28.04	282.15	4.24	8.61	27.58	2.03	0	0	2.427
S4bSna*	0.400	59.53	313.64	4.71	6.75	19.44	1.43	167	7	2.553
S5bSna*	0.400	59.53	313.64	4.71	6.95	20.02	1.48	167	7	2.553
S6bSna*	0.400	59.53	313.64	4.71	6.10	17.57	1.29	167	7	2.553
S7bSna*	0.453	67.50	321.61	4.83	6.95	19.52	1.44	167	7	2.553
S8bSna	Arrest									
S9bS00	0.322	47.95	302.06	4.53	7.24	21.65	1.60	0	0	2.553

*Stability results after 7 days of detectable leakage for these multiple flaw cases only (S4b through S7b)

Table 7-6
Sensitivity Matrix Case Through-Wall Crack Results at Load Margin Factor of 1.2

Case and Step	Fraction Xsection Cracked	Crack Face Force (kips)	Max tot Faxial (kips)	Max Pm Based on CF (ksi)	Support. Pm (ksi)	Support. Pb (thick) (ksi)	Stability Margin Factor	Time since TW (hrs)	Time since TW (days)	Time since 1 gpm (hrs)	Time since 1 gpm (days)	Leak Rate (gpm @ 70°F)
01cS36	0.568	33.21	82.55	3.15	3.80	6.89	1.21	5350	223	2623	109	5.806
02cS37	0.574	33.61	82.95	3.17	3.85	6.43	1.21	6255	261	2839	118	5.886
03cS38	0.580	33.93	83.26	3.18	3.88	5.95	1.22	7357	307	2998	125	6.221
04cS34	0.558	36.29	98.94	3.40	4.19	7.07	1.23	5252	219	2685	112	5.219
05cS37	0.574	37.36	100.01	3.44	4.15	5.90	1.21	7615	317	3288	137	5.806
06cS41	0.529	26.45	86.87	3.88	4.70	9.23	1.21	1741	73	989	41	4.042
07cS62	0.573	28.64	89.06	3.98	4.79	5.75	1.20	3389	141	1706	71	5.436
08cS34	0.553	36.00	85.03	2.92	3.58	8.21	1.23	4643	193	2375	99	5.575
09cS41	0.586	38.10	87.13	2.99	3.63	5.93	1.21	8942	373	3453	144	6.561
10cS38	0.582	18.05	45.92	3.31	3.98	5.89	1.20	6450	269	1760	73	3.805
11cS39	0.587	18.21	46.09	3.32	4.09	5.54	1.23	7996	333	1745	73	3.698
12cS33	0.575	15.83	48.00	3.89	4.66	5.69	1.20	3801	158	1163	48	3.538
13cS34	0.582	16.04	48.21	3.91	4.83	5.10	1.23	4414	184	1295	54	3.486
14cSna	Arrest											
15cSna	Arrest											
16cSna	Arrest											
17aSna	Arrest											
17bS73	0.331	49.30	303.42	4.55	5.45	16.24	1.20	829	35	829	35	69.279
18aSna	Arrest											
18bS21	0.591	88.03	342.15	5.14	6.15	5.84	1.20	1022	43	1022	43	15.794
19bS32	Arrest											
20bSna	Arrest											
21aS20	0.270	15.78	65.12	2.49	10.47	24.04	**4.21**	2272	95	509	>>21	1.277
22aS20	0.271	15.84	65.18	2.49	11.46	22.47	**4.60**	2295	96	400	>>17	1.247
23aS21	0.278	13.91	74.34	3.32	10.05	23.06	**3.02**	2085	87	891	>>37	1.666
23bS33	0.517	25.84	86.26	3.86	4.64	9.18	1.20	4354	181	4160	173	6.442
23cS20	0.387	19.34	79.76	3.57	10.08	21.57	**2.83**	2296	96	497	>>21	1.272
24aS19	0.270	13.48	73.90	3.30	13.31	19.26	**4.03**	2115	88	508	>>21	1.307
25aS75	0.330	49.10	303.22	4.55	5.49	16.36	1.21	1868	78	1868	78	98.510
25bS70	0.329	49.02	303.13	4.55	5.50	16.39	1.21	1746	73	1746	73	92.157
26aS09	0.383	57.09	311.21	4.67	12.24	12.79	**2.62**	958	40	958	>>40	5.401
27bS68	0.337	50.12	304.24	4.57	5.50	15.64	1.20	919	38	919	38	70.433
28bS30	0.424	63.08	317.20	4.76	5.71	12.00	1.20	655	27	655	27	28.752
29bS08	0.560	83.38	337.50	5.07	6.07	8.38	1.20	267	11	267	11	8.491
30bSna	Arrest											
31cS40	0.588	38.59	87.92	2.99	3.58	6.00	1.20	9163	382	3507	146	6.433
32cS31	0.552	28.50	77.84	3.37	4.07	7.91	1.21	3616	151	1769	74	4.799
33cS35	0.560	36.46	99.10	3.40	4.11	6.94	1.21	6338	264	2964	123	5.268
34cS34	0.561	36.51	99.16	3.41	4.11	6.93	1.21	4709	196	2363	98	5.516
35cS18	0.528	26.38	86.80	3.88	4.76	9.35	1.23	1393	58	776	32	3.672
36cS24	0.529	26.43	86.86	3.88	4.70	9.24	1.21	1870	78	1013	42	3.989
37cS57	0.503	25.16	85.58	3.83	4.58	9.14	1.20	2193	91	1170	49	4.971
38cS58	0.504	25.21	85.63	3.83	4.58	9.12	1.20	2239	93	1204	50	4.983
39cS55	0.504	25.22	85.64	3.83	4.60	9.16	1.20	2117	88	1124	47	4.873
40cS63	0.501	25.05	85.47	3.82	4.59	9.16	1.20	2424	101	1273	53	5.182
41cS52	0.508	25.39	85.81	3.84	4.60	9.14	1.20	2009	84	1052	44	4.698
42cS15	0.534	26.71	87.13	3.90	4.66	9.12	1.20	927	39	927	39	2.970
43cS30	0.525	26.26	86.68	3.88	4.68	9.21	1.21	2170	90	1135	47	4.843
44cS18	0.581	16.01	48.18	3.91	4.80	5.84	1.23	2125	89	898	37	2.641
45cS37	0.573	15.78	47.95	3.89	4.69	5.73	1.21	4397	183	1113	46	3.861
46bS44	0.330	49.07	303.18	4.55	5.48	16.33	1.20	1755	73	1755	73	73.583
47bS86	0.332	49.44	303.56	4.56	5.45	16.22	1.20	540	22	540	22	65.023
48bS76	0.335	29.71	283.82	4.26	5.12	16.32	1.20	941	39	941	39	70.050
49cS86	0.628	31.37	86.98	3.89	4.67	1.13	1.20	7474	311	3470	145	8.567
50bS150	0.492	73.20	325.04	4.88	6.14	0.99	1.26	7034	293	7034	293	191.428
51bS48	Arrest											
52cSna	In Progress											
53bSna	In Progress											
S1aSna	Arrest											
S1bSna	Not Applicable -- @ TW Load Factor = 1.08 (1.03 at first leakage) / 2 days from TW to load factor of 1.0											
S2bS01	0.537	79.90	334.01	5.01	6.14	10.28	1.22	82	3 (Note 1)	82	3 (Note 1)	6.001
S3bS93	0.330	49.16	303.27	4.55	5.47	16.30	1.20	1772	74	1772	74	87.487
S4bSna	Not Applicable											
S5bSna												
S6bSna												
S7bSna												
S8bSna	Arrest											
S9bSna	0.415	61.74	315.86	4.74	5.17	14.81	**1.09**	829	35 (Note 2)	829	35 (Note 2)	69.279

Note 1: Case S2b showed 4 days from initial leakage (at 4.9 gpm) until load margin factor of 1.20 based on interpolation.
Note 2: Case S9b showed 29 days from initial leakage (at 2.6 gpm) until load margin factor of 1.20 based on interpolation.

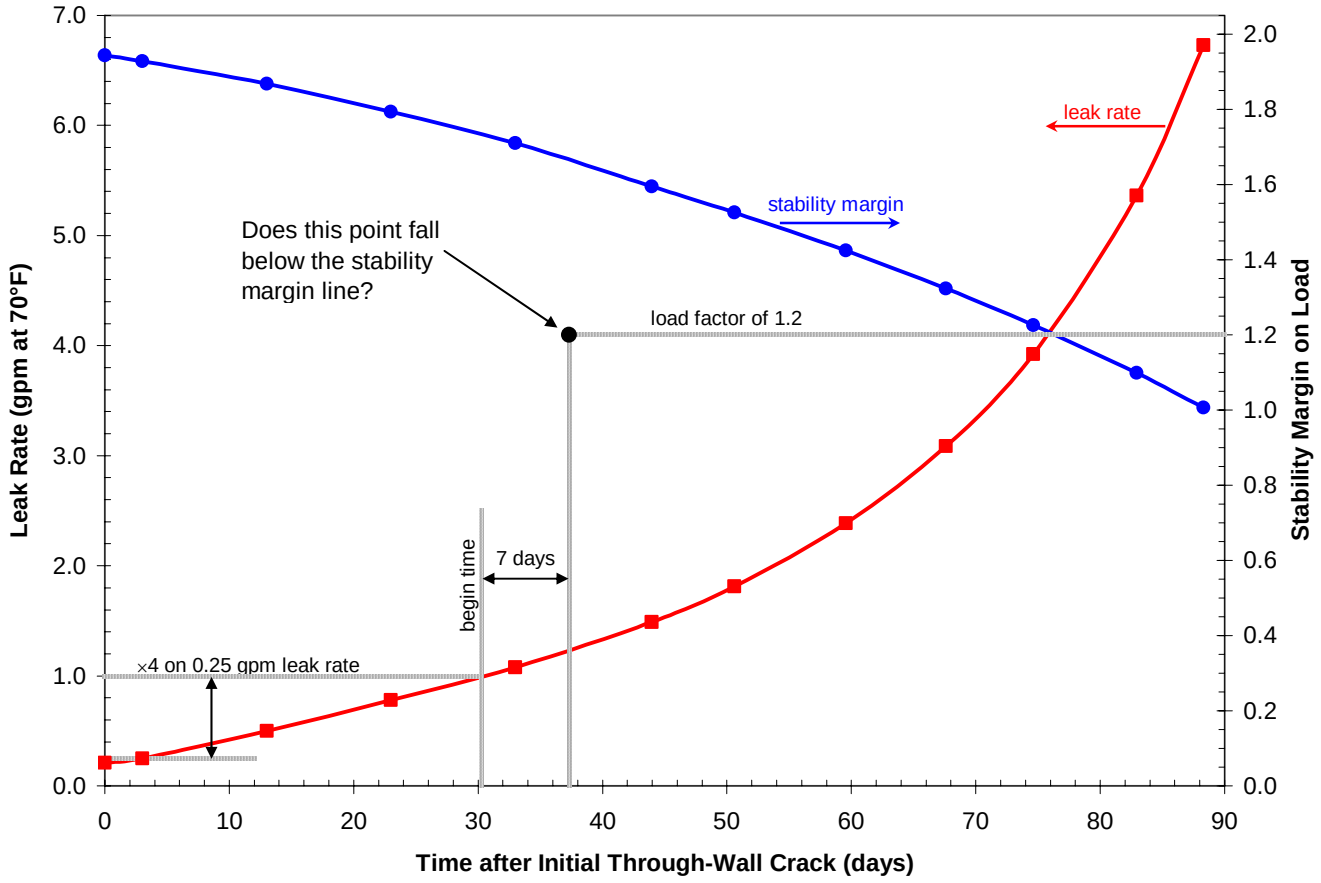

Figure 7-1
Illustration of Approach for Hypothetical Leak Rate and Crack Stability Results

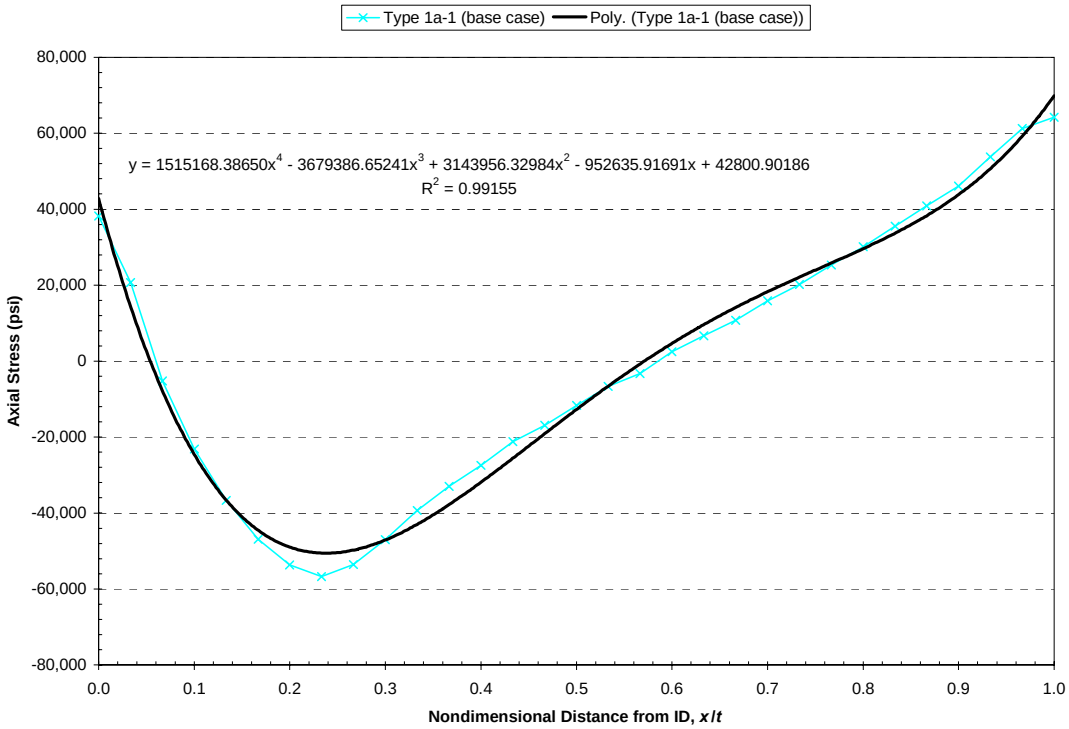

Figure 7-2
WRS Fit for Type 1 Safety and Relief Nozzle Including Effect of Stainless Steel Weld (with normal operating temperature applied)

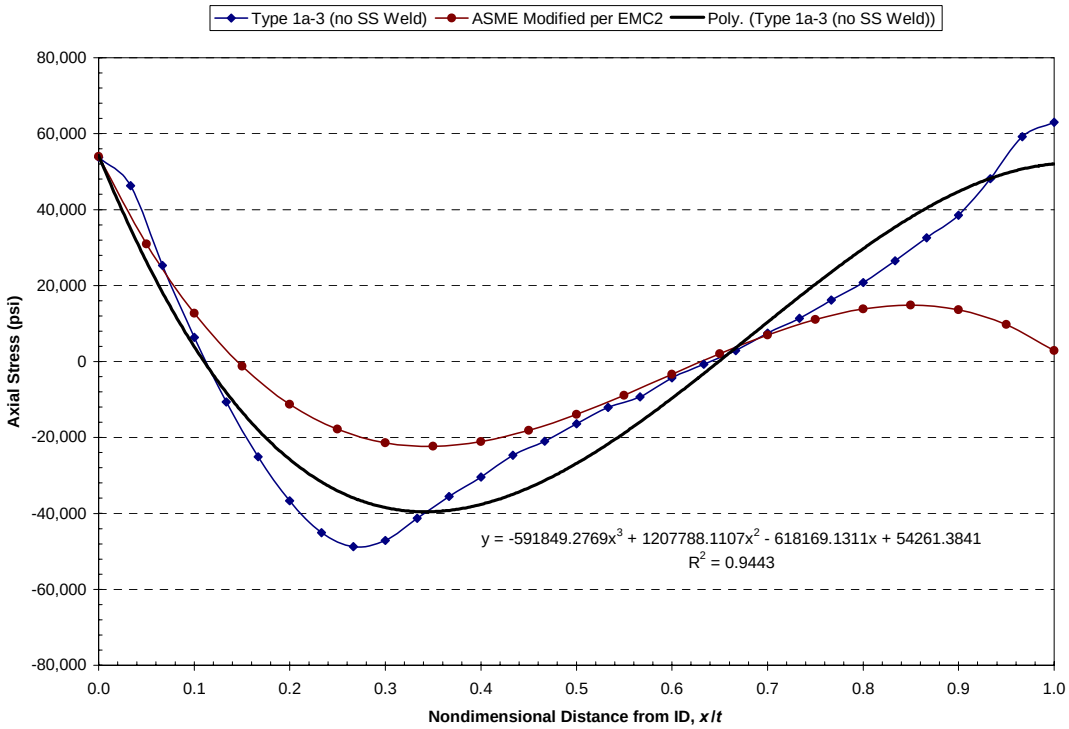

Figure 7-3
WRS Cubic Fit for Type 1 Safety and Relief Nozzle Excluding Effect of Stainless Steel Weld (with normal operating temperature applied)

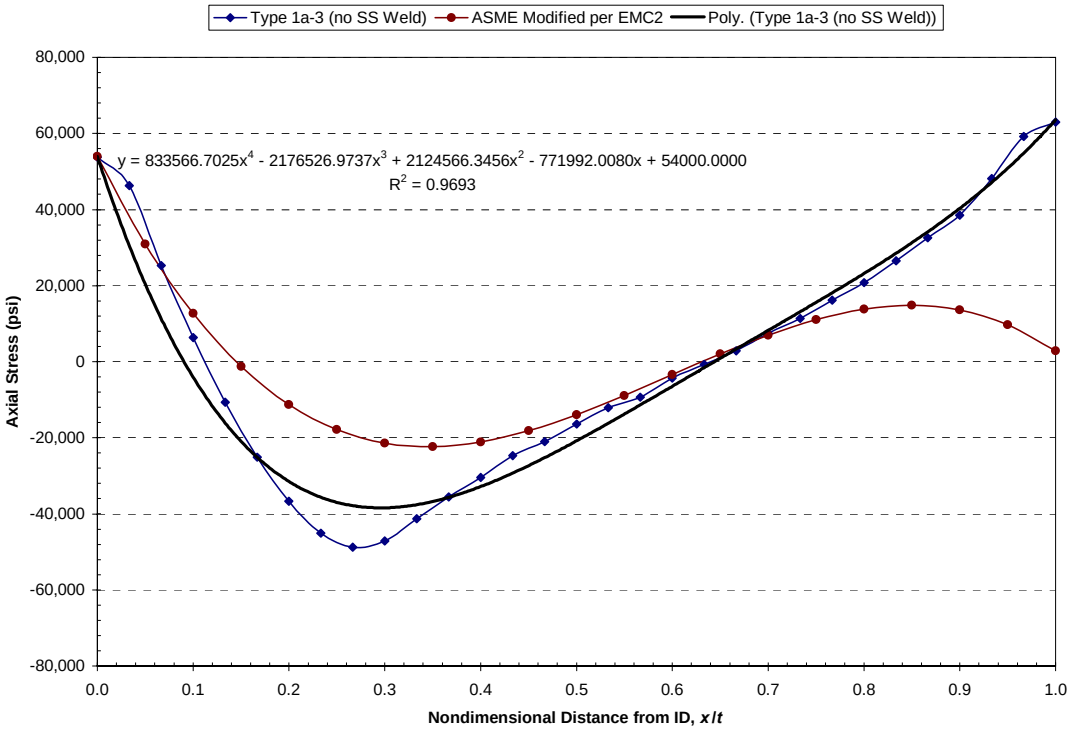

Figure 7-4
WRS Quartic Fit for Type 1 Safety and Relief Nozzle Excluding Effect of Stainless Steel Weld with σ_0 set to 54 ksi (with normal operating temperature applied)

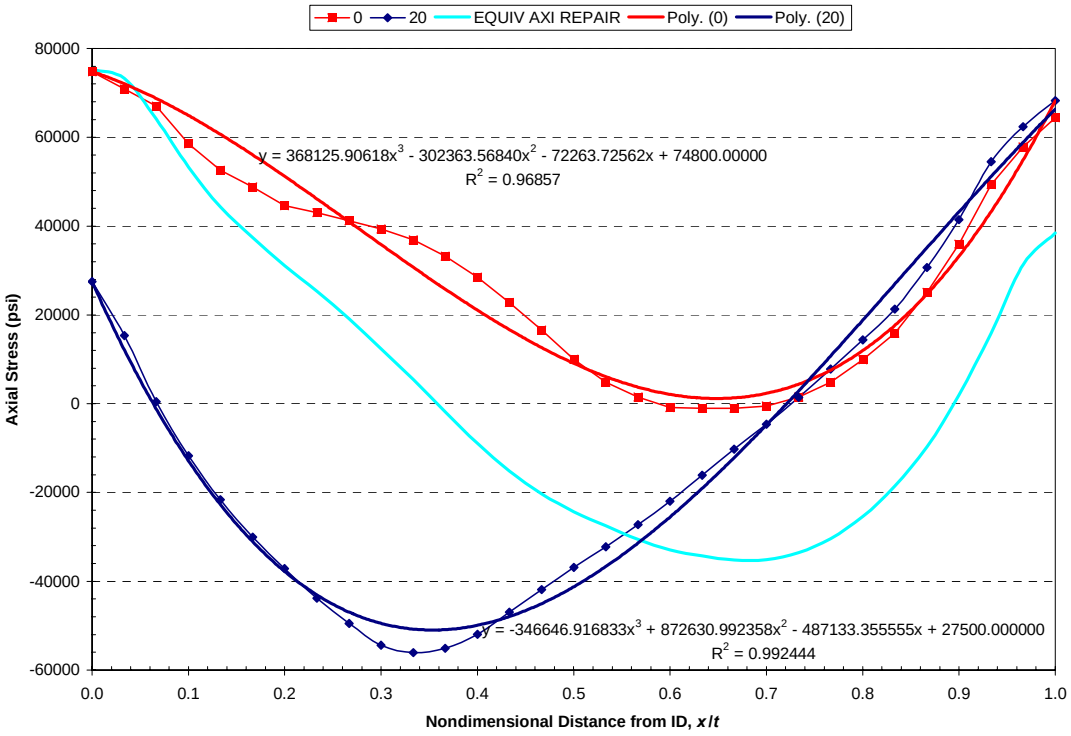

Figure 7-5
WRS Fits for Safety and Relief Nozzle with 3D ID Repair Excluding Effect of Stainless Steel Weld with σ_0 set to 27.5 ksi and 74.8 ksi (with normal operating temperature applied)

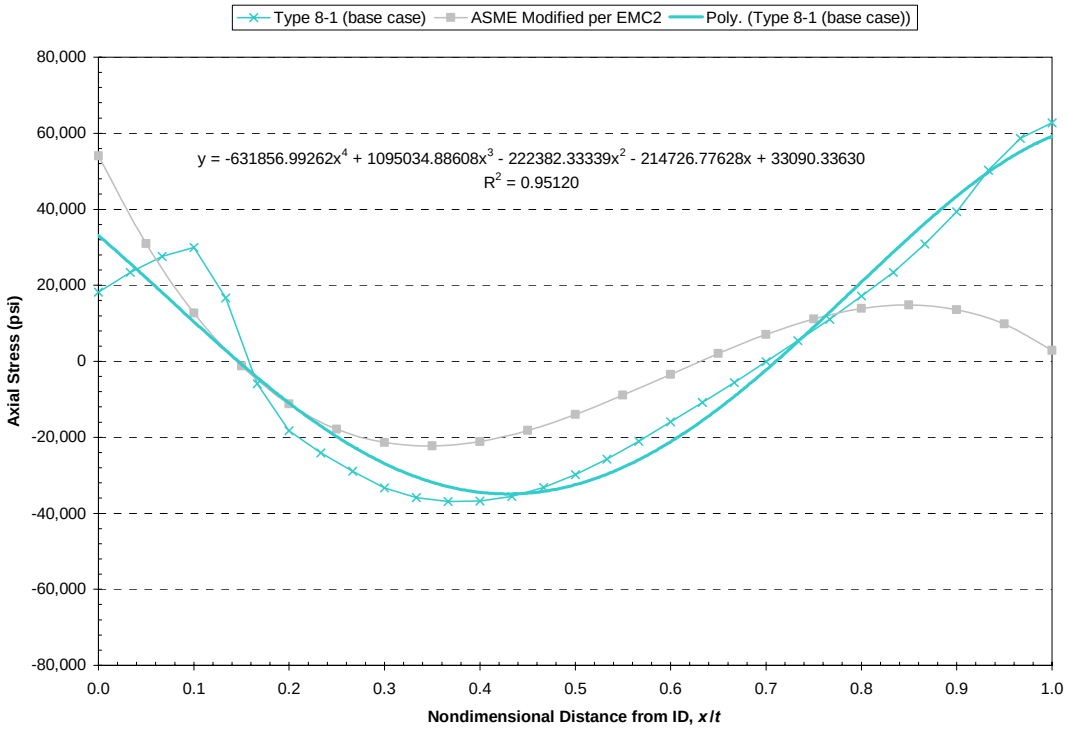

Figure 7-6
WRS Fit for Type 8 Surge Nozzle Including Effect of Stainless Steel Weld (with normal operating temperature applied)

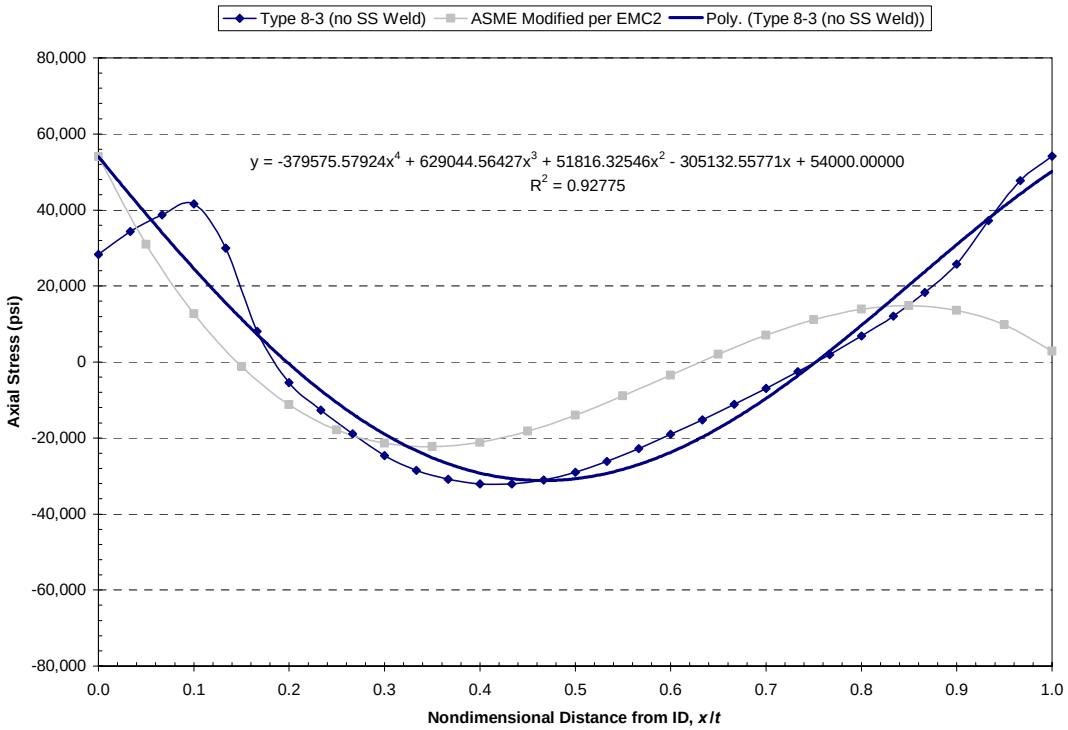

Figure 7-7
WRS Fit for Type 8 Surge Nozzle Excluding Effect of Stainless Steel Weld with σ_0 set to 54.0 ksi (with normal operating temperature applied)

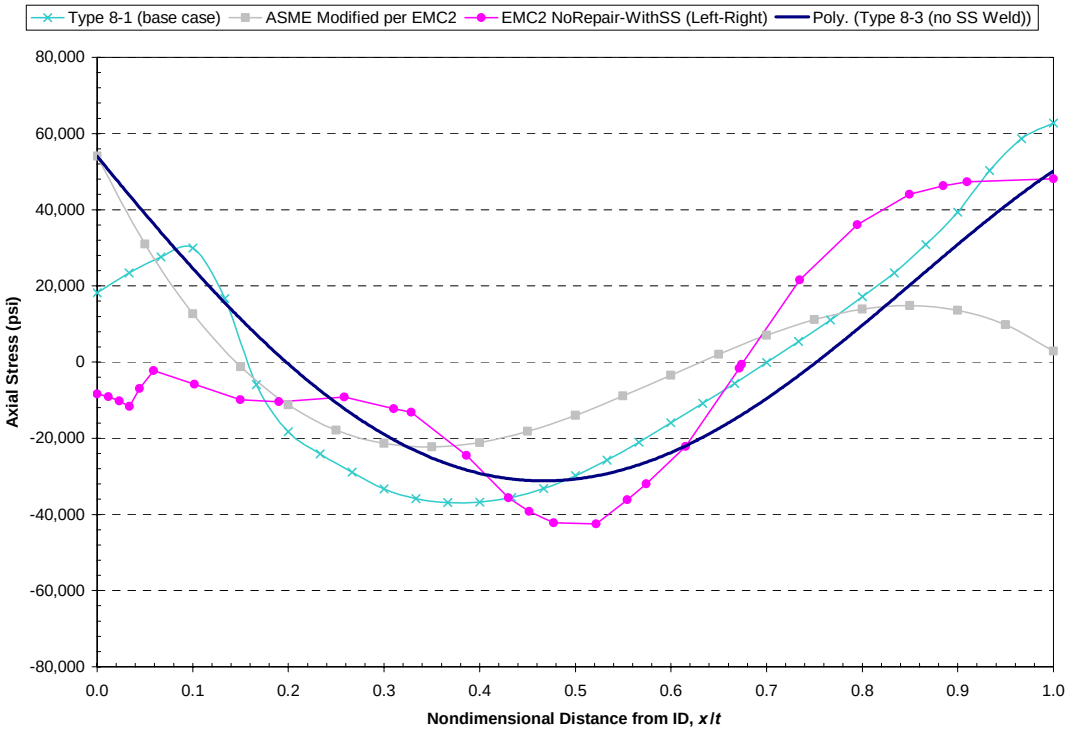

Figure 7-8
WRS Fit for Type 8 Surge Nozzle Excluding Effect of Stainless Steel Weld (Applied in Case 17b) Compared to DEI and EMC^2 WRS FEA Results Including Effect of Stainless Steel Weld

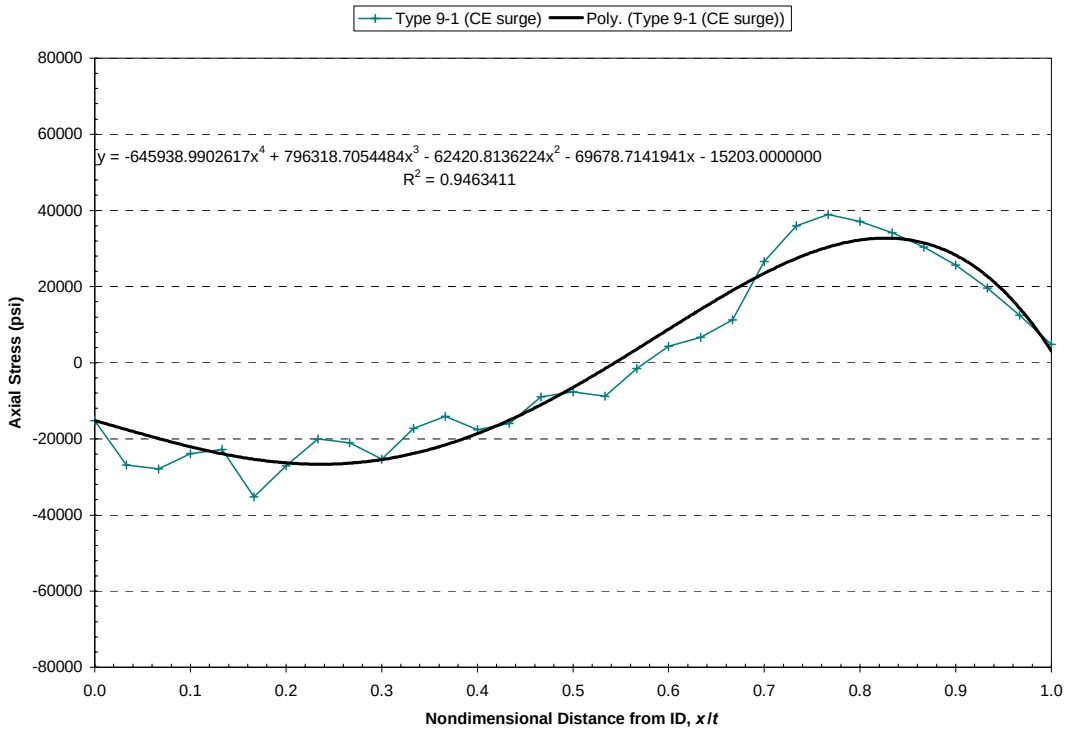

Figure 7-9
WRS Fit for Type 9 Surge Nozzle Excluding Effect of Stainless Steel Weld with σ_0 set to -15.2 ksi (with normal operating temperature applied)

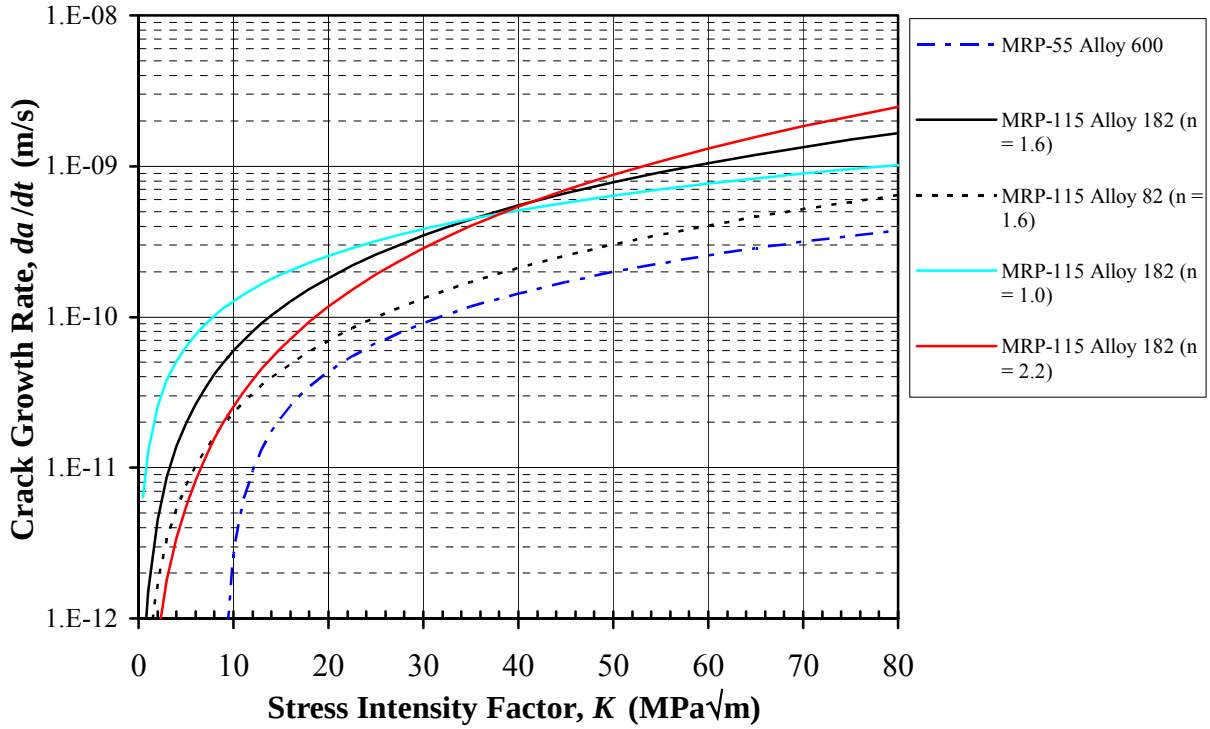

Figure 7-10
MRP-115 Deterministic Crack Growth Rate Equation for Alloy 82 and 182 (best-fit K-exponent of 1.6) and Newly Developed Curves for Alloy 182 with 5th and 95th Percentile K-Exponents (n = 1.0 and 2.2, respectively)

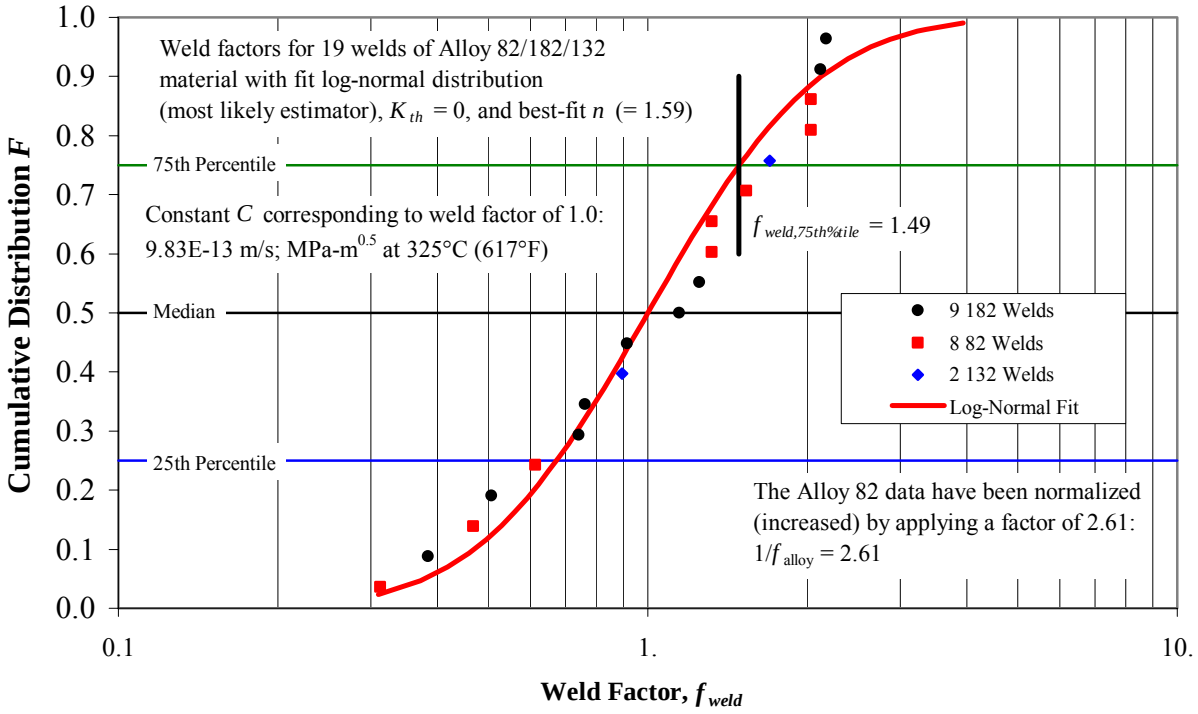

Figure 7-11
Weld Factor Fit Used to Develop Power-Law Constant for Best-Fit K-Exponent (1.59)

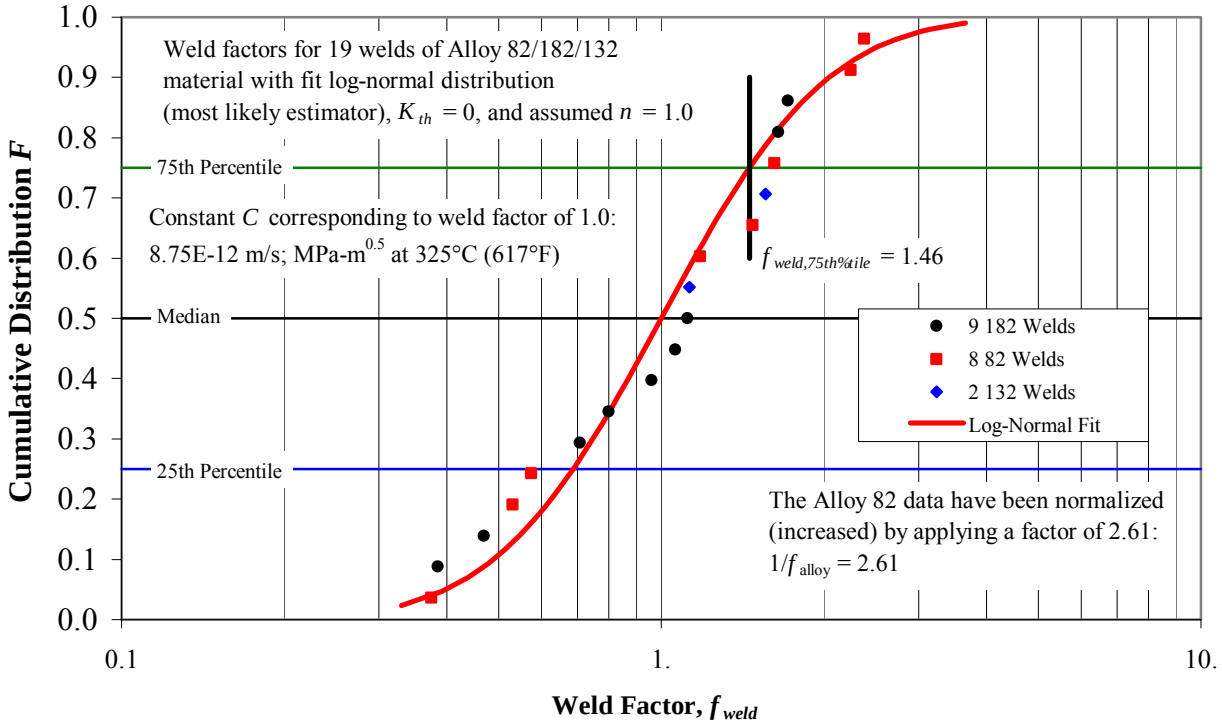

Figure 7-12
Weld Factor Fit Used to Develop Power-Law Constant for 5th Percentile K-Exponent (1.0)

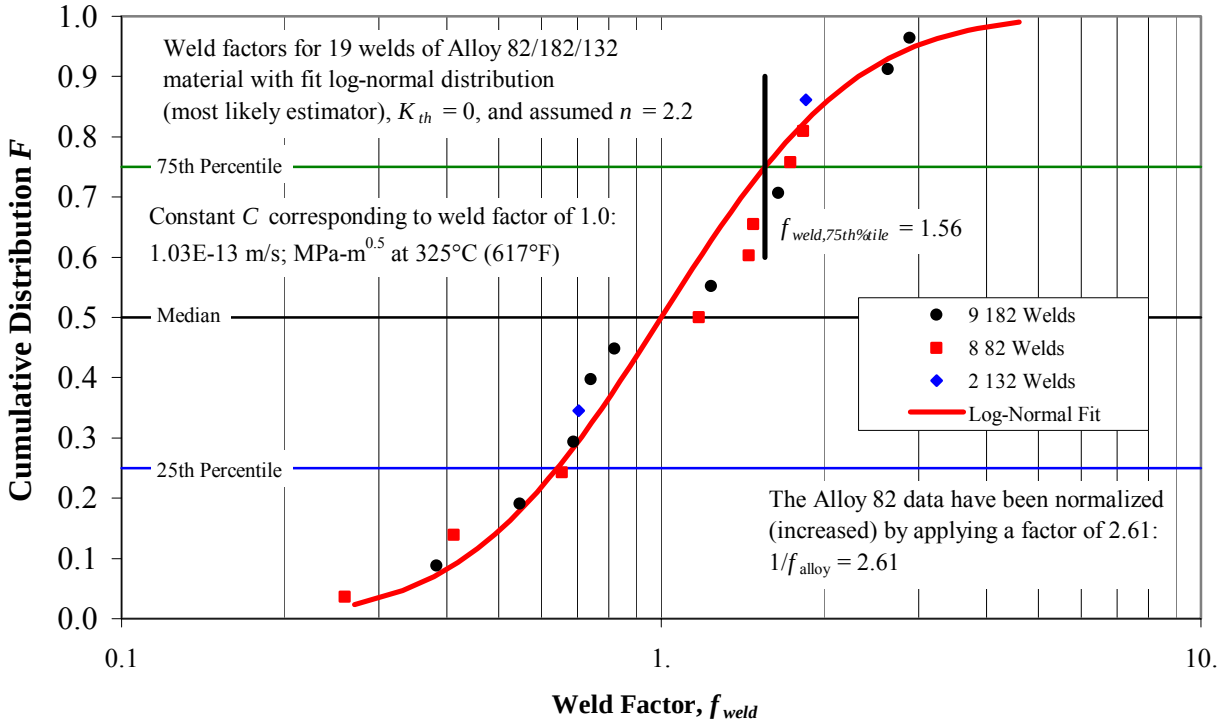

Figure 7-13
Weld Factor Fit Used to Develop Power-Law Constant for 95th Percentile K-Exponent (2.2)

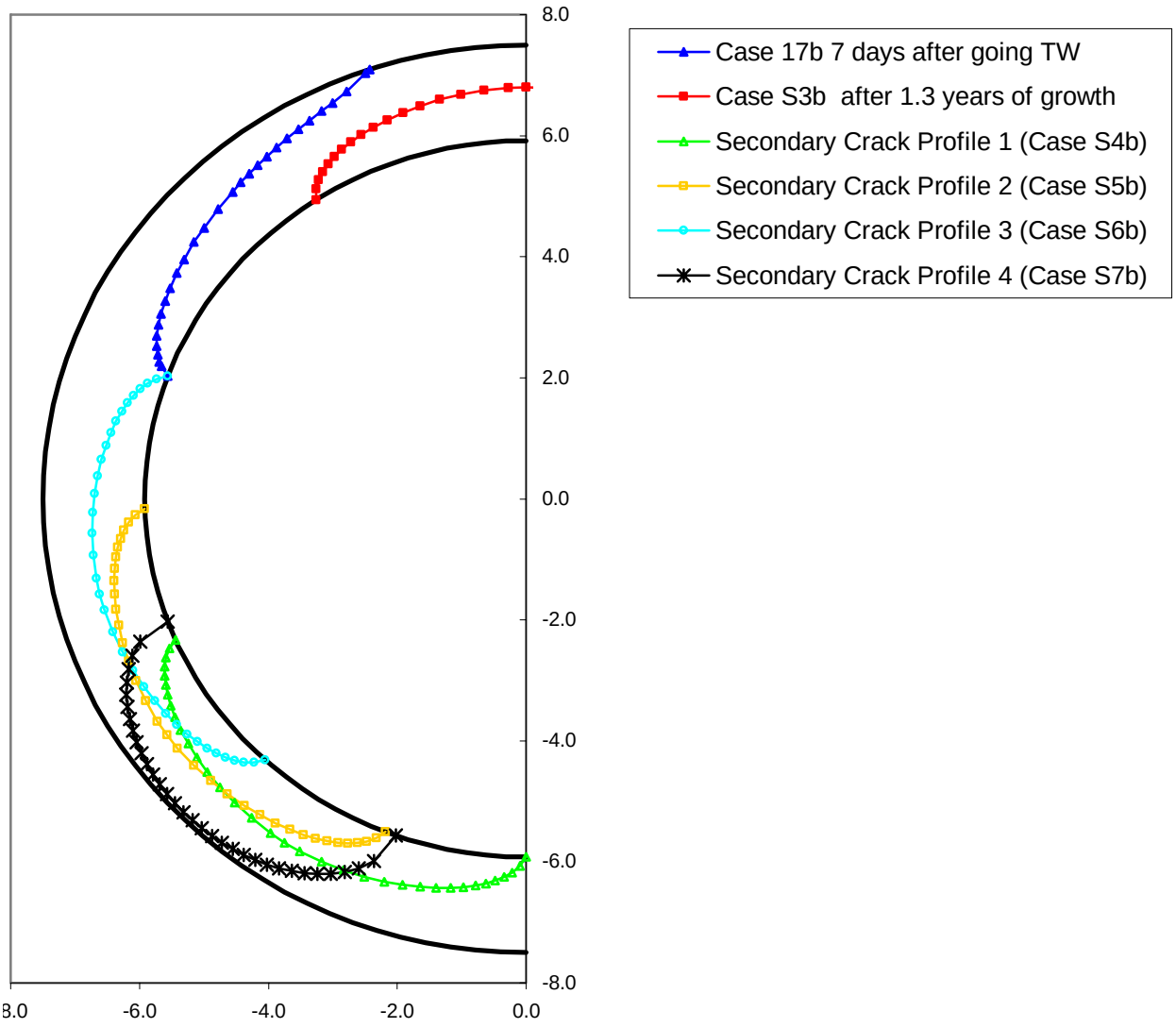

Figure 7-14
Profiles of Pairs of Additional Cracks Applied in Stability Calculations for Cases S4b through S7b Based on Case 17b

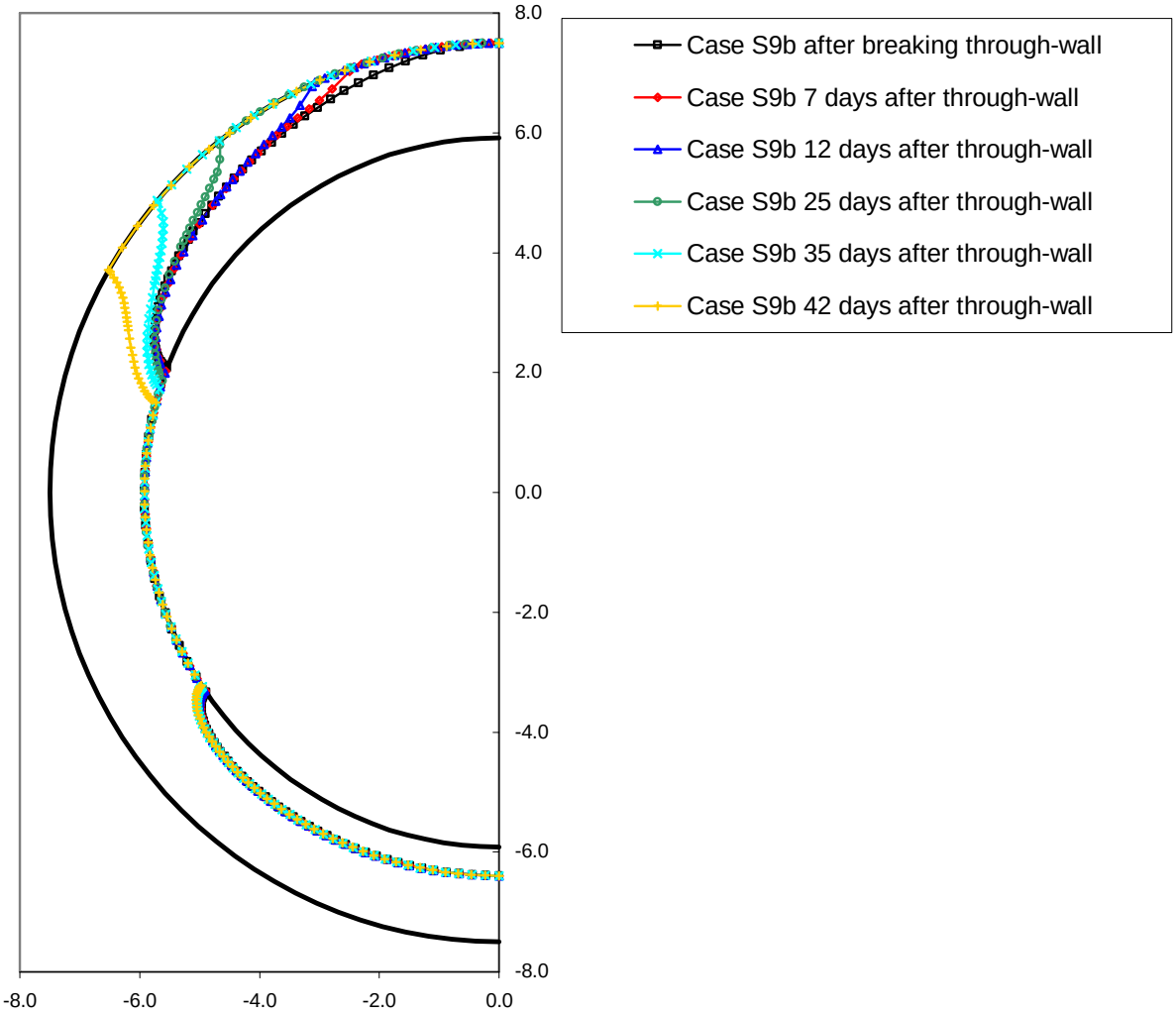

Figure 7-15
Case S9b Growth Progression Based on Individual Growth of Initial 21:1 Aspect Ratio 26% through-wall Flaws Placed at Top and Bottom of Weld Cross Section

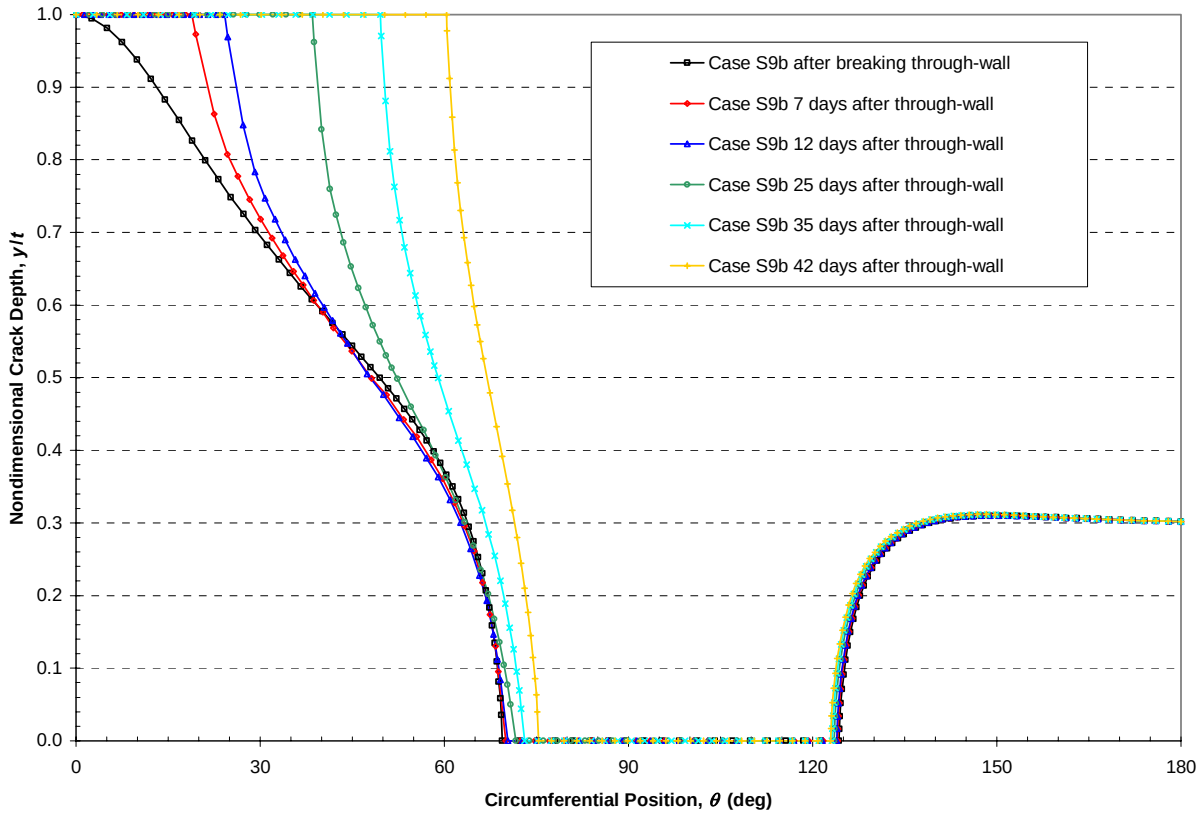

Figure 7-16
Case S9b Growth Progression Shown in Polar Coordinates

Figure 7-17
Example Crack Meshes for a Variety of Sensitivity Cases and Crack Types

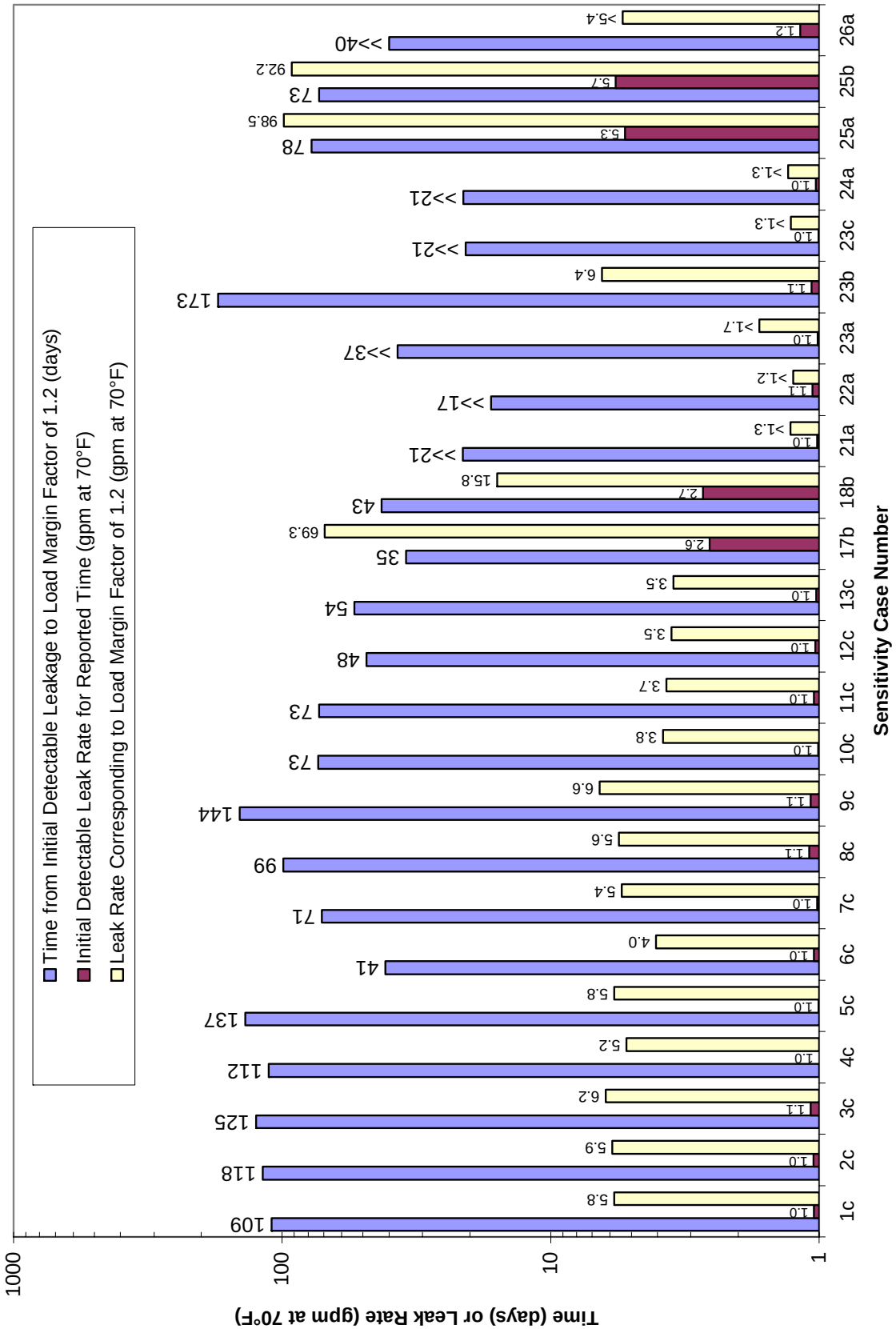

Figure 7-18
Key Time and Leak Rate Results for Geometry and Load Base Cases Including ID Repair

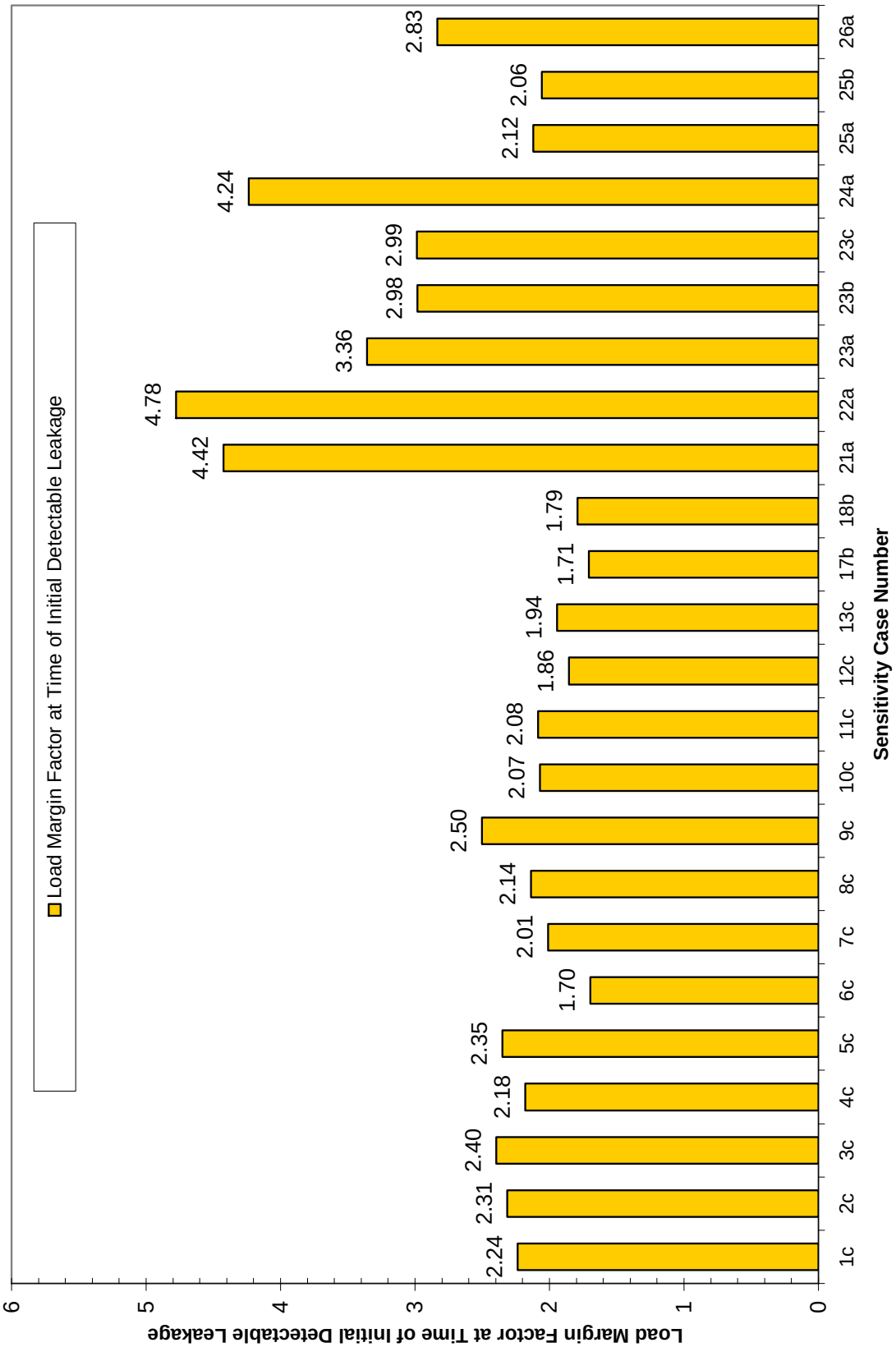

Figure 7-19
Key Load Margin Factor Results for Geometry and Load Base Cases Including ID Repair

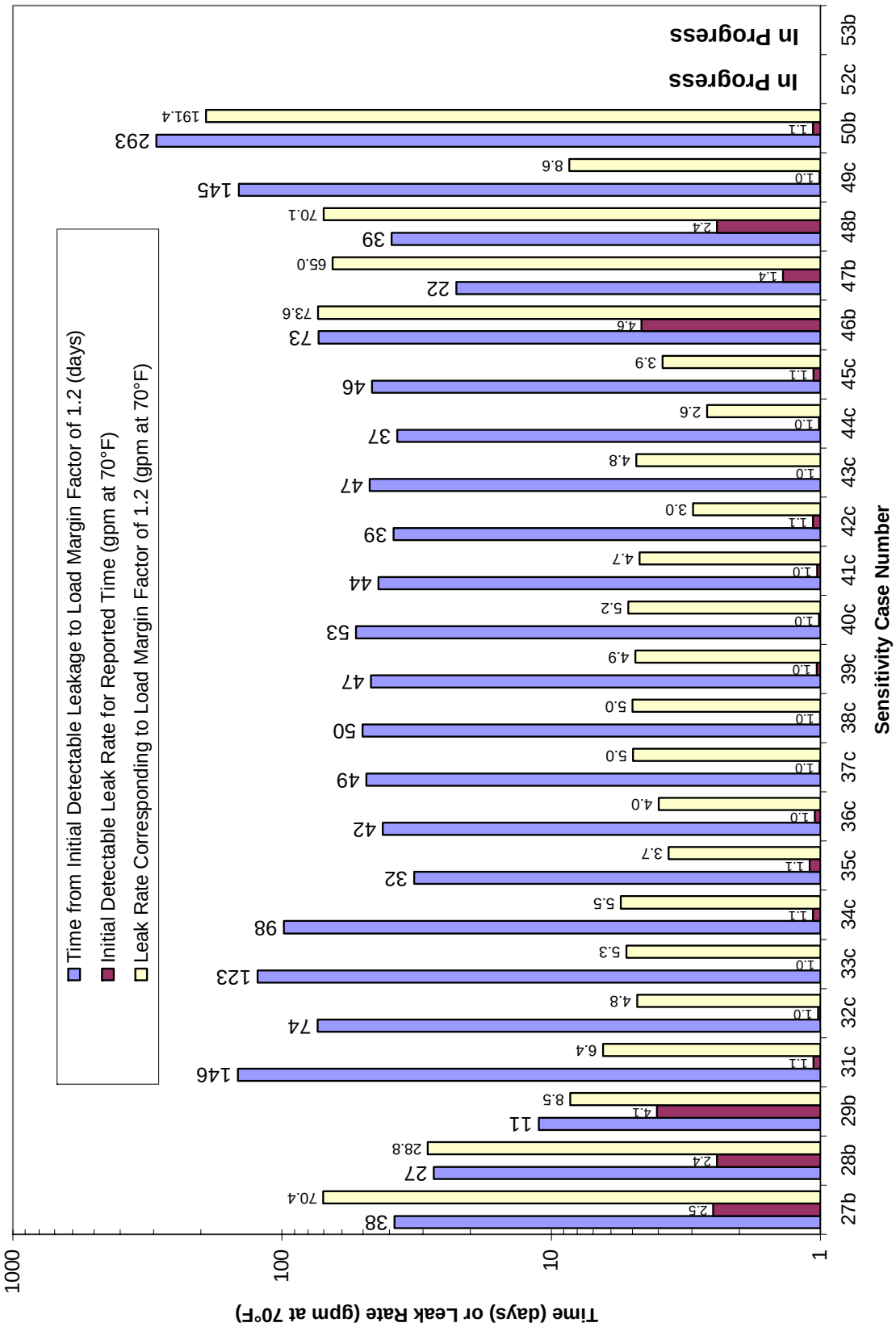

Figure 7-20
Key Time and Leak Rate Results for Other Main Cases

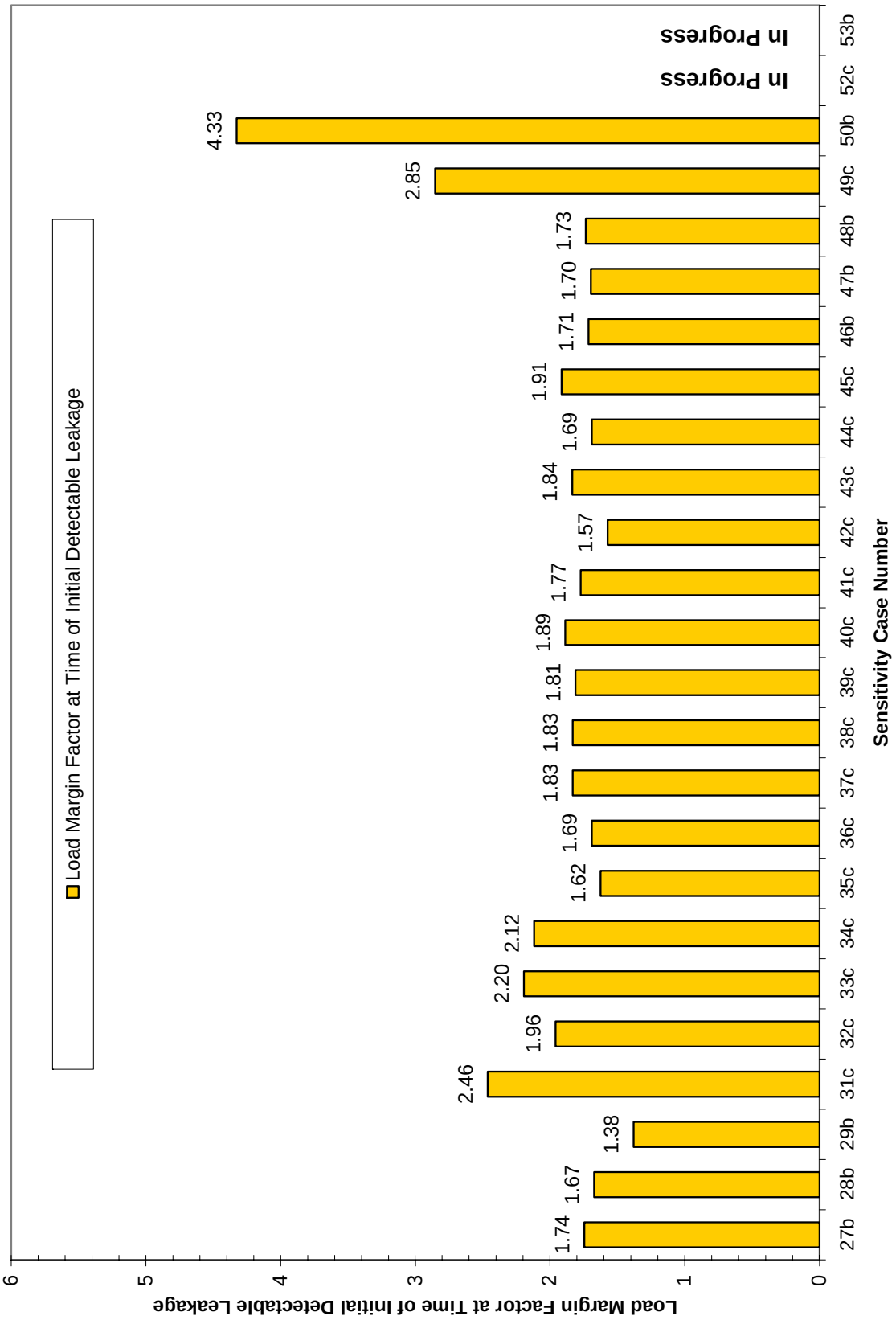

Figure 7-21
Key Load Margin Factor Results for Other Main Cases

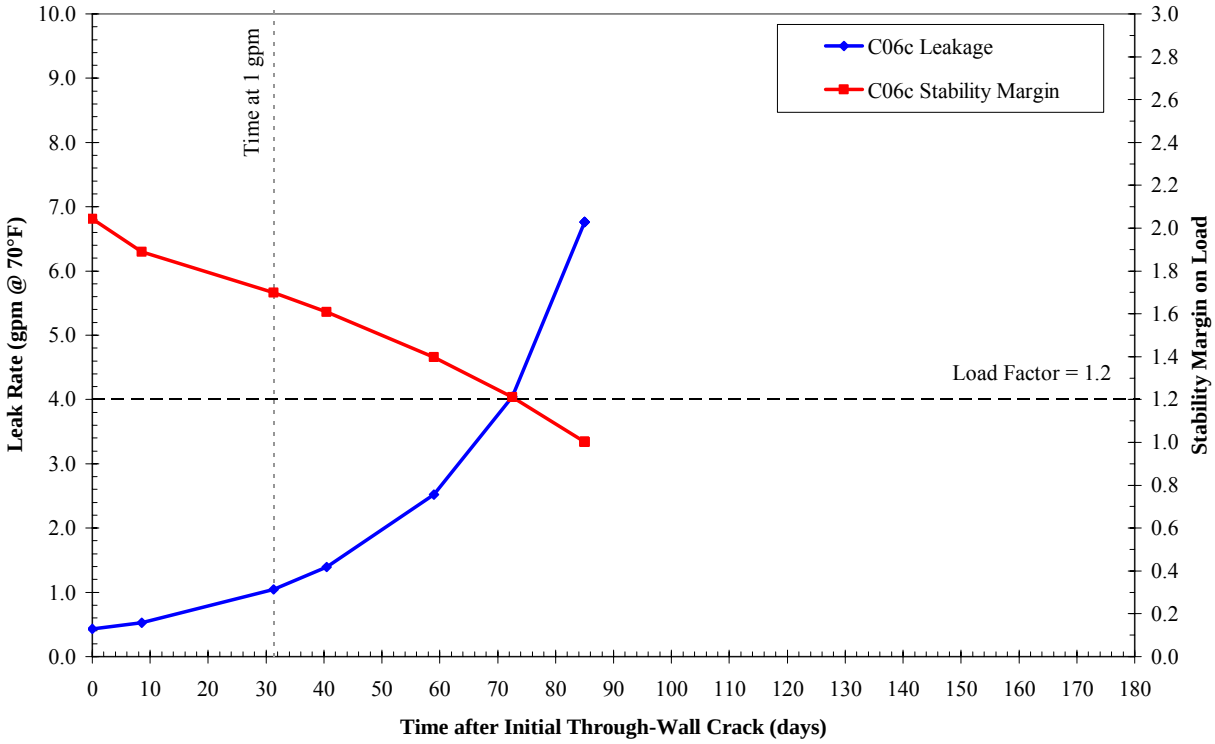

Figure 7-22
Leak Rate and Load Margin Factor as a Function of Time—Case 6c

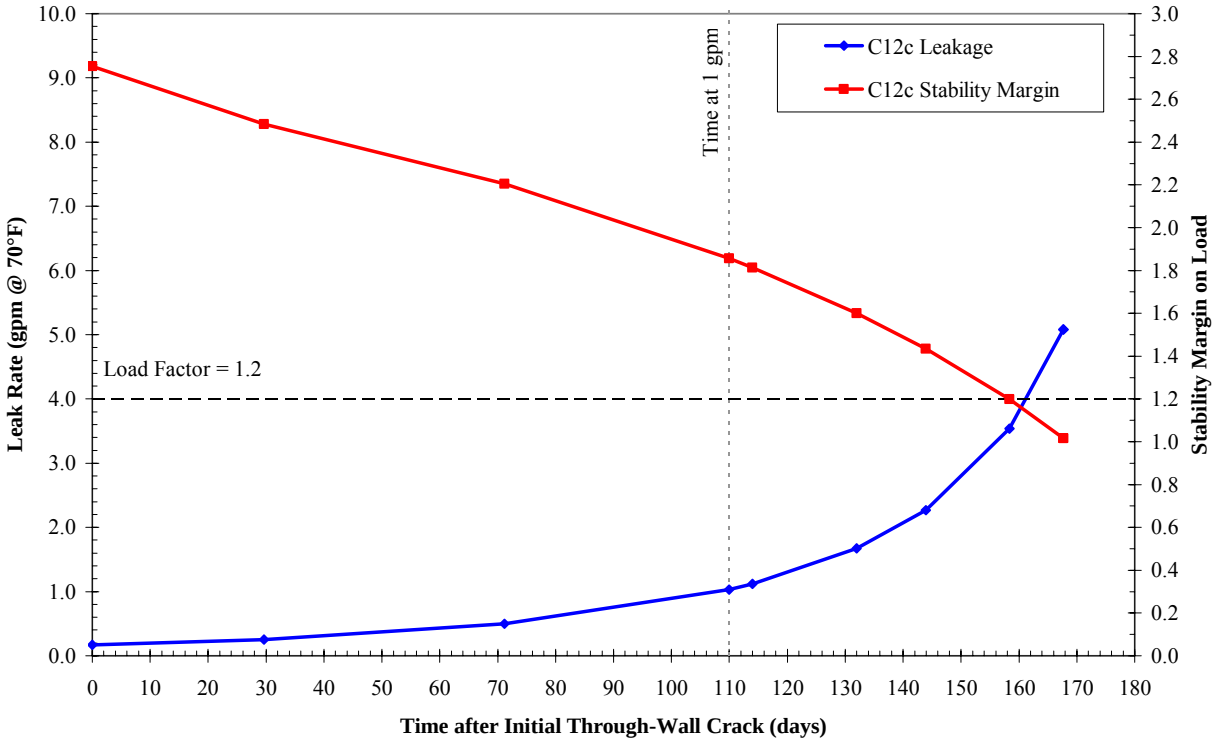

Figure 7-23
Leak Rate and Load Margin Factor as a Function of Time—Case 12c

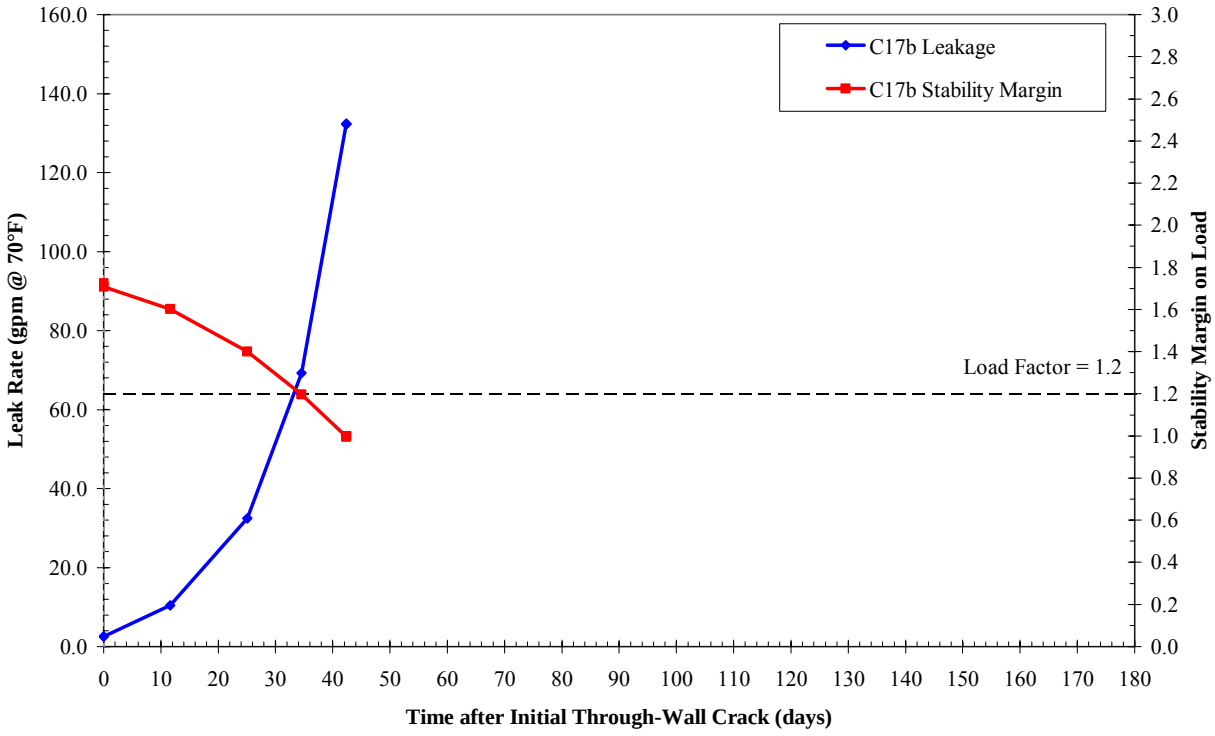

Figure 7-24
Leak Rate and Load Margin Factor as a Function of Time—Case 17b

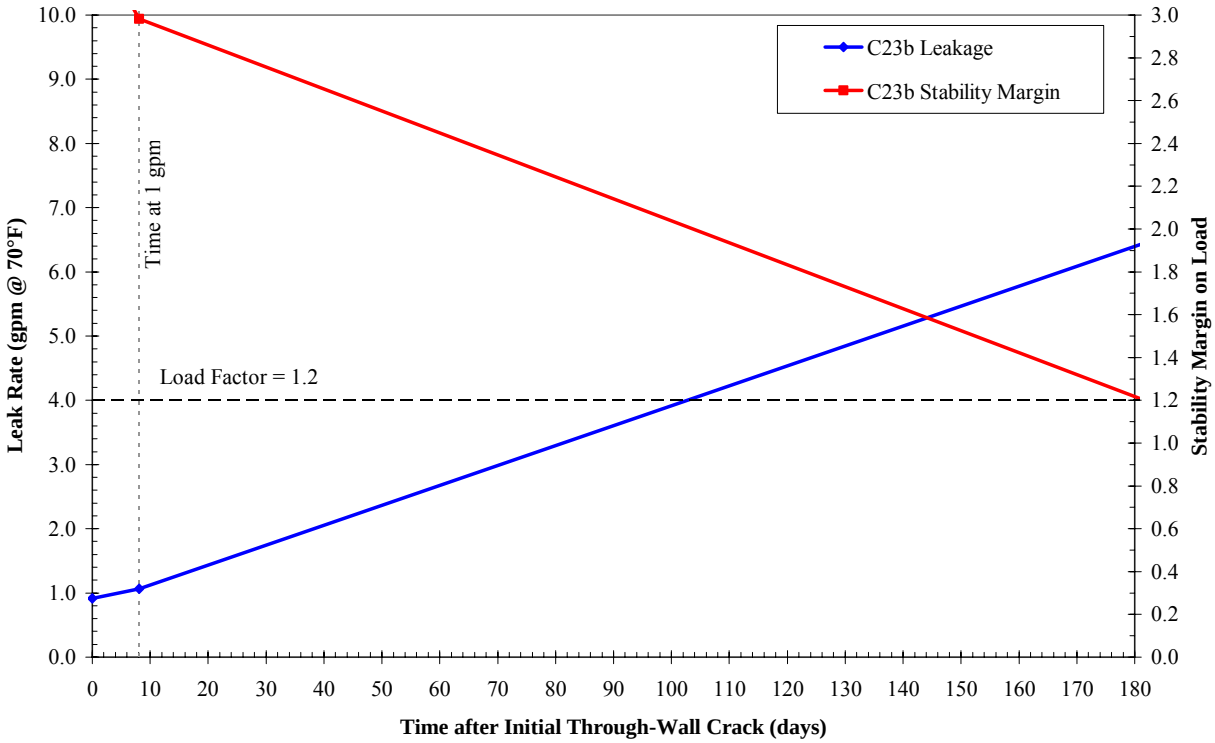

Figure 7-25
Leak Rate and Load Margin Factor as a Function of Time—Case 23b

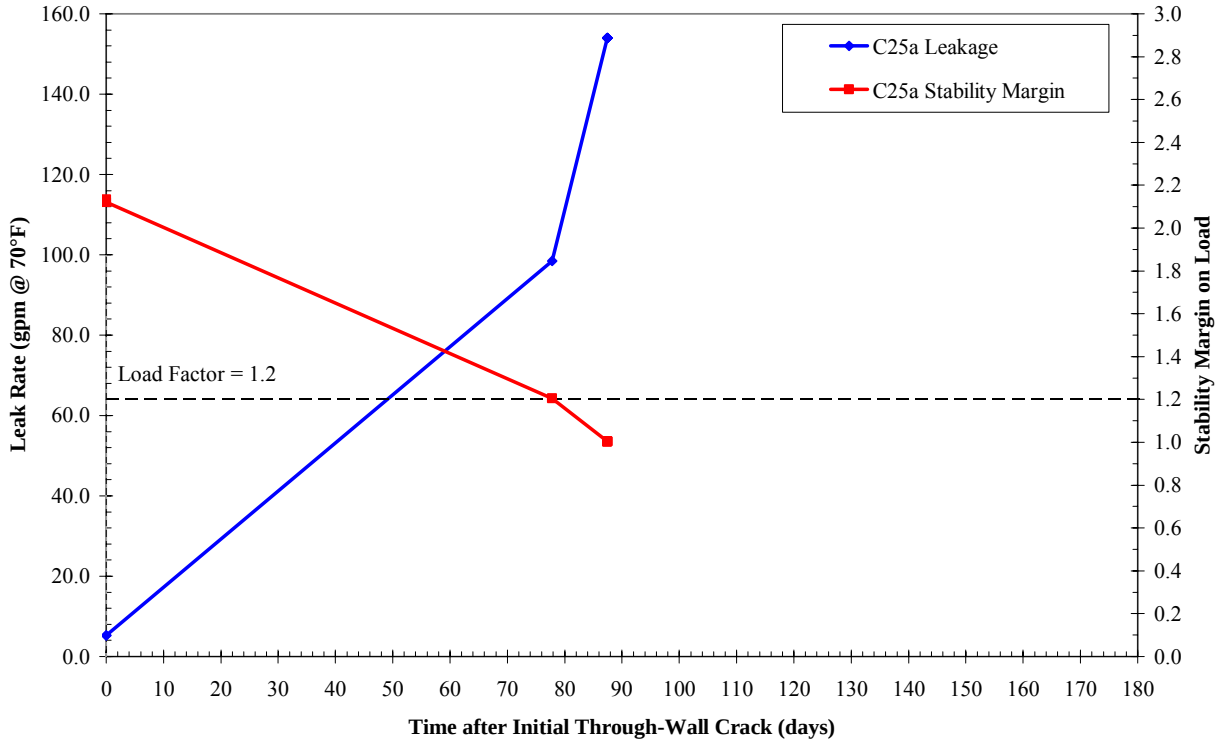

Figure 7-26
Leak Rate and Load Margin Factor as a Function of Time—Case 25a

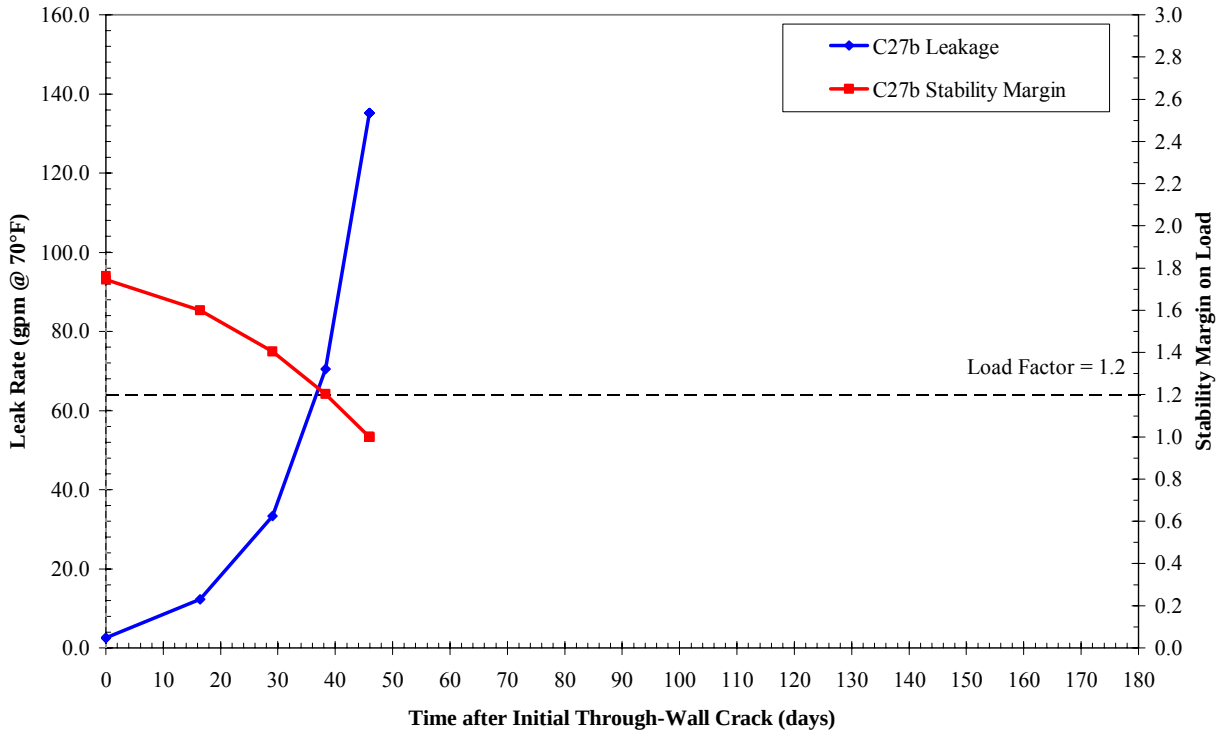

Figure 7-27
Leak Rate and Load Margin Factor as a Function of Time—Case 27b

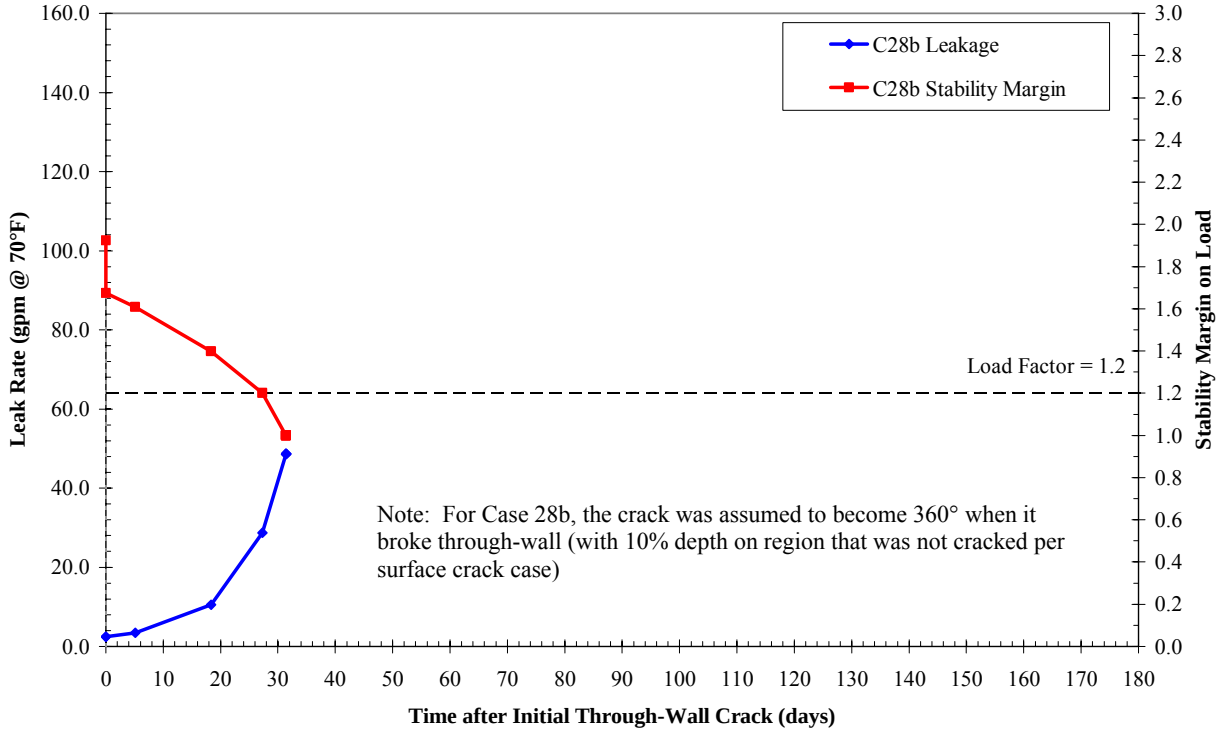

Figure 7-28
Leak Rate and Load Margin Factor as a Function of Time—Case 28b

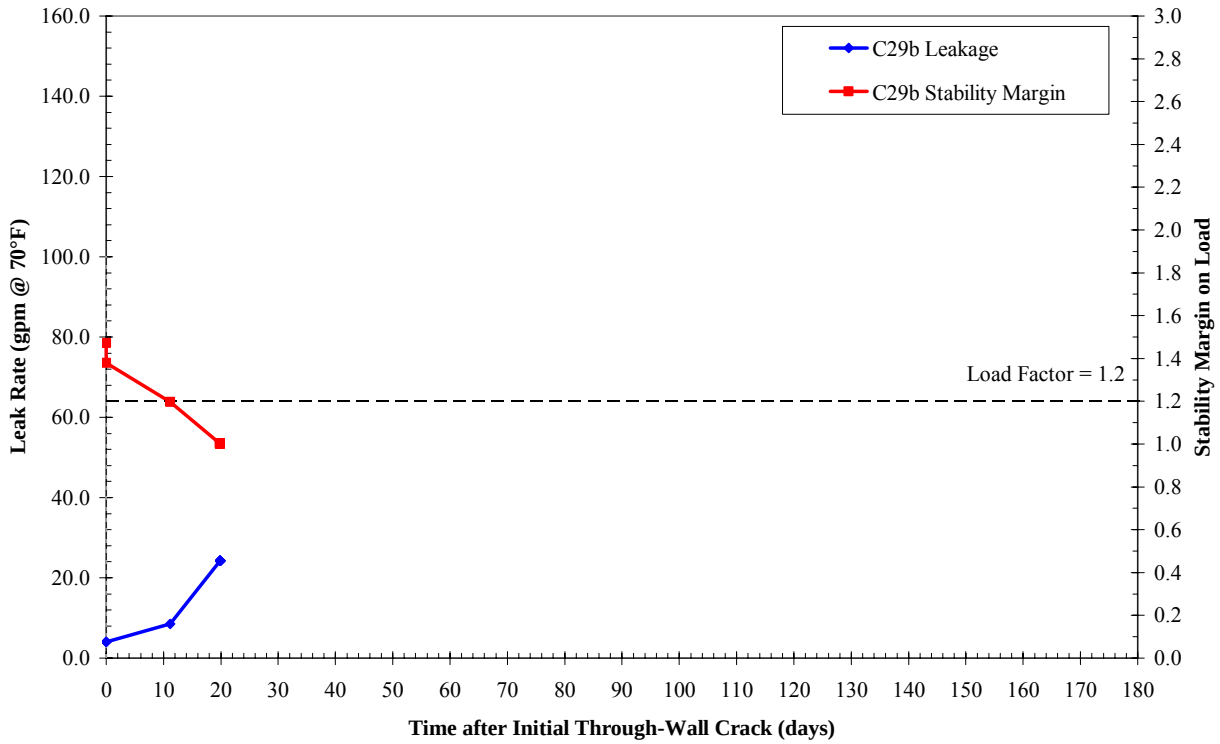

Figure 7-29
Leak Rate and Load Margin Factor as a Function of Time—Case 29b

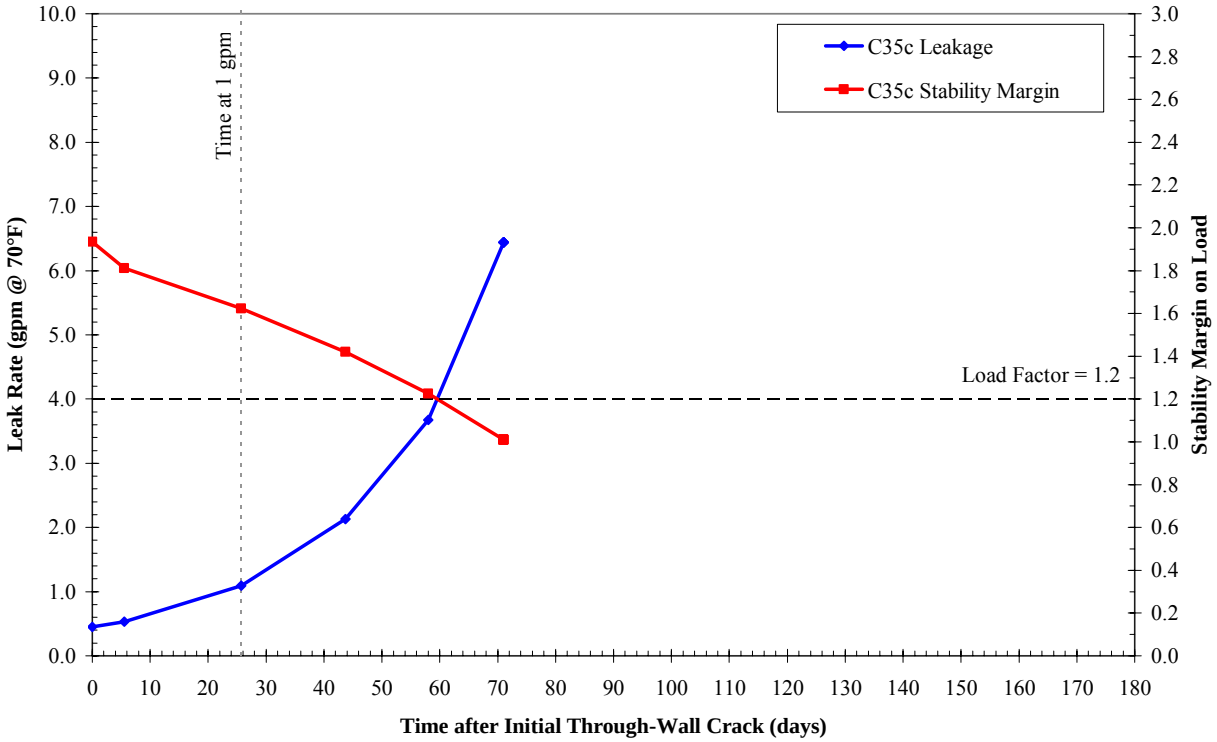

Figure 7-30
Leak Rate and Load Margin Factor as a Function of Time—Case 35c

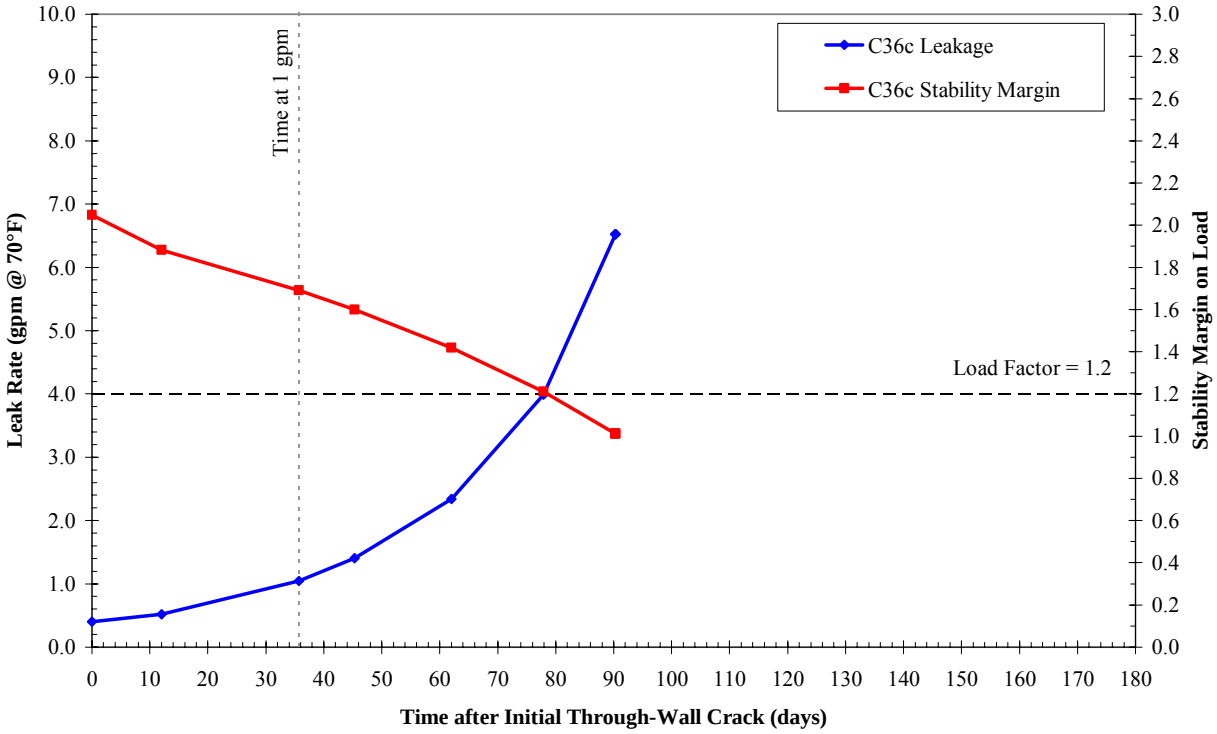

Figure 7-31
Leak Rate and Load Margin Factor as a Function of Time—Case 36c

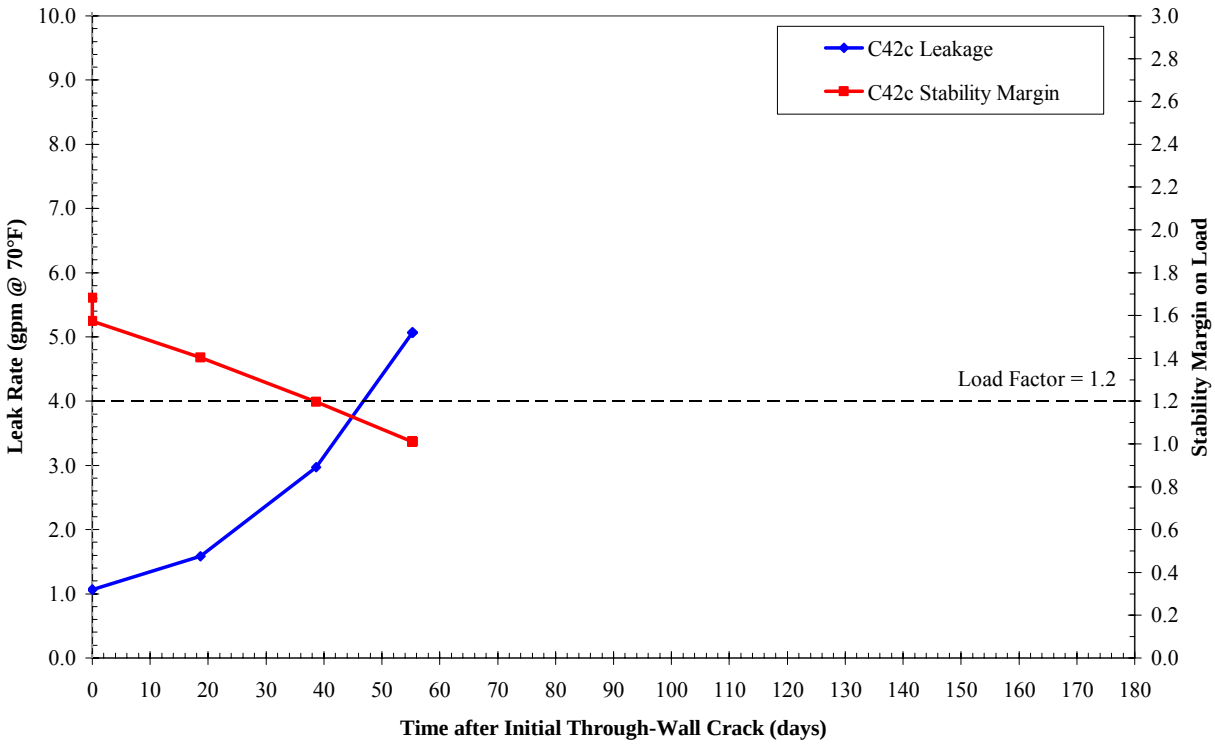

Figure 7-32
Leak Rate and Load Margin Factor as a Function of Time—Case 42c

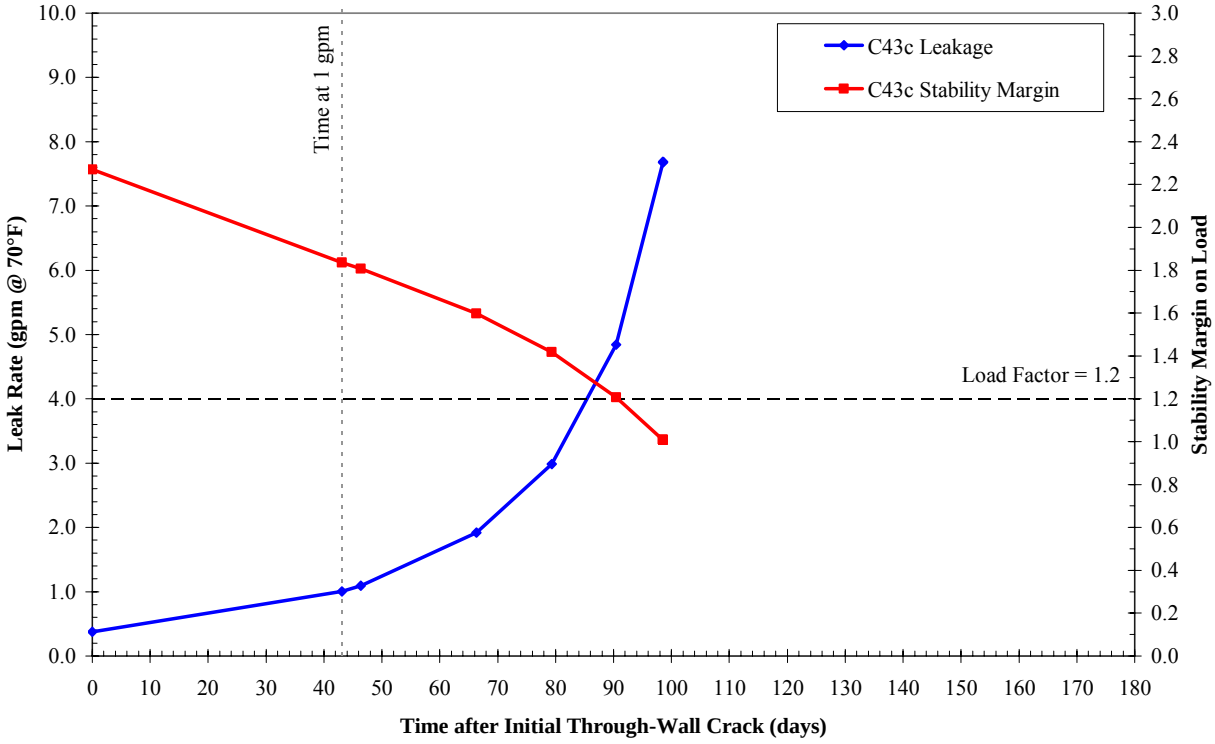

Figure 7-33
Leak Rate and Load Margin Factor as a Function of Time—Case 43c

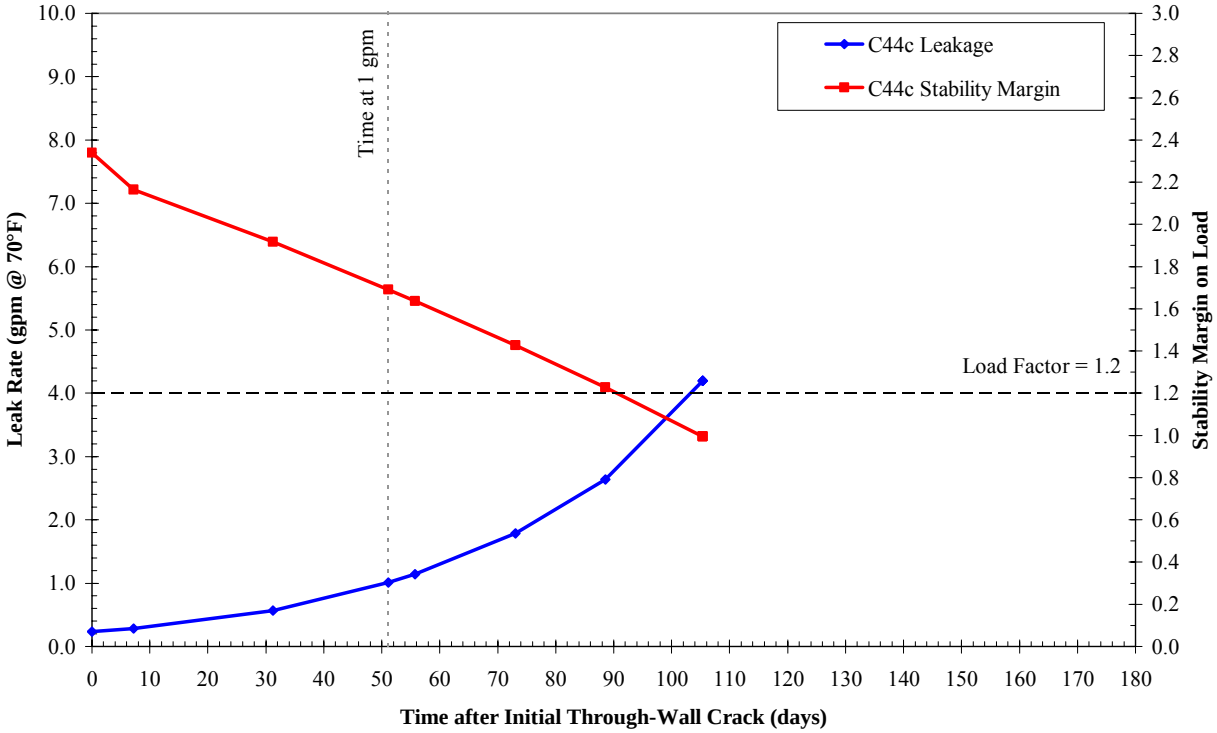

Figure 7-34
Leak Rate and Load Margin Factor as a Function of Time—Case 44c

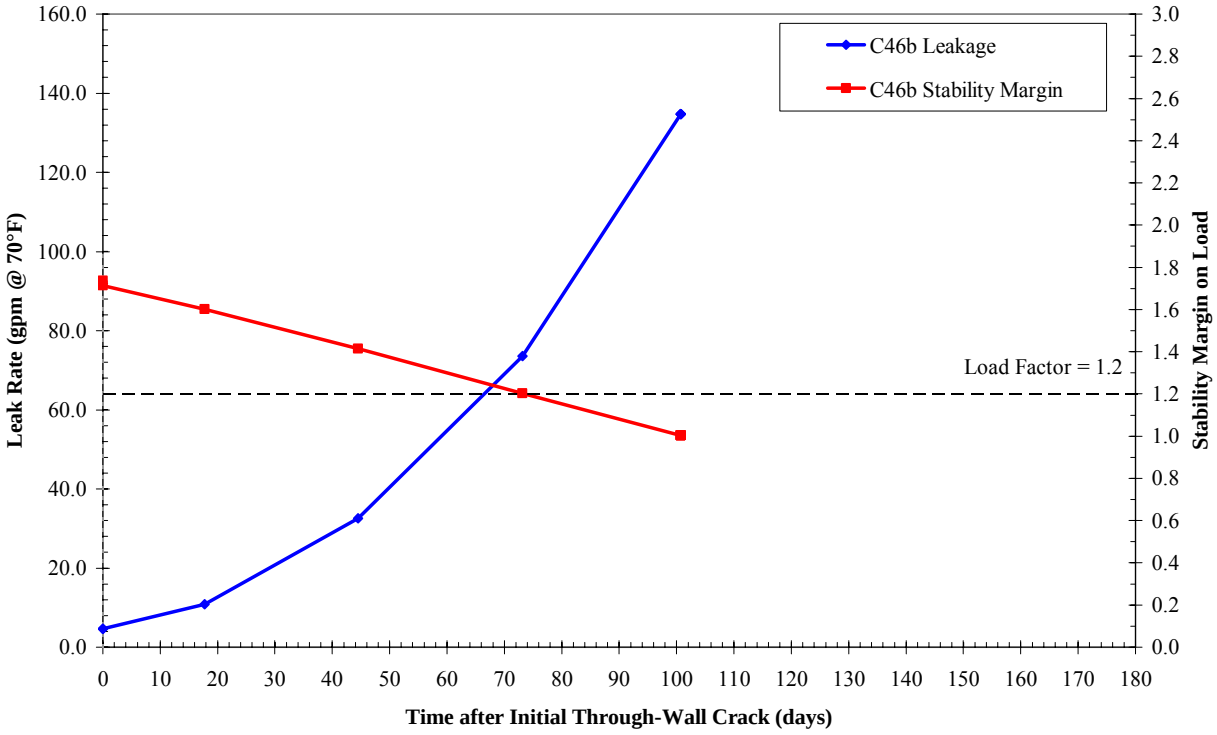

Figure 7-35
Leak Rate and Load Margin Factor as a Function of Time—Case 46b

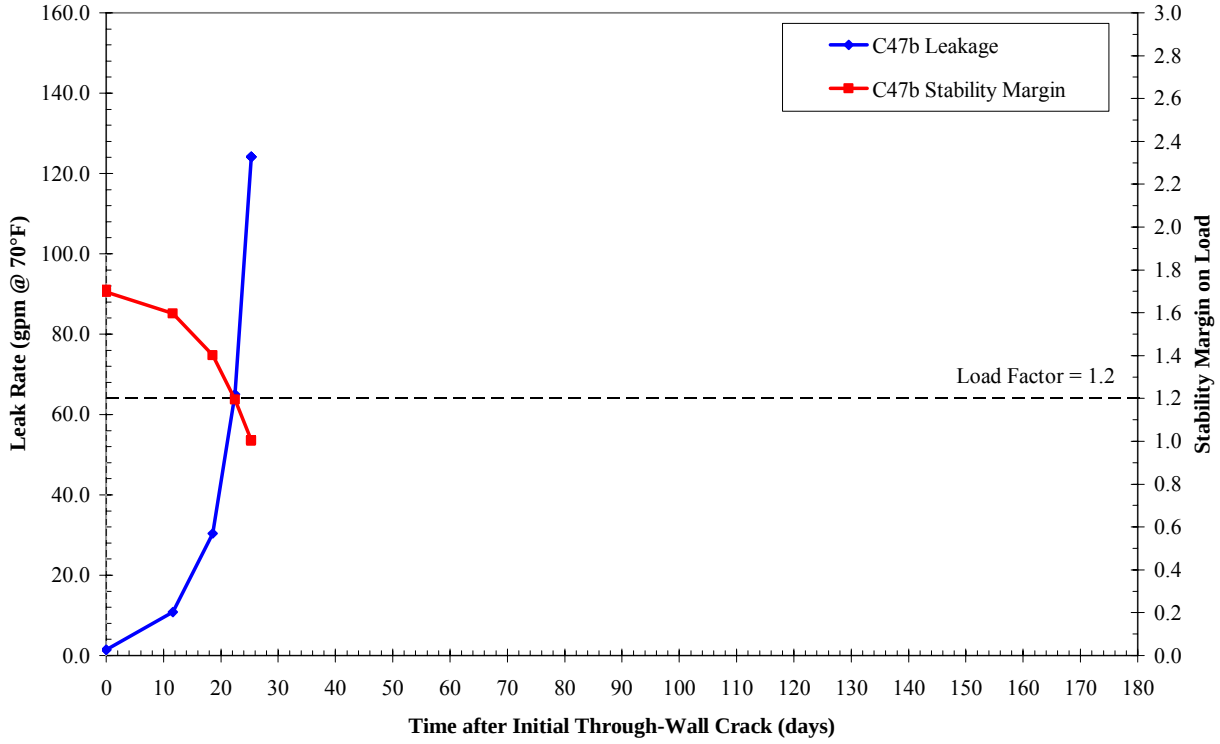

Figure 7-36
Leak Rate and Load Margin Factor as a Function of Time—Case 47b

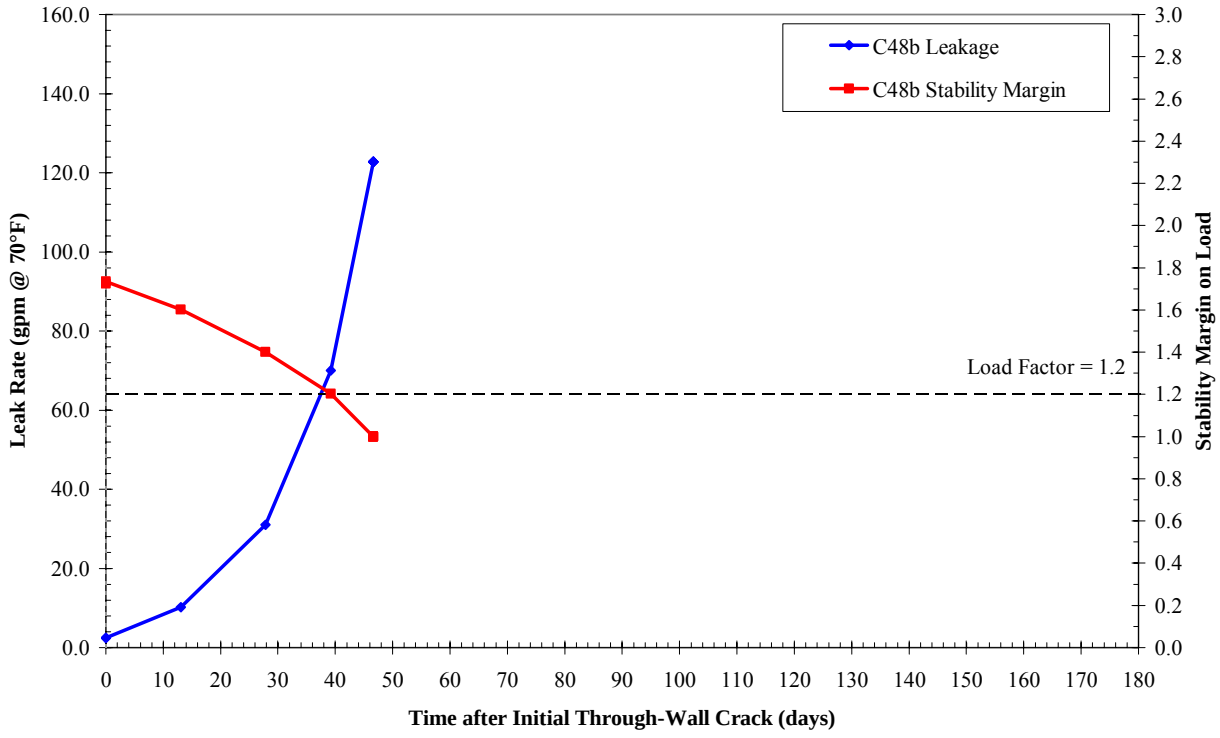

Figure 7-37
Leak Rate and Load Margin Factor as a Function of Time—Case 48b

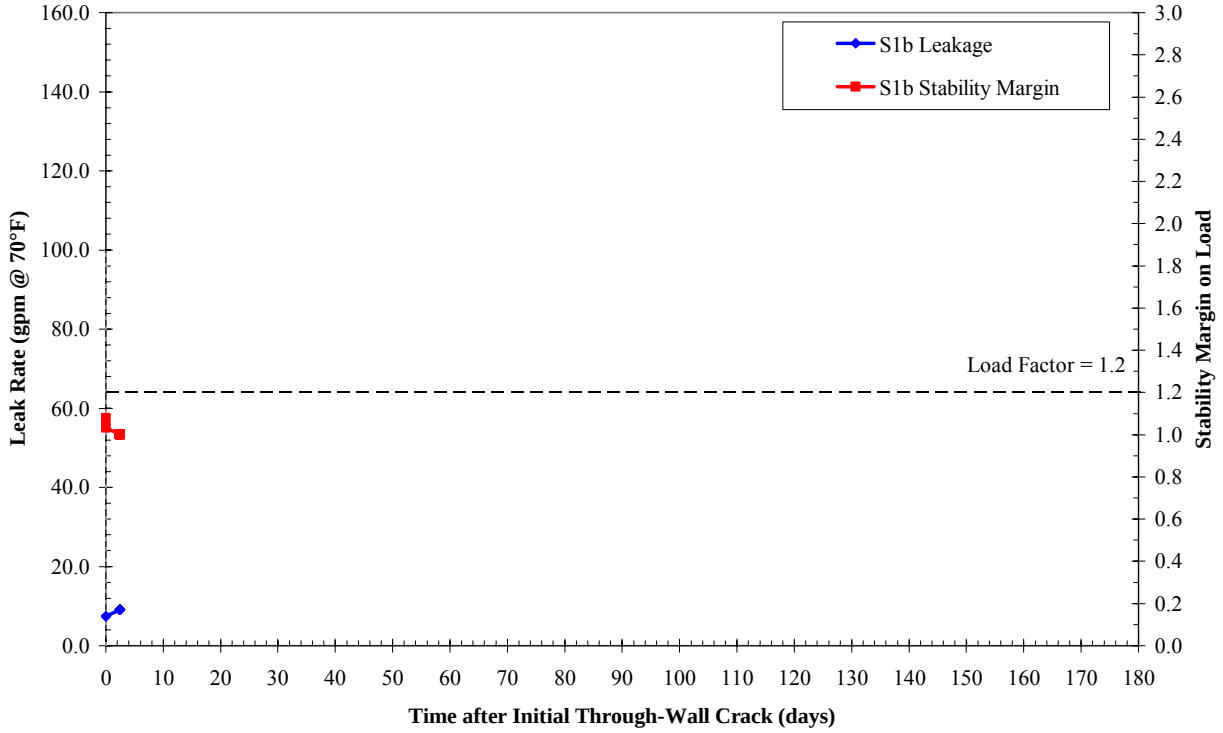

Figure 7-38
Leak Rate and Load Margin Factor as a Function of Time—Case S1b

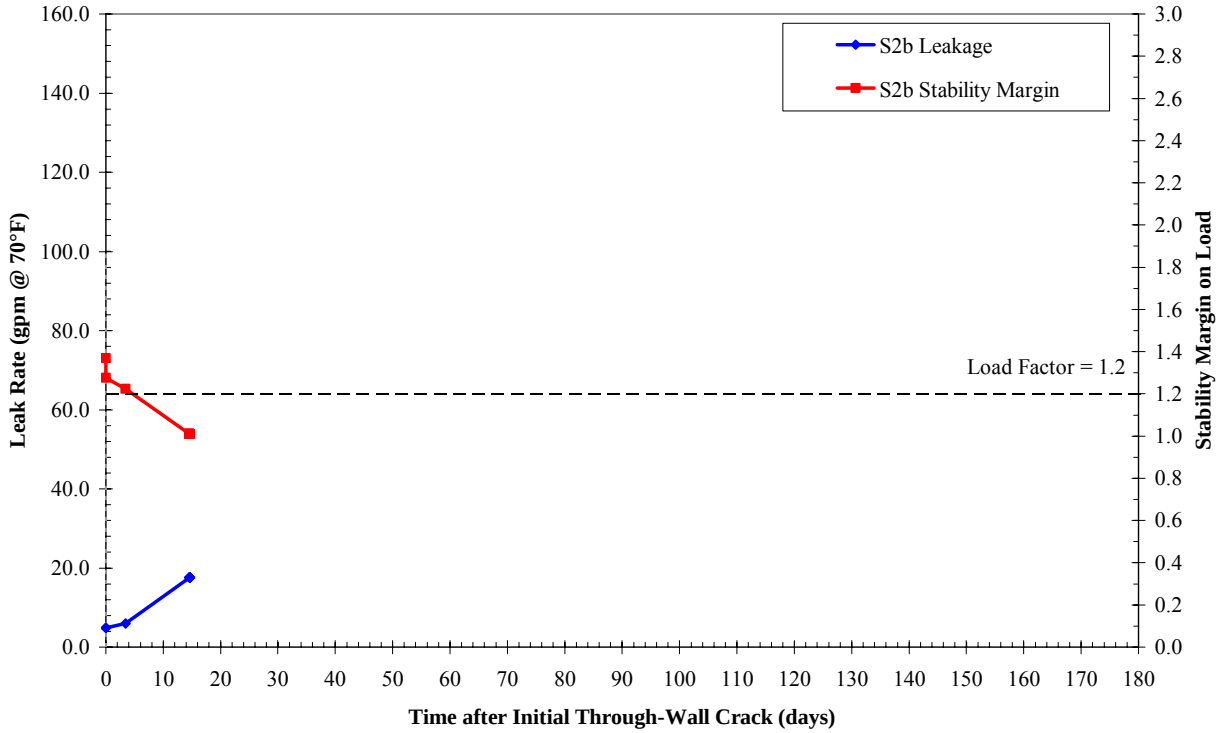

Figure 7-39
Leak Rate and Load Margin Factor as a Function of Time—Case S2b

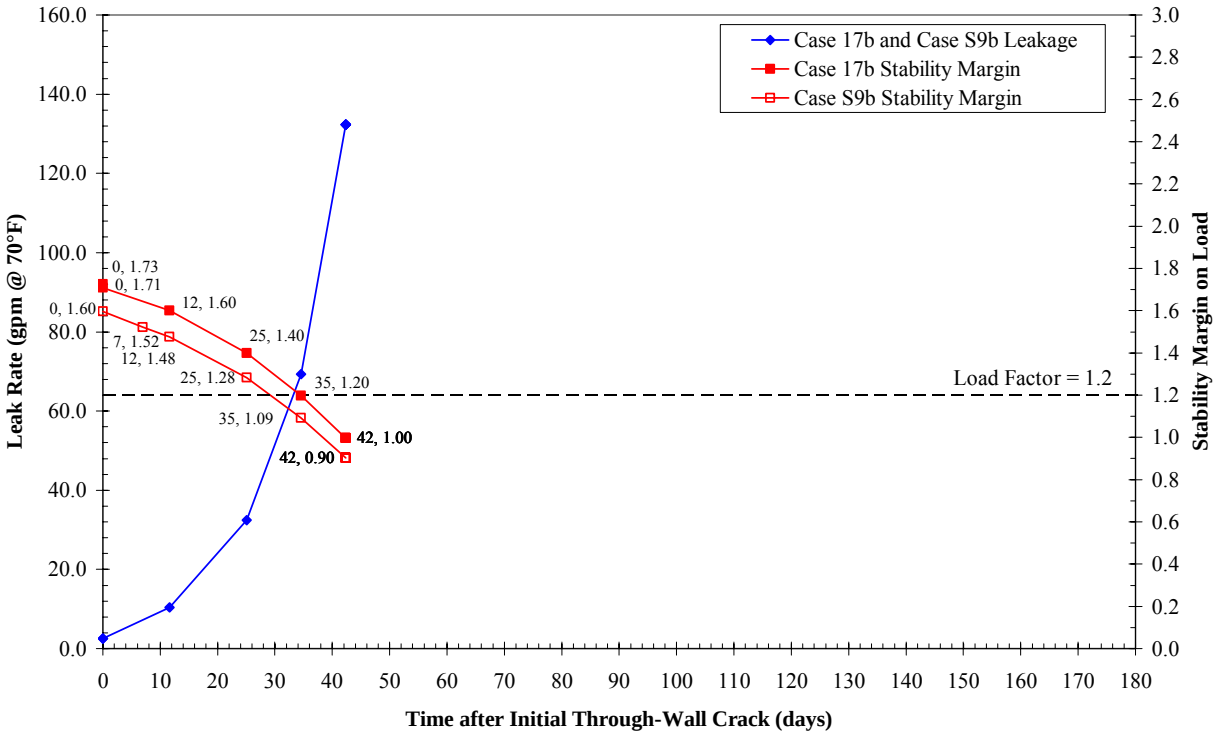

Figure 7-40
Leak Rate and Load Margin Factor as a Function of Time—Case S9b

8
SUMMARY AND CONCLUSIONS

A summary of the findings of this study, including main conclusions, are as follows:

- ELIMINATION OF OVERLY CONSERVATIVE ASSUMPTION OF SEMI-ELLIPTICAL CRACK SHAPE. A calculation methodology has been developed through extensions to the FEACrack software to model the shape progression of a circumferential PWSCC flaw based on the stress intensity factor calculated at each point on the crack front. This refinement in crack growth modeling eliminates the need to assume that the crack shape remains a semi-ellipse grown on the basis of the stress intensity factor at the deepest and surface points. This study demonstrates that this assumption of a semi-elliptical crack shape results in a large overestimation of the crack area and thus underestimation of the crack stability at the point at which the crack penetrates to the outside surface.
- COLLECTION OF PLANT-SPECIFIC INPUTS. Extensive weld-specific design and fabrication inputs were collected for the group of 51 subject dissimilar metal welds. Detailed geometry and piping load inputs were collected for each subject weld to ensure that all welds are appropriately addressed by the crack growth sensitivity matrix developed as part of this study. Weld-specific fabrication and weld repair data were also collected as a key input to the welding residual stress simulations addressing the subject population. The frequency of ID weld repairs in the subject population was found to be significantly less than that for the Wolf Creek pressurizer nozzle dissimilar metal welds.
- WELDING RESIDUAL STRESS SIMULATIONS. A matrix of welding residual stress (WRS) simulations were performed on the basis of the detailed design, fabrication, and weld repair information collected. Axisymmetric and non-axisymmetric weld repair WRS profiles were developed for input to the crack growth simulations under various assumptions in recognition of the uncertainty in calculation of WRS values. Validation work is still being completed comparing WRS simulation results to mockup stress measurements.
- CRITICAL CRACK SIZE METHODOLOGY. A critical crack size methodology was developed specific to the subject nozzle-to-safe-end geometry and materials. This methodology, which was implemented as a post-processing calculation to the crack profiles simulated in the crack growth calculations, is based on the net section collapse (NSC) equations for an arbitrary circumferential crack profile in a thin-walled pipe. Although new calculations and past experimental experience indicate that secondary piping thermal constraint loads will significantly or completely relax prior to rupture, normal thermal piping loads were included in the crack stability calculations. In addition, a Z-factor approach reducing the NSC failure load was implemented in consideration of the possibility of an EPFM failure mechanism. Available experimental failure data for complex cracks in materials similar to Alloy 82/182 show that the implemented critical crack size methodology likely results in conservative predictions of rupture.

- LEAK RATE METHODOLOGY. EPRI's PICEP software was applied to calculate the leak rate development for the simulated through-wall and complex crack profiles. The crack opening area at the weld OD calculated in the crack growth finite-element simulations was applied directly in these PICEP leak rate calculations. NRC's SQUIRT software was also applied in scoping leak rate calculations, and was found to predict slightly higher leak rates than PICEP.

- DEVELOPMENT OF EVALUATION CRITERIA. Based on the detailed input of the EPRI expert panel, a set of criteria were developed to evaluate the results of the crack growth, crack stability, and leak rate calculations for each sensitivity case investigated. These criteria provide guidance for applying the matrix results, and were developed in consideration of the many modeling uncertainties addressed in the detailed calculations performed. The evaluation criteria are based on explicit consideration of leak rate detection sensitivity, plant response time, and uncertainty in the crack stability calculations.

- CRACK GROWTH SENSITIVITY MATRIX DEVELOPMENT. An extensive sensitivity matrix of 118 cases was developed in order to address the weld-specific geometry and load input parameters for the set of 51 subject welds, plus key modeling uncertainties such as those associated with WRS, initial crack shape and depth, the K-dependence of the crack growth rate equation, and the effect of multiple flaws. For most cases a full arc 360° flaw having a depth of 10% of the wall thickness was assumed as the starting flaw. The Phase I scoping calculations indicated that in many cases a relatively long partial-arc surface flaw tends to grow to the same initial through-wall profile as an initial 360° flaw. Thus, the initial 360° flaw geometry was assumed in most cases to simplify the calculations. The assumption of an initial 360° flaw is also a conservative approach to addressing the concern for multiple flaw initiation and growth.

- CRACK GROWTH SENSITIVITY MATRIX RESULTS. All 108 cases in the main sensitivity matrix showed either stable crack arrest (59 cases) or crack leakage and crack stability results satisfying the evaluation criteria (47 cases). (Two other of the 108 cases in the main matrix are still being completed.) In most cases, the results showed large evaluation margins in leakage time and in crack stability.

  Several supplemental cases were added to further investigate the potential effect of multiple flaws in the subject surge nozzles. Conservative application of the three indications found in the Wolf Creek surge nozzle weld for surge nozzles with a fill-in weld and relatively high moment load gives results meeting the evaluation criteria with additional margin. In addition, considering a case with two long initial partial-arc flaws covering 46% of the ID circumference as opposed to a single initial flaw covering half this circumferential extent (and centered at the location of maximum axial bending stress) has only a modest effect on crack stability for these limiting surge nozzles. On this basis, it is concluded that the concern for multiple flaws in the limiting surge nozzles is adequately addressed by those supplemental cases that satisfy the evaluation criteria with additional margin.

  In summary, all 51 subject welds are adequately covered by crack growth sensitivity cases that satisfy the evaluation criteria presented in Section 7.2.

- TENDENCY OF CIRCUMFERENTIAL SURFACE CRACKS TO SHOW ARREST. An additional key finding concerns the significant number of crack growth sensitivity cases that showed stable

crack arrest prior to through-wall penetration. This type of behavior is consistent with the relatively narrow band of relative depths reported for the four largest Wolf Creek indications (23%, 25%, 26%, and 31% through-wall). It is statistically unlikely that these four indications would be found in this narrow depth band if they were in fact growing rapidly at the time they were detected. The basic reason that circumferential cracks may tend to arrest prior to through-wall penetration is that to the extent the through-wall welding residual stress profile is axisymmetric, it must be self-balanced at a particular circumferential position, meaning that a significant portion of the wall thickness must have compressive axial welding residual stresses.

- LARGE BENEFIT GIVEN RELAXATION OF SECONDARY LOADS UPON THROUGH-WALL PENETRATION. Two sensitivity cases showed a greatly increased time between a leak rate of 1.0 gpm and the load margin factor of 1.2 being reached when it is assumed that the piping thermal constraint loads are relieved upon through-wall penetration. These case confirm the expectation of a large benefit if the piping thermal constraint loads are significantly relaxed once the crack grows through-wall. Detailed evaluations tend to support this kind of behavior, but such relaxation was conservatively not credited in the base assumptions of the critical crack size methodology developed for this study.

9
REFERENCES

[For Draft C, the references cited in each individual section will be consolidated in this Section 9.]

1. *Materials Reliability Program (MRP) Crack Growth Rates for Evaluating Primary Water Stress Corrosion Cracking (PWSCC) of Alloy 82, 182, and 132 Welds (MRP-115)*, EPRI, Palo Alto, CA: 2004. 1006696.

2.